A NOVEL CROSS-VALIDATED NONDESTRUCTIVE EVALUATION FRAMEWORK FOR DAMAGE DETECTION USING ACOUSTIC EMISSION

A Thesis
Submitted to the Faculty
of
Drexel University
by
Prashanth Abraham Vanniamparambil
in partial fulfillment of the
requirements for the degree
of
Doctor of Philosophy
June 2014

DEDICATION

With the deepest love, I dedicate this PhD thesis to my beloved mother, Mrs. Anita Abraham and my sister, Ms. Priyanka Anna Abraham for their constant support and above all their love and prayers that has helped me achieve this Doctorate Degree. The initial apprehensions I had were soon transformed to positive reinforcements and in particular my mother's positive attitude, dedication in life for her children and the never say die spirit were the qualities I set in mind when I embarked on this journey towards my doctorate degree. My family has always stressed on the fact that education is the biggest gift that a person can get and this gift can be never be stolen from you. With education you gain wisdom which I shall continuously strive to achieve in life. I love you mom and Pri!!

Yours Lovingly,
Prashanth

ACKNOWLEDGEMENT

I would like to take this opportunity to acknowledge my advisor, Dr. Antonios Kontsos, who has been extremely supportive and a wonderful mentor throughout my research with the utmost patience and belief. His thoughtful and philosophical advice has helped me immensely in mitigating the hardships encountered and taught me some valuable lessons which I shall cherish forever. He has always given me the free will to learn!! Thank You Dr. Kontsos!!! I would also like to express my gratitude to my co-advisor, Dr. Ivan Bartoli, whose invaluable guidance and support has been instrumental in this research. I have learned quite a lot from him and the conversations we shared have always been enjoyable and valuable.

This research would not have been possible and importantly an enjoyable experience, if I had not got the opportunity to work with my lab colleagues, who are now my friends, Kavan Hazeli, Jefferson Cuadra, Shane Esola, Rami Carmi, Raghavendra Saralaya, Eric Schwartz, Satish Rajaram, Alison Krick, Lara Branco, Andrew Ellenberg, Aditi Ramadurgakar, Fuad Khan and Greg Hiley. I am thankful for such a great team and these memories shall last eternity.

I would like to extend my gratitude to the Department of Mechanical Engineering & Mechanics and the Office of Graduate Studies for their support throughout my years in Drexel University.

LIST OF FIGURES

ABSTRACT

A NOVEL CROSS-VALIDATED NONDESTRUCTIVE EVALUATION FRAMEWORK FOR DAMAGE DETECTION USING ACOUSTIC EMISSION

Prashanth Abraham Vanniamparambil
Advisor: Antonios Kontsos, PhD

Developing Structural Health Monitoring (SHM) techniques for monitoring and evaluation in civil, mechanical and aerospace applications has a direct impact on public safety, primarily because it is related to reduced downtime and life extension of critical aging components and structures. Such trends are further fueled by the observed shift in modern inspection from "time-based" to "condition-based" maintenance approaches, which promise targeted evaluations when and exactly where they are needed. In this context, the objective of this dissertation is to develop a novel cross-validated framework of using acoustics-based methods for non-destructive testing & evaluation (NDT&E) with the ultimate goal to improve infrastructure condition assessment related primarily to the aerospace industry. This framework is called cross-validated as the primary NDT method of interest, the Acoustic Emission (AE) method, is used in conjunction with several other NDT methods including Guided Ultrasonic Waves (GUW), Digital Image Correlation (DIC) and Infrared Thermography (IRT). The proposed work is built therefore upon the idea of implementing a multimodal NDE approach including both novel hardware integration and data processing techniques that can mitigate existing challenges in reliably using AE in SHM applications. The advantage of designing reliable damage detectors is realized by integrating acoustic features with heterogeneous features that can provide complementary information on the initiation and development of damage. Several demonstrations in static and dynamic conditions of the proposed framework ranging from fundamental plasticity investigations to applied structural analysis are described to demonstrate the efficacy of the novel approach.

TABLE OF CONTENTS

This page is intentionally left blank

CHAPTER 1: MOTIVATION

1.1 RESEARCH SYNOPSIS

Acoustic Emission (AE) has shown tremendous promise to transition from a laboratory material characterization technique to a reliable Structural Health Monitoring (SHM) technique [1-5]. In particular, AE provides certain unique advantages over other nondestructive testing (NDT) techniques. Specifically, AE can be utilized to track the **onset and progressive development of damage**. Additionally, it can be utilized to determine the location of damage in real time. However, the widespread use of AE for reliable damage detection is inhibited despite these unique characteristics, advances in AE instrumentation and improved signal processing techniques. Currently, the reliability of AE for various structural applications particularly aerospace monitoring has been an issue due to mainly lack of quantification of the recorded data, as well as difficulties in interpreting received AE signals due to complex wave propagation characteristics in structural geometries. The motivation of developing a reliable AE approach is therefore to identify early signs of structural deterioration and flag the presence of critical damage long before macroscopic failure is achieved. Such an approach would directly impact public safety and even change the current time-based maintenance mode to a condition-based mode.

This research introduces a novel AE framework built on extensive experimental testing, the use of full field optical imaging techniques, advanced signal processing techniques and **consequently developing new AE damage parameters** to reliably flag **the onset of damage** with the ultimate goal for in-situ damage detection. A summary of the research process is illustrated in the form of a quad chart in Figure 1.

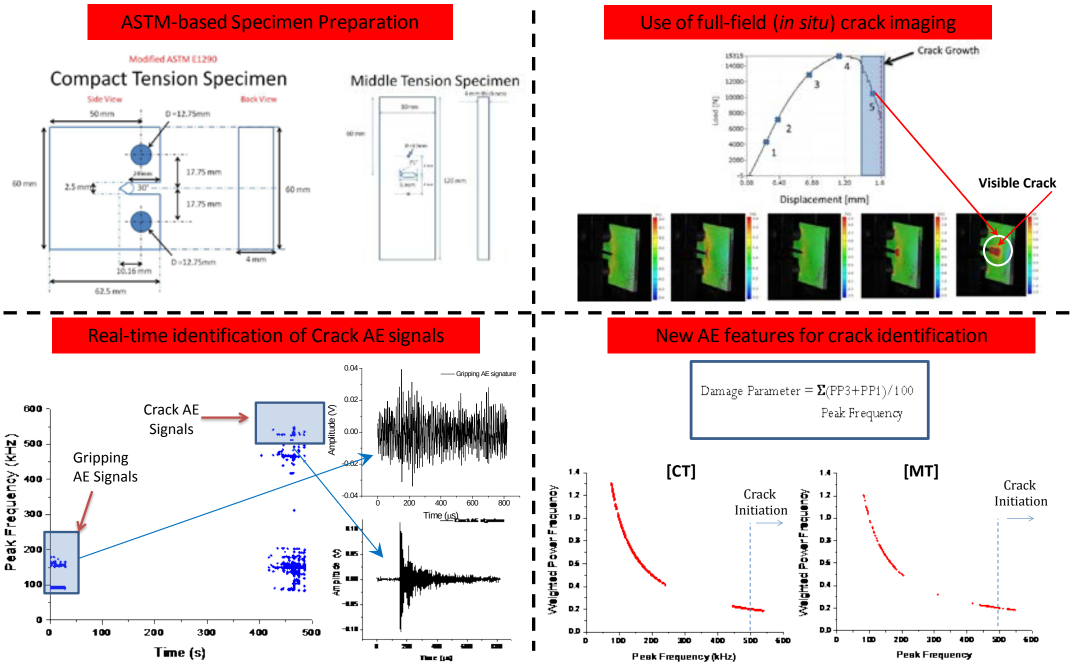

Figure 1: Research Overview

1.2 MOTIVATION

The need for developing reliable nondestructive testing and evaluation (NDT&E) methods for structural health monitoring (SHM) approaches is driven by the large number of ageing structures and the economical resources available for their maintenance. Such trends are further fueled by the observed shift in modern inspection from the so-called "time-based" to "condition-based" maintenance approaches, which promise targeted evaluations when and exactly where they are needed. Such maintenance programs could greatly minimize unwarranted inspection costs while significantly reducing downtime associated with regular maintenance. A critical motivating factor to accomplish such a shift in the maintenance practices would be the development of techniques for early detection of structural deterioration which could contribute towards preventing catastrophic disasters and the development of irreversible deterioration conditions.

An example of interest in recent history that motivates research in this field is the midair rupture in the roof of a Southwest Airline jet in April 2011 as seen in Figure 2[6]. The cause of rupture was attributed to the fatigue cracks developed near the rivets of the fuselage as a result of repeated take-off and landing of the aircraft. Notably, a comprehensive inspection check (D-check) was performed prior to this incident in which no ominous cracks were detected. In fact, modeling and previous flight data assumed that no crack development was possible in this region of the fuselage. Upon further inspection, several other flights were found to have similar crack development in the fuselage and this incident prompted aircraft manufacturers to identify and design a maintenance program tailored for this section of the aircraft.

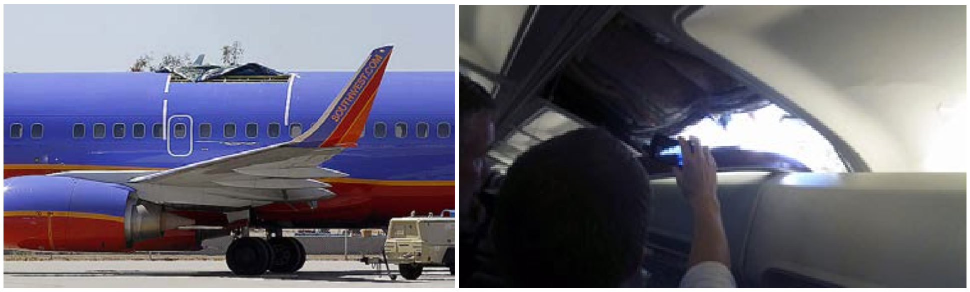

Figure 2: Mid-air rupture in the roof of an airline [6]

Furthermore, and over the past decades there has been an increasing use of fiber reinforced composites in modern aircrafts. Two of the newest airlines, the Airbus A380 [7] and the Boeing 787 Dreamliner [8] utilize a large percentage of carbon fiber composites for their fuselage, wing box and their tail fins. These advanced engineering materials provide significant benefits over traditional metallic materials, since they are light weight and have a better strength to weight ratio, while they are also corrosion resistant and have increased fatigue resistance. However, composites are also known to have low impact resistance and high manufacturing and maintenance costs. Additionally, damages caused by impact loads on composites are not always visible on the surface yet cause internal defects that reduce the strength of structures significantly [9] while they are hard to detect by surface or visual inspection methods [10]. In fact, when detailed investigation of the aircraft wings was performed due to engine debris impacts, it was revealed that several cracks were seen on the brackets that connect the external skins to the central spars [11] as seen in Figure 3. Also, additional inspection of similar other aircrafts revealed the same cracking phenomenon with cracks between the vertical flanges and the wing spars.

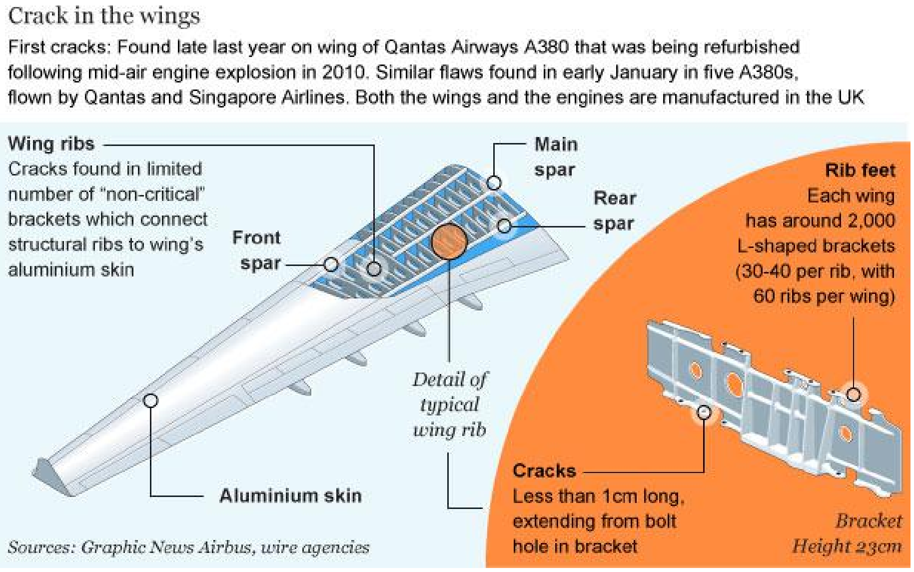

Figure 3: Cracking in wing spars [11]

In order to address these issues and ensure structural integrity of aircrafts even during periodic inspection cycles, Airbus proposed a stepwise SHM roadmap for optimal structural maintenance as depicted in Figure 4 [12]. To realize the final goal of efficient maintenance and quality control for in-service monitoring, it is essential to integrate on-line sensors that are capable of diagnosing the current state of the structure and provide information that is sensitive to damage. Hence, it becomes imperative to utilize volumetric inspection techniques to continuously scan the structure and report any anomalous activity observed while in service so that such incidents can be detected well in advance. Thus, there is an instant need to develop reliable condition-based maintenance techniques capable to notify engineers of the current integrity of the structure.

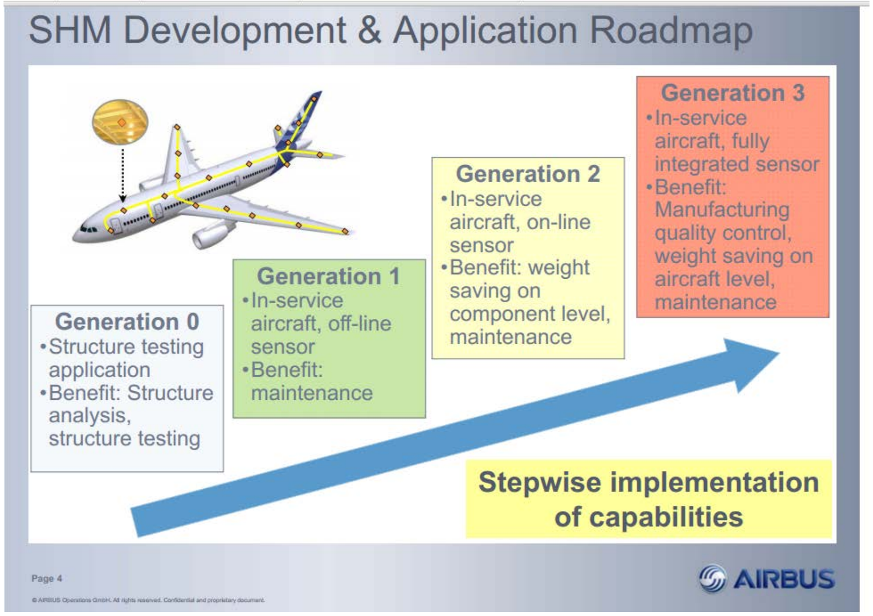

SHM Development & Application Roadmap

Generation 0
- Structure testing application
- Benefit: Structure analysis, structure testing

Generation 1
- In-service aircraft, off-line sensor
- Benefit: maintenance

Generation 2
- In-service aircraft, on-line sensor
- Benefit: weight saving on component level, maintenance

Generation 3
- In-service aircraft, fully integrated sensor
- Benefit: Manufacturing quality control, weight saving on aircraft level, maintenance

Stepwise implementation of capabilities

Page 4

© AIRBUS Operations GmbH. All rights reserved. Confidential and proprietary document.

Figure 4: Airbus SHM roadmap [12]

1.3 THESIS STRUCTURE

This research addresses some of these goals by introducing a novel cross-validated approach for damage detection using AE. Chapter 2 presents a detailed background on the theory and the current state of the art approach to deconvolve the complex AE signals. Chapter 3 provides detailed information on the proposed novel AE framework designed for reliable detection and proposed vision of this research. Chapter 4 presents the author's experimental work performed on understanding the fundamental origins of

AE in various materials from local plasticity to global yielding in metallic materials. This chapter sets the tone for investigating a wide range of AE features and selecting specific AE features sensitive to known AE sources.

Chapter 5 presents a novel approach in detecting the onset and quantifying the crack growth using data mining techniques. Particular, this chapter provides a detailed experimental procedure utilized to reliably flag the presence of crack in aluminum alloys using a novel AE damage parameter. Chapter 6 presents the extension of this acoustic approach to detect the onset of debonding in carbon fiber reinforced polymer skin stiffener components. Particularly, pattern recognition algorithms are implemented based on existing and novel AE feature descriptors to distinguish and identify the AE signals associated with debonding.

Chapter 7 illustrates the application and validates the use of an integrated acoustic approach for Civil SHM applications. Specifically, the unique advantage of utilizing full field optical techniques with AE is demonstrated and importantly, a new approach to quantify the behavior of partially grouted masonry walls is presented. Finally, chapter 8 provides recommendations and the roadmap ahead for this research and highlights the major contributions of this research.

CHAPTER 2: AE METHOD

2.1 NONDESTRUCTIVE EVALUATION

Nondestructive evaluation (NDE) is formally defined as the development and application of technical methods to examine materials or components in ways that do not impair future usefulness and serviceability in order to i) detect, locate, measure and evaluate flaws; ii) to assess integrity, properties and composition; and iii) to measure geometrical characteristics [13]. The terms, NDE and Nondestructive Testing (NDT) terminologies are often interchangeably used in the literature to describe the process involved in assessing the quality of the structural integrity without affecting its future usefulness. However, in this thesis, NDT refers to the physical process (including setup) involved in examining material defects while NDE refers to the comprehensive process that includes NDT and the further analytical process involved in evaluating and post processing the observed indications obtained from the application of one or more NDT methods.

The basic process flow involved in NDE is described in Figure 5. NDT relies upon the use of instrumentation but is not limited to sensors to record data and observe and identify initial indications (response of the recorded data) about the material/structural quality. Subsequently, the indications are then analyzed and interpreted to determine if the observed indication is false, non-relevant or relevant. If the indications are false or non-relevant, often caused by spurious sources such as operational or environmental conditions, then the NDE process is terminated. Conversely, if the initial indications are relevant (damage/flaw), the recorded signals are comprehensively evaluated, identified and further processed. Consequently, based on the evaluation of the signals and damage tolerance criteria established during the formulation of the NDE process, the recorded signals are accepted or rejected

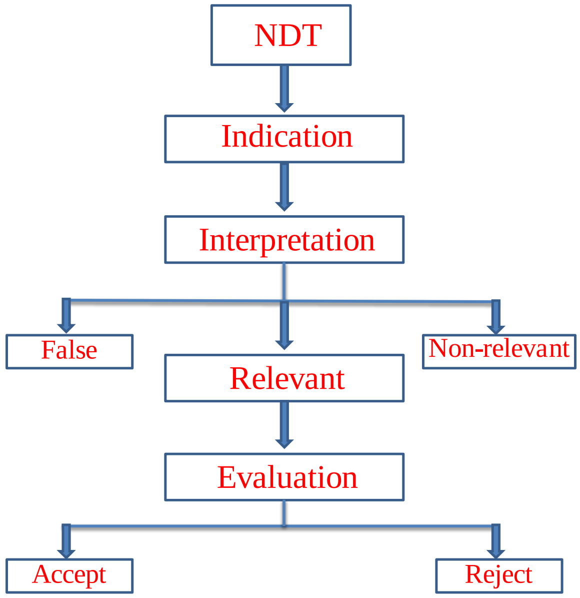

Figure 5: NDE Process Flow [13]

Critical to the NDE process flow is accuracy in detecting damages and minimizing the false positive signals. In order to achieve this successfully, the concept of damage must be well defined. The term 'damage' assumes slightly different variations from a mechanical (continuum mechanics) and physical perspective. From a continuum mechanics standpoint, damage is defined as the creation and growth of micro voids or micro-cracks which are discontinuous in a medium considered as continuous at a larger scale. From a physical standpoint, damage is referred to as an irreversible change that results in a significant strain accumulation in the material [14]. Examples of damage at different length scales i.e. micro-scale, meso-scale and structural scale is illustrated in Figure 6.

Figure 6: Damage scale (a) micro-scale [15] (b) meso-scale (c) structural scale

The integrity of the structure is greatly compromised by the presence of damage which could result in unfortunate disasters that directly affect public safety and property. In order to prevent such disasters, several NDT tools that operate on different principles are adopted and employed with the goal to identify, locate and assess the severity of damage. The effective use of NDT techniques for diagnostics depends on several factors including nature of damage sought, structural geometry, material condition, limitations associated with the inspection tools and economic factors. For instance, if the objective of the evaluation process is simply to determine if a defect/flaw is present, then certain techniques such as dye penetrant testing, thermography, ultrasonic testing, eddy current testing, acoustic emission, radiography, advanced visual techniques etc. would be sufficient to perform this task. However, if certain limitations surrounding the evaluating process are present such as lack or limited access to the potential damage region, material type (metallic vs. non-metallic) or minimal surface preparation, then the list of above mentioned NDE tools is reduced. Furthermore, if the objective is to assess the quality of the structural integrity and locate the damage region, then only inspection techniques that can perform a volumetric scan of the structure will suffice. Another major factor associated with structural inspection is the cost. Detailed section by section inspection could result in huge cost and loss of revenue due to the labor, downtime and energy required to do so. Thus, it is important to realize and understand the purpose of the evaluation process, the nature of the medium, the associated costs, and the theory of the NDE technique used and more importantly their limitations. The major NDT techniques utilized for a wide range applications and its working principle is presented in TABLE 1.

Visual inspection is the most basic and widely used NDT technique employed for various applications and utilizes either direct contact or remote access tools. Direct contact visual tools include mirrors magnifying glasses, etc while remote access tools relies upon the use of visual tools such as borescopes [16], fiberscopes [17] and other advanced video techniques for structural component inspection. Traditionally, inspection techniques on structural components are carried out on a time based maintenance mode. Typically, structures are first visually inspected after certain periods (cycles or years depending on the structural domain) in service and followed up with other NDT techniques such as eddy current inspection or ultrasonic testing for further detailed damage characterization.

TABLE 1: Major NDT Techniques [18]

METHOD	PRINCIPLES	APPLICATION	ADVANTAGES	LIMITATIONS
VISUAL INSPECTION	Uses reflected or transmitted light from test object that is imaged with the human eye or other light sensing device	All materials	Inexpensive, minimal training,	Requires direct access to the damage material and surface preparation, restricted to surface damage, high illumination necessary,

PENETRANT TESTING	A liquid containing fluorescent dye is applied to surface and the discontinuity is mapped by the trapping of the dye	Most materials that are nonabsorbent	Inexpensive, high sensitivity, minimal training, versatile	Requires direct access to the damage part and surface preparation, restricted to surface damage, challenging in porous or contaminated materials
MAGENETIC PARTICLE TESTING	Test part is magnetized and the discontinuity/defect is mapped by the alignment of the ferromagnetic particles	Ferromagnetic materials	Ease of use, high sensitivity, quick	Requires direct access to the damage part and surface preparation, restricted to surface and subsurface damage, only ferromagnetic materials
RADIOGRAPHIC TESTING	The exposure of the radiographic film is affected by the discontinuity/defect	Most materials	Permanent record of the damage, extremely sensitive to both surface and internal damage, limited direct access required	Health hazard, orientation of planar discontinuity is critical
ULTRASONIC TESTING	High frequency waves are inputted and the discontinuity/defect is defected from the reflection of waves	Most materials that don't have air gaps	Highly sensitive to surface and internal damage, damage characterization capabilities, limited direct access required	Orientation of defect is critical, material attenuation, sensitive to the impedance of the material
EDDY CURRENT TESTING	Localized electrical fields are inducted into a conductive test specimen by electromagnetic induction	All conductive materials	Quick, non-contacting, adaptable for in-situ monitoring	sensitive to only surface and subsurface, limited to conductive materials, lift off effects
THERMAL INFRARED TESTING	The discontinuity/defect are detected by temperature variations using thermal cameras	Thermally conductive materials	Provides permanent record of damage, quick inspection, inexpensive	Surface and sub surface defects only, high skill level essential

ACOUSTIC EMISSION TESTING	Discontinuity/defect release stress waves within the material that are picked up by sensors	Most materials	In situ monitoring, requires no direct access to damage, tracks the dynamics of damage process, Sensitive to surface and internal defects and predict the failure	High skill set required, highly sensitive to pseudo sources and noise, challenging to quantify damage, history of testing is beneficial

Although NDE techniques are primarily utilized for damage detection, they are also widely utilized for material characterization, property determination [19-23] and structural health monitoring [24-27].

2.2 STRUCTURAL HEALTH MONITORING (SHM)

NDE plays an important role in designing next generation SHM application. Typically structural components are either inspected periodically, e.g. every 2 years [28] or every 500 flight cycles [29] based on industry standards through the use of several NDT techniques. These periodic maintenance procedures are carried out on components critical by design, or designated as damage prone by previous inspections or based on historical records [30]. This method of periodic inspection has shown to be insufficient in detecting damage precursors to prevent structural disasters. Hence, currently there is the need to shift from periodic maintenance to condition-based maintenance where an "intelligent" system could provide signs of structural anomalies developed during operation. To achieve this, there is need to shift to SHM systems that can provide on demand information about the physical condition of the structure.

In general, SHM is defined as the process of implementing a damage detection strategy for aerospace, civil and mechanical infrastructures [31]. However, in particular for aerospace structures, SHM is defined as "the continuous, autonomous in-service monitoring of the physical condition of a structure by means of embedded or attached sensors with minimum manual intervention to monitor the structural integrity [32]. This definition of SHM stems from the desired shift of periodic (time or cycles) based maintenance procedures to condition (length/state of damage) based inspection which requires sensing systems that are integrated with the structure and are capable to notify the operator in real-time about the initiation of new and/or the development of existing damage. Farrar [19] and Sohn [33] describe the SHM concept as a comprehensive process that utilizes sensing platforms to identify and extract damage sensitive features and perform statistical analysis on the extracted features to identify the structural integrity in real time. This comprehensive SHM strategy is illustrated in Figure 7.

Damage identification in SHM is a comprehensive strategy involving a four step process [34] consisting of: i) Operational Evaluation, ii) Data Acquisition, normalization and cleansing, iii) Feature Extraction and data condensation; and iv) Statistical Modal development. In Operational Evaluation, the socio-environmental conditions governing the structural performance are identified. This step enables the engineer to factor in the potential damage sources influencing the structure and decide between global and local techniques. Additionally, the limitations on acquiring data in the operational environment are identified. This also factors in the input received from designers, maintenance workers, financial analysts and regulatory officials [35]. The evaluation of this process is dependent on the operator's experience and prior information. In Data Acquisition, a combination of inspection methods and the kind, number and location of appropriate sensors are decided. Since, the accuracy of damage detection is highly dependent on the recorded signals, it is imperative to set up a filtering technique to remove the environmental noises and other spurious sources. In addition, given that the intensity of recorded values can fluctuate drastically, it is advantageous to normalize the data. In the Feature Extraction step, an attempt to extract features sensitive to specific damage sources is performed. Since environmental conditions such as hail or rain can also be recorded by the acquisition system, it is imperative to cautiously select damage-sensitive features. In addition, since many damage identification techniques are intended to be implemented for continuous monitoring it is also favorable to condense the recorded data for memory storage. Finally, in the Statistical Modal development, the goal is to develop an algorithm to assess the condition of the damage by processing the recorded activity. Designed algorithms can be based on supervised or unsupervised modes of learning as described later in this report. When prior information regarding both the damaged and undamaged state of the structure is available, the mode of learning is referred to as supervised, whereas when information regarding the damaged structure is not available, it is referred to as unsupervised.

The development and implementation of effective SHM has the potential to significantly revolutionize the maintenance process with targeted inspections on structures at specific locations only if absolutely warranted. Specifically, with the introduction of advanced engineering materials and novel manufacturing concepts in the construction of aero-structures that are not fully yet characterized and evaluated, there is a critical need to implement SHM tools to detect critical changes in the material that could result in catastrophic disasters. Additionally, the realization of SHM system will also greatly benefit structural owners in adopting time efficient inspection protocols that could result in minimal downtime and economical benefits.

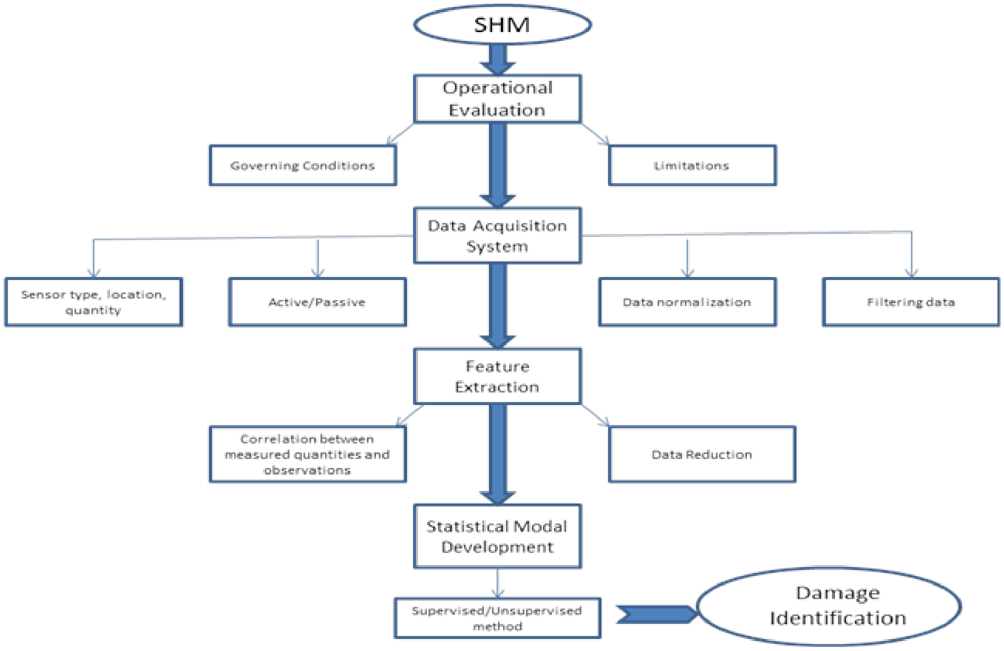

Figure 7: Concept of SHM

2.3 ACOUSTIC EMISSION

Among the various NDT techniques adopted, only certain methods can be extended to SHM applications due to the requirement of providing 'on-demand' continuous information during in-service monitoring. Central to the success of a SHM system is to diagnose early signs of damage irrespective of the location of the attached/embedded sensing platforms. In this context, Acoustic Emission (AE) is a powerful NDE technique that has the capability to transition from a NDE tool to a reliable SHM method. The AE is the "class of phenomena whereby transient elastic stress waves are generated by the rapid release of energy from localized sources within the material" [13,18,36,37]. Thus, all class of materials ranging from fundamental metals to novel metamaterials produce AE when subjected to external loading. These loading sources include mechanical, thermal and chemical excitations.

2.3.1 CONCEPT OFAE TESTING AND ITS SIGNIFICANCE

Damage sources release energy stored in the material when it is subjected to externally applied loads [38]. In the case of metals, these sources include plastic deformation mechanisms, phase transformations, fatigue and corrosion cracking, while in composites AE sources include impact damage, debonding, fiber fracture etc. The elastic waves generated in the medium travel in the form of high frequency waves when subjected to external loading (typically in the range 30kHz - 1MHz). The waves travel along the continuum with a circular wave front and are subsequently recorded by AE sensors mounted at various locations along the object's surface. The concept of AE testing is depicted in Figure 8. These stress waves create a local mechanical vibration on the surface of the material as they propagate radially outwards. Typically, piezoelectric sensors are utilized to convert these local mechanical vibrations to electrical voltage signals which are then fed to a data acquisition system. These signals are then comprehensively analyzed and several signal processing tools are employed to extract sensitive features from the recorded AE waveforms. Threshold based AE feature descriptors are commonly extracted from the received waveforms (e.g. amplitude, rise-time, counts, duration) as shown in Figure 9a. Additionally other features in the time domain are also extracted such as energy, counts to peak, absolute energy etc. Furthermore, the acquired AE waveforms are also analyzed using Fast Fourier transforms (FFT) (Figure 9b) to extract frequency domain characteristics such as frequency centroid, peak frequency etc. The measure of the value of these features could be directly related to the severity of damage induced in the material.

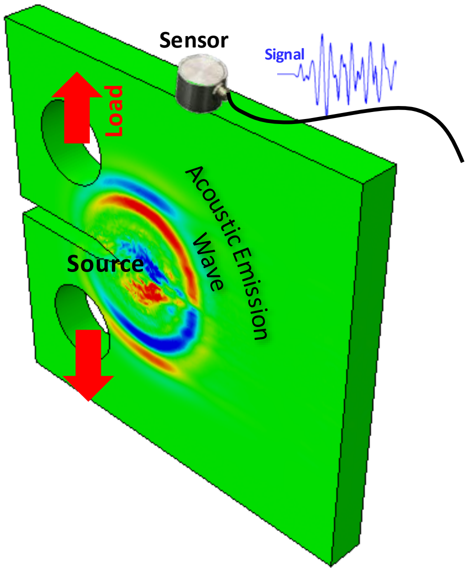

Figure 8: AE Testing

The significant aspects that make AE a unique SHM tool in comparison with other NDE techniques are the following. First, AE testing is a **passive** technique i.e. the energy is released by the test object itself rather than an external source, as in the case of ultrasonic testing or eddy current testing. Second, the use of multiple sensors permits not just the detection of damage but also the **location** of the region of damage in real time. Third, AE testing can be used to identify the **dynamic degradation**, i.e. it detects movement rather than geometrical discontinuities of material allowing it to detect both the onset and progressive nature of the damage. These unique capabilities of AE testing make it an attractive SHM tool as it can be used for i) in-service monitoring, ii) intelligently and efficiently direct other NDE characterization techniques to specific regions and minimize structural downtime and iii) formulate damage prognostics framework for efficient usage of the structure.

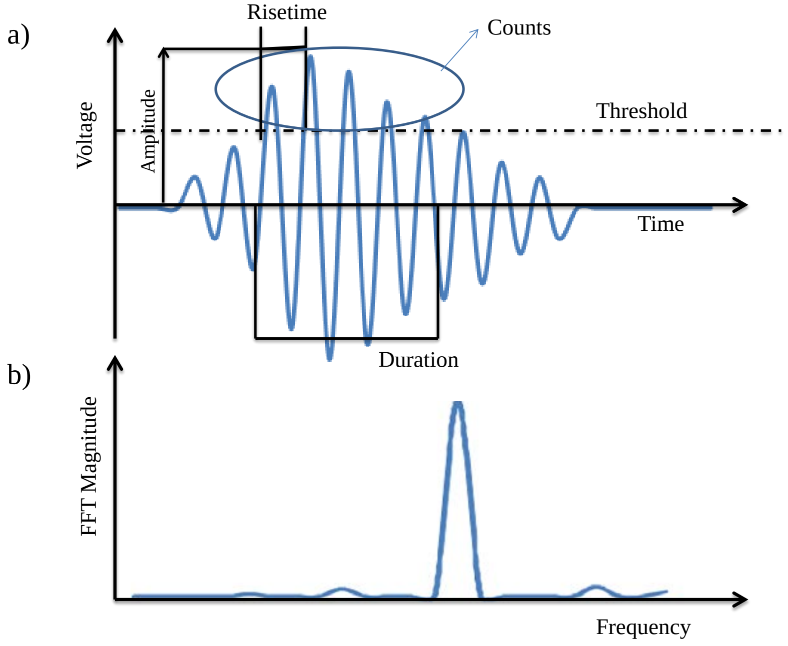

Figure 9: AE Feature Extraction (a) Temporal domain (b) Spectral domain

An overview of the factors that tend to affect the relative amplitude of the recorded AE signals is provided in TABLE 2. It should be mentioned that these factors that tend to decrease the amplitude of the AE signals are not limitations but rather provide a general idea regarding the conditions for which AE can be utilized for material characterization and damage detection as well. As a result, AE testing has been used for various applications including material characterization [39, 40], fatigue crack growth monitoring [41, 42], wire breaks in bridge cables [43], debonding in composite structures [44] and failure mode characterization in fiber reinforced composites [45-47]

TABLE 2: Factors affecting the amplitude of AE signal [37]

Increase	Decrease
High strength	Low strength
High strain rate	Low strain rate
Low temperature	High temperature
Anisotropy	Isotropy
Heterogeneity	Homogeneity
Thick sections	Thin sections
Brittle failure	Ductile failure
Material containing discontinuities	Material without discontinuities
Martensitic phase transformations	Diffusion controlled phased transformation
Crack propagation	Plastic deformation
Cast materials	Wrought materials
Large grain size	Small grain size
Mechanically induced twinning	Thermally induced twinning

2.3.2 AE METHODOLOGY

In order to address some of the challenges mentioned and develop AE as a reliable SHM technique, several aspects of AE testing are being widely researched upon and developed. A general methodology utilized for damage detection using AE testing is summarized in Figure 10. The AE damage identification strategy is the effective integration of both hardware and software approaches. For instance, innovative approaches are concurrently being investigated on multi-physics based sensing platforms and data fusion techniques to reliably identify and cross-validate the presence of damage in the structure. The damage identification process of AE spans different aspects including forward based approaches involving physics based modeling of AE sources, the use of multi-modal sensing platforms, optimization of data filtering, location and synchronization algorithms, combination of multi-phenomenon NDT techniques for cross validation, data fusion approaches based on multi-variate approaches, and advanced signal processing techniques using pattern recognition analysis

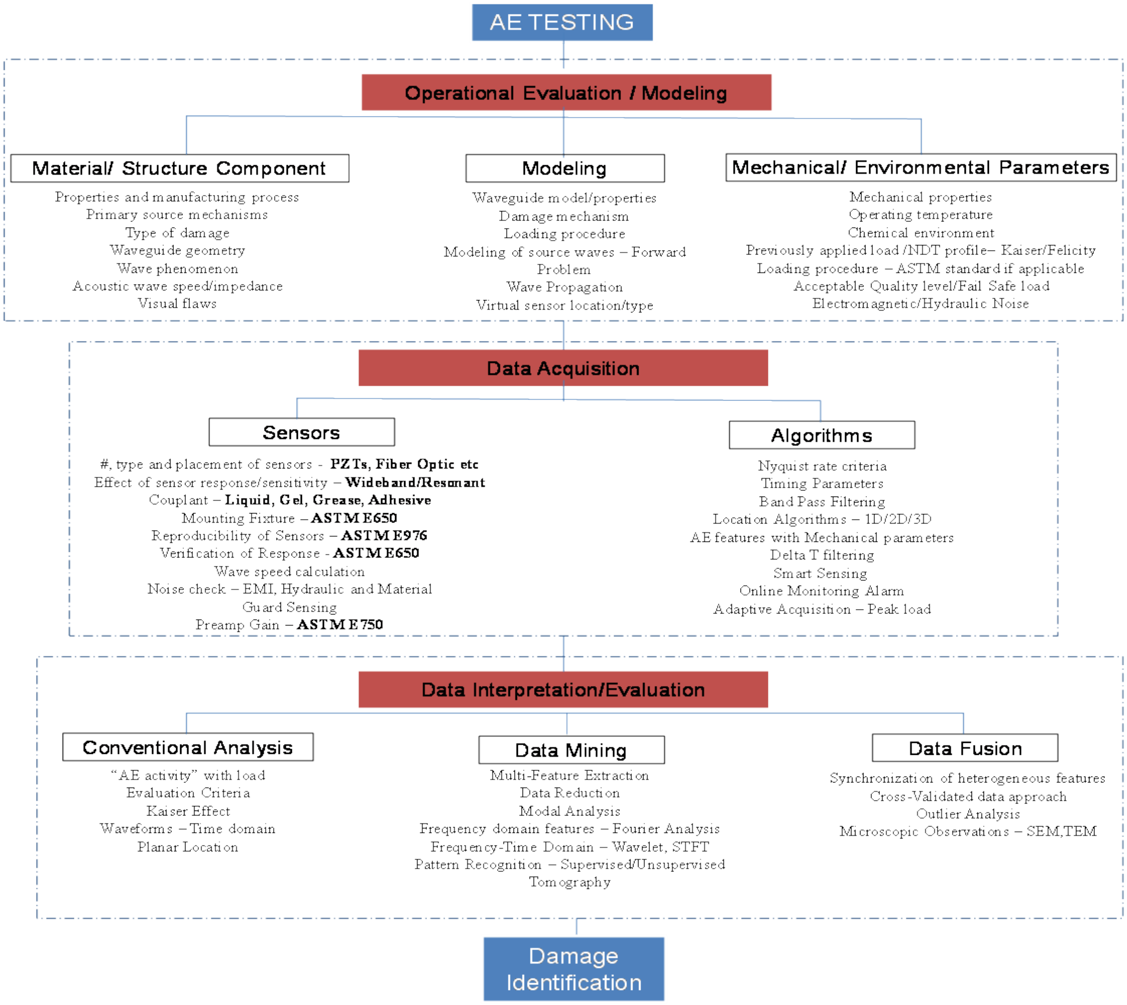

Figure 10: AE Testing Methodology

2.3.3 BRIEF HISTORY

The origin of modern AE study is credited to Joseph Kaiser. Kaiser observed that all materials under loading emitted acoustic emission and that the AE phenomenon was irreversible. Kaiser postulated that no acoustic emissions were produced until the previous maximum load applied was exceeded. This phenomenon referred to as the Kaiser Effect is still used as an indicator of structural deterioration and is illustrated in

Figure 11. It can be observed as the material is being loaded from point A to B, AE activity is noted but as the specimen is being loaded from point B to C and back to B, no AE activity is seen since the previous maximum load has not been exceeded. This effect is referred as the Kaiser effect. Again, as the load is further increased from B to D, AE activity is noted. However, as the material is loaded from D to E and back to D, AE activity is noted (point F) prior to the maximum applied load (point D). This effect whereby AE activity is noted prior to the previously applied maximum load is referred to as the Felicity effect. Essentially, Felicity effect is the absence of the Kaiser effect.

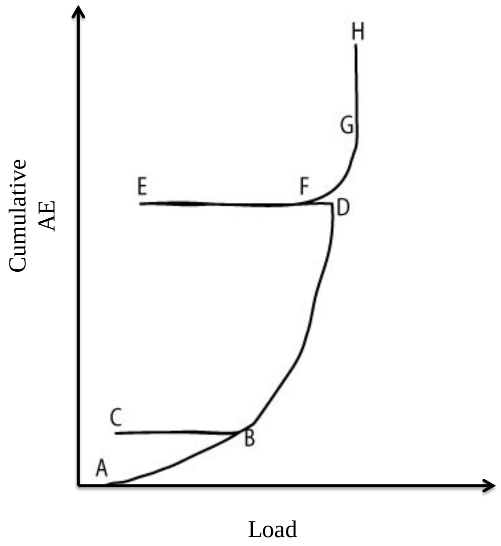

Figure 11: Kaiser Effect and Felicity Effect [48]

Based on the felicity effect, a felicity ratio was introduced as a damage indicator for pressure vessels monitoring and is expressed as

$$FR = F/D$$

The first major AE research in the US is traced back to the study performed by Bradford H. Schofield in 1954. His research activities were related to the origins of the AE source and concluded that the AE phenomenon is mainly a volumetric effect rather than a surface effect [49].

2.3.4 AE SOURCES

AE is a passive method, whereby the energy is released by localized sources within the material. Consequently, the driving force of the AE phenomenon are the internal sources itself. As a result, AE is a naturally occurring phenomenon in most materials and are recorded by mounted sensors placed at various locations. An analogy of the AE phenomenon can be made with the seismic waves. Seismic waves are produced as a result of the energy release from the earth's focus caused by the rupture of the fault planes (Figure 12a) and these waves then propagate along the earth's surface with a circular wave front (Figure 12b) and are picked up by seismometers placed at various locations of the earth. Similarly, AE sensors are sensitive in detecting relatively small vibrations produced in the material which makes it both a powerful yet challenging technique for SHM applications. This is attributed to the fact that in addition to the primary sources (produced by true damage sources such as crack initiation, growth, fiber fracture etc.), secondary and noise signals can be detected and commonly affect/mask the primary AE sources in the material. The secondary AE sources in the material include sources produced after the formation of primary sources such as crack rubbing, cracking fretting that do not produce new irreversible changes and also sources that are not part of the original fabrication such as corrosion, hydrogen embrittlement etc [18]. Noise sources include any unwanted signals produced either due to environmental variations, operational conditions, electromagnetic interference and external mechanical noise. Common noise sources include impact such as flying debris, construction/maintenance work, etc., harsh climatic conditions such as rain, snow, hail, strong winds etc., and friction such as loose bolts, movable joints etc. The identification and separation of the noise sources from the primary and secondary AE sources is the fundamental challenge associated with AE testing and currently requires high skill and extensive data analysis.

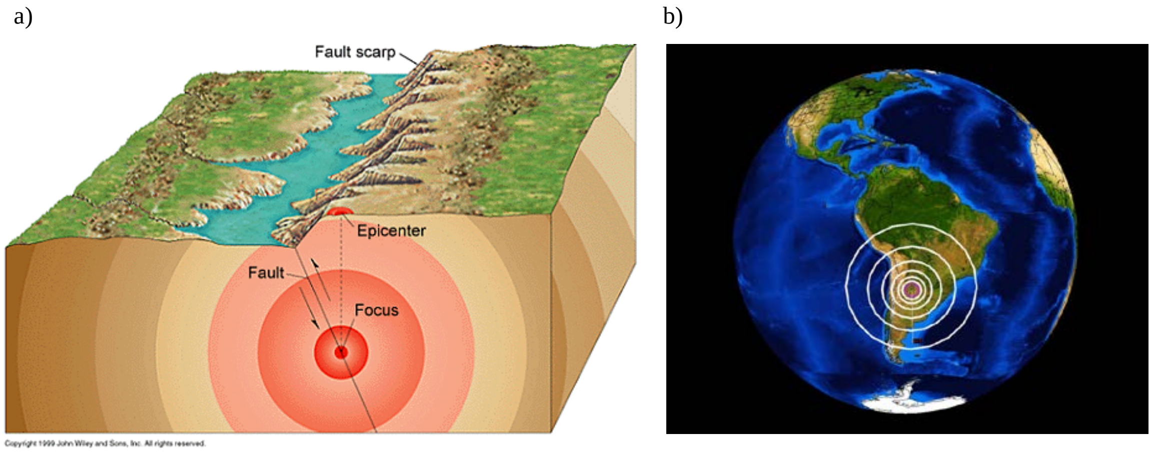

Figure 12: Seismic Waves (a) produced in the earth's volume (focus) [50] (b) propagating along the surface [51]

The AE sources can be broadly categorized into macroscopic and microscopic based on scale of the sources. In metals, the macroscopic sources include plastic deformation [52-55], crack initiation and growth [56-59], fatigue [60, 61] and corrosion [62, 63]. In composites, macroscopic sources include delamination [64, 65] and debonding [66, 67]. In metal-matrix composites, a combination of these macroscopic sources are active AE sources. However, these macroscopic AE sources are formed as a result of microscopic origins in the material (Figure 13). For instance, the physical origins of cleavage micro fracture in iron carbon alloys is illustrated in Figure 13a. In iron based carbon alloys, cleavage cracks initiate on certain crystallographic planes and are induced by the presence of pre-existing discontinuities, dislocation pileups at internal boundaries or by intersection of edge dislocations on slip planes [37]. Conversely, ductile crack growth (addressed in Chapter 5) is traced back to the initiation and development of several micro mechanisms as depicted in Figure 13b. In metal alloys, the eccentric stress concentrations at the inclusions materials causes the disbonding of the inclusions from the metal matrix interface. Subsequently, with increasing stress, significant plastic deformation occurs at these interfaces causing the voids to nucleate at the interface of the inclusions and the matrix. These voids then act as stress risers causing further plastic deformation and consequently micro-voids are developed at other inclusions or precipitates interfaces which then intensify the plastic deformation in the region. These chain of microscopic events then facilitate the coalescence of micro-voids to initiate the crack at the macroscopic level.

Mathis et al [68] explored the microscopic sources responsible for plastic deformation in metallic materials. The various microscopic sources that contribute to plastic deformation and their probability of detection are presented in TABLE 3. The AE signals generated due to dislocation motion at Frank-Read sources in aluminum alloys were noted be continuous type AE signals [69]. It was further concluded that AE generated by a single dislocation is a extremely weak source and only avalanche (or concurrent) dislocations were detectable by AE. Additionally, it was noted that hard ionic single crystals produce strong AE which is proportional to the dislocation velocity in comparison to soft ionic single crystals [70, 71].

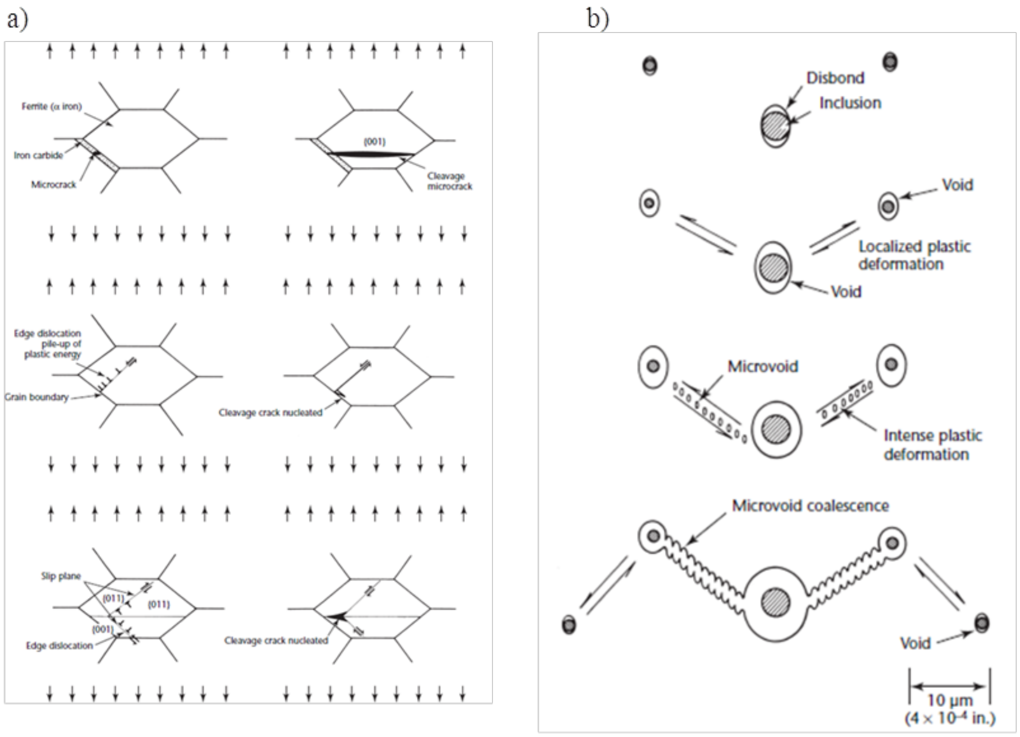

Figure 13: Microscopic AE sources (a) during cleavage crack nucleation (b) during ductile crack growth [37]

TABLE 3: Plastic deformation micro-mechanisms [68]

Mechanisms of plastic deformation	Strength of AE signal
Frank-Read source	Strong
Twin nucleation	Strong
Yield phenomenon	Strong
Cutting of coherent precipitates by dislocation	Strong
Orowan bowing	Weak
Twin growth and thickening	Negligible
Grain boundary sliding without cracking	negligible

Similarly, twinning activity reported in hexagonal closed packed (hcp) materials is a strong source of AE. The twinning mechanism is divided into three stages i) nucleation, ii) growth and iii) thickening and the nucleation is the strongest source of AE. This is attributed to the fact that the twin nucleation is a result of the collective motion of several hundred dislocations [69] and results to a large reorientation of the crystal lattice. It was experimentally demonstrated that the dislocation velocity caused by twin growth is significantly lower than that caused by twin nucleation and hence twin growth is a weak source of AE[72]. The grain size and the loading mode play a pivotal role in the activation of twinning mechanism. In particular, the effect of the small grain size for the activation of twinning in magnesium alloys is stronger in compression rather than in tension [73] which in turn affects the strength of the material as well [39]. Consequently, the AE count rate was observed to be extremely sensitive to the activation of the twinning activity in magnesium alloys (AZ31) as noted in Figure 14. Additionally, it was reported that AE count rates decrease rapidly in compression (Figure 14b) than in tension (Figure 14a). The rapid decrease in the AE count rate in compression is attributed to the growth of twins rather than the formation of new twins [74] while in tension, the gradual decrease of the AE count rate is attributed to continuous nucleation of twin as twin nucleation in tension requires higher stress while twin growth is limited in tension loading [75].

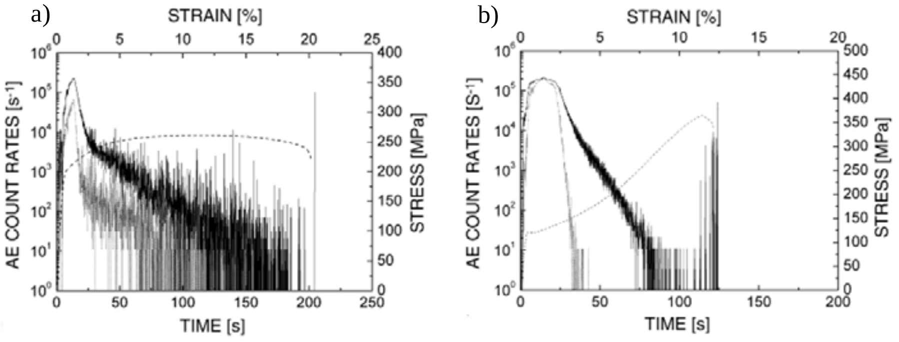

Figure 14: Stress strain curve of AZ31 correlated with AE count rate (a) Tension (b) Compression [73]

In advanced composite materials such as fiber reinforced polymer composites, several micro-failure mechanisms are good sources of AE. Failure in laminated polymer composites is driven by various micro-failure mechanisms including matrix cracking, fiber breakage, interfacial debonding, transverse ply cracking, and ply delamination [76-78] and these sources have been shown to exhibit AE [79-82]. Barre et al [83] correlated the micro-failure mechanisms using scanning electron microscopy (SEM) images to AE amplitude behavior. It was noted that fiber fracture released the highest AE amplitude while matrix cracking were observed to be quite low. Additionally, De Groot et al [84] showed that the AE frequency characteristics differs among the micro-failure mechanisms and can be used to differentiate and identify the activation of these sources more reliably using the peak frequency. Consequently, advanced signal processing methods and multi-parametric analysis are performed based on these AE feature descriptors to separate the observed signals into classes (Figure 15) and associate them to a particular failure mode.

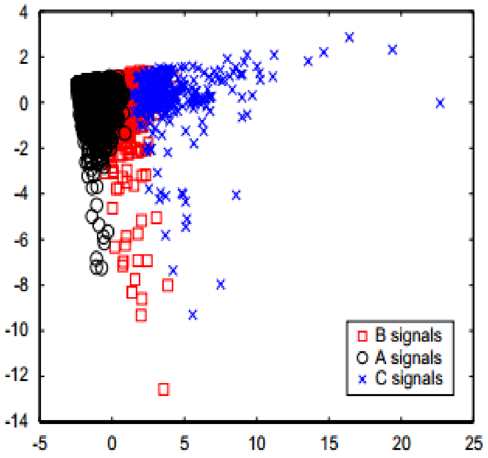

Figure 15: Identification of damage mechanisms in fiber polymer composite using multi-parametric analysis [85]

2.3.5 AE WAVE TYPES AND MODES

Central to signal interpretation and source identification of AE testing is understanding wave characteristics and wave propagation in the continuum. The AE waves propagating in a continuum medium are characterized into two main types i) continuous type (Figure 16a) and ii) burst type (Figure 16b). The continuous type emission is characterized by a relatively constant amplitude and long duration. AE sources such as dislocation glide and phase transition are known to produce continuous type emissions [86]. Conversely, burst type emissions are produced by rapidly occurring sources and have relatively higher amplitude and shorter duration. AE sources such as twin nucleation, crack growth and fiber fracture are typical examples of burst type emissions. Thus, the wave shape of the acquired signal provides a good description of the AE source mechanism present in the material. Further, AE features extracted from the waves using signal processing techniques provide a qualitative indication about the severity of the AE source.

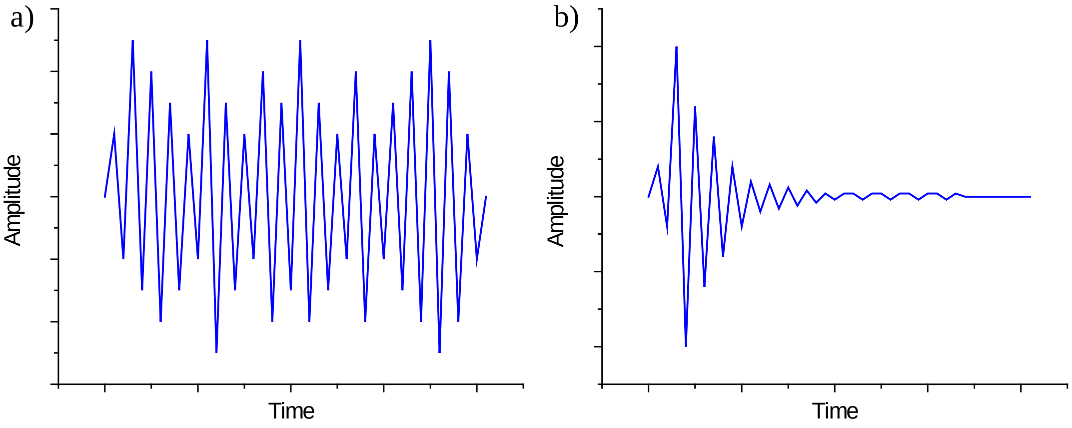

Figure 16: AE Wave types (a) continuous emission (b) burst emission

Additionally, these AE waves travel in the continuum in various modes namely longitudinal (P waves), Transverse (S waves), surface (Rayleigh) and lamb waves (plate waves). In bulky and semi infinite media, AE wave modes are mainly composed of only longitudinal and shear modes. In longitudinal or P waves, the particles move parallel to the direction of the propagating wave as shown in Figure 17a while in transverse or S wave, the particles move perpendicular to the direction of the propagating wave as shown in Figure 17b. The velocity of these wave modes is directly proportional to the elastic properties of the material as seen in equation 1a and 1b.

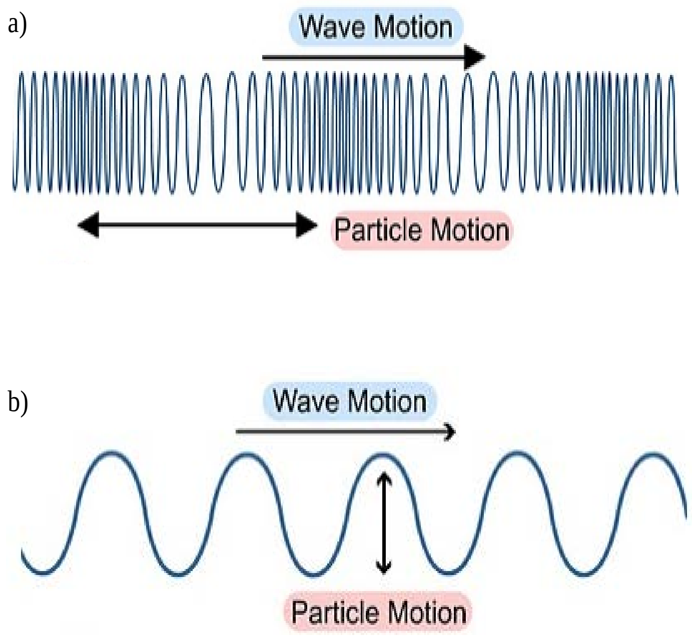

Figure 17: Wave modes in semi-infinite medium (a) Longitudinal (b) Transverse waves [87]

$$V_l = \sqrt{\frac{E}{\rho}} \qquad \text{1a}$$

$$V_s = \sqrt{\frac{G}{\rho}} \qquad \text{1b}$$

In thin and finite geometries, AE waves are dominated by guided modes for which signal reflections at the boundaries are considered which are typically encountered in practical applications. Surface waves are formed as the longitudinal and transversal wave modes interact in the medium and travel along the surface of the medium similar to the acoustic waves produced by stone pelting in water. This was first observed by Lord Rayleigh in 1885 and thus surface waves are commonly referred to as Rayleigh waves. The amplitude of the Rayleigh waves decrease exponentially with the depth of the test object. Unlike P and S waves, the velocity of Rayleigh waves are highly dependent on the propagating distance and propagate slower than P and S wave modes. However, in most practical application of AE testing, AE waves propagate as lamb waves in thin plates as shown in Figure 18. Lamb waves are guided waves that are formed as the result of the interaction of P and S waves in a medium whose thickness is comparable to the propagating wavelength and can propagate for long distances. The lamb waves detected by AE sensors placed at various locations are analyzed and contain most of the sensitive information regarding the damage nature.

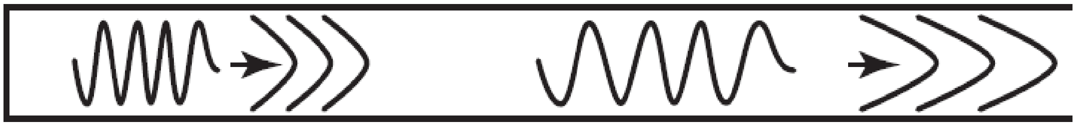

Figure 18: Lamb waves in thin plates [88]

Lamb waves propagate in plates with infinite symmetric and anti-symmetric modes. The first order symmetric (S_o, also known as extensional mode) and anti-symmetric modes ($A_{o,}$ also known as flexural mode) are shown in Figure 19a and b respectively. Lamb waves are known to propagate long distances but their propagation characteristics are highly dispersive, i.e. the velocity of the propagating mode is highly influenced by both the frequency and thickness of the plate. The dispersive nature of lamb waves in a 1mm thick aluminum plate is shown in Figure 20. It can be observed at 2MHz.mm that three different lamb wave modes, including first order symmetric mode (S_0) as well as the first and second order anti-symmetric modes (A_0 and A_1) exist in the thin plate.

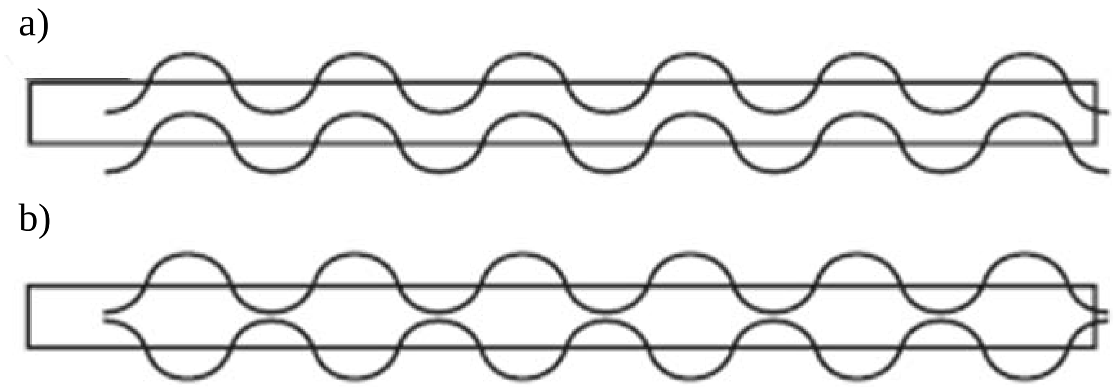

Figure 19: Lamb waves modes (a) symmetric (b) anti-symmetric [88]

With increasing frequencies, the propagating lamb waves become more complex and additional modes are noted to exist. Further, some of these modes tend to travel with similar velocities at further distances which makes the signal interpretation extremely challenging. In most AE testing applications, however, the operating frequencies of the sensor is limited between the range of 10kHz - 1MHz and this allows the detection of only the first few symmetric and anti-symmetric modes. As the waves propagate in the medium, the amplitude of the lamb waves attenuate as a function of the propagating distance. The attenuation phenomenon is attributed to mainly four factors such as beam spreading (the amplitude of the wave decreases as the radius increases), scattering effect, dispersion and material absorption. These attenuation phenomenon has to be considered when placing the AE sensors and should be factored in while analyzing the recorded data.

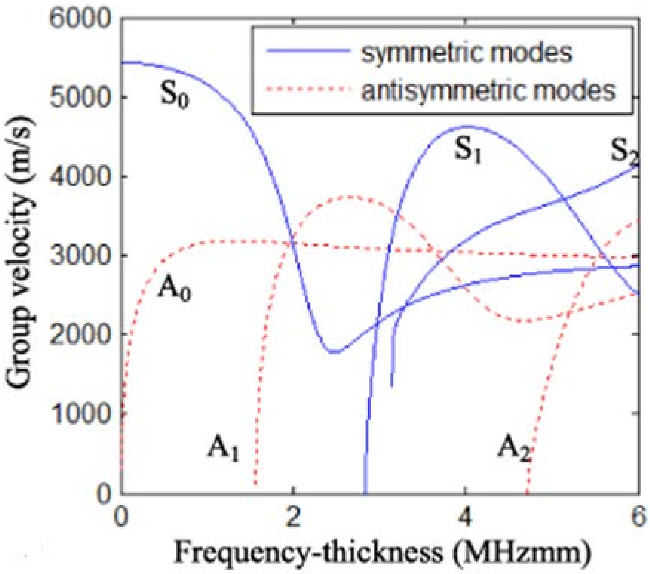

Figure 20: Dispersive nature of Lamb waves [89]

2.3.6 AE SENSORS

The third critical component in AE testing after the AE source and wave propagation is the utilized AE sensor. As mentioned previously, the operating frequency bandwidth of AE sensors is typically between 10kHz -1MHz which is different than the transducers utilized for ultrasonic testing for instance. Typically, the surface motion caused by the release of elastic waves in the material are recorded by piezoelectric AE sensors that convert this surface motion in to an electrical signal. Thus, the signals acquired during AE testing are plotted as waveforms of electrical voltage vs. time. However, the accurate detection of the elastic waves and the conversion into voltage is a function of the specific sensor utilized during the test. Piezoelectric sensors can be classified into two main types based on their frequency response i) resonant sensors and ii) broadband sensors.

Figure 21: Various AE sensors [90]

Broadband sensors have a wide frequency bandwidth with relatively equal sensitivity throughout their operating range. An example of broadband sensor response is depicted in Figure 22a. It must be noted that the sensor response in Figure 22a does not resemble that of an ideal wide band sensor but it has a relatively wide operating range (100-500kHz). Broadband AE sensors are highly useful in applications where the frequency response of the damage source is unknown. Thus, for research applications, broadband sensors are extensively utilized for material testing and failure analysis. However, broadband sensors are less sensitive than resonant sensors [91] and are susceptible to noise and thus are not preferred for field testing. Resonant sensors exhibit the highest sensitivity at a particular frequency and operate with a relatively narrow frequency range. An example of a resonant sensor response is shown in Figure 22b.

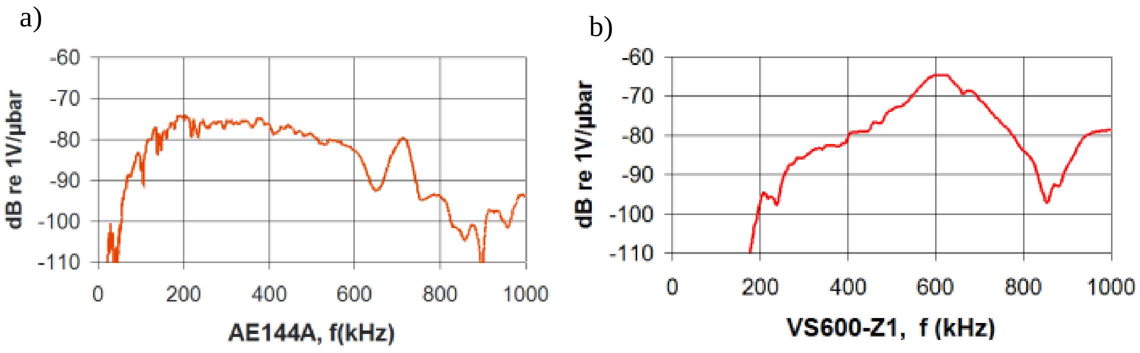

Figure 22: AE sensor response type (a) broadband (b) resonant [92]

In both sensor types, the sensing element utilized is made of a piezoelectric crystal such as lead zirconate. The basic components of the piezoelectric sensor are depicted in Figure 23. The piezoceramic element is housed in a case that is immune to electromagnetic interference. Two electrodes are attached to either faces of the piezoceramic element with one connected to electrical ground and the other connected to the electrical lead. The piezoceramic element is protected by the wear plate and is surrounded with a damping material usually made of curing epoxy containing high density tungsten particles [37]. The amount of damping material utilized in the sensor determines the broadband sensor response. The piezoceramic element thickness and the contact surface area determine the frequency response and the area covered by the utilized AE sensor. The received AE are recorded by the piezoceramic element which converts the motion into an electrical voltage and passes it to an acquisition system through the electrical lead. To minimize the impedance mismatch between the air and sensor contact surface and to ensure maximum transfer of the acoustic waves in to the AE sensor, a thin layer of couplant is applied between the sensors' surface and the test surface. Some of the commonly utilized couplant for AE testing are shown in TABLE 4.

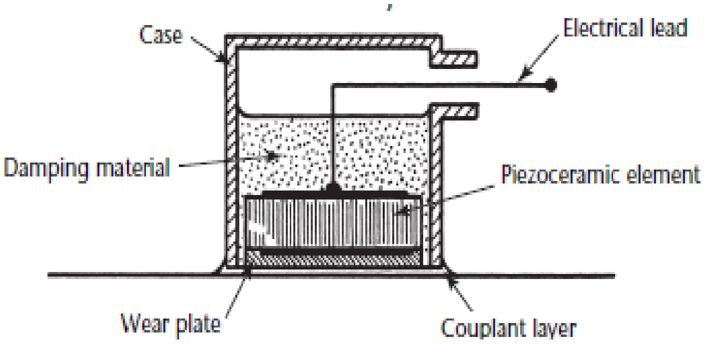

Figure 23: AE sensor components [37]

TABLE 4: Couplant Types

Couplant	Type	Clamp Required?	Viscosity	Temperature Range
Silicone oil	Liquid	Yes	Very Low	Low
Propylene glycol	Liquid	Yes	Very low	Medium
Glycerin	Liquid	Yes	Medium	Medium
Ultrasonic gel	Gel	Yes	Medium	Low
Brown grease	Grease	Yes	High	Low
Silicon grease	Grease	Yes	High	Medium
Petroleum jelly	Grease	Yes	High	Low
Honey	Sticky paste	Yes	High	Low
Silicone compound	Adhesive	No	Elastic solid	Medium
Hot melt glue	Adhesive	No	Elastic solid	Low
Cyanoacrylate	Adhesive	No	Rigid	Low

In addition to utilizing typical piezoelectric sensors, there has been an increasing focus on developing novel AE sensing platforms based on non contact optical sensing [93], fiber optic sensing [94-96], MEMS sensors [97, 98] and electromagnetic acoustic sensors [99, 100]. In particular, fiber optic sensors based on the principle of fiber Bragg [101] present a multi-modal sensing approach that is sensitive to temperature, mechanical strain and acoustic wave propagation.

The dual nature of fiber optic sensor stems from the fact that fiber Bragg gratings reflect a specific wavelength of light called the Bragg wavelength while transmitting all other wavelengths. Subsequently, the change in the fiber Bragg wavelength is directly proportional to the longitudinal strain applied and the temperature [102, 103] as described in equation 2 .

$$\frac{\Delta\lambda_B}{\lambda_B} = C_\varepsilon \varepsilon + C_T \Delta \mathrm{T} \tag{2}$$

where λ_B is the Bragg wavelength, ε is the strain, C_ε is the coefficient of strain, $\Delta \mathrm{T}$ is the change in temperature and C_T is the coefficient of temperature. The time dependant longitudinal strain is related to the amplitude of AE wave using the formula

$$\varepsilon(t) = A_{AE} \cos(kx - \omega t) \tag{3}$$

where A_{AE} is the amplitude of AE, k is the wave number, x is the longitudinal direction, ω is the angular frequency and t is the time. The principle of AE detection using fiber optic sensors is illustrated in Figure 24. The change in the Bragg wavelength from the original Bragg Wavelength (λ_o) determines the intensity of light transmitted into the sensor which is linearly proportional (20-80% of the Bragg gratings' maximum reflectively) to the wavelength is then converted into an electrical output for AE detection. The original Bragg wavelength changes as a function of the strain (decreases in the case of compression and increases in the case of tension) and this change shifts the area enclosed by the transmitted and reflected light as noted in Figure 24.

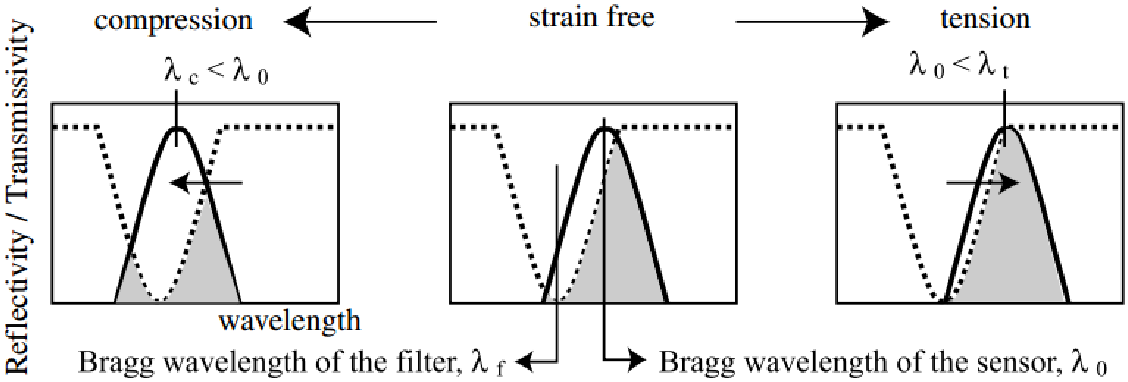

Figure 24: Principle of AE detection using fiber optic sensors [104]

However currently, the signal to noise ratio of FBG sensors in comparison with typical piezoelectric sensors is relatively low [105]. Similarly, MEMS based AE sensors are being explored for SHM applications. Unlike piezoelectric sensors, MEMS based AE sensors are light weight and significantly smaller enabling it to be embedded in structures for SHM applications. Ozevin et al [98] compared the performance of MEMS sensor with that of typical piezoelectric AE sensors. Currently, it was observed that the signal strength of MEMS sensors is lower than the piezoelectric sensors for a given source amplitude and consequently, have a lower signal to noise ratio. However, unlike piezoelectric sensors, MEMS based sensor offers the detection of multi-modal sensing parameters which is beneficial in discriminating spurious sources from primary AE source mechanisms.

2.4 DATA ANALYSIS THROUGH SIGNAL PROCESSING

It is assumed that the AE signal detected by a sensor is a convolution of the source function, propagation characteristics and the sensor transfer function. Thus, to identify and deconvolve the unknown AE signals recorded by the sensors and associate them to specific sources, the use of signal processing techniques has been adopted. The approach of deconvolving the AE signals is mainly divided in to two categories i) source inversion approach and ii) forward based approach. In either cases signal processing techniques are heavily used.

2.4.1 SOURCE INVERSION APPROACH

The source inversion approach (or backward approach) is to identify the AE source given that the AE signal recorded by the sensor is known. Essentially, signal processing techniques are utilized to identify feature characteristics of the output signals that assist in identifying the input source and hence the term 'backward approach'. This is accomplished through a number of signal processing methods such as i) parametric analysis ii) waveform analysis (wave let and modal analysis) and iii) pattern recognition analysis

2.4.1.1 PARAMETRIC ANALYSIS

The parametric analysis relies upon the extraction of features in the temporal and/or spectral domain. Essentially, time based history outputs or frequency characteristics of the acquired AE signal are extracted and any change in their respective features are noted and correlated either to the operational conditions (loading profile, temperature, strain) or validated with other NDT techniques or microscopic observations. In the temporal domain, several features such as amplitude, energy, rise time are extracted using signal processing techniques. Typically, time based features provide a qualitative indication of the waveform shape (damage magnitude) while the frequency based features provide a qualitative indication of the waveform content (damage source). A detailed list of all the extracted temporal domain AE features is shown in TABLE 5. The amplitude of the AE signal is reported in decibel (dB) and is obtained from voltage using the equation below.

$$dB = 20\log\left(\frac{V_{\max}}{1\mu V}\right) - PG \tag{4}$$

where V is the voltage and PG is the preamplifier again

TABLE 5: AE features in the temporal domain

AE Time Features	Definition
Amplitude	Peak Voltage of the AE waveform
Counts	Number of threshold crossing
Duration	Time difference between the first threshold crossing and last threshold crossing
Energy	Integral of the rectified voltage signal over the duration
Risetime	Time difference between the first threshold crossing and peak voltage
Counts to Peak	Number of threshold crossing from first threshold to peak voltage
Absolute Energy	Integral of the square voltage signal divided by the reference resistance over the entire duration

Additionally, other features descriptors are extracted from the frequency domain using Fast Fourier transform (FFT) [106] such as peak frequency, frequency centroid, partial power frequencies etc. FFT algorithms converts the time domain signal to frequency domain (X(k)) using the equation

$$X(k) = \sum_{1}^{N} x(n) e^{-i\frac{2\pi k}{N}}; k = 1 : N \tag{5}$$

where is x(n) is the time domain signal and N is number of signals A list of the frequency features extracted during AE testing is shown in TABLE 6.

TABLE 6: AE features in the spectral domain

AE Frequency Features	**Definition**
Peak Frequency	The frequency corresponding to the maximum power in the power spectrum
Frequency Centroid	$\frac{\sum(M * f)}{\sum M}$
Partial Powers	The ratio of the sum of the power spectrum in the a specific frequency range over the total power over the entire frequency range multiplied by 100

Besides the above mentioned AE features, other AE features are calculated from the extracted features. A list of these calculated features are presented in TABLE 7. Empirical correlations are then made between the extracted features and the material parameters to predict the failure in the material. For instance, the number of counts to failure (N_f) in a ductile steel can be calculated using the formula

$$N_f = D \frac{\pi K_C{}^2}{8\sigma_y{}^2} \tag{5}$$

where D is proportionality constant, K_c is the critical stress intensity factor and σ_y is the yield stress of the material. Additionally, the extracted features are also correlated with operational parameters such as load and temperature to identify changes in the feature characteristics and interpret the acquired AE signals using the principles of Kaiser/Felicity effect or other approaches.

TABLE 7: Additional AE Feature Descriptors

AE Frequency Features	**Definition**
Rise Angle	Rise Time /Amplitude
Decay Angle	(Duration – Rise Time)/Amplitude
Average Frequency	Counts / Duration
Initiation Frequency	Counts to peak / Rise time
Reverberation Frequency	(Counts – Counts to peak)/(Duration – Rise Time)

2.4.1.2 WAVEFORM BASED ANALYSIS

Another data analysis method utilized for AE analysis is based on analysis of the acquired raw AE waveform itself. Contrary to the parametric based analysis, waveform based analysis is continuously recording a single waveform for the entire test which is referred to as data streaming in modern AE boards. This method provides the advantage of not implementing a user defined threshold at the beginning of the test and also reduce the influence of AE features based on a predefined threshold such as amplitude, energy, counts etc. Instead, it allows the flexibility of implementing a threshold after the test is performed and specifically identify how certain signals change with respective to the ambient or baseline condition. The features extracted from this approach could vary from the parametric based analysis which relies on extracting features based on a specific hit length and threshold definition both of which are predetermined prior to the actual test performed. This sort of analysis also provides the added flexibility of improving localization of the AE sources based on improved triangularization methods.

Another waveform approach is based on modal analysis of the AE signals. In particular modal analysis can be utilized to differentiate between in-plane and out of plane sources. As stated previously, AE produced in thin geometries such as plate like structures produces guided waves that contain both an extensional and a flexural mode. In-plane sources such as matrix cracking and fiber fracture in composite materialss are dominated by extensional modes while out-of plane sources such as delamination are dominated by flexural modes [107]. This is not to say that the orientation of the sources produce only a single mode as the received waveform is a function of the propagating distance and sensor response as well. However, it is easier to identify these modes based on the source orientation. Extensional modes are known to travel faster than the flexural modes while also being less dispersive in nature. Flexural modes tend to attenuate faster as they propagate in the medium. This is the reason why amplitude (or any AE feature dependant on threshold) based damage detection is not a reliable approach as amplitude of the AE changes with propagating distance. Conversely, damage detection based on modal analysis provides more robust approach for source inversion approaches. The modes of the waves can be identified through the dispersion curves of the material [108] which in turn can be assessed by evaluating the frequencies of the arriving waves.

In this context, FFT algorithms prove futile to evaluate non-stationary or transient waves which is the typical nature of AE. Moreover, using FFT algorithms, it is difficult to identify the contributions of the wave packets in terms of the frequency characteristics As a result, wavelet based analysis [1, 109-111] are effective in tracking the time evolution of frequencies generated by the AE wave.

In particular the Gabor wavelet transform [112] has found to have the optimal resolution in the time and frequency domain [113]. The Gabor function for a sinusoidal function can be in the time domain is described as [114]

$$\Phi(t) = \exp(-\alpha^2 t^2)\exp(-i2\pi f_o t) \tag{6}$$

where α is the sharpness of the Gaussian function and f_o is the center frequency of the signal. The corresponding Fourier transform of the Gabor function is expressed as [114]

$$\Phi(f) = \sqrt{\frac{\pi}{\alpha^2}}\exp(-\frac{\pi^2}{\alpha^2}(f - f_o)^2) \tag{7}$$

Subsequently, the Gabor function is applied to the wavelet transform to identify the time evolution of frequency. This form of waveform analysis indicates which wave packet corresponds to a particular frequency and consequently identify the wave modes present in the AE signal.

2.4.1.3 PATTERN RECOGNITION APPROACHES

In order to classify the usually large number of acquired AE signals and associate them (ideally) to a particular source mechanism, advanced signal processing techniques based on multivariate data analysis approaches are utilized. It is assumed that a particular source mechanism would have similar characteristics of several AE feature descriptors. Consequently, pattern recognition algorithms [85, 115-117] are employed to group similar AE signals into clusters (or classes) based on ensemble feature descriptors using unsupervised pattern recognition approaches with the difficulty of labeling each cluster [81, 118]. The steps involved in the pattern recognition process of the AE signals are illustrated in FIGURE 25. The first step involved in pattern recognition analysis of the AE signals is to identify a group of least correlated AE features from the extracted feature set to be used as input features for the clustering methodology. The selection of the least correlated AE features is performed using a dendrogram [118] (FIGURE 26) which establishes the correlation factor among the features. The dendrogram utilizes a hierarchical clustering approach that is based either on single or complete link algorithms. In the single link approach, the correlation of the features is based on the minimum distance between the features while in the complete link approach, it is based on the maximum distance between the features [119]. A correlation factor less than 0.6 is a good measure of uncorrelated features [118].

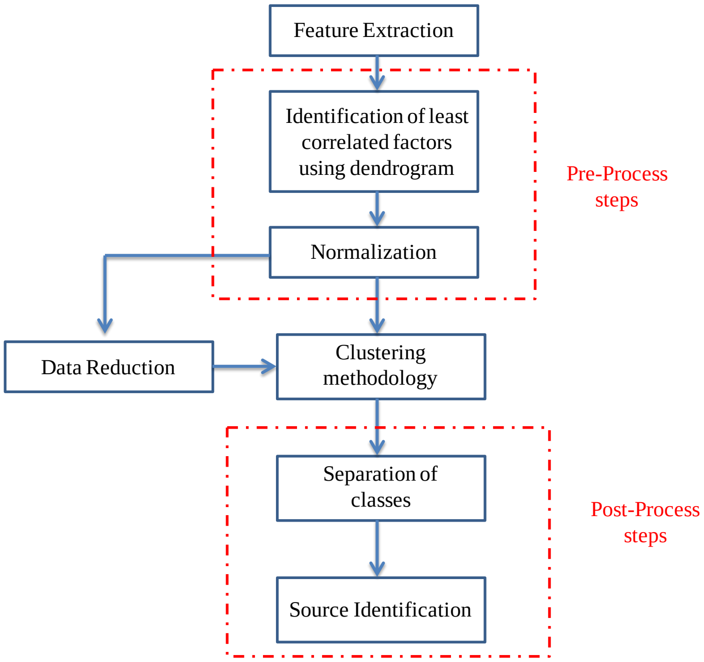

Figure 25: AE Pattern Recognition Flow Process

The next step involved in the pattern recognition process is the normalization of the selected features. This step is carried out to minimize the effect of a particular feature that has high values to influence the clustering methodology. Thus, all the features are normalized either between 0 to 1 values or -1 to 1 values and consequently equal weights is applied to all the selected features. Subsequently, the AE data set is classified into several clusters based on various unsupervised pattern recognition approaches such as k-means [120, 121], principal component analysis [122, 123], fuzzy clustering [124, 125] and neural network techniques [126, 127] are widely utilized for clustering of AE signals. In particular k-means clustering algorithm is widely utilized as it requires minimal initial conditions for the clustering methodology. Consequently, k-means clustering methodology is predominantly utilized in this thesis.

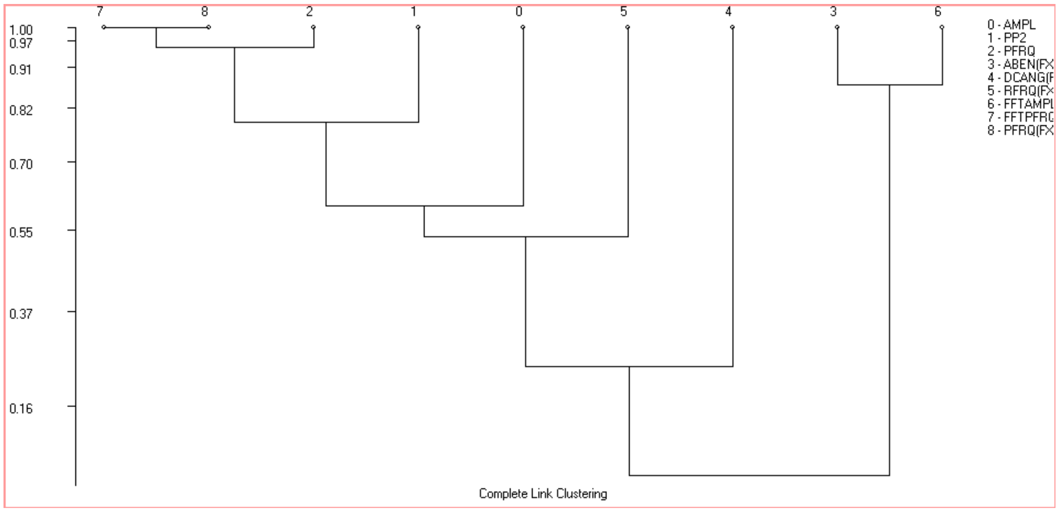

Figure 26: AE Dendrogram

<u>k-means approach</u>

The k-means approach is a statistical pattern recognition approach with the objective to group the AE signals into k classes in which each data point belongs to the cluster with the nearest centroid. This is achieved by minimizing the objective function presented below [128]

$$\mathrm{J}_K = \sum_{k=1}^{K} \sum_{i \in C_k} (x_i - m_k)^2 \tag{8}$$

where $X = (x_1, x_2, \ldots . x_n)$ is the input data, m_k is the centroid of a cluster k. Initially, the centroid is obtained by guessing an initial value. The data points are then clustered based on their proximity to the centroid. Consequently, the centroids are updated by calculating the mean of the data points belonging to the cluster. The centroids are updated until the mean of the cluster does not vary and subsequently, the objective function is minimized based upon a tolerance value.

2.4.2 FORWARD-BASED APPROACH

A possible way to address the difficulties in interpreting experimental AE recordings, is to implement a forward AE approach in which dominant source mechanisms active in a specimen at some length scale are modeled and, therefore, the dimensionality of the parametric space related to the standard detection-localization-identification-classification NDE process can be reduced [129]. Such forward approaches for AE source modeling have been suggested using both analytical [130-133] and computational techniques [134-140] which produced wave content that was used to investigate interactions with the materials' constitutive behavior, their geometry, as well as with defects. In general, such forward approach would be beneficial in: a) simulating the primitive, as it is usually referred to as, source signal, b) optimizing sensor placement and spacing allowing more effective NDE and SHM applications, iii) quantifying the scattering effect at various structural features, and iv) filtering recorded spurious signals (i.e. noise) [136, 141].

Furthermore, it is important to note that AE is intimately related to wave propagation which is also an important aspect of a possible forward modeling scheme, as it is this transient energy release that is captured by different types of sensing systems in actual NDE/SHM applications. In this context, several approaches have been used to model stress wave propagation in elastic media. For semi-infinite media for example, wave propagation has been modeled using both numerical and analytical techniques. Early modeling techniques of AE adopted the theory of elastodynamics based on the use of Green's functions [130, 131, 138]. In an isotropic medium, appropriately defined Green's functions can be used to calculate the displacement at a point due to an arbitrary applied force. A typical method to extract the Green's function between two points is through a direct pulse echo measurement. Alternatively, the Green's function can also be obtained through passive measurements between two points using the cross-correlation approach. Derode et al [142] provided a direct physical interpretation of the emergence of the exact Green's function and the role of scattering in the reconstruction of the Green's function from far-field correlations. Wapenaar et al [143] compared two different approaches, the principle of time-reversal and Rayleigh's reciprocity theorem, to derive the Green's function. The time reversal approach exploits the superposition principle in a homogenous medium, while the Rayleigh's reciprocity theorem utilizes the equation of motion and the stress-strain relation in the space-frequency domain to obtain the Green's Function. In addition, Ouyang et al [141] utilized the Green's function to resolve the moment tensor to quantify the fracture process in center-notch and off-center notch concrete beams. Further, the eigenvalue of the moment tensor was used to quantitatively characterize each of the microcracks in the concrete beam.

In thin and finite geometries, AE waves are dominated by guided modes for which the signal reflections from the boundaries are considered and correspond to more practical applications. In this context, Prosser et al [136] utilized and compared two different approaches to model AE waveforms in thin plates, the Mindlin plate theory (MPT) and the dynamic finite element method (DFEM). The two approaches were implemented to model the flexural mode component of a simulated out of plane AE source in both isotropic and anisotropic plates; discrepancies were observed in the wave propagation at longer time intervals. This discrepancy was attributed to the differences of the boundary conditions for the two approaches and their corresponding signal reflections. It was concluded that the DFEM approach has better agreement with experimental measurements, as it was based on exact linear elasticity, while the MPT approach was suited mainly for flexural modes at relatively low frequencies where the basic Mindlin assumption (normal to the plate mid-surface remains straight) is sufficiently accurate.

For a viscoelastic plate, Giordano et al [135] modeled the corresponding AE wave propagation and predicted the displacement at a certain location based on ray theory. In this approach, the displacement response produced due to a longitudinal wave generated at a certain distance from the source was assumed to be a superposition of the different rays produced by reflection at boundary surfaces. Furthermore, Minozzi et al [144] introduced a lattice model to study the AE process associated with the dynamic fracture in a disordered medium. Specifically, a 2D lattice was subjected to mode III type loading and resulting accelerations were captured at various locations resembling that of potential

NDE transducers. The cumulative AE energy calculated based on acceleration waveforms revealed a direct power relationship with the total number of disbonds (internal damage) in the model. Moreover, the acoustic energy distribution was noted to decay as a power function independent of the loading rate. Along a similar direction, Sause et al [145] stated that source radiation direction and the elastic properties of the medium cause distinct changes in the generated waveforms. Sause further reported that in isotropic media, the orientation of the in-plane sources produce S_o dominated wave mode along the normal to crack surface, while as the source sensor angle varied so did the contributions of the S_o wave mode with the A_o wave mode remaining constant.

At the atomistic level, Landa et al [146] performed wave propagation simulations due to various AE sources at the crack tip using the molecular dynamic method. To this aim, a single edge notch sample was modeled and loaded in mode II and the AE wave propagation due to eight local atomistic nodes were analyzed. Initially, scattering of the waves produced due to the loading process were observed at the crack faces. However, as the sample was further loaded, the waves produced by each of the eight atoms due to the crack extension were seen to interfere, with the initial waves and the distances between each wave front was proportional to the time it took for the crack to grow through the atoms. It was noted that the waves produced by the crack extension are characterized by very high frequency pulses.

2.5 FUNDAMENTAL CHALLENGES OF AE TESTING

The widespread use of AE as a NDT technique has been limited due to several challenges attributed to the complex inherent nature associated with it. These challenges affect the capability of AE to reliably determine the presence and evolution of damage. The proposed research herein targets therefore some of the major challenges that limit the potential of the AE as a diagnostic system, as described in this section.

2.5.1. "CLEAN" AE SIGNALS AND WAVE PROPAGATION

Over the last two decades, although the AE technology has progressed significantly, there still exist major misconceptions about the actual capabilities of AE as an NDT method for advanced applications that require actual on-board/online and condition-based monitoring. This "bad reputation" can be attributed to a number of practical reasons including the need for advanced computational resources and signal processing techniques required to interpret AE signals, as well as more fundamental reasons that have to do with the origins of AE and the way concepts such as mechanics and physics of solids can contribute to both deeper understanding of what is being recorded in laboratory and field conditions, as well as to the design of the next generation of NDT technology based on AE. In this context, the constant advancement of computational resources, sensor technology and signal processing techniques have enabled the storage, filtering and processing of large datasets, as well as the application of the technology to field applications. For example, AE testing has been widely accepted and matured for proof testing of pressure vessels [147]. However, the same cannot be said for other in-service SHM monitoring applications such as in the aerospace industry.

Furthermore, the signal shaping effects of the source wave are by nature complex and highly variable based on each testing specifications. A major hurdle associated with acoustics based NDT testing is the challenge associated with wave propagation in waveguide geometries. High frequencies tend to attenuate significantly as they propagate along materials and structures. Thus, the true signature of the source mechanisms is not detected and hence an accurate recording of the health of the structure is not obtained. In addition, the reflections at the structural boundaries further complicate and change the true signature of the source mechanism. The reflections at the boundaries can greatly influence the wave signature and potentially raise a false positive alarm. In this context, the type, characteristics, reliability, accuracy and use of sensors and their role in decoupling effects that are related to the core of the AE method still need to be quantitatively factored so that both research and development of NDT and SHM applications based on AE is possible. For example, the signal produced by a source is influenced by the waveguide geometry, the sensor and the signal conditioning electronics [38]. In addition to primary AE sources, secondary sources such as fretting, friction, dislocation movement, mechanical and electromagnetic noise etc, can be present and certainly affect the characteristics of what the actual AE user is called to analyze. AE signals can be continuous or intermittent and their analysis can greatly influence the reliability of their interpretation. In addition, "noise signals" can also trigger the data acquisition system and mask the primary AE sources creating difficulties in truly inspecting for e.g. structural integrity.

2.5.2. IDENTIFICATION OF PRIMARY AE SOURCES

To further complicate the difficulty of identification of AE sources, materials exhibit several damage mechanisms prior to final failure. This is especially true in the case of materials used in e.g. aircrafts or combat vehicles/vessels. With the intention of developing lighter yet strong structural bodies, manufactures have been utilizing composite and hybrid metal composites, e.g. in the fuselage. The advantage of these materials is that they offer better strength-to-weight ratios resulting e.g. in fuel efficiency. Additionally, these materials demonstrate a damage tolerant behavior prior to final fracture. This damage tolerance is associated with the development of progressive failure caused by several damage mechanisms activated in the material. For instance, composites exhibit several damage mechanisms such as matrix cracking, interfacial failure, delamination, fiber pullout and fiber breakage prior to macro failure. However, the basic difference between this type of advanced composites and e.g. metals is the fact that this damage development process in composites is far more difficult to detect, since in many occasions significant subsurface damage does not produce significant effects on accessible surfaces. In addition, aging of composite structures is still an active research field and therefore concepts such as fracture mechanics and damage-proof design cannot be readily applied for highly heterogeneous and anisotropic media. The reliable identification of such mechanisms across length and time scales and for a variety of structural materials is of paramount importance to develop an effective early damage warning system based on NDT. However, these damage modes could occur simultaneously and therefore detecting their "signature" is a challenging process also for AE testing.

2.5.3 SIGNAL SHAPING EFFECTS

The recorded AE by the sensor produced in the material by localized sources is a convoluted transfer function of several different factors as outlined in Figure 27. The original AE signal produced by the source is affected by the material and geometry, i.e. the same material but different geometry can influence the original AE signal and alter the original characteristics of the AE signal. The signal is further colored/influenced by the implemented sensing platform and AE instrumentation. For instance, it is critical to evaluate and factor in the sensor response to accurately determine the true characteristics of the source mechanism. Thus, the recorded AE signal is severely influenced by both the material/geometry characteristics and the electronics of the acquisition system. This signal shaping affect complicates the damage detection process and consequently make AE testing a challenging technique for reliable damage diagnosis.

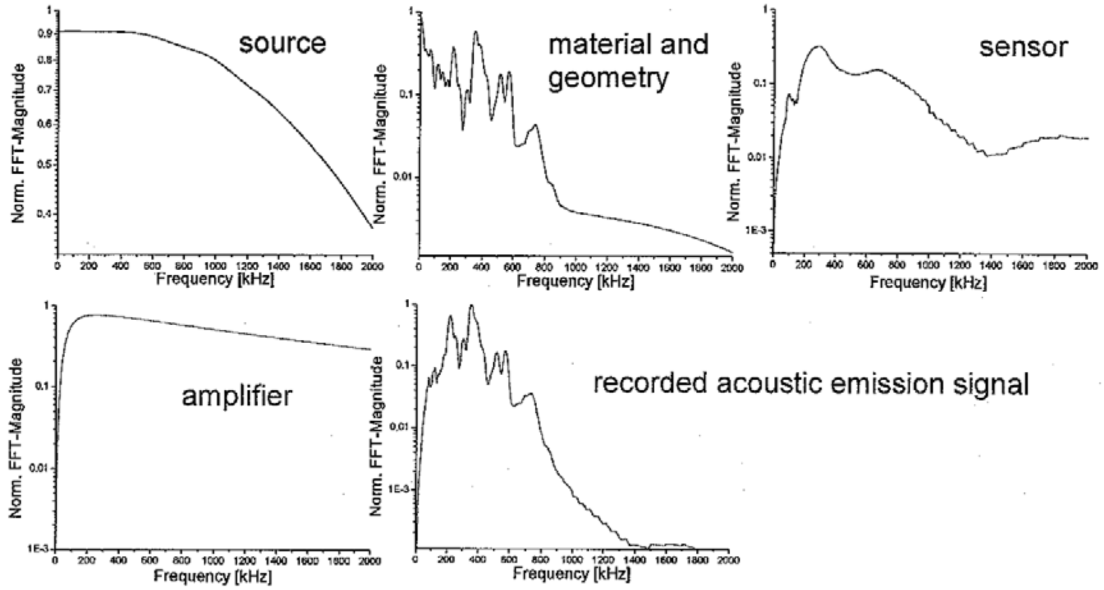

Figure 27: AE Signal Shaping Effects [148]

2.5.4 LACK OF RELIABLE DAMAGE PARAMETERS FOR DAMAGE DIAGNOSIS

Another limiting factor of AE testing is the over-reliance on threshold based AE feature analysis and the lack of reliable damage parameters to flag the presence of damage for in-situ and field applications. For instance, one of major reasons that ultrasonic testing has matured and extensively utilized across various applications (medical, body scanners, quality control etc) is due to the ability to flag and visualize the presence of damage by utilizing quantifiable damage parameters extracted from the ultrasonic waves.

While it is possible to track the initiation and development, it is quite challenging to quantify the severity of damage. One of the reasons for this paradox is the irreversibility nature of the acoustic emission phenomenon. The irreversible behavior of AE stems from the fact that once AE from accommodating that stress has ceased, no additional AE will occur until the previous maximum load has been surpassed [149]. This irreversible behavior notably seen in metals is referred to as the Kaiser Effect. Due to the Kaiser Effect, AE can be non-repeatable and thus unique to the loading procedure. Furthermore, several intrinsic factors such as scattering, attenuation and the dispersive nature of the wave modes coupled with the extrinsic factors such as variable loading and environmental effects all directly affect the quality of the recorded signals. Importantly, in order to quantify the severity of damage, every mechanism in different materials must behave the same. This is often not the case since each material has different elastic properties which directly affect the wave speed in the material and the signature. Additionally, even the same material but different phase properties can also have an influence on the wave signature, speed and its feature characteristics.

CHAPTER 3: RESEARCH OVERVIEW AND PROPOSED VISION

3.1 OBJECTIVE AND HYPOTHESIS

The objective of this thesis is to develop a novel acoustics based framework for cross-validated nondestructive testing and evaluation (NDT&E) to improve the reliability in assessing the quality of the material performance and structural integrity using Acoustic Emission (AE). The focus is on the AE method which in the research described herein is used in conjunction with several other NDT methods including Guided Ultrasonic Waves (GUW), Digital Image Correlation (DIC) and Infrared Thermography (IRT). The novelty of this framework is based upon a number of key innovations including i) the hybrid use of full field optical NDT methods such as DIC and IRT with volumetric inspection methods such as AE and GUW, ii) the implementation of advanced signal processing algorithms for data filtering, efficient damage diagnosis and probable prognosis and iii) a novel AE damage detector to flag the presence of damage for in-situ applications

In Chapter 2, certain challenges limiting the wide application of the AE technique were described. To mitigate some of these challenges and reliably identify the onset of damage, this research adopted a hierarchical approach in terms of length scale to gain fundamental knowledge of AE and then apply it for reliable identification of damage mechanisms based on the research hypothesis shown in Figure 28. The major contribution of this framework would be to present a reliable AE monitoring paradigm for full scale structural testing. The combination of AE with full field optical techniques presents a novel opportunity to correlate internal/hidden defects with visible and quantifiable surface deformation/damage. As a result, optical techniques such as DIC and IRT add a new dimension to the interpretation of AE signals and provide greater reliability in identifying the AE source that are challenging to judge based on conventional AE monitoring only.

These challenges include extrinsic factors posed by variable environmental and operational conditions, limitations in the hardware/software tools available for data recording and post-processing, as well as intrinsic factors such as complex geometries/materials, synchronous activation of AE sources and progressive development of multiple failure modes. To address these limitations to the effective use of the AE method, the approach proposed in this research is based on innovative research in several topics, including: i) design of a novel cross-validated acoustics-based NDT&E system, ii) development of classification algorithms to formulate an intelligent diagnostic system capable to be used in challenging operational conditions and to provide effective and condition-based asset management, and iii) estimation of current structural health state and prediction of remaining lifetime. The crux in this research was to tailor the obtained information towards assessing the quality of structural integrity of next generation aerospace components and perhaps estimate the remaining useful life of the component/part so that structural developers and/or owners could be better informed when scheduling maintenance time and know if it is absolutely essential to change or retire the part.

The research hypothesis is built upon six critical elements (i) modeling of AE source wave propagation in the waveguide geometry (ii) performing targeted experimental activities from typical mechanical testing to specific failure mechanisms to reliably characterize the AE signatures (iii) utilizing complementary and full field monitoring techniques (iv) implementing signal processing techniques and multi-parametric study to identify sensitive and robust ensemble feature descriptors (v) designing pattern recognition algorithms based on statistical methods and neural techniques to distinguish damage specific AE data from the secondary and other unknown AE sources and (vi) developing data fusion algorithms to enhance the reliability of damage detection and quantify the extent of the severity of damage.

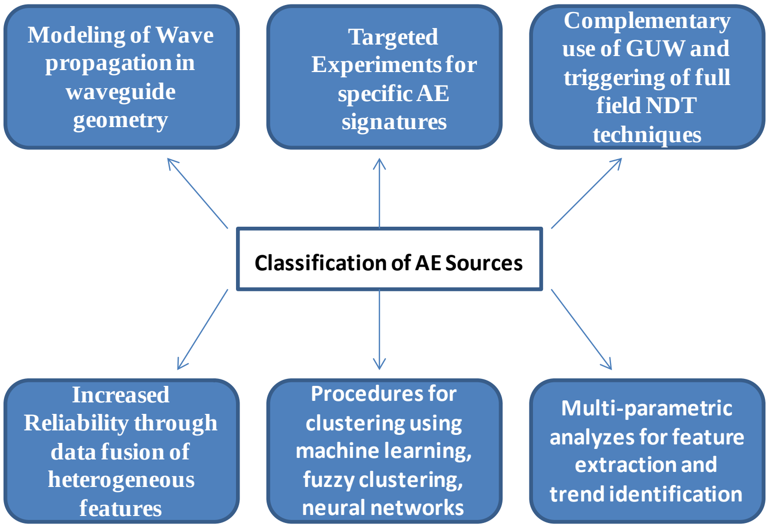

Figure 28: Research Hypothesis

3.1.1 MODELING OF AE SOURCE WAVE PROPAGATION IN WAVEGUIDE GEOMETRY

All materials when subjected to external loading (mechanical, acoustic, thermal, electrical, chemical etc.) produce AE that travel with a circular wave front similar to seismic waves [84]. Depending on the source and geometry, the elastic wave generated assumes certain inherent characteristics, some of which is affected as it propagates along the medium. The propagation of the elastic waves in any medium is inherently complex in nature. These traveling elastic waves are picked up by AE sensors that are mounted on the surface of the object and are stored for feature extraction. However, the original wave nature of the AE source is greatly altered by the medium of propagation and the sensing platform and is referred to as the signal shaping effect [13]. Consequently, relying on source inversion techniques alone is challenging and it is beneficial to undertake a forward approach of simulating AE from a specific source in the medium. A major hurdle associated with acoustics based NDT testing is the challenge associated with wave propagation in waveguide geometries. High frequencies tend to attenuate significantly as they propagate along materials and structures. Thus, the true signature of the source mechanisms is not detected and hence an accurate recording of the health of the structure is not obtained. In addition, the reflections at the structural boundaries further complicate and change the true signature of the source mechanism. The reflections at the boundaries can greatly influence the wave signature and potentially raise a false positive alarm. In this context, the type, characteristics, reliability, accuracy and use of sensors and their role in decoupling effects that are related to the core of the AE method still need to be quantitatively factored so that both research and development of NDT and SHM applications based on AE is possible. In addition to primary AE sources, secondary sources such as fretting, friction, dislocation movement, mechanical and electromagnetic noise etc, can be present and certainly affect the characteristics of what the actual AE user is called to analyze. AE signals can be continuous or intermittent and their analysis can greatly influence the reliability of their interpretation. In addition, "noise signals" can also trigger the data acquisition system and mask the primary AE sources creating difficulties in truly inspecting for e.g. structural integrity. Thus, it is essential to develop procedures to effectively filter out and minimize this type of secondary sources and to design a reliable damage identification system

3.1.2 TARGETED EXPERIMENTAL TESTING TO IDENTIFY SPECIFIC AE SIGNATURES

One of the major reason that AE has not accepted widespread use as a SHM technique for wider applications is attributed to the complex skills required to interpret the AE signals. This is partly due to the fact that conventional AE monitoring simply relies on activity based features which can be influenced significantly by the operational conditions, environmental effects, sensor response and other effects including the complex wave propagation effect mentioned in the previous section. Mechanical testing of metallic materials are well studied and documented in the literature. Most metallic materials exhibit a well defined elastic and plastic behavior prior to final fracture and are typically characterized by its yield strength, elongation and ultimate strength. In fact, these deformation and micro failure mechanisms are strong sources of AE. Plastic deformation [40], fatigue crack initiation and growth [41, 150], fretting crack [151] and crack closure [152] are known to produce AE during mechanical testing of metallic materials.

To develop a reliable SHM system based on AE monitoring, it is crucial to identify and characterize these mechanisms in terms of their AE signature and then transfer this knowledge to other geometries of the same material. To realize this, several metallic coupons coupled with AE sensors will be mechanically tested and their fundamental behavior will be evaluated in terms of their AE characteristics. This knowledge will be utilized in interpreting the unknown AE signals obtained from other complex specimens of the same kind and identify a robust trend across different specimens. For this purpose, several different type of loading profile including axial testing, 3 point bending, cyclic loading and fatigue will be performed and their AE characteristics will be compared and evaluated.

3.1.3 COMPLEMENTARY USE OF FULL FIELD NDT TECHNIQUES

The major component of this acoustics based framework is the integration of complementary full field NDT techniques in parallel with the AE method. The fundamental challenges associated with AE testing is its high sensitivity to noise and the complex skill required in interpreting the AE signatures. Along with implementing a forward approach, it is advantageous to combine DIC and IRT techniques to cross-validate the AE indications and interpret the AE signatures. All the monitoring systems will be synchronized using parametric inputs such as load, displacements etc. to correlate the acoustic indications with mechanical and thermal observations. Such a correlation will serve several purposes such as i) filtering/cleaning unwanted AE signals collected during the test, ii) identify critical material phenomenon in terms of their AE signatures and iii) increase the reliability of damage detection process. The DIC and IRT techniques provide both the required visual and quantitative component in effectively interpreting the AE indications.

3.1.4 ADVANCED SIGNAL PROCESSING TECHNIQUES AND MULTI PARAMETRIC ANALYSIS FOR TREND IDENTIFICATION

Conventional AE monitoring relies on AE activity based indications to evaluate the quality of the structural integrity. However, traditional activity based monitoring is highly dependent on the source-sensor relationship, operational and environmental conditions.

Thus, dependence on such type of AE activity based monitoring proves to be futile in challenging field applications. Consequently, an alternate approach is transferring from the temporal domain to the spectral domain and extracting frequency based features to identify trends related to specific damage sources. As noted in chapter 2, this approach has shown to have great potential in identifying the damage source in material and has shown good correlations with the mechanism nature. However, evaluating the AE source by the peak frequency characteristic alone is challenging as this is greatly influenced by the sensor characteristics itself. Additionally, the constant presence of secondary and/or pseudo sources can mask the peak frequency of the primary AE source. Thus, advanced signal processing techniques are critical for reliable trend identification that are robust across different length and geometry scales.

To achieve a reliable trend identification, this research will follow six major steps as depicted in Figure 29. This first step will initially focus on correlating the in-situ recorded AE amplitude with the applied loading conditions to filter noise sources and identify trends. However, dependence on the AE amplitude for reliable trend identification can be misleading due to the fact that amplitude is highly influenced by the source-sensor distance and the magnitude of the source mechanism. Alternatively, the acquired AE signals are transformed from the temporal domain to the spectral domain and novel AE feature descriptors are identified. Consequently, the AE amplitude that reveal distinct trends are analyzed in terms of their wave signature to characterize the wave shape and subsequently transformed to the frequency domain using FFT algorithms. The next step involves the use of wavelet analysis to identify the evolution of the frequency of the extracted waveform and recognize the frequency associated with the source mechanism and the structural geometry. Further, these waveforms will be then segmented into four different frequency ranges and the percentage of energy (partial powers) in each frequency range will be analyzed. Finally, novel AE damage parameters based on empirical observations will be developed based on advanced signal processing techniques for robust trend identification.

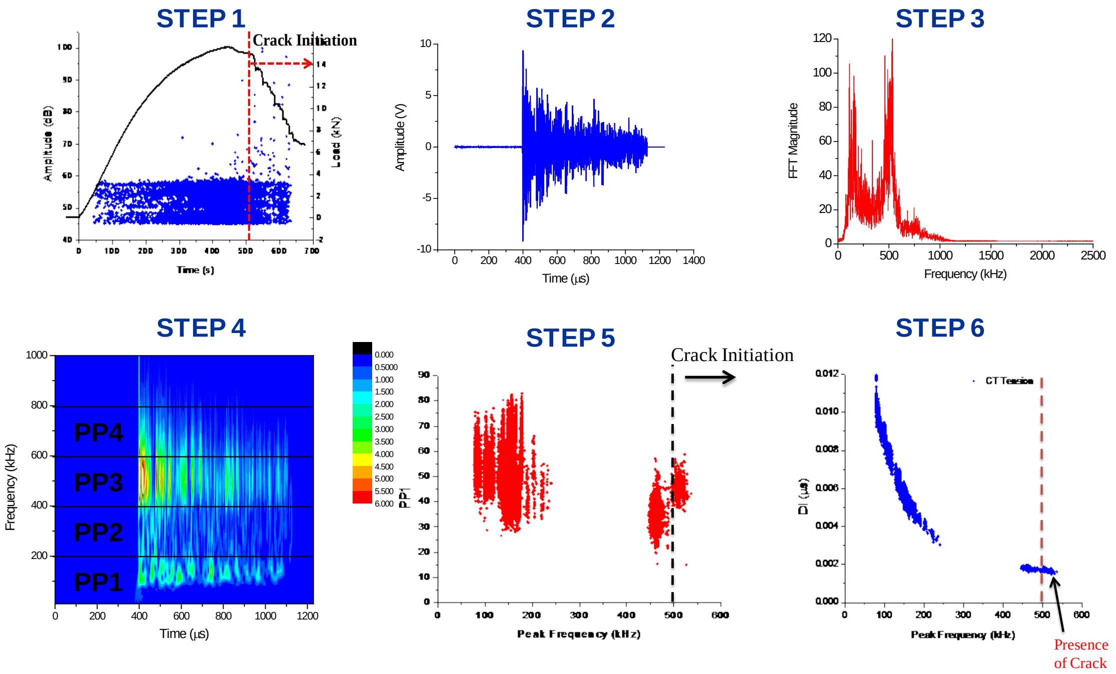

Figure 29: Reliable trend identification process

3.1.5 PATTERN RECOGNITION APPROACHES

To recognize the goal of condition based maintenance (CBM) procedures rather than periodic inspection schedules, it is crucial to develop an automated detection algorithm in addition to detecting and locating the damage source. For this purpose, SHM systems need to be trained to identify and distinguish specific AE characteristics that are particular to the damage from the entire data set using supervised learning algorithms.

The success of this training algorithm will depend on identifying the natural clusters from a testing set using unsupervised learning algorithms.

Consequently, statistical pattern recognition methods and neural network techniques will be explored to identify the natural clusters of the obtained data set. The ensemble feature descriptors and the novel features identified in the previous stage will be utilized as the input vectors to the clustering process. Subsequently, the recorded data set will be clustered into several classes based on a mathematical criteria defined by the statistical methods or biologically inspired learning algorithms. In this research, several statistical pattern recognition methods such as k means, Forgy and max-min will be utilized to classify the various AE signatures in the different data set and identify a common class across several specimens. Additionally, learning vector quantization (LVQ) technique will also be utilized to check the robustness of the clustering methodology and cross-validate the statistical pattern recognition approaches.

3.1.6 DATA FUSION

It is a fact that no single technique is capable of completely evaluating the quality of the structural integrity due to several factors including material type, limited surface access, high sensitivity to noise, complex geometry etc. AE is a promising technique for real time inspection of the structure and can identify the different stages of damage, i.e., the initiation and propagation of the damage source. This is performed based on the repetitive testing and evaluation of the AE signals obtained from multiple experiments and then validated for subsequent tests. The indications of the damage are then analyzed in terms of their statistical outputs. These statistical outputs are calculated from every AE hit that is typically higher than a pre-determined threshold. The threshold serves as the first line of filtering and eliminating the noise signals (unwanted signals) present in the environment, operation (hydraulics etc), wave reflections etc. However, a single line of filtration is often inadequate and the proposed NDE approach would serve both as an efficient filtering process and assist in the interpretation of the unknown AE sources.

The simultaneous use of several NDT methods for effective SHM, as proposed in this paper, is based on the extraction of damage-sensitive features and the successful data fusion of heterogeneous information for robust damage detection. For this purpose, NDT features are commonly treated as statistical variables and correlations with damage are established by using several approaches. Among these techniques, novelty detection methods have become increasingly popular in SHM. Novelty or Anomaly Detection [153] establishes whether or not a new configuration of a given system (in this case the structural component under observation) is discordant or inconsistent from the baseline configuration, which consists of an existing dataset (or patterns) that describe the normal operative conditions of the undamaged component. Examples of methods for novelty detection include: outlier analysis [153, 154], probability density estimation, and artificial neural networks [155].

Hence, an integrated NDT approach coupled with an experimental data-driven methodology is undertaken to execute this acoustics based framework with the ultimate goal to improve infrastructure condition assessment particularly aerospace structures. Central to this cross-validated acoustics framework is the integration of non-contact full field optical techniques that can serve both as an independent monitoring technique and also provide visual and quantitative evidence to the unknown AE signals generated during the test. Conversely, the author is aware that it is not possible to have the luxury of the non-contact techniques at all times, thus it essential to use these techniques to better interpret and cross-validate AE signals so that the reliability of AE can be enhanced and be implemented for SHM applications.

3.2 PROPOSED VISION

Hybrid Acoustic Ultrasonic Testing (HAUT) System

An ideal SHM system must satisfy the Rytter's hierarchy [156], i.e. detect, locate and classify the extent of damage in structures. The ultimate goal of this research framework is to develop a reliable SHM strategy for condition based maintenance for primarily aerospace inspection as shown in Fig. xx. In order to achieve a condition based maintenance approach, it is critical that adopted system provides real time feedback during in service operations about the structural integrity. This approach will ensure optimal structural safety and importantly ensure structural downtime only if absolutely essential. Thus, the proposed SHM vision will consist of a hybrid acoustic ultrasonic testing (HAUT) system that includes onboard and/or wireless AE sensors and active GUW transducers that will serve as a cross-validated NDE system especially in challenging environmental conditions. It is envisioned that the AE sensors in the future will shift from the typical piezoelectric sensors to advanced light weight multi sensing modalities such as MEM sensors [14, 15], fiber bragg grating [16, 17]. These advanced sensors could potentially be developed as a self cross validating technique where complementary statistical data such as strain and AE amplitude could be combined with simultaneous change indicating damage activity.

The AE sensors will be placed at the critical points (such as the T ribs) along the wing structure while the GUW transducers will be placed along the skin. Initially, the passive

AE sensors will be trained to pick up in-situ indications of the integrity of the aircraft wing based on the **pre-defined ensemble feature characteristics** identified during laboratory testing and automated using pattern recognition algorithms. In addition to detecting the damage signals, the use of multiple AE sensors would be utilized to locate the region of interest based on triangulation. Subsequently, the SHM system will then shift to an active mode by GUW transducers to generate guided waves in the structure using a pitch-catch approach. The received signals will then be passed through a novelty damage detector scheme (such as the one shown in section x.x) the signals that cross the predefined threshold and demonstrate major AE activity will be color coded into three main categories. Category I, **land & inspect** would represent the group of signals that would deviate significantly from the threshold and high AE activity indicating severe damage of the aircraft and would require urgent attention. Category II, **inspect ASAP**, would signify the group of signals that deviates slightly from the threshold and contain less AE activity indicating considerable deterioration and requires inspection upon landing. The final category, **no immediate action required,** would indicate negligible deterioration and would not require any action. These signals could mainly be attributed to environmental variation, operational conditions or insignificant damage.

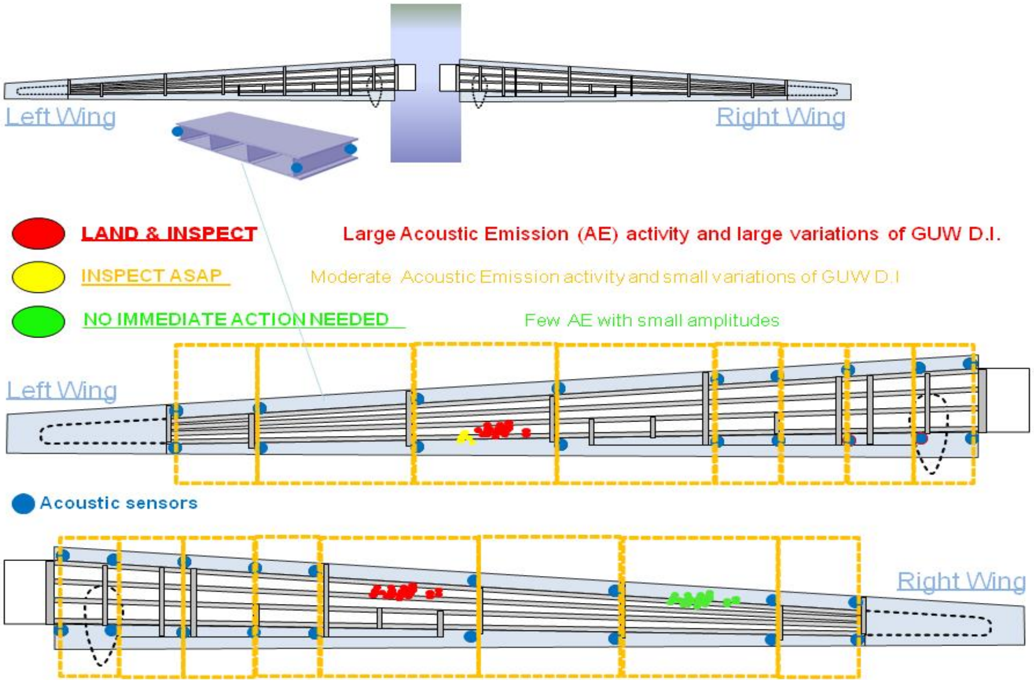

Figure 30. Proposed vision for next generation aerospace SHM system

3.3 PROPOSED FRAMEWORK

The proposed approach for this research is adopted from Farrar's SHM paradigm [19] with specific changes in each steps. A **Novel Optico-Acoustic Sensing (NOAS) framework** is developed with the capability of using it as independent monitoring techniques to aid in the interpretation of the AE signals and also with exclusive triggering protocols to activate the optical techniques smartly based on the AE system. These advanced capabilities of the system makes it extremely convenient to not just utilize as a cross validating system but also utilize an energy conservative sensing approach for SHM applications. This approach presents and implements both the hardware and software integration of the NOAS system. Central to developing this cross validating approach is the four main steps i) Operational Evaluation, ii) Data Acquisition iii) Data Post Processing and iv) Data Mining.

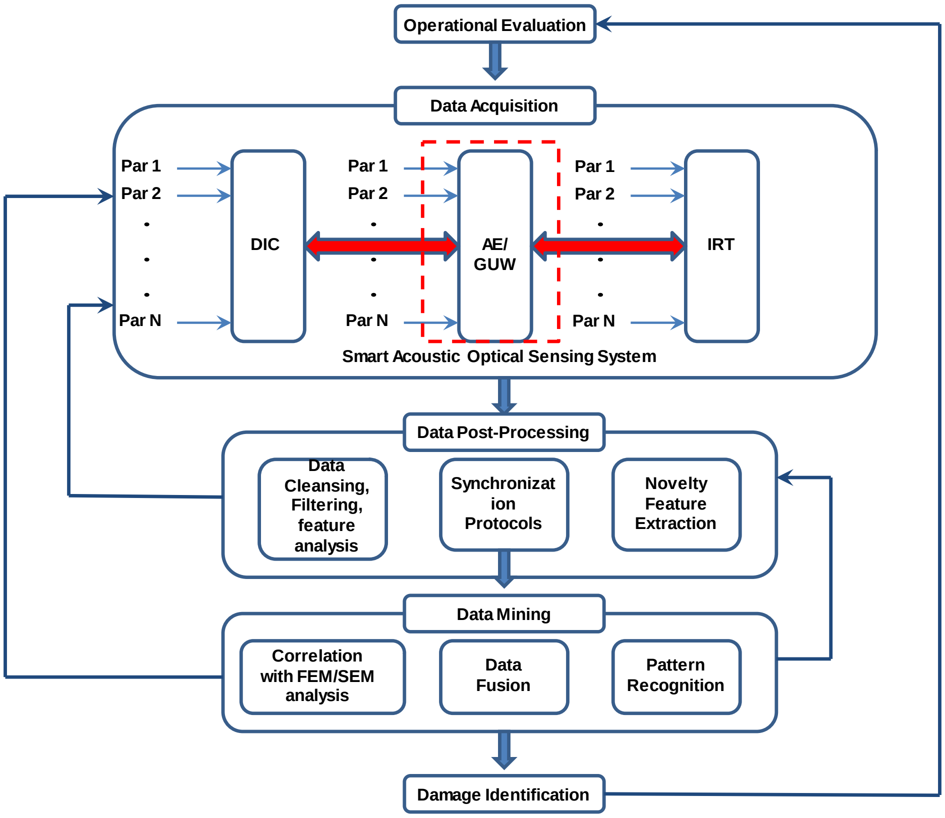

Fig 31. Proposed NOAS approach

3.3.1 OPERATIONAL EVALUATION

The first step in the approach is evaluating the nature of the damage sought and subsequently the goals of the damage identification strategy. It is important to tailor the process to the specific damage sought and material condition to reliably identify both damage precursors and the damage itself. It is well known that various sources produce specific AE signatures. However, in order to recognize these signatures reliably, it is critical to design targeted experimental plan with specific loading profiles. In order to associate a specific AE signature to a particular failure mechanism, it is crucial to filter out the loading effect, geometry of the material, the tertiary sources associated with the testing of the specific specimen and the effect of the structural features on the wave propagation. Consequently, an experimental data driven approach that factors in both the loading and geometry effects will be undertaken to identify similar AE signatures and features associated with a specific type of damage across different specimens.

3.3.2 DATA ACQUISITION

The second step in the proposed approach is the data acquisition process which involves the hardware integration of the NOAS system during experimental testing. The NOAS utilizes the simultaneous use of the Acoustic Emission technique in parallel with the full field optical techniques such as DIC and IRT with the goal to reliably detect and identify the initiation and development of damage modes. This NOAS approach has been successfully applied for material characterization and targeted failure detection for a range of materials as will be seen in the subsequent chapters of this thesis. The core of this sensing approach is based on identifying the primary AE signatures in the material by adopting a heterogeneous combination of AE features with full field DIC and IRT data.

The AE monitoring system consisted of a multichannel acquisition board, piezoelectric sensors, preamplifiers, parametric box and the acquisition software manufactured by Mistras (Fig.x). Two different multichannel acquisition boards (as shown in Fig.xx and Fig.xx) were utilized in this research in order to i) evaluate the effect of the electronics on the received AE signals and ii) to robustly identify AE trends irrespective of the acquisition system. The specifications of these AE boards can be found in [20]. The DiSP 4 board consisted of a 4 channel, 16 bit PCI/DSP 4 with a maximum sampling rate of 10 MS/s system and the PCI 2 board consisted of a 2 channel, 18 bit with a maximum sampling rate of 40 MS/s system. The AE acquisition boards were housed in a Micro-II industrial chassis.

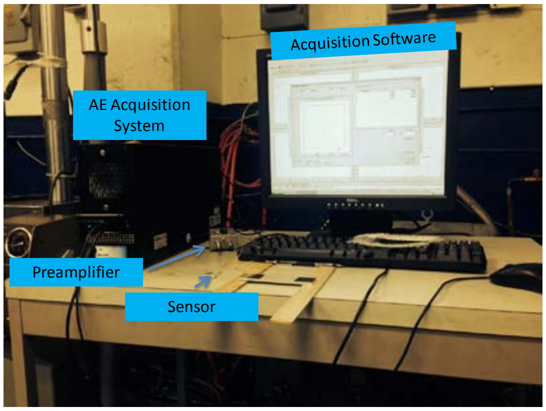

Figure. 32 AE monitoring system

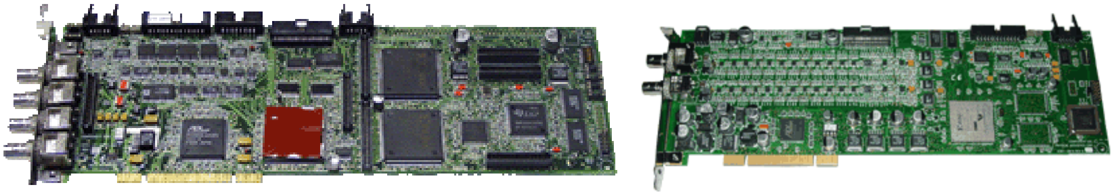

Figure. 33 AE Acquisition board (a) DiSP 4 (b) PCI 2 [20]

Additionally, the utilized acquisition board has the capability of receiving eight different parametric inputs to record operational and/or damage parameters for accurate interpretation using the parametric box shown in Fig.x. Specifically, mechanical parameters such as load and displacement were fed into the AE parametric box through a BNC connector and correlated with the AE parameters in real time. The parametric input box was connected to the Micro-II chassis using an I/O cable. The parametric box also supports four parametric outputs ports that can be utilized to develop smart monitoring strategies for alarm warning and also for triggering other NDT methods.

Figure. 34 AE parametric input box

A critical element in the AE analysis is the choice of the sensors utilized for the experiment. AE sensors are broadly classified into resonant and wide band sensors. This research primarily utilized two different wide band sensors (pico and Nano 30) as defined by their sensor calibration chart supplied by the manufacturer. The sensor calibration chart for the pico and nano 30 sensors are shown in Fig.x and Fig.x respectively. The operational range of the pico sensors was between 200-750 kHz with its peak frequency at 500kHz. The operational range of the nano 30 sensors was between 125-750 kHz with its peak frequency at 300kHz. The sensors are mounted on the surface of the specimen using hot melt glue.

The received AE signals from the sensors are then preamplified using a 2/4/6 (20/40/60 dB gain) preamplifiers with a uniform gain of 40 dB. The preamplifiers had a band pass filter of 20-1200kHz. Finally, the amplified signals are then fed in to the acquisition software for real time monitoring. Depending on the operational conditions, a fixed threshold between 40-50 dB was utilized for all the experimental tests.

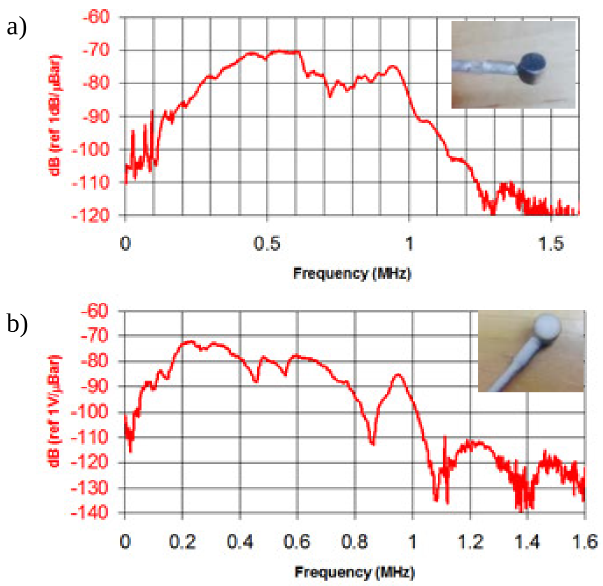

Figure. 35 Sensor calibration chart (a) Pico (b) Nano 30

The threshold used minimized the recordings of unwanted AE signals arising due to the hydraulics, friction at the fixtures etc. For metals, the peak definition time (PDT), hit definition time (HDT) and hit lockout time (HLT) were 200, 500 and 700 µs respectively with a maximum duration of 1ms while for composites, the PDT, HDT and HLT were 40, 80 and 300 µs respectively. A sampling rate of 5 MSPS was utilized for all the experimental tests. Prior to every experimental test, the AE sensors were calibrated in accordance with ASTM E976 to check the response of the sensors [21].

To perform this, 0.3mm mechanical 2H lead pencil with a shoe is broken against the tested material as shown in Fig.x. The lead breakage releases a sudden stress wave in the material that is repeatable and represents an ideal AE wave. This calibration technique was introduced by Hsu and Nielsen and is referred to as the Hsu-Nielsen test. It is essential to note that care must be taken while performing the Hsu-Nielsen test and a minimum spacing of 10 cm must be ensured between the point of impact and the sensor.

Additionally, a 30 degree angle between the lead and the test surface and a lead length of 2-3mm must be ensured. Finally, Hsu-Nielsen tests were also utilized to calculate the wave speed in the material based on the sensor spacing. The wave speed in the material was calculated based on the time of arrival and the distances between the sensors. Both 2D and linear location algorithms were implemented for location of critical regions and spatial filtering of AE signals in real time.

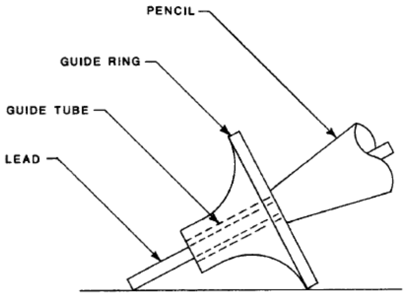

(a) Nielsen Shoe on Hsu Pencil Source

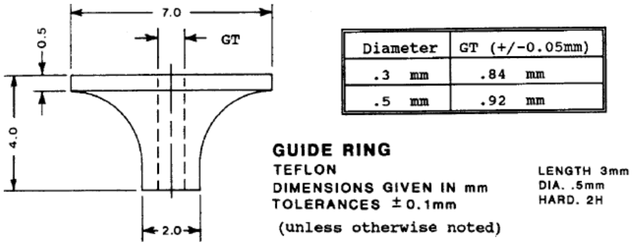

Figure 36. Hsu-Nielsen Test

The DIC system consisted of two 5M Baumer TGX15 monochrome camera, 50mm lens, sensor controller and the acquisition software as manufactured by GOM. The DIC system has a maximum acquisition rate of 7 frames per second at full resolution while it can be further increased to 29 frames per second at half resolution. The cameras are placed on an item bar (Figure 37) which is then mounted on a tripod with an adjustable base that has two degrees of freedom enabling the cameras to translate and pivot along the item bar. The lens are connected to the cameras using a thread mount. The cameras are then connected to the sensor controller using a coaxial optical cables and in turn the controller is then connected to a laptop containing the acquisition software using a GIGE LAN connection. Similar to the AE parametric box, parametric inputs such as load and displacement can be fed into the DIC system through the analog inputs in the sensor controller (Figure 38). Additionally, the DIC cameras can also receive TTL trigger inputs from external devices such as the AE system through the trigger port. In fact, another unique achievement of this research was the development of a Smart Acoustic Optical Triggering (SAOT) system.

Figure 37. DIC Camera and sensor controller

Figure 38. Analog inputs and trigger ports

The tables provided by the manufacturer is utilized to achieve optimal measuring parameters for the specific field of view (FOV). For a 65 x 55 mm^2 FOV, a base distance of 136mm and a measuring distance of 395mm was utilized. A focused laser beam is projected on the test surface and used as an intersecting reference in adjusting the camera positions to obtain a suitable camera angle (α). Central to obtaining accurate deformation measurements, is calibrating the cameras using a calibration block that best fits the required field of view. A calibration block of 55 x 44 mm^2 was used to adjust the focus and ensure optimal lighting conditions for the measurement. The camera focus was adjusted until all the ID numbers and coded markers were crisply obtained. Optimal lighting conditions was ensured by adjusting the LED lights along with the cameras and by entering an appropriate shutter time. A shutter time of 35ms was found to be appropriate across all the experimental tests. Additionally, a violet and blue false image was primarily utilized as the ideal lighting condition to ensure accurate measurements.

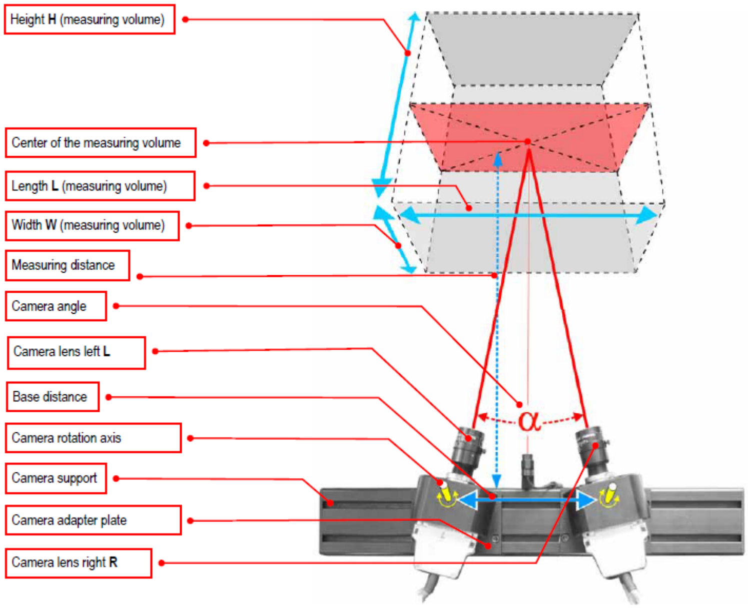

Figure 39. DIC calibration principle

Subsequently, a series of calibration block images at different orientations and positions relative to the cameras were taken and computed to evaluate the sensitivity and resolution of the DIC measurements for the given FOV. The above mentioned measuring parameters resulted in a 24° camera angle with a deviation of 0.05 pixels. A random speckle pattern was then applied on the test specimen as shown in Figure 40a to create the required surface contrast. Typically, fine black spray dots are applied on a white background to track the deformation of the test sample. The specimen was then mounted according to its final test configuration Figure 40b and a few snapshots were taken before the application of load to establish the noise floor and minimum sensitivity.

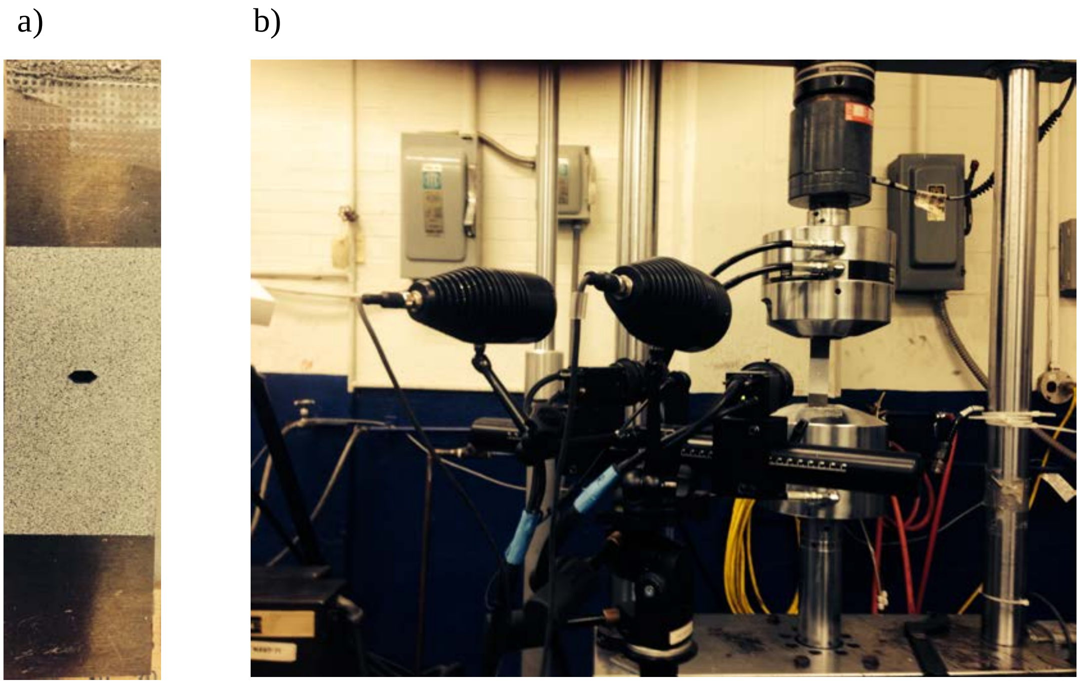

Figure 40. (a) DIC speckle pattern (b) DIC camera configuration

The IRT system consisted of a FLIR A320 camera (Figure 41) with a 320 x 240 pixel resolution, 18mm focal lens and spectral resolution of 7.5-13 µm with real time heat measuring capability. The camera has a dual object temperature range of -20°C to

+120°C and 0°C to 350°C depending on the thermal conditions. The camera has a maximum sampling rate of 60Hz. During the quasi-static experiments, a sampling rate of 30 Hz and working distance of 50mm was utilized to obtain the best spatial resolution.

Figure 41. FLIR A320 IR camera

Unlike the AE and DIC system, the IRT system does not support external parametrics. Thus, in all the experiments performed in this research, IRT camera was initiated along with the DIC to synchronize the loading information with the IRT images in post process. A detailed specification of the IRT camera is presented in Table 1. as obtained from the manufacturer's website.

TABLE 1: FLIR A320 Specifications

Measurement	
Object Temperature Range	-20°C to +120°C 0°C to +350°C
Accuracy	± 2°C or ± 2%
Image and Optical Data	
Field of View	25° x 19°
Spatial Resolution	1.36mrad
Thermal Sensitivity	70mK @ +30°C
Detector Data	
Spectral Range	7.5-13 µm
Detector Pitch	25 µm

3.3.3 DATA POST PROCESSING

The third step in the SHM process is the Data Post Processing stage, which focuses on data cleansing, synchronization and feature extraction. The significant advantage of NOAS approach is the heterogeneous yet valuable integration of multi-domain and multi-phenomenon type of data set. This unique integration provides critical information about the damage that can act as physical classifiers and ensemble feature descriptors for damage identification. Typically, conventional AE data relies on an significant or subtle change of parameters to provide any indication of damage. However, this change of parameters could be significantly affected by the recording of unwanted signals (noise). Thus in order to identify and characterize the genuine AE signals, it is imperative to develop a reliable methodology to filter and clean the unwanted AE signals.

A possible approach of cleaning noisy AE signals is utilizing a spatial filter based on 1D/2D/3D location algorithms and cross correlating it with the applied loading phenomenon. Although there is significant merit in adopting this approach, subtle or local changes in the material cannot be identified by this approach. Consequently, high resolution optical imaging techniques provide an accurate tool to identify local changes in the material and cross-validate the AE signals. Thus, the optical full field visualizations will be extensively utilized to clean and filter the noisy signals. Subsequently, statistical analysis will be extracted from the full field data and multi-modal analysis will be utilized to characterize accurately the AE sources associated with damage. This kind of multi-modal data mining can significantly assist in the interpretation and identification of AE signatures.

Furthermore, in addition to the time extracted features and multi-modal features, AE features will be extracted from the frequency and joint frequency domain as well. Typically, AE signals in the time domain are converted into the frequency domain using the Fast Fourier transform (FFT) algorithm. Consequently, frequency characteristics such as peak frequency, frequency centroid, FFT width 30%, etc are then extracted and utilized for feature analysis. However, the FFT algorithm takes into account the entire signal length and can conceal the local frequency changes that are indicative of subtle changes [26]. Additionally, wavelet [25, 26] based feature extraction techniques will be explored to identify the evolution of the frequency characteristics of the signal.

In order to analyze the complex heterogeneous data set obtained from the multiple NDT techniques, a combination of different analytical tools including commercially available software and in house developed scripts. The scripts, written in MATLAB, were utilized to develop for both feature extraction and to develop novelty damage detector using a data fusion scheme. NOESIS [23], commercially available analysis software data was primarily utilized for advanced processing of all the obtained AE data for feature extraction and pattern recognition. ARAMIS [24] and FLIR EXAMINR, commercially available software were heavily utilized to analyze the DIC and the IRT images respectively. In addition to performing NDT analysis, other validation tools such as scanning electron microscopy (SEM) and ABAQUS were also utilized to cross validate and interpret the AE indications.

3.3.4 DATA MINING

The simultaneous use of the multiple NDT techniques presents an unique data set regarding several damage characteristics. This combined data set when leveraged intelligently provides a robust approach in extracting critical information such as location and severity of damage and effectively interpreting the unknown AE signals. Conventional AE analysis can raise false positive signals if extensive and detailed analysis is not performed during laboratory testing owing to environmental or operational variations. In order to characterize and interpret AE signals effectively, it is beneficial to adopt a data mining approach either through combining multi-modal data or through heterogeneous pattern recognition analysis.

In the previous section, the focus was on extracting sensitive features from the multiple NDT set and synchronizing them for data interpretation. This is further improved by correlating the heterogeneous features to cross-validate the changes in the AE features. For instance, the change in AE amplitude at the same time instant that the strain and the heat changes does provide a strong indication of potential damage in the material. This could also serve as a reliable tool in detecting impending (damage precursors) failure of the structure. Additionally, another approach that would be explored to enhance the data interpretation process is through the creation of multimodal damage index. This would be based on the integration of features extracted from the different techniques and combining them using novelty damage detectors based on outlier analysis to reliably detect and quantify the damage in the material.

Finally, pattern recognition algorithms utilizing heterogeneous AE features and novel feature descriptors would be utilized as input vectors for the pattern recognition process.

CHAPTER 4: THE IDENTIFICATION OF PRIMARY AE SOURCES

4.1 INTRODUCTION

AE relies on the recording on mechanical vibrations traveling in the form of elastic stress waves produced by the irreversible changes (primary AE sources) in the material when subjected to external loading. This phenomenon makes the AE technique extremely sensitive to the faintest surface movement (along the order of 10^{-12}) can detect change in the material. This extreme sensitivity makes the AE also a challenging technique to interpret as it is sensitive to every mechanical disturbances produced by and in the material by various sources including the noise sources. The primary challenge associated with AE testing is the presence and interference of 'noise signals' with the primary AE signals produced by the material.

These noise sources are anything that does not constitute primary AE source, including in some cases secondary AE sources such as crack rubbing and fretting. In general, the sources of noise include electromagnetic interference (EMI), environmental variations, operational conditions, as well as hydraulic and mechanical component influence. These signals could significantly affect not only the quality of the recorded AE data but also inaccurately trigger and mask the primary AE sources. The consequences of these sources are that it could portray a false perception of the integrity of the structure. Hence, ideally these sources should be identified before the test and subsequently filtered out from the actual test information to obtain a reliable and "clean" AE data set. Additionally, it is also important to understand and identify the primary AE sources in the material to make accurate interpretations regarding the presence of damage in the material/structure.

Consequently, this research will adopt an extensive and comprehensive AE study to i) identify the characteristics associated with typical AE noise sources and ii) identify the primary AE sources that includes experimental studies of fundamental behavior of materials and classification of AE signals. This extensive analysis will comprise of the following steps

1. Experimental simulation of AE signals including noise sources such as EMI, metal friction and sudden impact.
2. Correlation of AE signatures to fundamental mechanical behavior including microscopic validation when possible and using feature descriptors to characterize the AE signatures
3. Classification of AE signals

4.2 IDENTIFICATION OF AE SIGNALS

4.2.1 NOISE AND INTERPRETATION OF AE SOURCES

The first step in this research was to identify the signatures of some of the noise sources and understand their behavior. Furthermore, the features of these sources were extensively analyzed to recognize their characteristics. Specifically, four AE sources namely pencil lead break (PLB), friction, hammer impact and electromagnetic interference (EMI) were artificially simulated on a thin aluminum plate at specific time intervals as shown in Figure 5. It should be mentioned that the EMI signals were simulated by toggling the preamplifier gain between 40-60dB. Four pico sensors were placed at the four edges of the plate to detect the stress waves produced by these AE sources. A threshold of 45dB was utilized for the simulations and a sampling rate of

5MHz was utilized for the signal acquisition. A band pass filter of 100-400kHz was utilized for this simulation. All the acquired signals were recorded using the AEWin DiSP system and the 2/4/6 preamplifier were used with a uniform gain of 40dB expect for the EMI source. The peak definition time, hit definition time and hit lockout time of 200µs, 700µs and 1000µs were utilized.

PLB Friction

Impact EMI

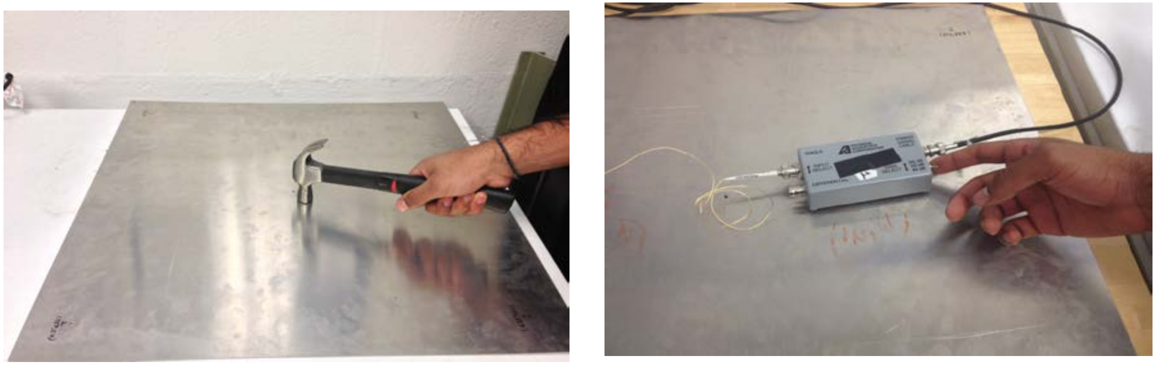

Figure 42: Simulated AE signals

All the simulated AE sources produced characteristic AE waves in the material and were easily picked up above the threshold. Several features were then extracted from these waveforms in both the temporal and spectral domain. The extracted AE amplitude and duration for the four different sources are shown in Figure 43. Expectedly, the amplitude of the PLB tests is the highest among all the sources and is about 90dB. This is attributed to the fact that the PLB waveforms represent an ideal AE fracture source and thus is prescribed as a ASTM standard procedure to calibrate the sensors used during the test. PLB test are performed prior to the actual test at a certain distances from the sensor to calibrate the response of the sensor in accordance with ASTM standard. The response of the AE sensors are then evaluated based on the amplitude of the recorded PLB signals. An ideal sensor response would record an amplitude of 100dB while anything greater than 95dB is generally acceptable during the calibration process. In this particular simulation, the amplitude of the PLB signals were recorded to be around 85-90dB. This is attributed to the attenuation effect on the propagating waveform as the exact point of the PLB was far from the sensor locations.

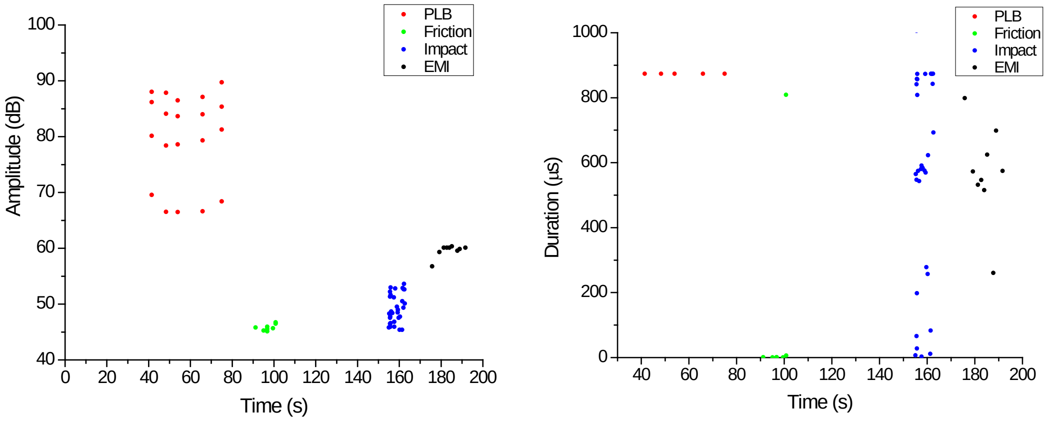

Figure 43: Simulated AE feature characteristics

It can be observed that the friction had an amplitude of 45dB, mechanical impacts had an amplitude between 45-55dB and the EMI had an amplitude of 60dB. Thus, the amplitude of the four sources were seen to be quite different for all the sources. The extracted duration is also shown in Figure 43. The duration of these sources were also seen to exhibit a similar trend as the amplitude although the duration of the friction source was extremely low. Additionally, the duration of the impact source was noted to be more widespread in comparison with the other sources. Further, the counts and energy were also extracted and are shown in Figure 44.

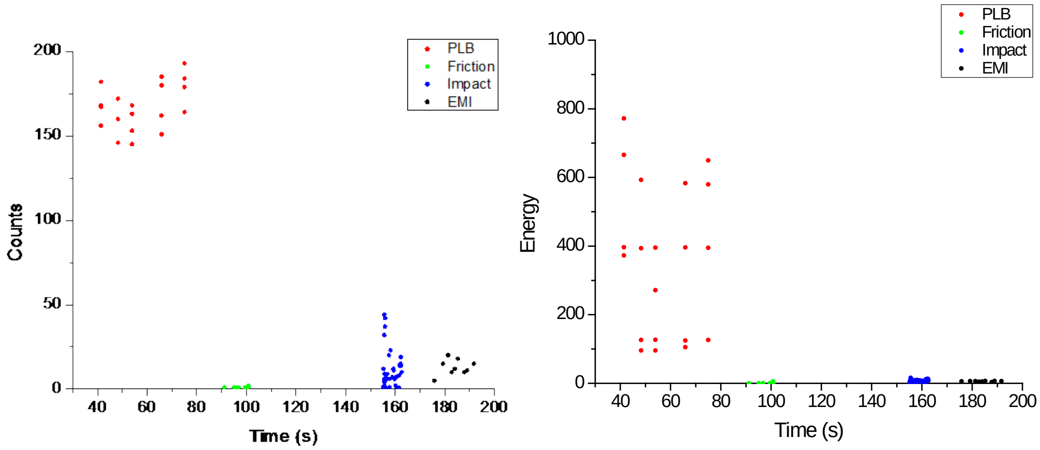

Figure 44: Simulated AE feature characteristics

It can be noted that the counts exhibit a similar trend to that shown previously with the amplitude. Conversely, the energy was not a good feature to separate the AE signals as the energy of the three sources were seen to be similar. This proves that the reliance on AE activity based time features by itself is insufficient and unreliable for damage identification. It is imperative to shift towards AE waveform based analysis and advanced frequency analysis for AE source interpretation. Consequently, the waveforms corresponding to the four sources were extracted and comprehensively analyzed. The acquired AE waveforms from the different sources are shown in Figure 45.

The signatures of these sources clearly showed a distinct behavior as well. The acquired data was sampled at 5MHz and a pre-trigger of 150μs was utilized. The raw amplitude of the waveforms confirmed the previously observed feature trend. However, the acquired waveform shows that the shape is characteristic of the source. The waveforms acquired from the PLB and EMI are shown to possess a burst type emission while friction and impact revealed a continuous type emission. Another important observation noted was that there was significant activity in the pre-trigger for both the friction and mechanical impact sources. Thus, it is essential to utilize a pre-trigger to observe the activity of source mechanisms and understand their nature.

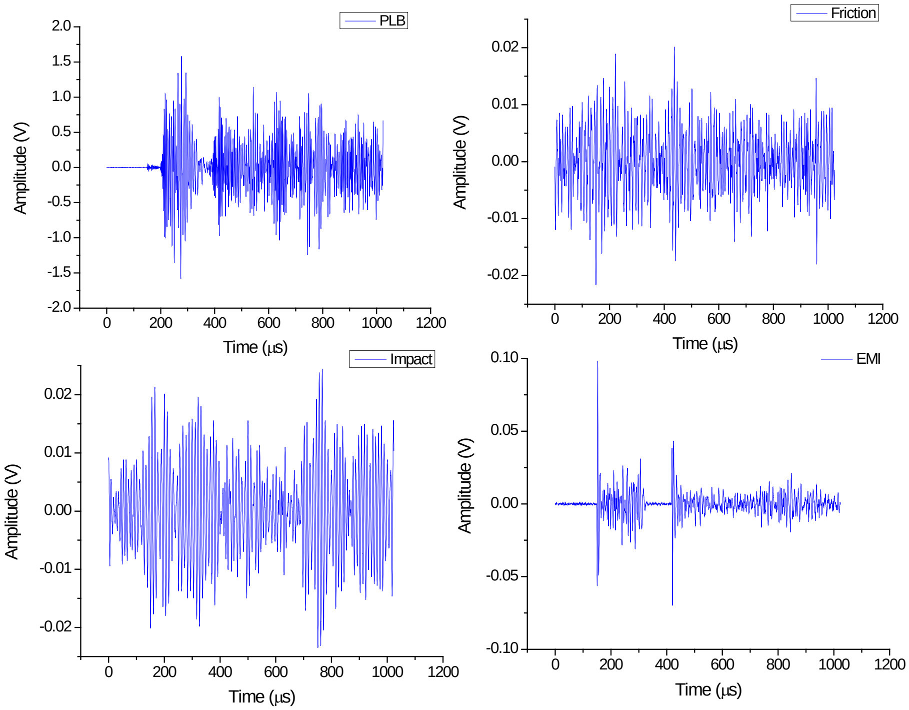

Figure 45: Simulated AE waveforms

To understand their behavior further, a joint time-frequency analysis was performed using a wavelet transform. Figure 46 shows the frequency evolution of the PLB waveform. It can be seen that the associated first arrival wave packet is seen to lie between 200-350kHz. However, the frequency associated with the subsequent wave packet is noted to have a constant frequency at 125kHz. Interestingly, waveform exhibited a periodicity in their frequency behavior with the high frequency and low frequency oscillating in time. Since, the first arrival is associated with the actual source, it can be noted that the relative high frequency component of the waveform is associated with pencil lead break test while the subsequent wave packets can be associated with the reflections at the boundaries. Further, the attenuation of the waveform is also noted with the wavelet coefficient decreasing as a function of time.

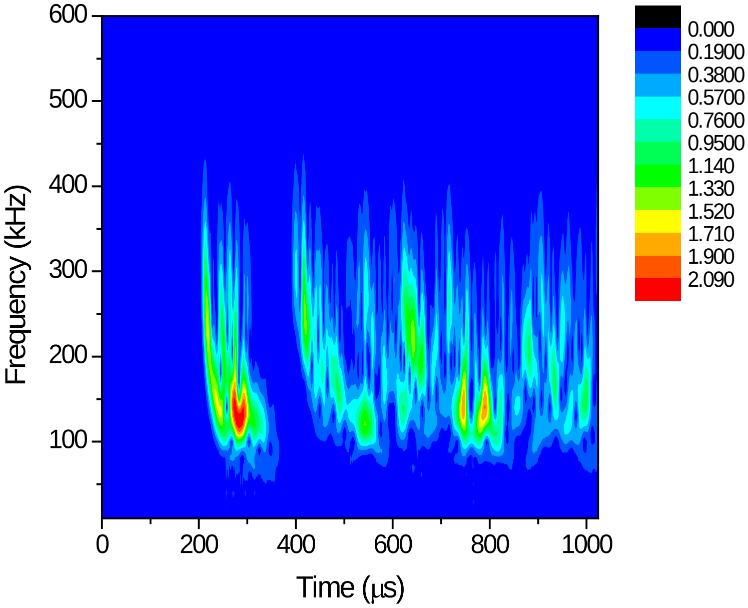

Figure 46: Frequency evolution of the PLB waveform

The frequency evolution of the friction waveform is shown in Figure 47. It must be pointed out that the wave amplitude of the friction waveform (represented by the color limit) is significantly lower than the friction waveform. Unlike, the PLB waveform, the frequency of the friction waveform is seen to have a constant peak frequency around 100-125kHz for the entire duration of the waveform. However, the wavelet analysis also reveals that the friction waveform has a low amplitude but a consistent wide spectral behavior associated with it.

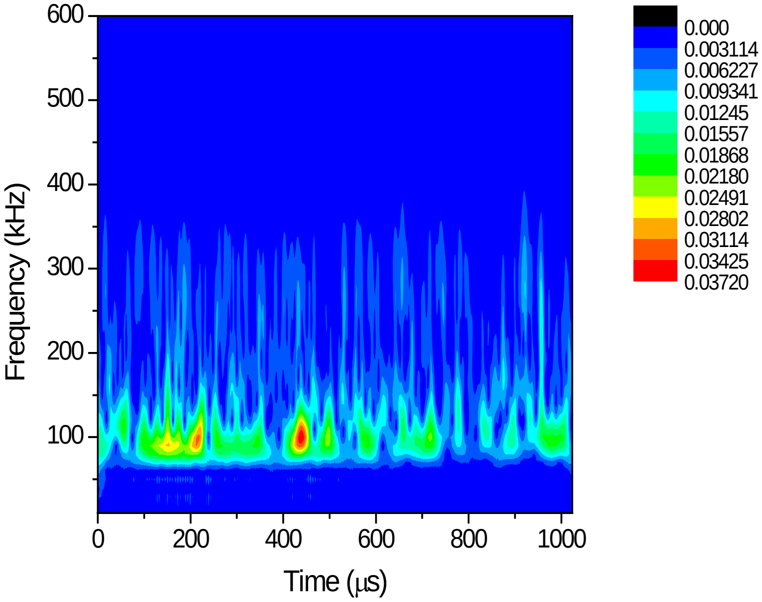

Figure 47: Frequency evolution of the Friction waveform

Similar to the friction waveform, the impact waveform also revealed a continuous behavior. The impact waveforms had a similar peak frequency behavior as the friction waveform although the amplitude of the impact waveform was higher (Figure 48). However, the impact waveform does not demonstrate a wide spectral behavior as the friction waveform. The maximum frequency of the impact was noted around 200kHz. Finally, the wavelet analysis revealed that the EMI waveform (Figure 49) had a peak frequency between 100-200kHz. It is clearly noticed that whenever there was a sudden spike in the amplitude, these wave packets had a wide spectral behavior while the other wave packets had much more narrow behavior. The second spike in the amplitude is due to the reflection of the first spike at the boundary.

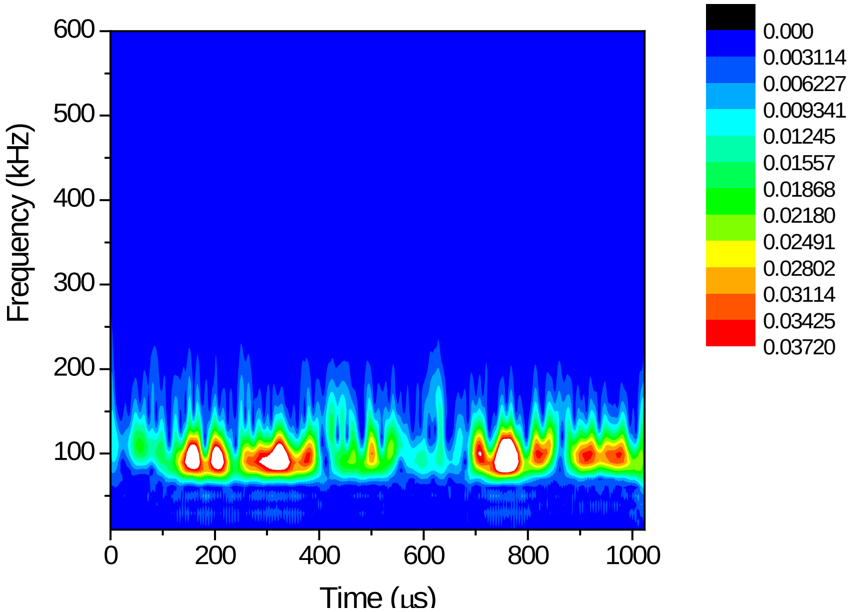

Figure 48: Frequency evolution of the impact waveform

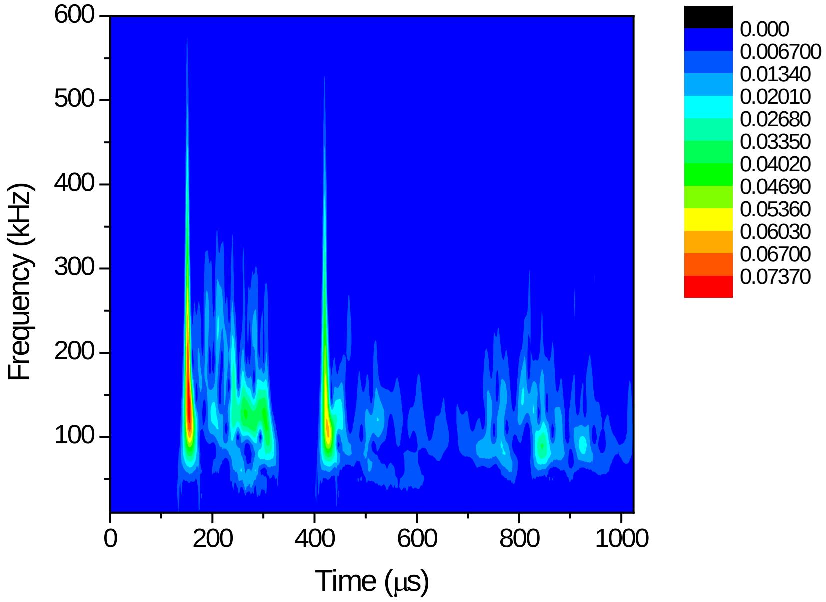

Figure 49: Frequency evolution of the EMI waveform

Evidently, all the four sources simulated included a frequency content at 100-125kHz either during the first arrival or immediately after the first arrival. The common feature between the four sources was only the sensor and the medium of propagation (material).

The pico sensor response was illustrated in the previous chapter and it can be recalled that the utilized sensors had a resonant frequency at 450-500kHz. Thus, it can concluded that the 125kHz noticed across the four sources cannot be attributed to the sensor response but to the medium of propagation. Consequently, although the peak frequency value is sufficient to discriminate between two sources, it is inadequate to reliably distinguish between all the four sources. Conversely, it was observed although the friction and impact had similar peak frequencies, their broad spectral behavior was not the same. The friction source had a wider spectral content than the impact but a very less amplitude in those higher frequency ranges.

Alternately, it is advantageous to segment the frequency behavior into different ranges and compute the magnitude in each frequency range as a reliable feature descriptor to distinguish the source mechanisms. As a result, the acquired waveforms from all the sources were extracted and converted into the frequency domain using FFT. Subsequently, the frequency vector was then divided into four evenly spaced intervals as 0-200kHz, 200-400kHz, 400-600kHz and 600-800kHz and the percentage of energy in each of these intervals was calculated. The partial power 1 (PP1) refers to the percentage of energy in the 1st range (0-200kHz) while the PP2 refers to the percentage of energy in the 200-400kHz. The PP3 and PP4 refers to the percentage of energy in the 400-600kHz and 600-800kHz respectively. The partial power analysis for the four sources are shown in Figure 50.

A very interesting observation can be made from the partial power analysis. The impact source has the maximum PP1 but very low PP2, PP3 and PP4. On the other hand, PLB has the maximum PP2 while the friction source has a high PP1 but a low PP2. Similarly, the EMI has a low PP2 but a high PP1. Every source is seen to be extremely active in the PP1 but mostly dormant in the PP3 and PP4. Although, all the sources are active in PP1, it can be observed that the sources have different percentage of energy.

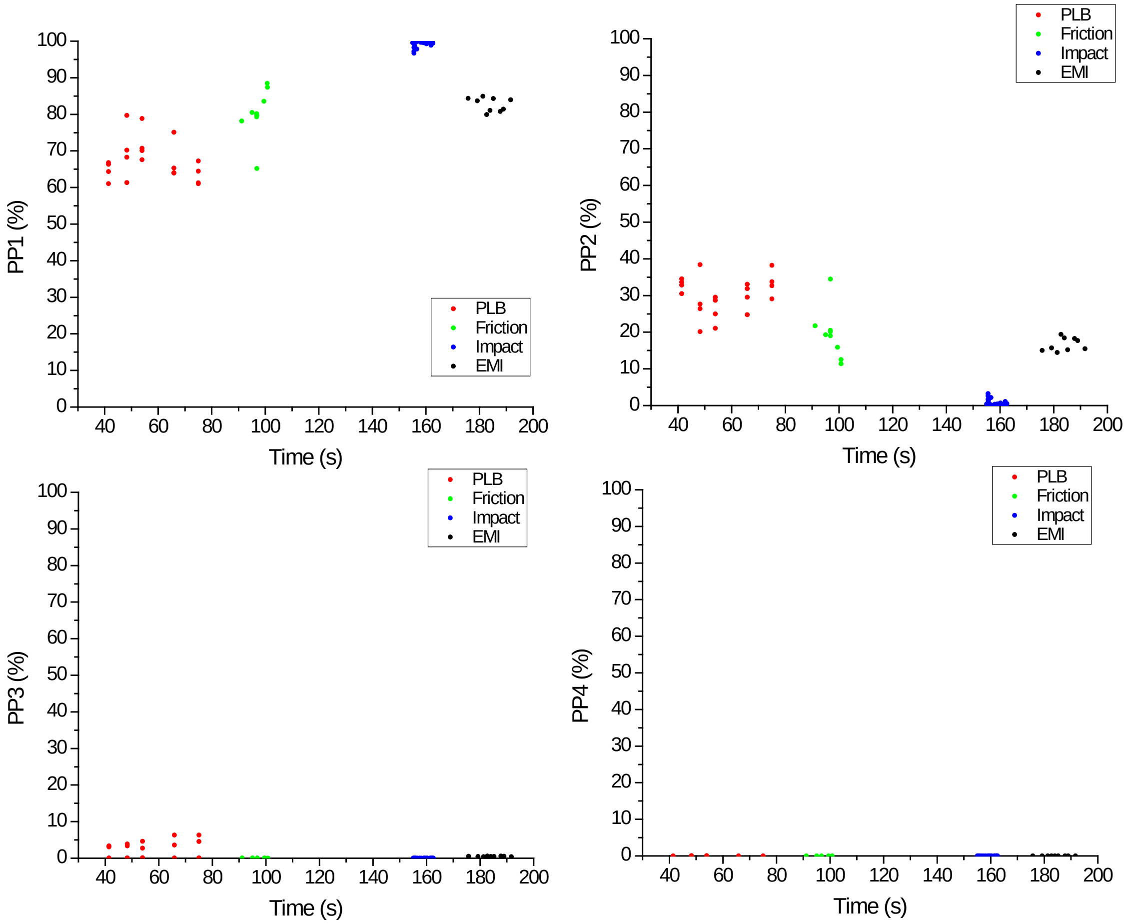

Figure 50: Partial Power analysis of the simulated sources

It was earlier noted from the wavelet analysis that the impact source is mostly active around the 0-200kHz range and consequently it has an extremely high PP1 and low PP2. The friction source that had the same peak frequency characteristics as the impact source is noted to have lower PP1 but a higher PP2 value than the impact source. Thus, the partial power analysis clearly separates the four simulated source characteristics. As a result, the partial power analysis is a more reliable feature descriptor for source separation. However, it must be added that the partial power features must be utilized in conjunction with other frequency based features for source interpretation and damage identification. The partial power analysis by itself cannot characterize the acquire waveform shape (signature) but is more robust than FFT as it factors the magnitude across a wider frequency range.

4.2.2 PATTERN RECOGNITION OF THE AE SIMULATED SOURCES

Finally, in order to reliably distinguish the different simulated AE sources in the aluminum plate, statistical pattern recognition (SPR) analysis was performed and the results are shown in Figure 51. The results of the classification process are heavily dependent on the chosen input features and the classification results will vary depending on the input vectors. Thus, it is critical to select features that are true to the source and importantly are uncorrelated. Typically, correlation dendrograms are utilized to measure the correlation factor between the features and the redundant features are discarded from the input feature set. The features that are least correlated are then chosen as the input vectors. Following this process, normalization procedures are then implemented to apply equal weights to all the chosen input features. This is particularly important, as the different features would have different ranges and thus if not normalized will influence the small range features significantly. Finally, different classification methodologies are implemented based on certain mathematical criteria are utilized to separate the obtained data set into different clusters (or classes).

In this particular analysis, four AE features, decay angle, partial power 3, frequency centroid, and peak power were selected and utilized. It should be mentioned that only the features from channel 1 was utilized for this classification process. This is because certain sources such as EMI was not picked up by the other three channels. The correlation factor for these four features were less than 0.4. The features were then normalized between the ranges of 0 to 1. K means clustering algorithm was subsequently implemented with an initial class as 4 and iteration of 300 steps. The validity of the classification results were evaluated using the R and Tou criteria which resulted in 0.40449 and 2.7832 respectively. The classification methodology separated the four simulated sources with good success. The class 0 was associated with the PLB, class 3 with friction, class 1 with impact and class 2 with EMI signals. The amplitude, which was not used as an input feature, is seen to be different for the four sources as was noted earlier as shown in Figure 51. Similarly, the peak frequency was also noted to be clearly separated for the four sources

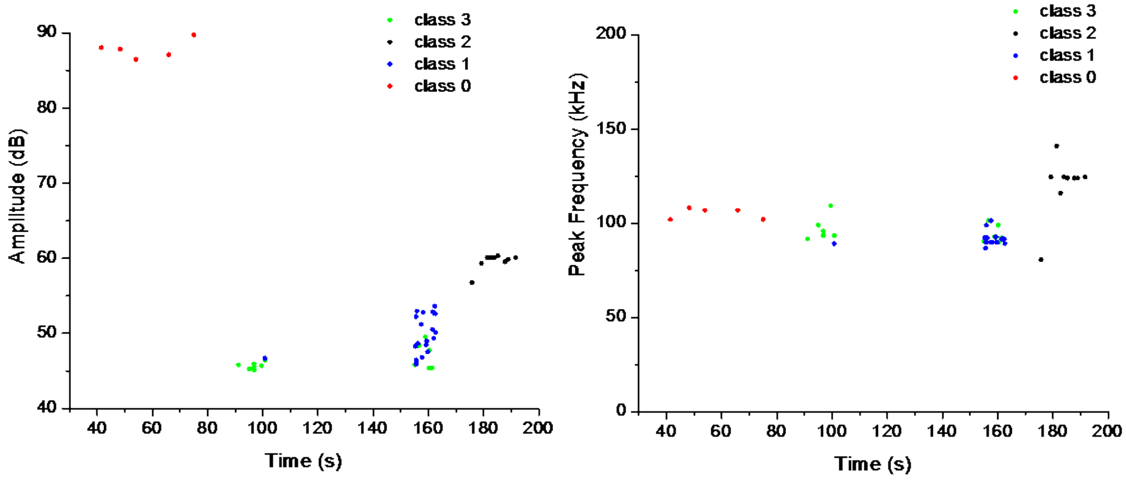

Figure 51: Pattern Recognition Analysis of the AE simulated sources

Considering that chosen K means classification methodology was successful in separating the simulated AE sources based on the chosen input AE feature set, other feature descriptor combinations were also investigated and analyzed. In particular, the combination of the rise angle and decay angle feature descriptors presented further insight and approach in distinguishing continuous type of emissions from burst type of emissions. It can be observed in Figure 52 that PLB (class 0) and EMI (class 2) sources were noted to have a high rise angle while impact (class 1) and friction (class 3) sources were noted to have mostly low rise angle. It was earlier shown that the PLB and EMI waveforms were of burst type emissions but the EMI waveform is noted to have a very low decay angle in comparison with the PLB waveform. Similarly, the friction and impact were known to have a continuous type of emission and similar peak frequency characteristics, but clearly their decay angle is significantly different from each other. Consequently, primary (genuine) burst type signatures can be associated with a high rise and decay angle while continuous type signatures are associated with low rise angle and decay angle.

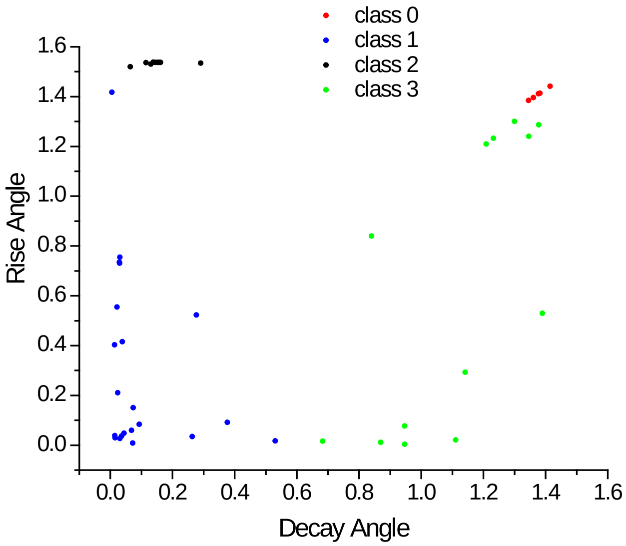

Figure 52: Pattern Recognition Analysis; Rise angle vs. Decay angle

Thus, this relationship of rise angle and decay angle proves to be a robust feature descriptor in differentiating between the continuous type and burst type emissions. Thus, selected feature descriptors mostly waveform based features rather than in-situ obtained features, is more robust in successfully separating the active AE sources in the material.

4.3 CORRELATION OF AE SIGNATURES TO FUNDAMENTAL MECHANICAL BEHAVIOR

Mechanical testing of different materials has been performed in conjunction with the NOAS approach to understand the fundamental material behavior in terms of the AE signals. The knowledge obtained from each of the mechanical test was used to identify and track the damage characteristics and identify the primary AE signature associated with the dominant mechanism. Presented herein is an explanation of the various experimental test performed and the methodology behind obtaining a fundamental knowledge of the damage.

4.3.1 CORRELATION TO FUNDAMENTAL ONSET OF PLASTICITY TO AE

Aluminum alloy (Al 2024 T3) specimens were first tested in quasi-static tension under a constant displacement rate of *0.5mm/min*. Tests were performed on a MTS servo hydraulic frame using an extensometer of 10 mm gauge length and traveling movement of ±1.5 mm. Similar specimens were tested under tension-tension fatigue using R=0.1 (max stress = 0.8 yield stress) and rate of 3 Hz. In the tensile tests, AE and DIC data were recorded simultaneously, while in the fatigue tests, DIC data were recorded only at predetermined time intervals.

Two pico sensors were mounted on all tested specimens using hot-melt glue. The received signals were amplified using 2/4/6 AST preamplifiers and were band pass filtered between *20kHz-1MHz*. An amplitude threshold of *44dB* was employed to eliminate background noise. Additionally, the use of two sensors permitted the application of 2D location algorithms. Furthermore, PLB tests were performed in accordance with ASTM E976 to calibrate the sensitivity of the sensors and to obtain the wave speed in the material (estimated to be 5800 m/s). The 5 M GOM 3D DIC was used to acquire DIC data. The cameras were mounted on a bar and calibrated for a field of view (FOV) of *55x44 mm*. The two cameras were positioned *40cm* away from the specimen to capture the required FOV. A random speckle pattern (black dots on white) was applied on the surface of the specimen to track the deformation process and a few pretest images were taken to check the sensitivity of the strain measurements (found to be in the order of $60\mu\varepsilon$). For the monotonic tests, images were recorded at a rate of *1Hz*, while similar images were recorded at a rate of *29Hz* in the fatigue tests.Several tests were performed to correlate the mechanical behavior and failure of aluminum specimens with NDE information obtained by NOAS. Specifically, surface strain values obtained using DIC were validated by extensometer measurements. The elastic modulus was determined from the elastic portion of the stress-strain curve in Figure 53a and was equal to 70 GPa, the yield stress was 400 MPa and the elongation at failure was measured to be 13% (Figure 53b).

It can be seen that the AE amplitude reaches a maximum (~95dB) near yielding, it subsequently decreases in the plastic region and it increases again during final fracture. It is further noted that the peak frequency obtained during the yielding of the Al2024 alloy is around 150kHz while the frequency shifts towards higher frequency with subsequent loading. To investigate this behavior, the waveform corresponding to the signals obtained pre-yielding were compared with the waveform obtained post-yielding. The waveform and its wavelet analysis extracted pre-yielding is shown in Figure 11a. The AE signature pre yielding is noted to be of burst type emission characterized by relatively high amplitude and a short rise time. In addition, the wavelet analysis revealed that AE waveform at yielding is dominated by low frequency with its peak frequency around 100-150kHz. However, it also noted that the first wave packet does contain high frequency components (450-600kHz) as well. The waveforms obtained post yielding (Figure 54b) are seen to be dominated by the high frequency components.

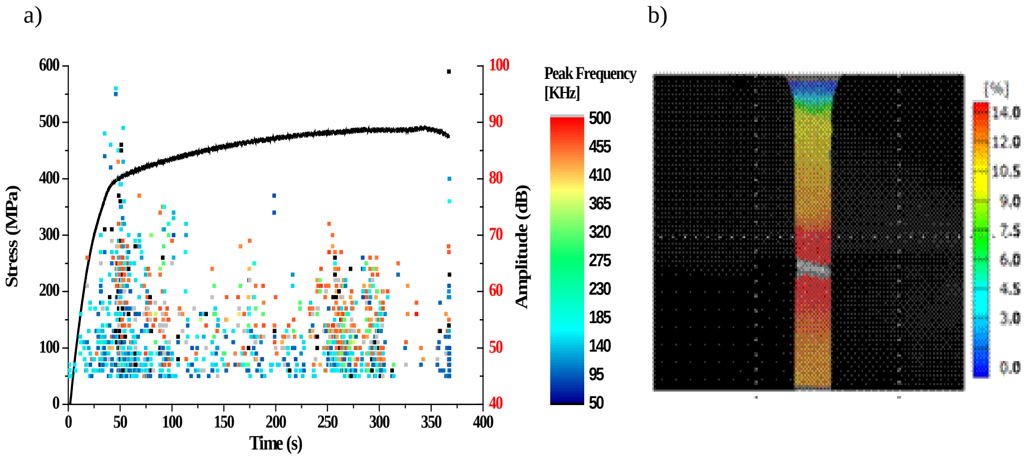

Figure 53: Al 2024 Tensile (a) Stress strain curve correlated with in-situ recorded AE amplitude (b) Full field strain maps at failure

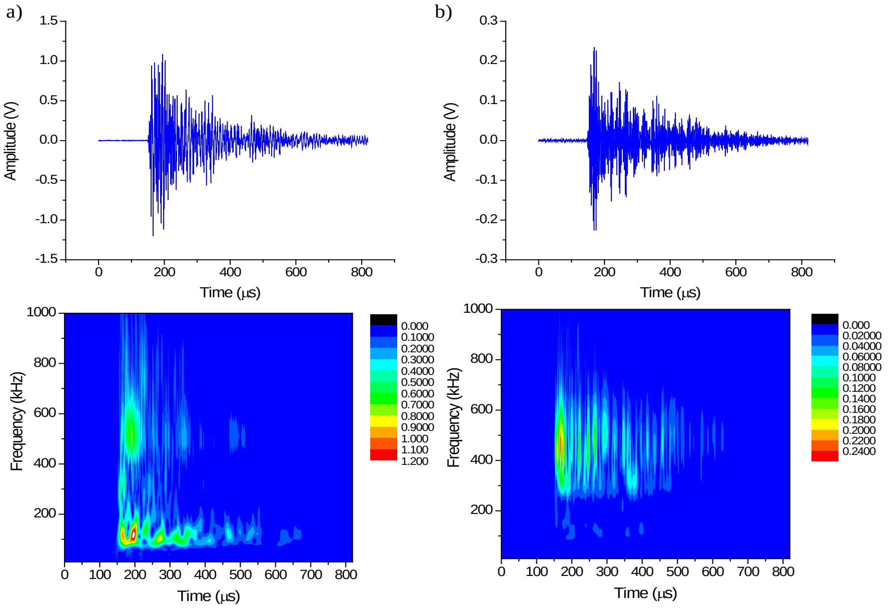

Figure 54: Al 2024 Tensile; Wave signature and its wavelet analysis (a) at yielding (b) post yielding

Further the partial power analysis was performed for the same frequency intervals described in the previous section. The four partial power analysis correlated with the applied load profile is shown in Figure 55. It is noted that PP1 is active much before yielding and dominates the pre-yield region while post yielding of the material, PP2 and PP3 are seen to pick up. Specifically, at yielding and immediately after yielding, PP3 is noted to dominate which then remains nearly constant until final fracture. PP1 is observed to be active throughout of the test while PP2 increases during the later stages of plasticity.

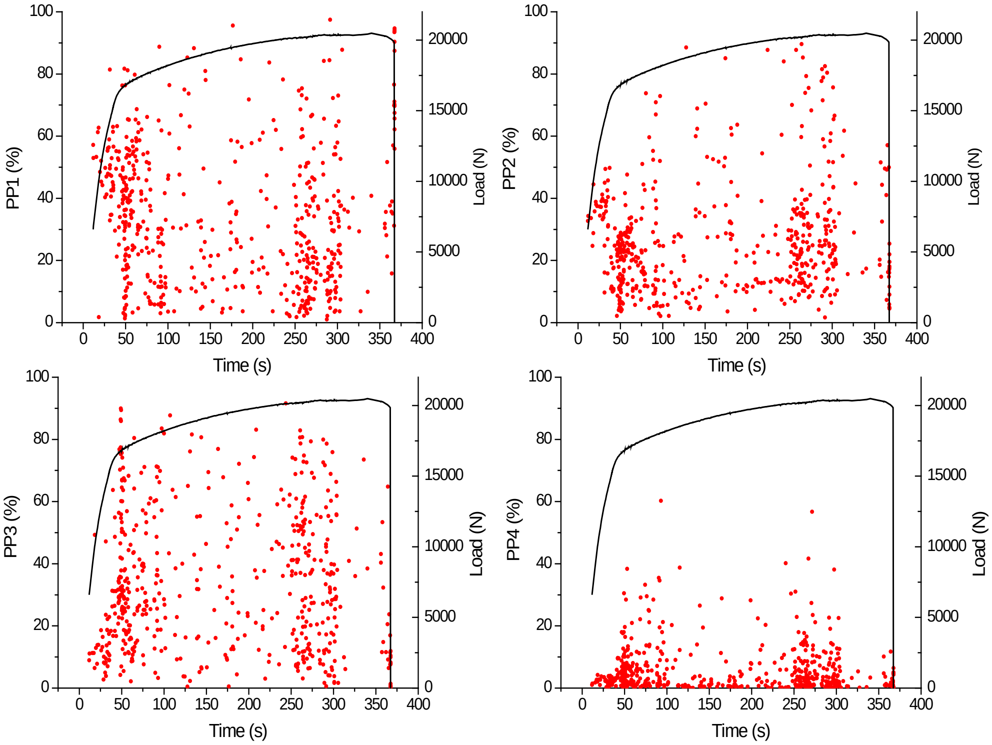

Figure 55: Al 2024 Tensile; Partial Power analysis

Aluminum specimens were also loaded in fatigue. The maximum load used was 80% of the yield stress. Some of the AE features extracted from the fatigue test are shown in Figure 56. It can be noted that all the AE features show a distinct change after the specimen reaches 18% of its life fraction. In particular, the AE amplitude is noted to increase at this point after which it decreases again similar to the AE amplitude profile obtained during the tension testing of the specimen. In the tension test, the initial increase in the AE amplitude was noted near the yielding of the specimen. Similarly, the absolute energy and counts is seen to pick up at this life stage as well. Interestingly, the peak frequency reveals that high frequency signals (500kHz) are noted to pick up upon 18% of its life fraction and continue for the rest of its life fraction.

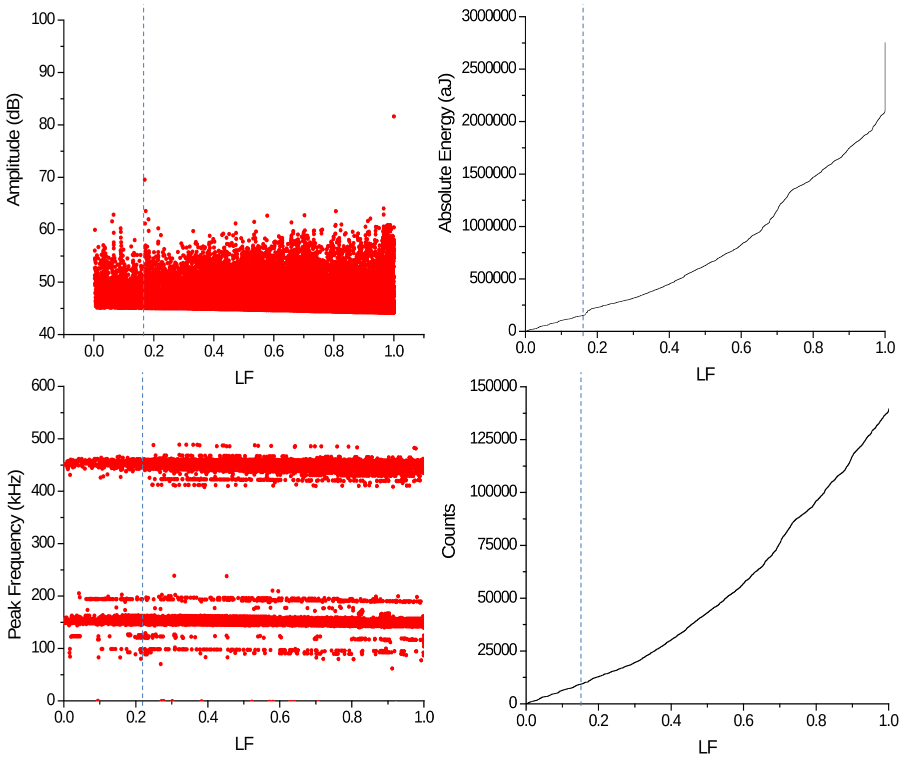

Figure 56: Al 2024 Fatigue Test; AE features as a function of the life fraction

The waveforms extracted from fatigue test present a similar pattern as that extracted from that extracted from the tension test. A representative waveform (Figure 57a) extracted from the early stages of fatigue show a burst type emission that is characterized by low frequency while the waveform (Figure 57b) extracted during the later stages are characterized by high frequency components.

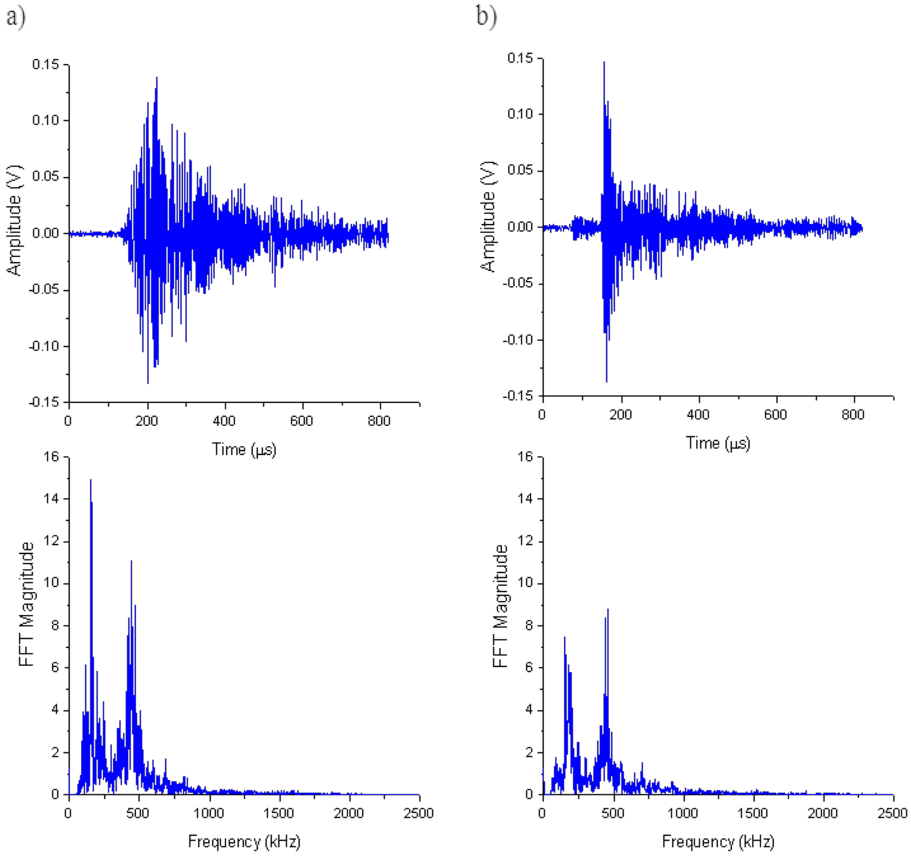

Figure 57: Al 2024 Fatigue Test; Representative waveform and FFT (a) LF < 18 % (b) LF > 18%

Furthermore, the partial power analysis extracted for the fatigue data is shown in Figure 58. It was observed that unlike the tension test, only PP1 and PP3 were mostly active. Interestingly, until 18% of the life fraction, PP1 is seen to dominate the AE signals generated during the test while PP3 is seen to increase subsequently. Thus, it can be concluded that PP1 and PP3 provide the basis for robust AE monitoring in Al 2024 alloys.

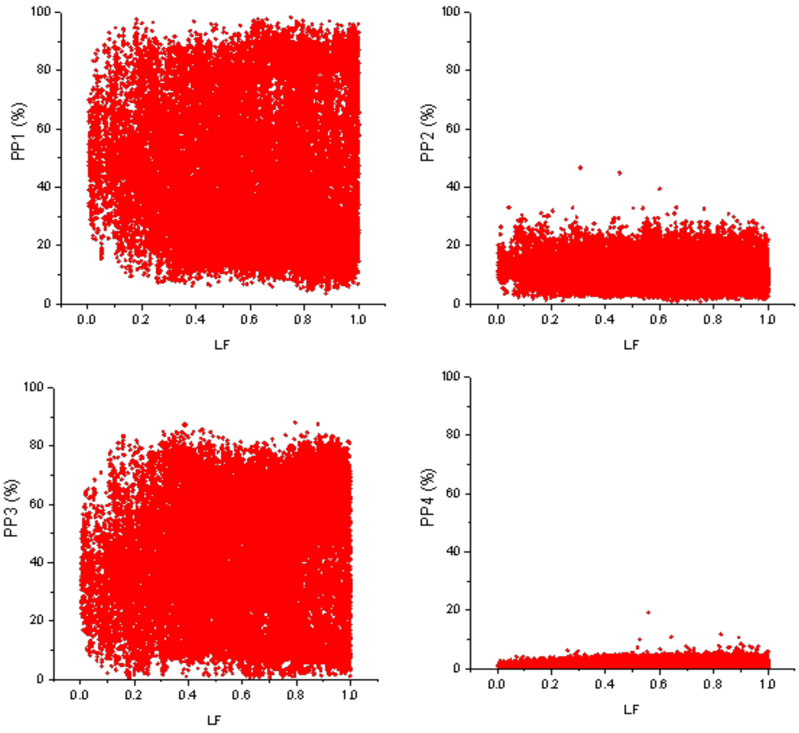

Figure 58: Al 2024 Fatigue Test; AE partial power analysis as a function of the life fraction

Similar to the classification analysis performed on the simulated AE source analysis, the next step was to distinguish the AE signals acquired from the tension and the fatigue data and identify similar patterns across the data sets if any. For this purpose the same features used for the classification of the simulated AE sources in the aluminum plate such as decay angle, PP1, frequency centroid and peak power were utilized as the input feature vector for the classification process. In addition to normalizing the features, the feature vectors were transformed into principal component axes using the principal component analysis. Only the first three principal components were then utilized for the classification process. Again the R and Tou criteria was utilized to evaluate the validity of the classes and is shown in Figure 59. It can be seen that four classes produced the best results in terms of the R and Tou values.

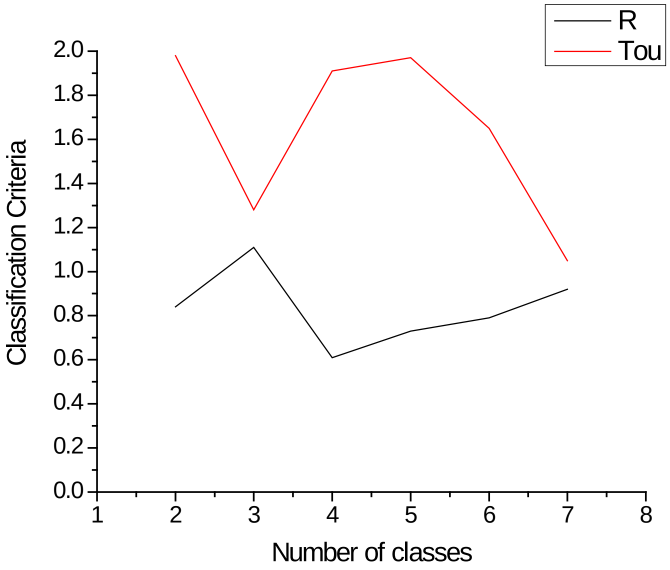

Figure 59: Al 2024 Tensile; R and Tou criteria

Consequently, the classification methodology revealed four classes of signals based on the selected input feature vectors. The amplitude and absolute energy plot as a function of time for the four classes is shown in Figure 60. It can be observed that class 1 signals are seen to have a maximum amplitude (95dB) around the yielding of the material while class 2 signals are noted to be active before yielding is observed. Conversely, class 0 signals are noted to pick up only after yielding and dominates the AE signals acquired just prior to final fracture while Class 3 signals were noted to have very low amplitude. Consequently, it can be inferred that class 1 signals are active near the yielding of the material while class 0 are seen to be active prior to failure. The cumulative absolute energy presents a similar story. It can be observed that class 1 signals are inactive post yielding and while class 0 signals pick up much later in time.

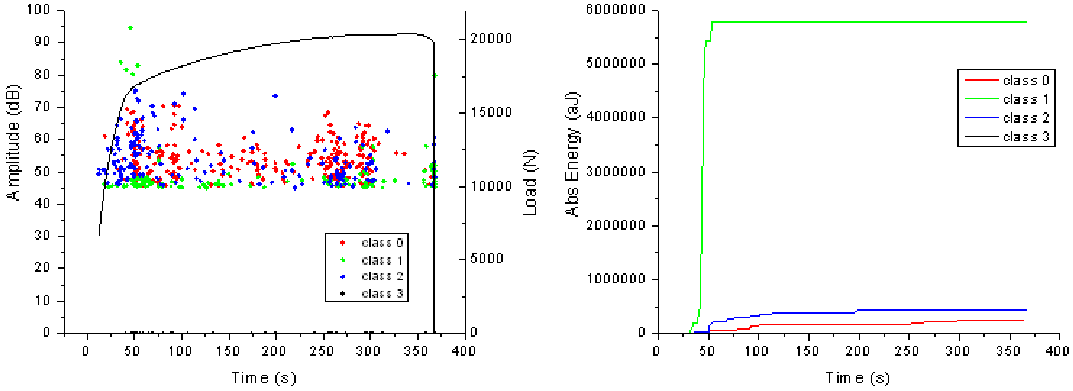

Figure 60: Al 2024 Tensile; Pattern Recognition Analysis

In order to identify robust feature characteristics across different across samples and tests including fatigue, other feature descriptor combinations were investigated that showed clear separation of the classes. Consequently, the peak power vs. PP1 and PP2 were analyzed and plotted for the four classes as shown in Figure 61. Interestingly, it can be noted that class 1 signals associated with yielding were seen to have similar behavior in PP1 and PP3. However, class 2 signals that began quite early in the test was seen to have high PP1 but relatively low PP3 while class 0 signals that arise post yielding are noted to have a low PP1 but relatively high PP3. Thus, it can be concluded that class 2 signals are dominated by low spectral behavior while class 0 signals are dominated by high spectral characteristics associated with it. The class 1 signals were noted to have frequency characteristics similar to wavelet analysis shown in FIGURE 13a with its peak frequency at 150kHz. This same pattern recognition procedure and analysis was repeated for the obtained fatigue data set as well and is shown in Figure 62

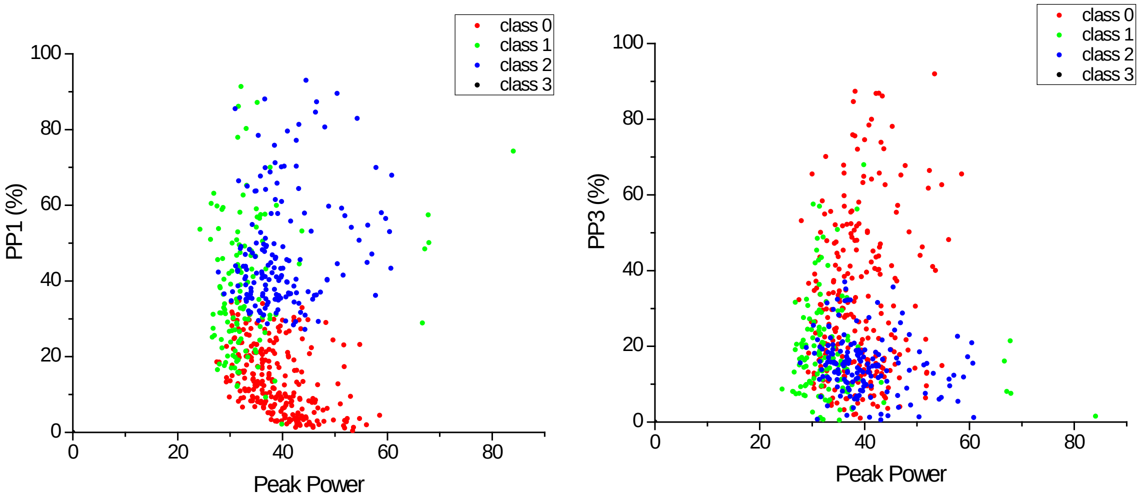

Figure 61: Al 2024 Tensile; Pattern Recognition Analysis

It should be mentioned that the correlation factor of the same features used in the tension data set was higher than 0.6 in the fatigue data set. The same feature characteristics were observed in the fatigue data set as well. Class 3 (red) were noted to have similar values in the PP1 and PP3 while class 2 (blue) signals were seen to have similar behavior with class 2 in the tension data set. Similarly, class 1 signals were noted to have similar characteristics with class 0 signals in the tension data set.

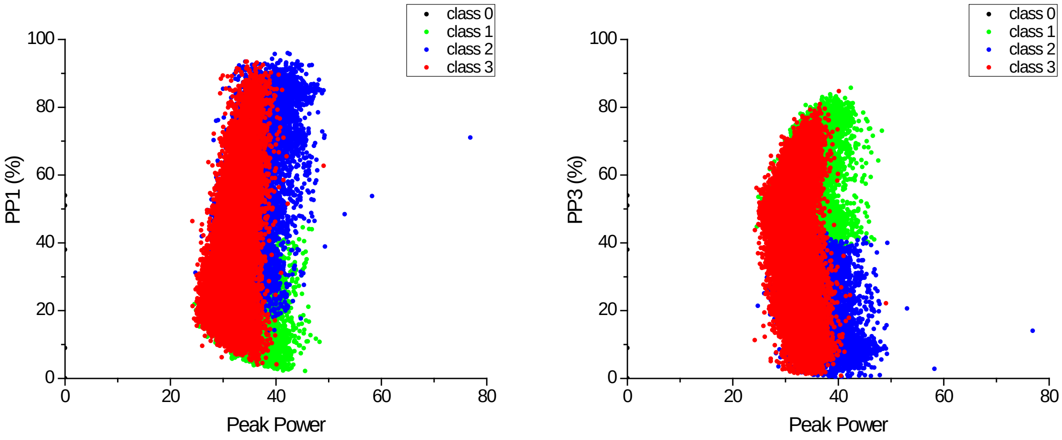

Figure 62: Al 2024 Fatigue; Pattern Recognition Analysis

Consequently, similar AE signatures across specimens and tests were identified using statistical pattern recognition techniques and selected input feature set which forms the basis to develop robust AE source identification for damage detection in aluminum alloys.

4.3.2 CORRELATION OF MICRO STRUCTURAL BEHAVIOR TO AE

To understand the sensitivity of AE to the active deformation mechanism, magnesium alloys (AZ31) were tested under quasi-static conditions. AZ31 cylindrical compression specimens were manufactured in accordance to ASTM E9. The specimens were loaded in compression at a constant strain rate of 4.5 x 10^{-4} s^{-1}. The microstructure of the specimen were carefully tailored and homogenized to identify the active deformation mechanisms in the alloy. A detailed description of the material preparation and microscopic analysis can be found in [49]. The mechanical tests were coupled with AE and DIC testing and followed up with microscopic observations to identify the in-situ AE indications. A PICO sensor was mounted on the back of the cylindrical specimen using a cyanoacrylate adhesive. The acquired signals were sampled at 5MHz and a threshold of 50dB was utilized to minimize the ambient noise. A PDT, HDT and HLT of 200µs, 500µs and 1000µs were utilized respectively. The GOM DIC system was utilized to obtain the full field strain measurements. The camera had a working distance of 395mm and the sensitivity of this measurement was about ± 150µm/m. The cameras were separated by a distance of 136mm and a picture was taken every 0.33s

The AE amplitude correlated with the measured stress-strain curve for the AZ31 is presented in Figure 63. The full field strain visualizations at specific instants are shown as well. Interestingly,

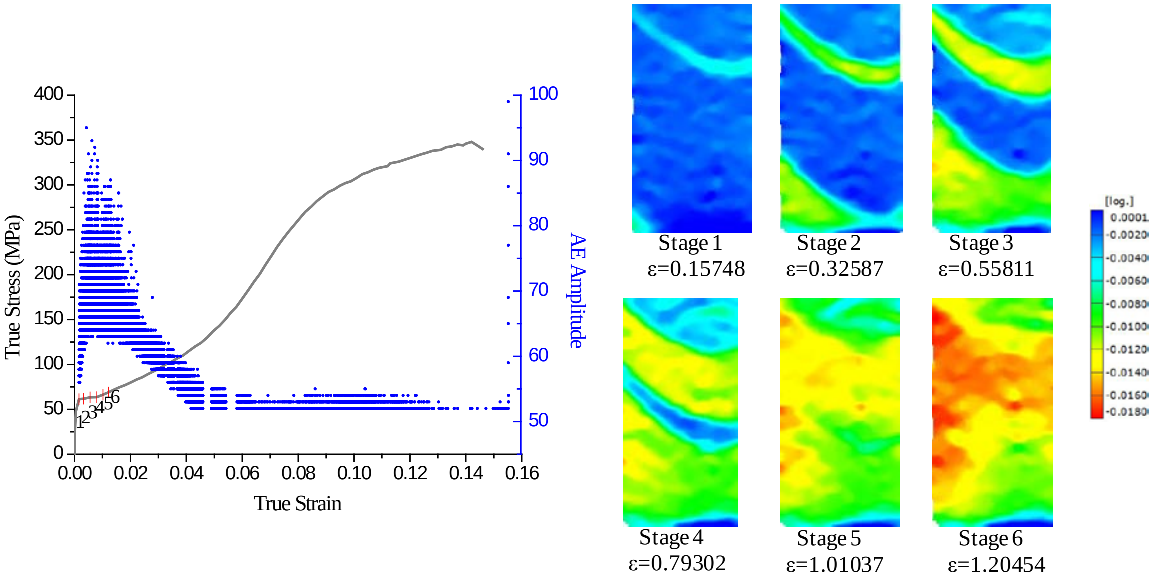

Figure 63: AE Amplitude correlated with the stress strain curve for AZ31 [49]

at the onset of plasticity (the knee), very high AE amplitude (~100dB) signals were obtained in-situ which correlated with localized strain band formation on the surface of the AZ31 alloy. It must be mentioned after the onset of plasticity, the AE amplitude decreased throughout until final fracture. Expectedly, at final fracture, again 100 dB signals were observed. It was noted that previously these 100dB signals were noted at the onset of plasticity, however no visual failure or fracture was observed at the surface at that instant. Several specimens were then tested and same behavior (in terms of the AE amplitude and localized strain band) was obtained exactly at the onset of plasticity.

Consequently, another test was performed and the experimental loading was interrupted upon the detection of high AE amplitude as shown in Figure 64. As it can noted, the high amplitude AE signals are obtained exactly at the onset of plasticity and the test was interrupted after 22s for detailed microscopic analysis.

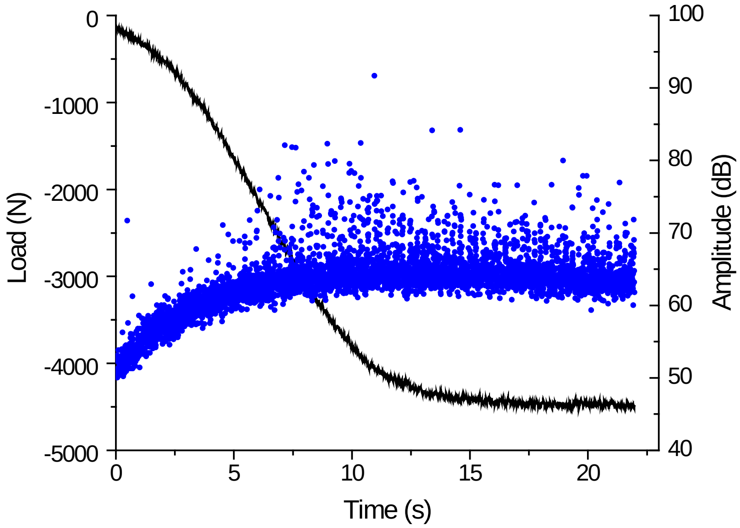

Figure 64: AE Amplitude correlated with the interrupted loading for AZ31

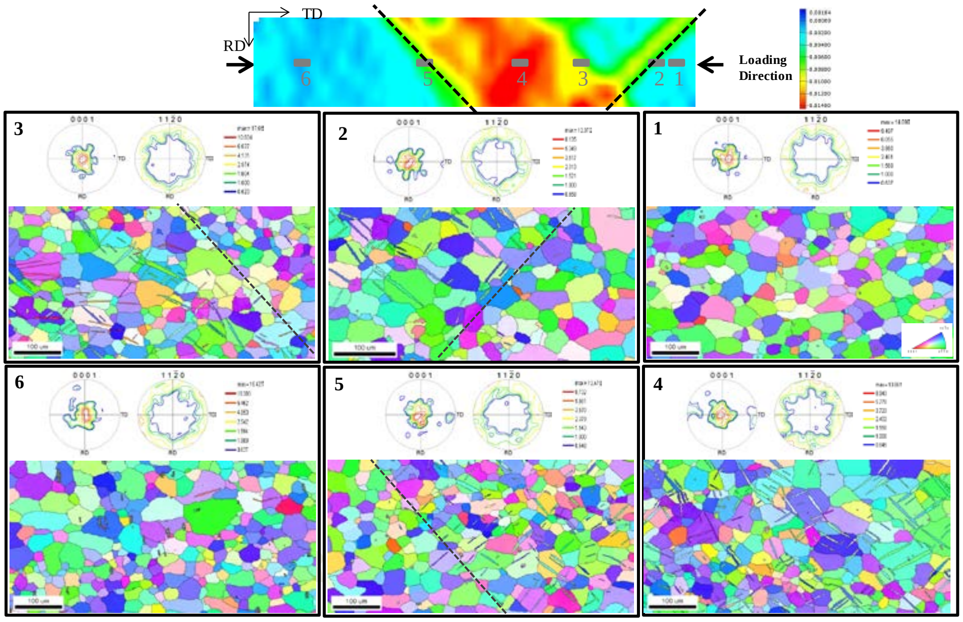

Figure 65: EBSD analysis [49]

The microscopic analysis was performed using electron beam scatter diffraction (EBSD) in six regions including the region where the localized strain formation was identified using the DIC. Targeted EBSD measurements in the localized strain regions (**point 3 and point 4**) revealed that all the grains within the dashed lines resulted in significant twinning mechanism. The regions outside of the dashed lines were free of twin formation and in particular region 4 corresponded to large number of twins. These localized strain bands were formed at the onset of plasticity as seen in Figure 63 which corresponded to high amplitude AE signals and consequently, it can be inferred that the **increase of AE amplitude** is attributed to the activation of the **twinning mechanism** precisely at that stage of loading.

Additional AE analysis provides further insight into the sensitivity of AE to the active micro structural change in the material. The AE signals obtained before the occurrence of the high amplitude signals (stage I) and after (stage II) were compared. It is known that high amplitude AE signals (stage II) corresponded to localized strain band formation which indicated the presence of twinning in the grains. The AE signature due to twinning is seen to be of burst type emission signature that corresponded to very high frequency content with a peak frequency around 425-450kHz. The signals are noted to have a short rise time and decay (attenuate) off quickly as it propagates through the medium. Conversely, the signals obtained from stage I which is typically associated with the slipping mechanism, were continuous type emission. The continuous AE signature due to slipping were noted to have low spectral content with a peak frequency around 70-100kHz.

Similar to the simulated source analysis in the thin aluminum plate, partial power analysis was also performed on the waveforms that were extracted from the interrupted load test. The same frequency intervals were utilized for the four partial power ranges and is shown in Figure 67. It is observed that at 6s, the PP1 value decreases and the PP3 value increases. Thus, it can be inferred that there is a decrease in the percentage of energy in the 0-200kHz signals and an increase in the percentage of energy in the 400-600kHz signals. As a result there is a shift in the frequency of the acquired AE signals as the alloy transitions from stage I to stage II. Thus, it can be confirmed that both the wave signature and the frequency shifts as the slipping mechanism leads to the twinning mechanism.

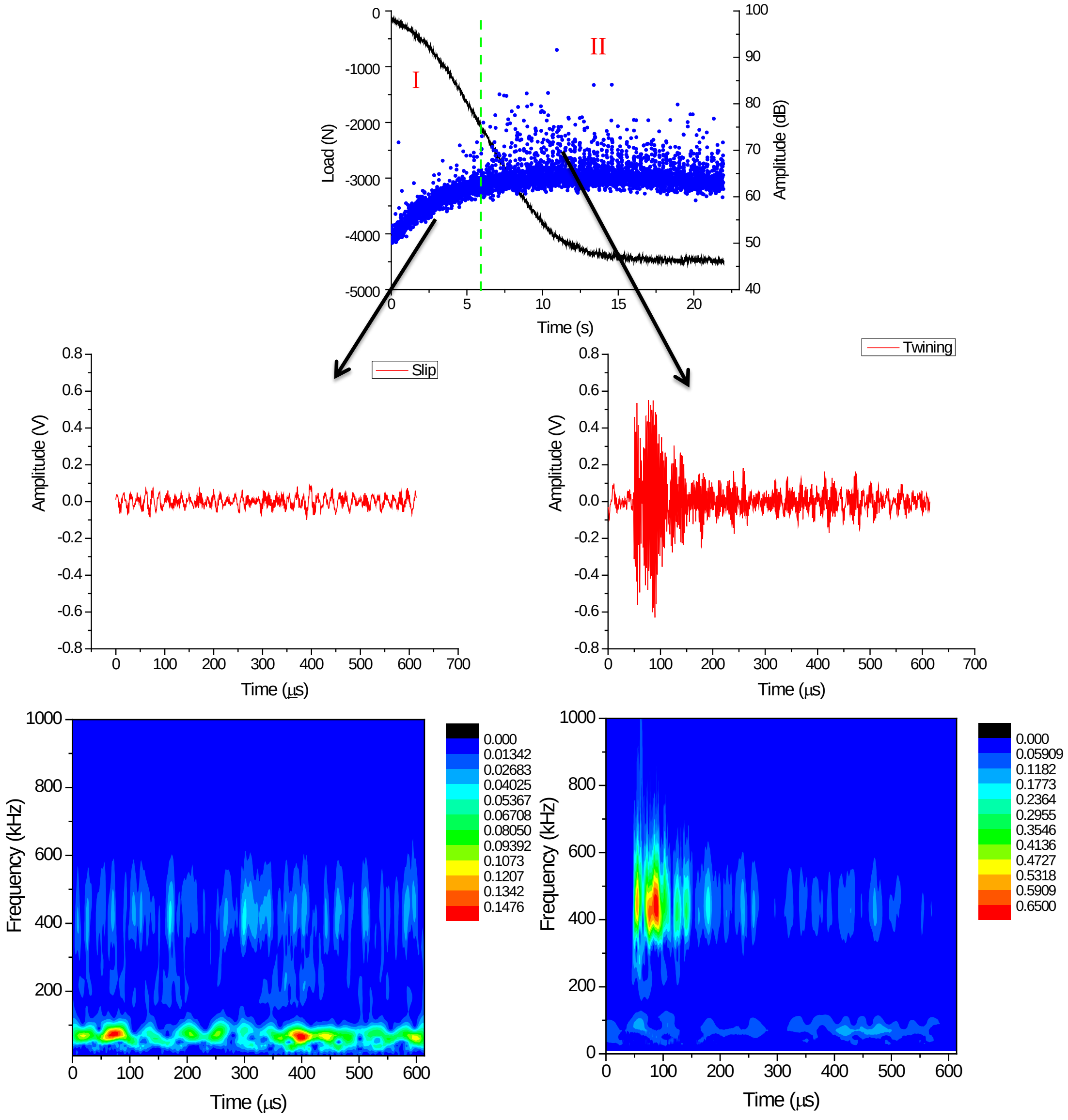

Figure 66: AE signature and its corresponding wavelet for the two stages of loading for AZ31

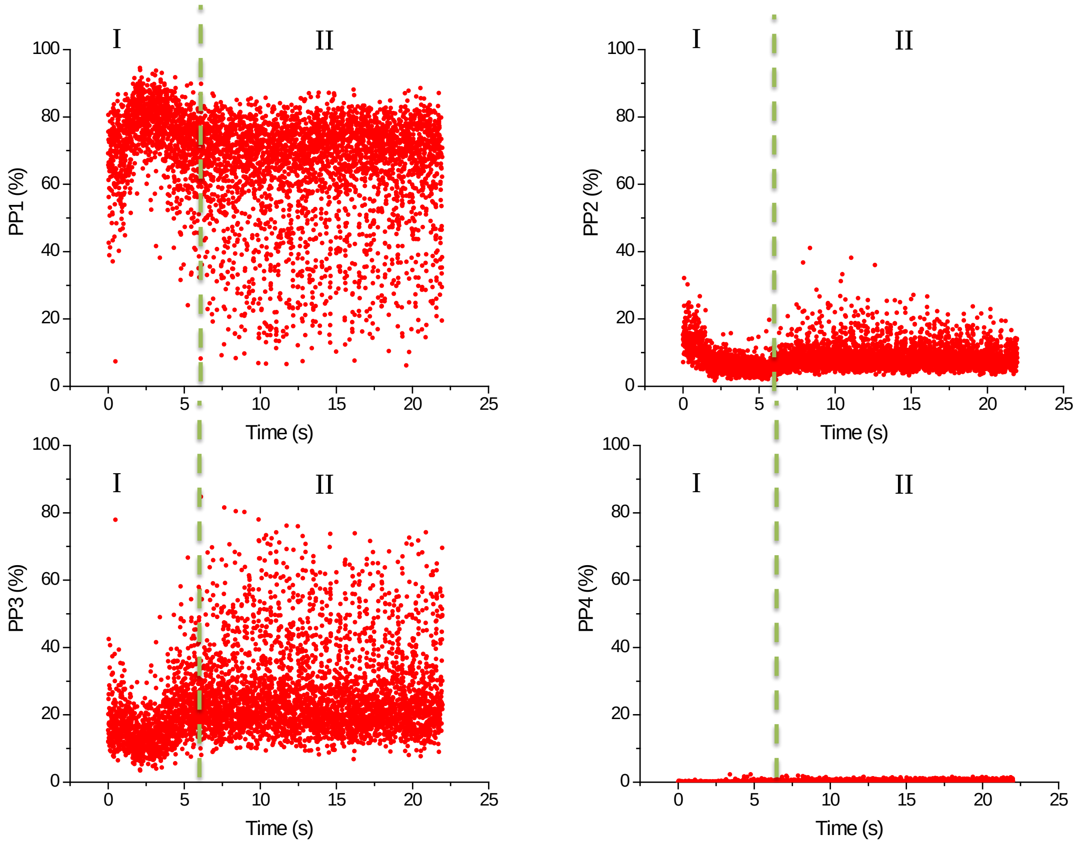

Figure 67: AE partial power analysis for the load interrupted test for AZ31

CHAPTER 5: THE IDENTIFICATION OF CRACK INTIATION IN ALUMINUM ALLOYS USING THE NOAS APPROACH

5.1 INTRODUCTION

To ensure the safety of metallic aircraft structures, two different safety design approaches are typically adopted, the Safe-Life design approach and the Fail-Safe design approach. Initially, aircraft structures were primarily designed using the safe-life design approach that was based on the probability of failure based on fracture mechanics theory. According to the safe-life approach, the failure of the structural component is evaluated based on the fatigue test results of the structural components [28]. The fatigue tolerance limit is designed based on the empirical relationships between the applied stress and the number of cycles (S-N). As a result, it is expected that the structure would not fail as long as the operational conditions are below its fatigue tolerance limits. In order to achieve this, a high factor of safety is implemented which often leads to over conservative designs. The fundamental drawback of this approach is that it assumes all the test specimens manufactured have the same intrinsic structure and properties. Hence, this approach does not factor in manufacturing defects or small defects caused by extrinsic factors such as impact, tool drop during maintenance etc. It has been demonstrated that small cracks grow much faster than large cracks and propagate below the large crack fatigue threshold limits [29]. Consequently, it is challenging to accurately implement 'safe-life' approaches and in this context, it is beneficial in adopting 'fail-safe' designs to ensure safety and/or to plan maintenance downtime. The fail-safe design approach was proposed as an alternate safety approach to the initially used "safe-life" approach by the

United States Air Force. A common fail-safe approach is to detect the crack growth before they reach a critical length and depending on the application domain (military vs. commercial jetliners), the minimum detectable crack size is different. The fail-safe design philosophy revolves around the principle that the structure can be utilized for normal operation despite the presence of damage but it can be detected before it reaches a critical state during routine inspection [27].

In order to realize this goal of adopting a fail-safe approach based on in-situ AE monitoring for aerospace applications, it is advantageous to identify robust AE features that are sensitive to the damage mechanisms. Since, it is extremely challenging to interpret the AE signals solely based on the AE, it is beneficial to implement a data fusion approach to identify the onset of crack initiation and characterize the AE signals associated with it. In this context, the proposed NOAS approach will be utilized to cross validate the crack initiation across various crack specimen and identify characteristic changes in robust AE features and design novel AE feature descriptors that can be used as a reliable damage warning index for crack initiation. For this purpose, two different type of specimen types and sensor influence will be evaluated extensively and robust AE parameters sensitive to crack initiation will be identified.

5.2 EXPERIMENTAL TESTING OF COMPACT TENSION AND MIDDLE TENSION SPECIMEN

5.2.1 6 MM COMPACT TENSION SPECIMEN

The compact tension (CT) specimens (Figure 5a) were manufactured from a 2024 aluminum alloy, 6mm thick plate and were designed and machined in accordance with ASTM E647-08. Prior to mode I testing, the CT specimens were pre-cracked under fatigue loading between a minimum and maximum load of 600 - 6000 N at a frequency of 10 Hz to ensure stable crack growth in accordance with ASTM E1290-08. The specimens were then monotonically loaded in Mode I using a MTS testing machine in displacement control (0.5mm/min), while simultaneously recording AE, DIC and GUW data.

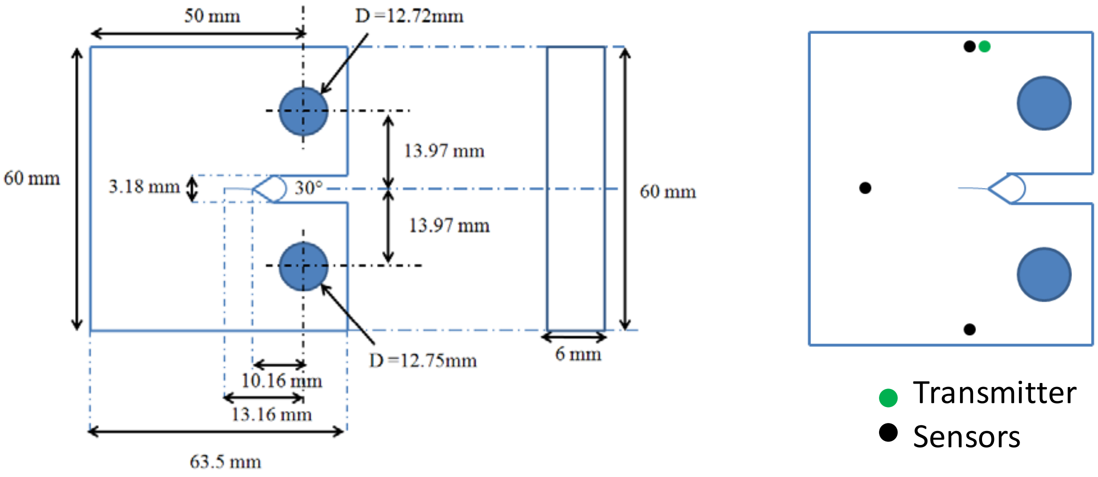

Figure 68: (a) The CT sample (b) The sensors and transmitter location on the sample

The AE-GUW data acquisition system consisted of the 4-channel AEWin DiSP system (Physical Acoustics) with four piezoelectric transducers (Pico) and preamplifiers with a uniform gain of 40dB. Three evenly spaced ultrasonic pulses centered at 100kHz, 250kHz and 500kHz respectively were generated with a sampling rate of 10 MHz using a waveform generator (WaveGen, Physical Acoustics) and fed to the Pico transmitter (Figure 5b) every 0.1 sec. The three remaining Pico receivers were strategically placed across the specimen as shown in Figure X. The sensors were bonded on the surface of the specimen by means of a cyanoacrylate adhesive. The received signals were amplified using 2/4/6-AST pre-amplifiers and a threshold of 60dB was utilized. The threshold used minimized the recording of unwanted noise such as mechanical vibrations introduced by the MTS testing machine. The recorded signals were band pass filtered in the frequency range of 100kHz-2MHz and the pick definition time, hit definition time an hit lockout time settings were 300, 600 and 1000 microseconds, respectively. This set-up allowed: (a) passive recording of AE activity induced by the growing damage, and (b) storage of the ultrasonic waveforms actively generated by the transmitter. During testing, 2-D planar source location algorithms were implemented using triangulation. The wave speed in the material was estimated in accordance with ASTM E976 and pencil-lead break tests were carried out to calibrate the sensitivity of the AE system.

The Digital Image correlation system used is the GOM Aramis 3D 5 megapixel Camera system. The controller for this equipment has analog to digital inputs that allow load recording from the MTS machine. For a 65 x 55 mm field of view the cameras were positioned 485mm from the sample and had a separation of 176mm. A calibration block was used for sharply focusing the 50mm camera lenses to the field of view. A few shots of the calibration block were taken and were used to determine the position of the cameras relative to each other and their distance from the sample in 3D space. A speckle pattern was placed on the surface of the material for tracking deformation, and a few pretest images of the sample were taken to determine the system's sensitivity. An exposure time of 50ms was used to eliminate blurring. For the given test a picture was taken every 3 seconds giving over 400 images for the duration of the test.

5.2.2 4 MM COMPACT TENSION SPECIMEN

CT specimens were also manufactured from a 4mm thick aluminum 2024 alloy plate in accordance with ASTM 1290 with the dimensions in Figure 69b. Unlike the 6mm CT specimens, the objective of 4mm CT specimens was to identify the crack initiation and additionally evaluate similar AE crack signals irrespective of the specimen thickness. It should be noted that no pre-crack was introduced in the 4mm specimen as the goal of this experiment was to characterize the AE due to crack initiation and not the crack growth\fracture toughness of the material. In order to reliably characterize the crack initiation AE signature, the thickness of the two test specimens with the same AE setup was utilized. The two test specimens were loaded in Mode I tension and tension-tension fatigue conditions. Prior to performing the Mode I tensile, the CT specimens were preloaded (~100 N) in order to identify the characteristics of the AE noise sources present before significant plastic deformation including the fretting at the pins.

For the Mode I tension test, the specimen was loaded using a displacement control mode at a rate of 0.5mm/min and 0.2 mm/min (TABLE 1) using a MTS hydraulic frame. Several CT specimen were extensively tested with different loading procedures. The AE sensors were placed on the CT specimen as shown in Figure 70 and two different type of AE sensors (Pico and Nano 30) were used for the test to identify the sensor influence on the acquired signals. In addition to the three mode 1 test specimen, two other specimen was tested in mode I condition but interrupted upon reaching the peak load. It should be noted that two different sensors were used to identify the plastic deformation signatures. For the tension-tension fatigue test, the specimen was loaded at a maximum load of 5kN using a load ratio of 0.1 at a frequency of 3Hz. The same AE setup was used for the fatigue test as well.

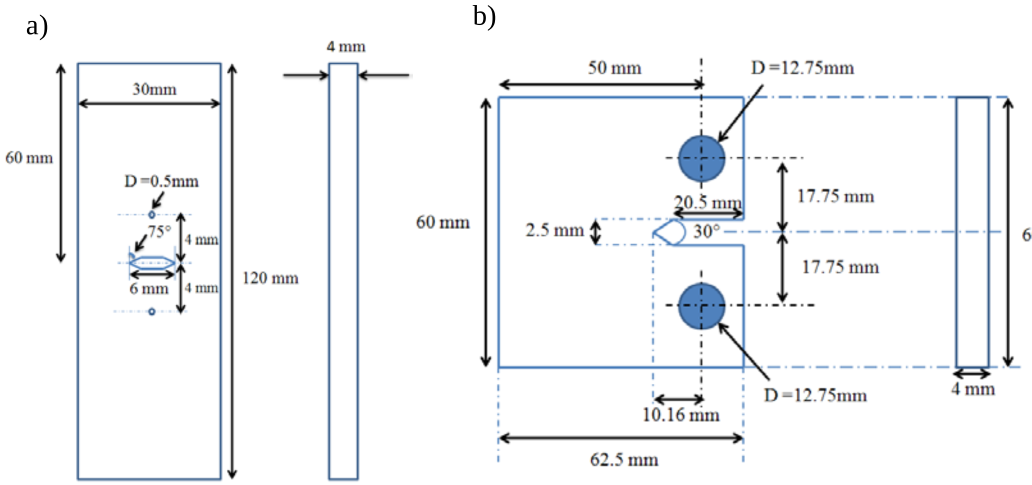

Figure 69: . a) MT Specimen b) CT specimen

5.2.3 4 MM MIDDLE TENSION SPECIMEN

To identify reliable AE characteristics associated with crack source mechanisms in the material and eliminate the effect of specimen geometry on the acquired AE signals, middle tension (MT) specimen were also manufactured from the 4mm thick aluminum 2024 alloy plate with the dimensions shown in Figure 69a. For the mode 1 tension test, several MT specimens were tested and also loaded at a displacement rate of 0.5mm/min. Only Pico sensors were used during these tests and the four sensors were placed as shown in Figure 71. For the fatigue tests, the MT specimens were loaded to a maximum load of 20 kN with a load ratio of 0.1 at a frequency of 3Hz.

The same AE PCI 2 system described in chapter 3 was used to record the AE signals from the 4mm CT and MT specimen. A threshold of 45dB and 50 dB was used to minimize all the ambient noise, hydraulics and other noise sources in the CT and MT specimens respectively. Prior to the application of the preload, a clean and inactive AE data recording was ensured. This was performed to separate the AE signals from that of visual crack initiation on the surface. The sensors were bonded on the surface of the specimen using hot glue and the received signals were amplified using 2/4/6-AST pre-amplifiers.

(a) Plastic Deformation

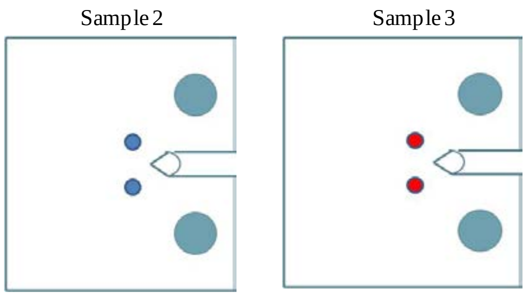

(b) Mode I Tension

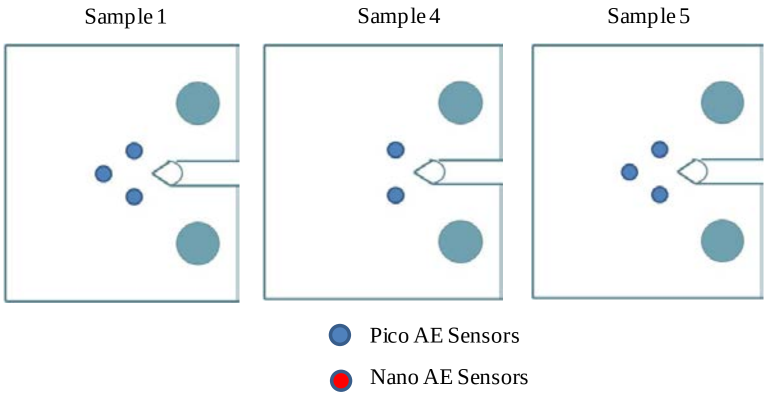

Figure 70. CT AE sensor setup

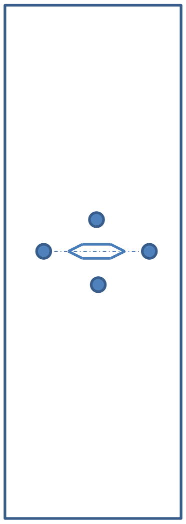

Figure 71. MT AE sensor setup

The recorded signals were band-pass filtered in the frequency range of 100kHz-1MHz and a sampling rate of 5MHz was utilized. Pencil-lead break tests were carried out to calibrate the response of the AE sensors in accordance with ASTM E976.

TABLE 8: CT Test Summary

SAMPLE	DISPLACEMENT RATE (mm/min)	MAXIMUM LOAD (kN)	TOTAL AE COUNTS	TOTAL AE ENERGY
1	0.5	14.5	7693998	1647869
2	0.5	12.1	431081	399871
3	0.5	14.8	11600364	3801027
4	0.5	15.3	6939420	1640957
5	0.2	15.8	9102945	1140725

The GOM DIC system was utilized to capture the DIC images. The cameras had a working distance of 485mm from the specimens with a lens separation of 176mm. Tables supplied by the manufacturer were used to apply the 50mm lens/5 M camera specific parameters for field of view (FOV) with size equal to 55mm x 64mm versus working distance, to achieve a 25° camera angle recommended by the manufacturer. A calibration block was used to sharply focus the 50mm camera lenses to the FOV. A few shots of the calibration block were taken and were used to determine the position of the cameras relative to each other and their distance from the sample in 3D space. A fine speckle pattern was sprayed on the surface of the material to track the deformation, and a few pretest images of the sample were taken to determine the system's sensitivity (~700με). An exposure time of 35ms was used to eliminate blurring. For the Model I tension test, the image acquisition rate during the test was set at 1Hz while for the fatigue tests, the

DIC images were recorded every 1000 cycles. The IRT camera had a working distance of 50mm to optimize the available pixel resolution of the camera. Due to the dynamic nature of this experiment, a high sampling rate of 30 Hz was used to investigate the change in temperature as a function of load. In addition, thermal data was correlated with crack growth by synchronizing full field hot spots with the data measured from the DIC. The IRT and DIC systems by using their relative sampling rates were synchronized in post mortem to allow direct comparisons.

5.3 RESULTS AND DISCUSSION

5.3.1 6MM CT SPECIMEN

5.3.1.1 FEM PREDICTION OF WAVE PROPAGATION IN CRACKED SPECIMENS

Numerical simulations were performed prior to experiments to observe the wave propagation pattern in the specimen (Figure 72a) and to optimize the placement of the sensors. The dynamic analyses were completed using a commercial Finite Element package (ABAQUS) and simulated the stress wave generated by the Pico transmitter. The force time history applied by the transmitter was a 5 cycles Hanning windowed toneburst centered at 500 kHz represented in Figure 72b. The Abaqus Explicit module was employed to perform the analysis assuming a total duration of 0.1 msec and time steps of 0.01 μsec. Based on the obtained FEM results it is clear that the initial propagation of the stress waves is not affected by the presence of the crack. Figure 72c shows the stress field in the vicinity of the source after only 6 μsec. As expected, due to the point-wise source the wave front is circular and the dispersive behavior of the propagating waves can be observed.

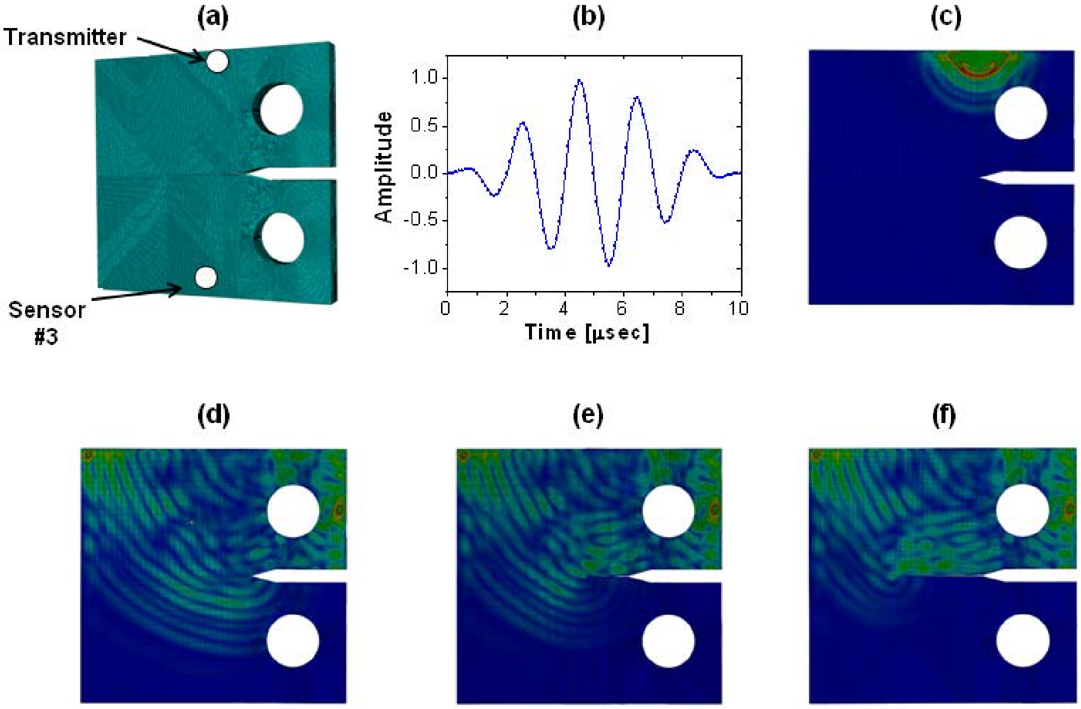

Figure 72: (a) Abaqus FEM model; (b) 5 cycles 500kHz excitation toneburst; (c) wave propagation pattern near the source after 6μsec; wave propagation pattern after 18 microsec for (d) uncracked specimen, (e) specimen with a 10mm crack, and (f) specimen with a 20mm crack.

Although, modest scattering phenomenon can be observed, the waveforms are seen to be unobstructed and have a direct propagation path between the transmitter and the sensor (Figure 72d). However, when a crack length of 10mm (Figure 72e) and 20 mm (Figure 72f) was introduced in the specimen, major scattering phenomenon was observed. This scattering phenomenon at the crack vicinity is attributed to the mismatch in the impedance of the air gap and the geometry. This scattering phenomenon played a significant role in delaying the time of arrival of the sensor waveforms due to the direct path between the transmitter and the sensor being obstructed. This scattering effect also led to the decrease in the amplitude of the received waveform which is quite evident once the cracks were of significant length. The three snapshots shown in Figure 72d-f were recorded at the same time instant of 18 μsec. The guided waves eventually reach the location of the receiver Pico #3, but are severely attenuated as well as delayed in the case of the damaged specimens

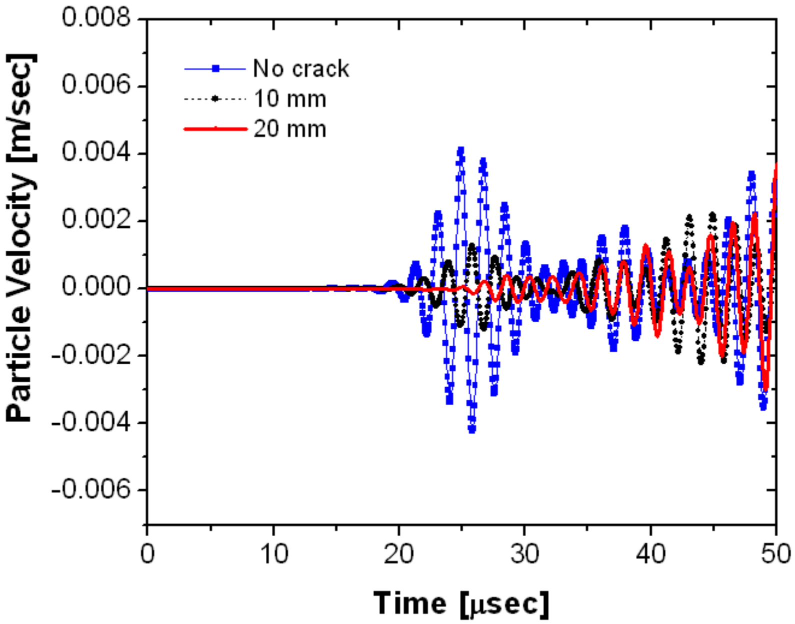

Figure 73: Time histories predicted by Abaqus: Comparison between FEM signals at Pico #3 for the pristine, 10mm and 20mm cracked specimens.

To further confirm these effect of the crack on the propagating waveforms, the sensor output for the pristine and damage cases were obtained for a time window of 50 μsec as shown in Figure 73. It is evident that the "unperturbed" waveform propagating in the uncracked specimen corresponded to a large amplitude signal while amplitude significantly decreased with increasing crack length. It was also noted that the time of arrival increased with the increase in crack length due to the scattering phenomenon.

5.3.1.2 CRACK GROWTH AND MECHANICAL DATA

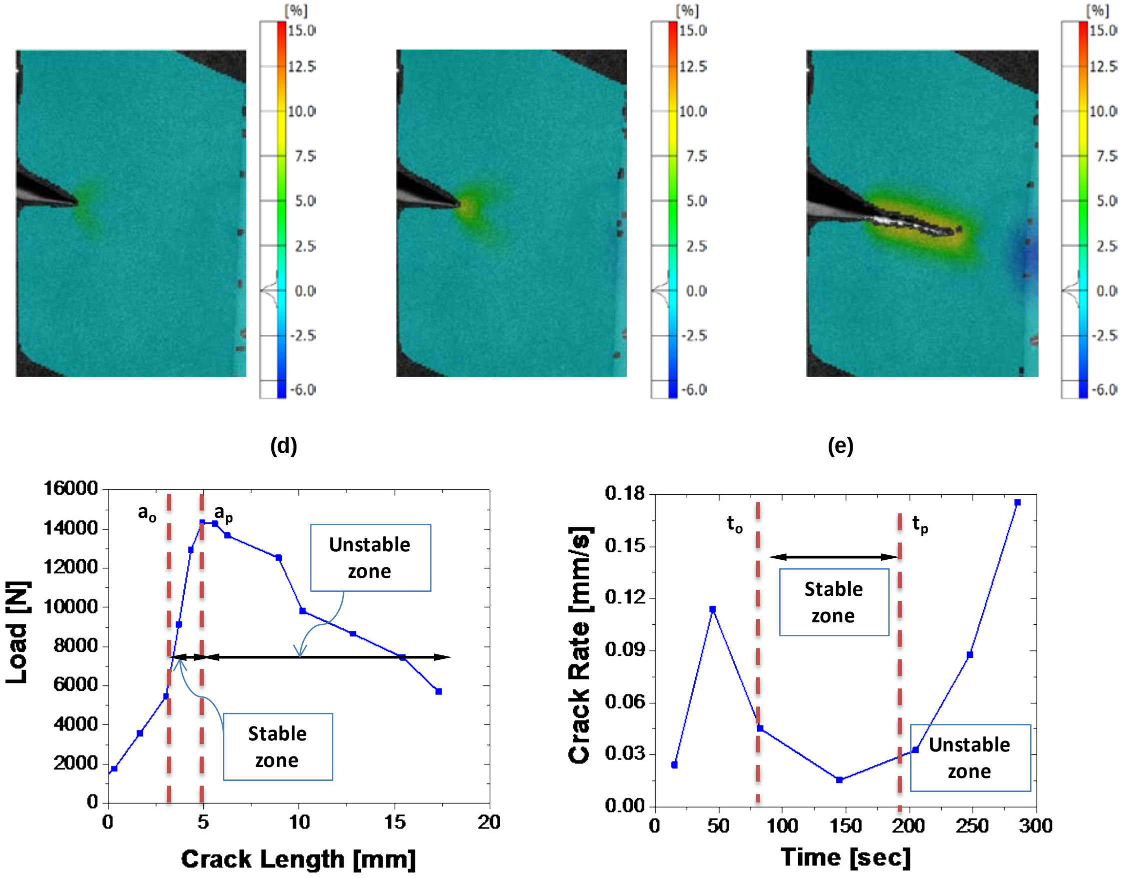

Figure 74: (a-c) DIC results for CT crack growth and (a) no crack extension, (b) stable, and (c) unstable crack growth. (d) Imposed load versus crack length measured by DIC, and (e) calculated crack extension rate.

Crack monitoring and associated full field strains in the vertical direction around the crack tip are shown in Figure 74 for three different regions of the crack development, namely: i) no extension (Figure 74a), ii) slow crack growth (Figure 74b), and iii) unstable crack growth (Figure 74c). The DIC system was capable of recording strains associated both with the process zone ahead of the crack tip, as well as the plastic wake as the crack extends. The applied load versus measured crack length (Figure 74d) and the crack growth rate in time (Figure 74e) clearly show the three regions of crack growth. It should be noted here that crack length was defined as the difference between the length of the observed crack by DIC minus the original length composed on the notch plus pre-crack sizes. A length equal to a_0 = 3mm was measured by the DIC system exactly at the time t_0 = 75 sec. Figure 74 show that at that time the slope of the load versus time line changes, indicating initial crack growth, as also shown by the increase of the crack rate.

After time t_0 and until time t_P = 185.13 sec the crack is slowly growing, as expected for this Mode I experiment, and the crack size at the peak load of about 14kN was measured to be a_P = 4.92mm. Figure 74e confirms the slow crack growth (stable zone) in this region. Past t_P the growth becomes unstable, as seen by the sharp increase of the crack rate and the load drop. Loading was interrupted when a crack length of 21mm was exceeded.

5.3.1.3 EXTRACTION OF ULTRASONIC FEATURES SENSITIVE TO CRACK GROWTH

Ultrasonic pulses were generated with a 10Hz repetition rate and waveforms were recorded at three different locations with a sampling rate of 10MHz. A typical tone burst excited is depicted in Figure 72b. Figure 75a-d show the waveforms recorded by Pico #3 for progressively growing cracks. Only the first arrival of the received waveforms was isolated using a 135 points window (Figure 75a) to discard reflected waves and unwanted slower guided modes. Feature extraction was performed on the windowed signal. As the crack began to grow, the windowed signal amplitude rapidly decreased as shown in Figure 75b-d.

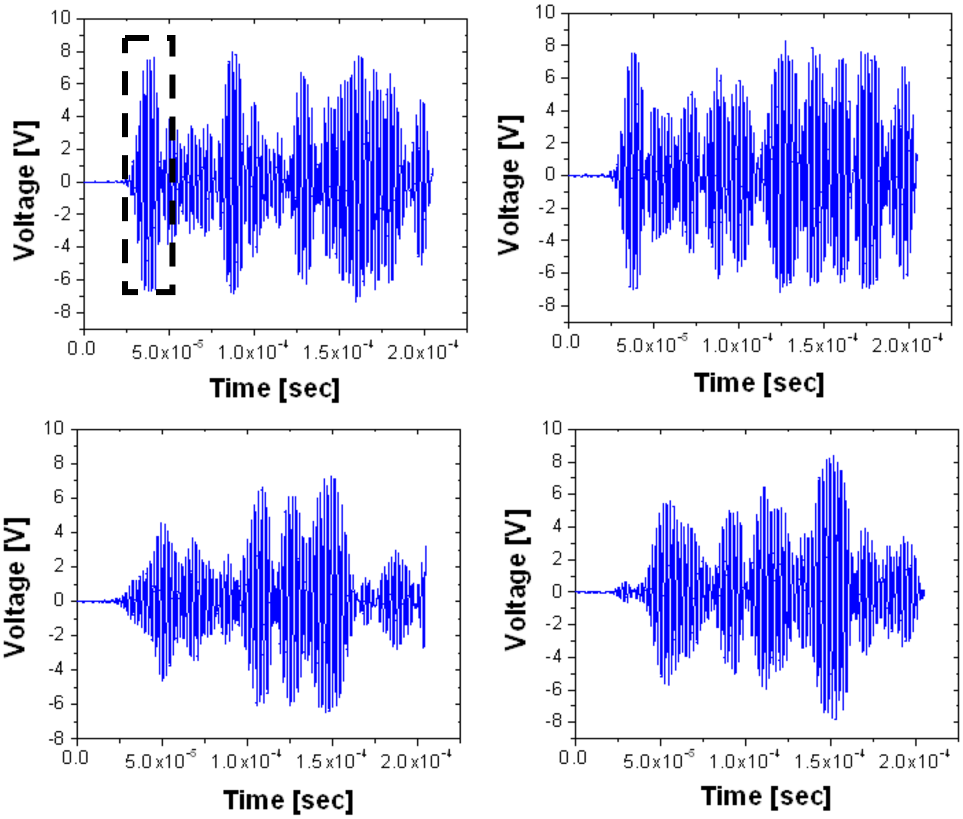

Figure 75: (a) Waveform recorded by Pico #3 for CT specimen with crack length a = 0mm, (b) a=3.5mm, (c) a=15mm, (d) a=18.5mm

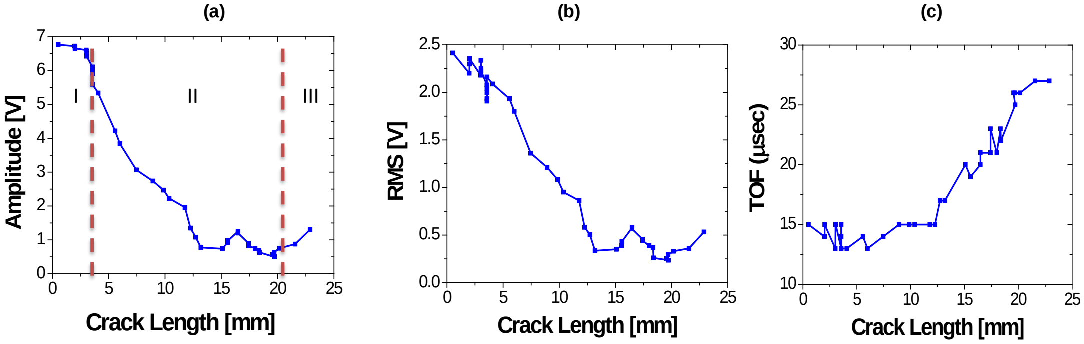

Figure 76: Features versus crack propagation length: (a) Amplitude, (b) RMS, (c) Time of Flight

Figure 76a shows the change of amplitude of the recorded ultrasonic waves versus crack length. In region I, where a small pre-crack (~3mm) was present, the amplitude decreased moderately. In region II, as the pre-crack evolved into a macroscopic crack, the signal amplitude decreased rapidly with increasing crack length due to the wave reflection at the extending crack boundary. In region III, the crack exceeded a length of 21mm and the test was interrupted. Interestingly, the drop in amplitude was not observed in region III. A possible explanation lays in the complex wave propagation pattern shown in Figure 72a-d where constructive interference of scattered waves can induce an unexpected increase of the wave amplitude. Furthermore, it should be noted that the AE-GUWs (passive-active) test set up required an independent trigger at each channel to simultaneously record AE and generated GUWs. As a result, windows were selected based on first threshold crossing that can be affected by limited accuracy. The latest is not the common approach for the GUWs pitch catch configuration, in which all channels are typically triggered simultaneously by the function generator. Consequently, the amplitude trend shown in Figure 76a could slightly vary using a different trigger source.

A second feature that demonstrated damage-sensitive characteristics is the Root Mean Square (RMS) of the windowed signal (Figure 76b). The RMS shows a trend similar to the signal amplitude due to the wave scattering occurring at the crack, which reduces the signal strength. The third feature investigated is the time of flight (TOF) defined as the difference between time of arrival in Pico #3 and Pico #1. The time of flight changed significantly with crack growth as shown in Figure 76c, increasing from 15 μsec for the pre-cracked specimen to approximately 30 μsec at the end of the test. As the crack progressed, the direct path of wave propagation was obstructed by the crack, and hence the increase shown in Figure 76c. This phenomenon was already observed and good agreement with the FEM simulation results shown in Figure 72b-d. The guided waves were partially reflected and were forced around the crack resulting in the observed change in the features.

5.3.1.4 EXTRACTION OF ACOUSTIC EMISSION FEATURES SENSITIVE TO CRACK GROWTH

Acoustic emission activity was monitored continuously during the CT experiment. The simultaneous use of the piezoelectric sensors and the AE data acquisition system for GUW and AE monitoring, proved challenging as damage related AE activity can potentially occur in intervals in which ultrasonic pulses were sent. To avoid signal loss due to traffic on the acquisition board, as well as to ensure that valid AE activity is recorded and is not compromised by signals originating from noise, reflections or friction, the threshold and time based settings (HDT, PDT and HLT) were carefully selected. Furthermore, baseline waveforms were collected both before the application of load, as well as at load hold levels for similar CT samples with grown cracks, and they were used for comparison with the population of AE waveforms recorded during loading and filtered using 2-D location algorithms. The use of multiple sensors in the experimental setup shown in Figure 5b, permitted the implementation of planar source location algorithms. Specifically, 2D location in the CT sample was determined using the time of arrival method described more in detail in [157]. The specimen geometry was specified in the data acquisition software and the three sensors (green circles) were placed as shown in Figure 77. Triangulation of these sensors were then used to determine the location of crack which confirmed AE events from the zone ahead of the crack tip as soon as the growth initiated. For comparison, and to test the capabilities of the implemented location algorithms the top cluster of events with a characteristic waveform that correspond to the transmitted GUW are also shown in Figure 77.

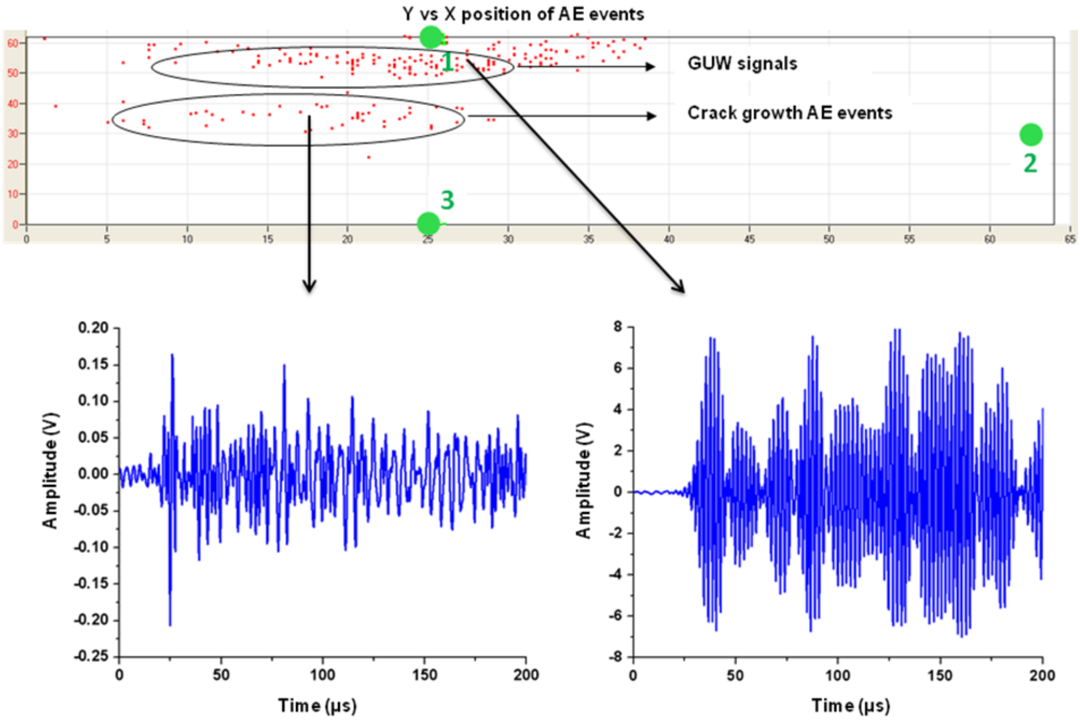

Figure 77: 2D Location

In addition, since many of the recorded waveforms were of continuous type (characteristic of friction of loose mechanical parts and fretting of existing fracture surfaces) with intermittent burst type emissions (characteristic of crack related AE activity) correlations in the time domain between DIC information related to finite crack growth increments and recorded AE hits were established to filter spurious data and 2D location algorithm were used as a spatial filter to retain the most reliable activity. Although this data filtering approach reduces the amount of available AE information and potentially discards valid AE activity, it complies with standard approaches employed in actual field applications in which only sparse data can be used to infer on damage development.

Both real-time and post-mortem features were extracted from the filtered AE waveforms and are plotted in Figure 78. All the AE data was processed using NOESIS and features were extracted from both time and frequency domain. Among all AE parameters, the amplitude, absolute energy, AE hits, counts and count rate were found to be the most sensitive to crack growth. It can be observed in Figure 78 that the amplitude was seen to increase almost immediately upon the beginning of the test and this increase continued until the end of the stable crack growth. The amplitude was noted to reach its maximum just as the load began to drop indicating crack growth in the specimen. After this stage, the amplitude of the AE signals was seen to decrease as a function of both the load and the crack length Figure 78b. The cumulative absolute energy revealed a more distinct change as a function of the crack length. It can be observed in Figure 78c that the energy increases until the onset of stable crack after which the rate changes. However, precisely at the onset of this stage, the slope of the energy is seen to increase significantly indicating intense AE release in the material during this stage and exhibited an almost linear behavior during this stable crack growth stage. Upon, the termination of this stage, the slope of the energy release was noted to change although it continued to increase. In comparison to the stable crack regime, the rate of the energy release was noted to decrease during the unstable crack region. Similarly, other AE features such as the counts rate (Figure 78e), hits (Figure 78d) and the counts (Figure 78f) were seen to change in-situ, thus providing the tool for online monitoring. In particular, a direct correlation between AE activity and crack initiation and growth is established in Figure 78, in which three AE features (AE amplitude, cumulative absolute energy and count rate) show a distinct change when the DIC system records the onset of cracking. This observation is critical in SHM applications as reliable volume monitoring of the initiation of dynamic processes, such as crack initiation, can be used to trigger other monitoring devices (the DIC system for example) that could allow not only damage detection but also quantification and source location.

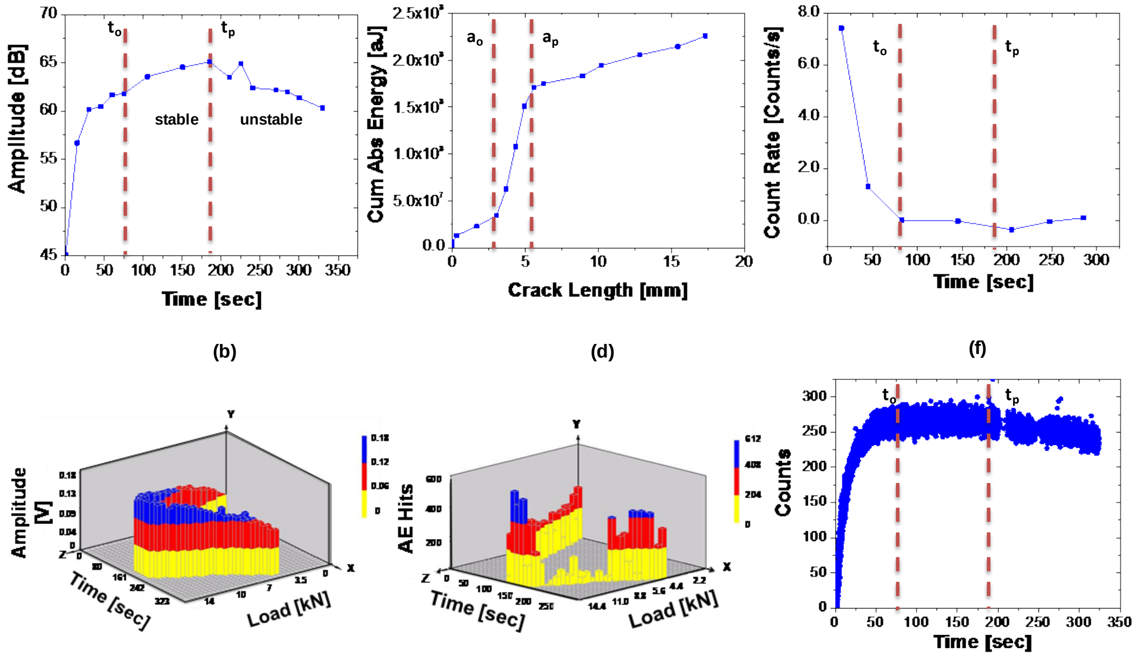

Figure 78: AE emission results including: amplitude versus crack length (a) and versus actual experimental time and applied load (b), cumulative absolute energy versus crack length (c), AE hits versus time and load (d), count rate versus time (e), and counts versus time (f).

Finally, the next challenge in designing a robust SHM system is to judge based on the periodically computed feature values, whether or not the current condition of a structural component has deviated from its normal operational condition, i.e. is damaged. To achieve this, heterogeneous data sets from multiple NDT techniques were combined using data fusion techniques to enhance the damage detection and develop a damage quantification model.

5.3.1.5 DATA FUSION USING OUTLIER ANALYSIS

The features extracted from GUW (RMS, Amplitude, Time of flight) were combined with data extracted from the DIC. The selected DIC features include: (a) the distance between a fixed spatial origin and the location of the crack tip, and (b) the distance from the same origin and the location of maximum strain. Clearly, the last two features would be sufficient to monitor the damage growth in laboratory conditions at least, while environmental and operational conditions could affect these measurements with unwanted noise in the field. It should be noted here, however, that the DIC method was used not only as a metrology device to monitor crack growth and validate AE and GUW parameters but as an actual and independent NDT technique that provides accurate measurements of mechanical fields for the establishment of procedures on more efficient damage related NDT monitoring and robust damage quantification.

The outlier analysis was employed to demonstrate this approach. An outlier is a datum that appears inconsistent with a set of baseline data; the baseline describes the normal condition of the structure under investigation (for example the uncracked specimen). For multivariate data (i.e. the case where *q* features are considered), a set of *q*-dimensional (multivariate) data consists of *n* observations in *q* variables. In the example shown a feature vector of dimension *q=5* includes three GUW features and two DIC features. Outlier analysis results into a straight-forward discordancy test. The discordancy test is provided by the Mahalanobis square distance D calculated as

$$D=(\mathbf{x}-\bar{\mathbf{x}})^{\mathrm{T}}\mathbf{S}^{-1}(\mathbf{x}-\bar{\mathbf{x}}) \qquad (3)$$

where **x** is the input vector containing the multiple features from the potential outlier, $\bar{\mathbf{x}}$ is the mean vector representing the baseline conditions, and **S** is the covariance matrix of the baseline conditions. The Mahalanobis square distance is a statistical distance between two points in the *q*-dimensional space. This distance takes into account the covariance or correlation between the *q* variables through the covariance matrix. In order to determine whether a new datum **x** is an outlier (i.e. a damaged configuration), the corresponding value of *D* has to be compared to a threshold. When the available number of baseline data is limited, it is common practice to compute the threshold based on a Monte Carlo simulation generating a large number of random data to properly represent the baseline statistical distribution. Alternatively, a large number of samples is often generated by corrupting the data with random noise. If the statistical distribution of the samples is sufficiently represented by a Gaussian curve, a Monte Carlo simulation is not required. Once the values of *D* of the baseline distribution are determined, the threshold value can be taken as the upper value of 3 standard deviations, i.e. 99.73% of the Gaussian confidence limit.

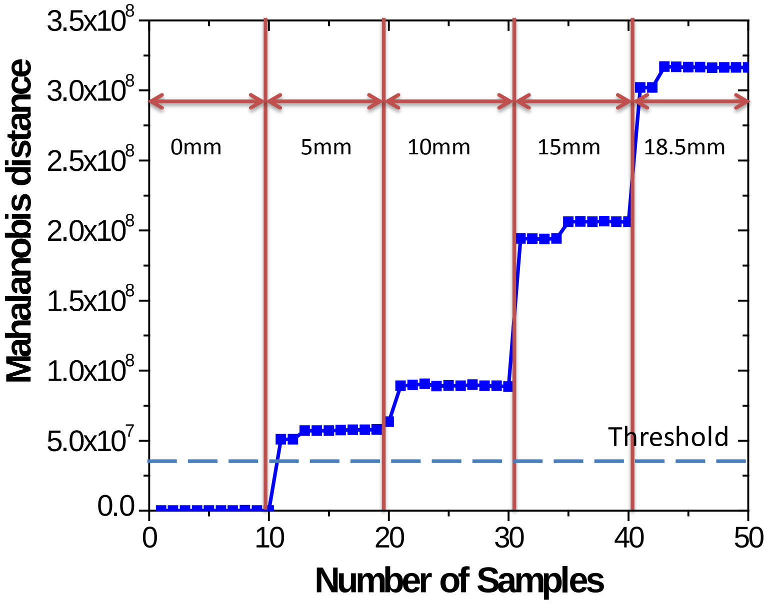

Figure 79: Outlier analysis

In the case shown in Figure 79, the mean vector and the covariance matrix were determined from 28 vectors. The 5 features included in the baseline vectors were computed using GUW waveforms and DIC images recorded before any crack growth. Similarly, the vectors were computed for different conditions of damage and were compared to the mean vector and the covariance matrix using the Mahalanolis distance formula (Equation 3). The Mahalanobis squared distance of all samples, including “undamage” data not included in the baseline and the damage data, are summarized in Figure 79. A stepwise trend is clearly observed where all damaged conditions are properly classified as outliers, thus there are no false negative indications. The values of the Mahalanobis squared distances for the damage data are several orders of magnitude larger than the corresponding values of the undamaged data. As a consequence, the sensitivity to damage is considerably improved when compared to one of single features. Consequently, the Mahalanobis squared distance could be used as a reliable damage index. It is evident that combining multiple features extracted from different NDT techniques in a multivariate analysis dramatically improves the sensitivity of defect detection and discrimination among different defect sizes.

As a result, it can be observed that implementing a data fusion scheme is evidently useful in not just identifying the damage but also quantifying the damage process in the structure. However, it is not possible to gain access to multiple NDT techniques at all times and particularly for in-situ damage identification. This form of analysis would be extremely valuable for damage prognosis to predict the remaining useful life of the structure upon reliably identifying the initiation of damage in-situ through AE initially. Thus, it is vital to identify reliably through AE analysis, the onset of cracking which requires characterizing the AE signatures due to crack initiation. The reliance on the above shown AE analysis could be misguided in the prescience of environmental and other noisy variations. Consequently, 4mm CT and MT specimens were further manufactured from the same material with the goal of identify and reliably detecting the AE signatures due to cracking across specimens.

5.3.2 4MM CT AND MT SPECIMEN

5.3.2.1 IDENTIFICATION OF NOVEL FEATURE DESCRIPTORS SENSITIVE TO CRACK INITIATION

The AE features extracted from the recorded signals upon the application of the **preload** is shown in Figure 80. The amplitude of the recorded signals were seen to be consistently low (< 50 dB) throughout the time of the test. Interestingly, the signals were noted to have three peak frequency characteristics centered around 80 kHz, 150kHz and 450kHz. Both the counts and the AE energy also revealed a trend similar to the amplitude.

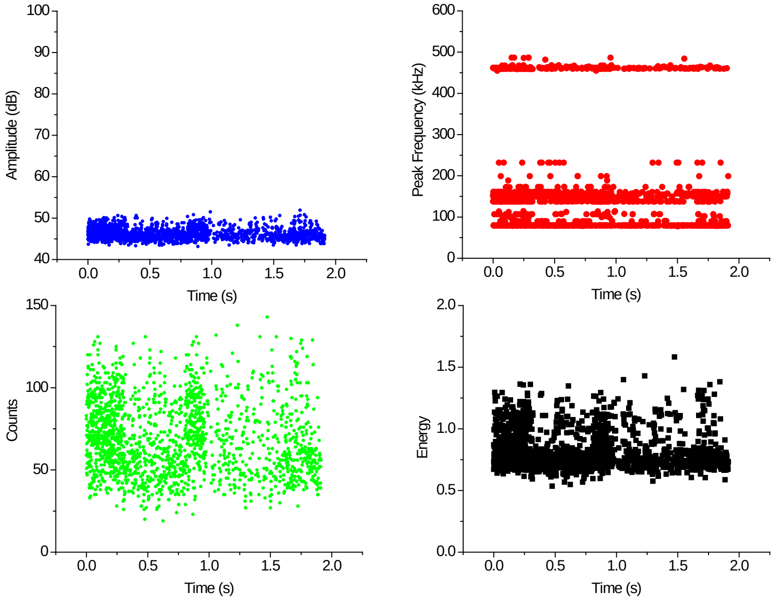

Figure 80: AE Feature analysis from preload testing

Representative AE waveforms obtained during the preload are shown in Figure 81a and Figure 81b. It can be observed that both the waveforms were of continuous type emission with a very low amplitude as noted earlier. The peak frequency of the extracted waveforms were calculated using the Fast Fourier Transform (FFT) algorithm and is shown in Figure 81c and Figure 81d respectively. The dominant frequencies of the signals were centered at 150kHz and 450kHz.

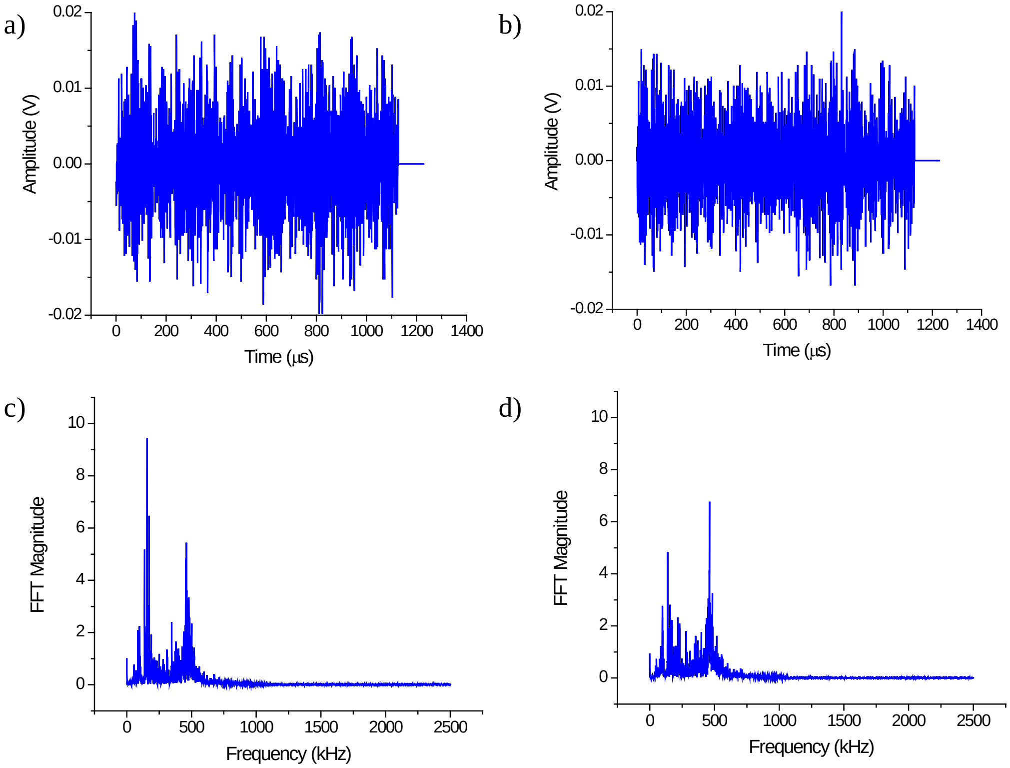

Figure 81: AE Waveform and its corresponding FFT from preload testing

Traditional AE frequency analysis simply relies on identifying the peak frequency using FFT algorithm. However, it is possible that two different AE sources can produce the same frequency analysis and thus it is essential to perform additional post-mortem analysis on the frequency characteristics of the obtained AE signals. To further investigate the frequency characteristics, all the obtained waveforms were segmented into four evenly spaced frequency ranges and the percentage of energy in each frequency range was analyzed. The four frequency ranges are shown in TABLE 9.

TABLE 9 : Advanced AE Frequency Analysis

Partial Power 1 (PP1)	$\int_0^{200kHz} \hat{U}^2(f)df \,/ \int_0^{2500} \hat{U}^2(f)df$
Partial Power 2 (PP2)	$\int_{200}^{400kHz} \hat{U}^2(f)df \,/ \int_0^{2500} \hat{U}^2(f)df$
Partial Power 3 (PP3)	$\int_{400}^{600kHz} \hat{U}^2(f)df \,/ \int_0^{2500} \hat{U}^2(f)df$
Partial Power 4 (PP4)	$\int_{600}^{800kHz} \hat{U}^2(f)df \,/ \int_0^{2500} \hat{U}^2(f)df$

A schematic representation of partial power analysis from the extracted waveform is shown in Figure 82. The PP1, PP2, PP3 and PP4 features are the percentage of energy extracted from the 0-200kHz, 200-400kHz, 400-600kHz and 600-800kHz respectively.

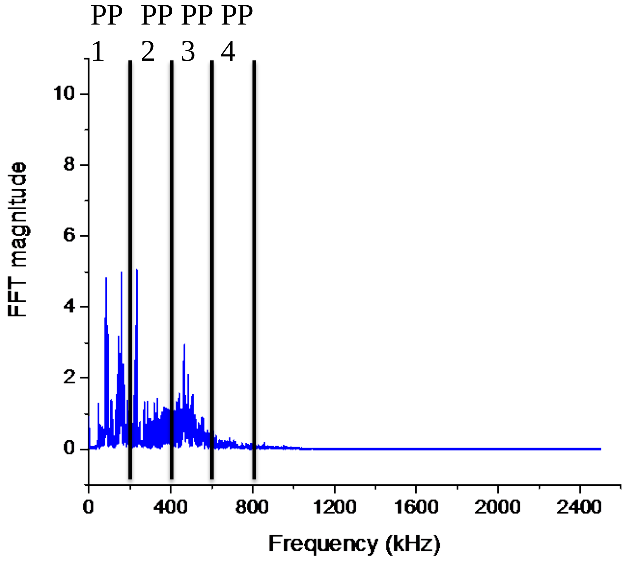

Figure 82. Schematic representation of partial power analysis

As most of the waveforms had a dominant frequency behavior around 150 kHz and 450 kHz, the PP1 and PP3 analysis is shown in Figure 83a and Figure 83b respectively. Since, all the waveforms is active across the entire spectral range, they will not be mutually exclusive in the defined partial power ranges. It can be observed that most of the acquired AE signals during the preloading testing were concentrated in the 0-200kHz range.

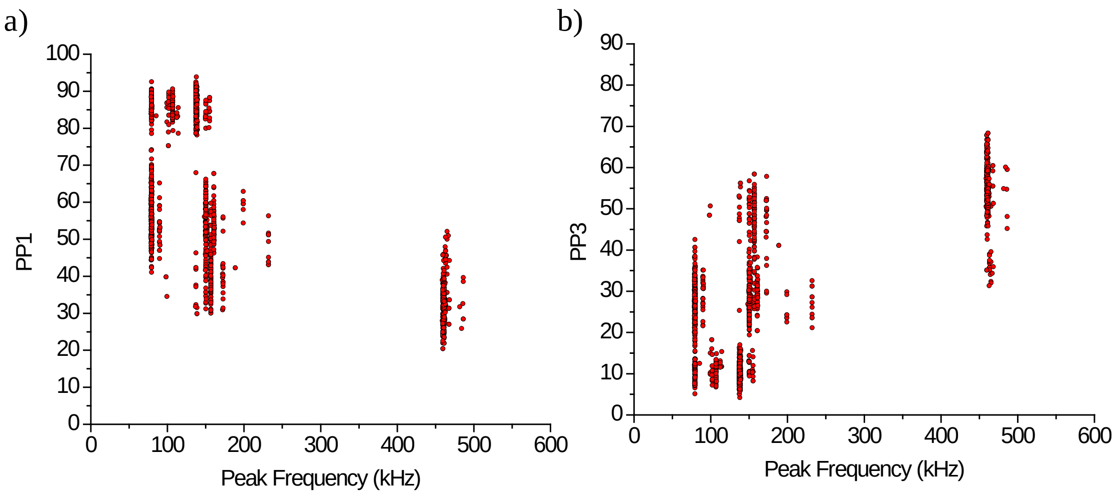

Figure 83. AE Partial Power Analysis

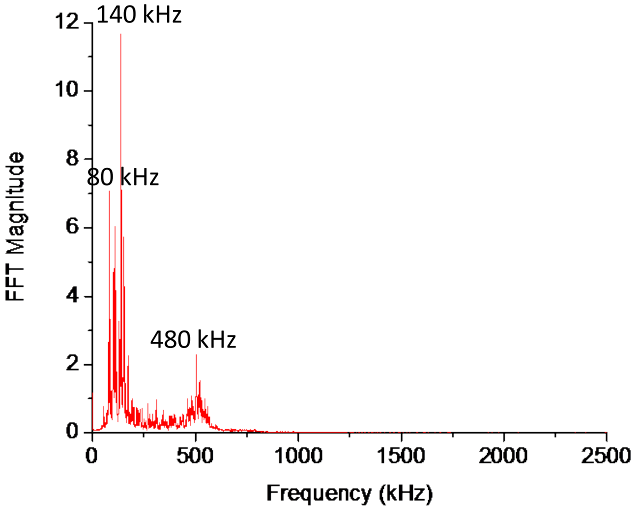

Figure 84. Weighted frequency Analysis

Further, 20 randomly extracted AE waveforms were selected and their weighted frequency analysis was calculated to eradicate the intrinsic effects on the signal and identify the true source characteristics. Although, the weighted analysis revealed the three distinct frequency characteristics, it was noted that most of the signal was contained in the low frequency regime (Figure 84).

The full field strain in the x direction (parallel to the notch) for the CT sample 5 at various loading stages is visualized in Figure 85. At 5kN (time = 75s), the onset of plasticity (point 2) can be observed around the crack tip. For visualization purpose, the limits was set between 0 and 1%. It should be recalled that the noise for this measurement was 0.07%. It can be noted that the plastic zone size increases as the load increases. At time 507s, the crack was noted to **initiate** after the load drop (point 5) as seen in Figure 85.

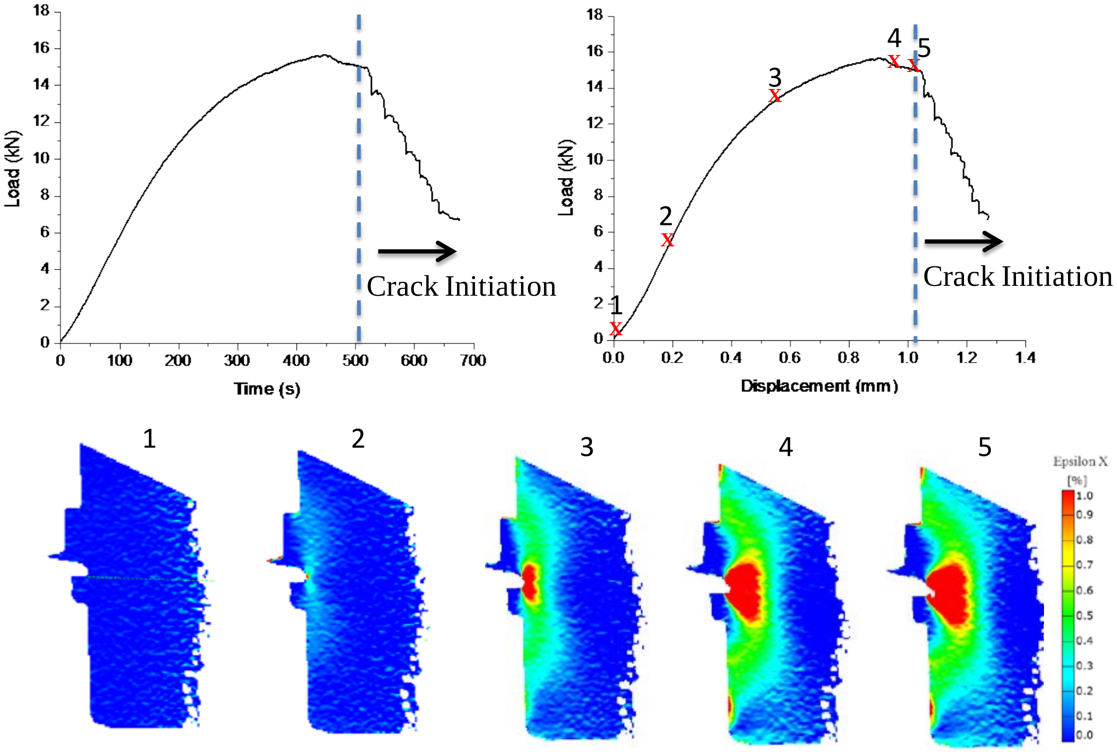

Figure 85: Full Field DIC Data

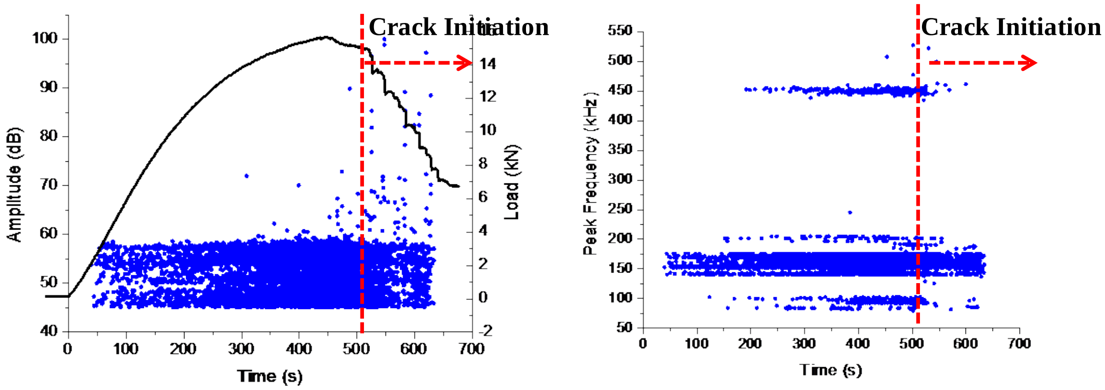

Figure 86: AE Analysis

The AE features monitored in-situ and correlated with the applied load are shown in Figure 86. the AE amplitude was noted to initiate at 50s which was a few seconds before the onset of plasticity was observed using the DIC. It should be mentioned that the onset of plasticity was identified based on the visualization limit shown in the earlier figure. The onset of plasticity could be earlier depending on the limits. However, in order to maintain an adequate signal to noise ratio, the visualization limits were set to 1%. Thus, the onset of plasticity would be more accurate to be associated with the onset of the AE amplitude. Further, it can be clearly observed as the crack initiated, there was a **sudden increase in the AE amplitude** precisely at the **exact time instant** that **visual crack** was observed to **initiate** on the surface using the DIC cameras. Importantly, it can also be noted that there was discrete increases in the AE amplitude prior to the crack initiation. Consequently, these discrete increases in AE amplitude serve as crack precursors and act as early signs of damage. Similar to the peak frequency analysis of the AE data obtained from the preload testing, the same three frequency characteristics were also obtained from this test. However, at the precise time instant that the crack initiated, a burst of high frequency (>500 kHz) was also noted (Figure 86). Therefore, these high frequency signals can be associated with the crack initiation in the CT specimen.

A representative waveform acquired after and before the load drop is shown in Figure 87a and Figure 87b respectively. The waveform corresponds to the precise time instant when the crack initiation was observed using the DIC and it can be observed that the wave signature due to crack initiation was of burst type emission. This was noted previous with AE signals associated with the cracking phenomenon in the 6mm CT specimens as well. However, similar to the waveforms collected during the preload testing, the waveforms collected before the load drop was also of continuous type emission. Since, the crack

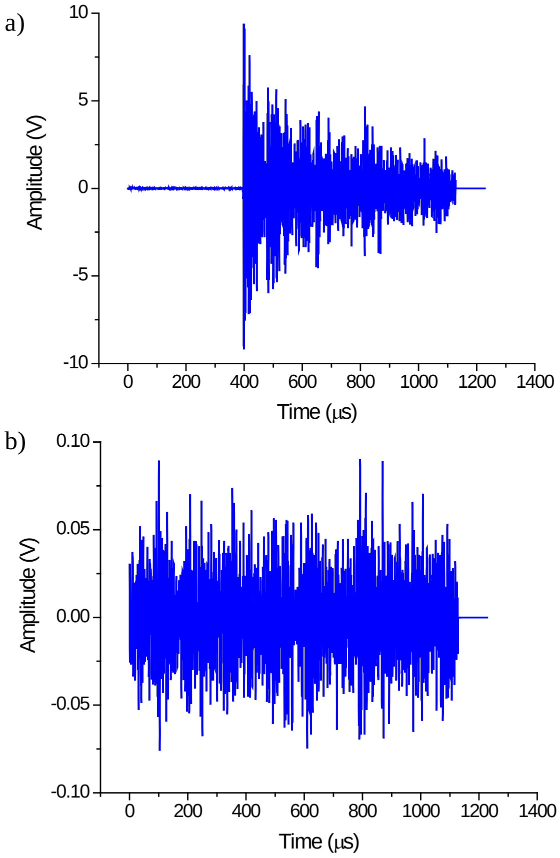

Figure 87: Representative AE waveforms (a) after load drop (b) before load drop

initiation process results in the sudden release of energy, it is expected that the AE wave form would have a short rise time and short duration characterized by a burst type signature. Furthermore, 20 random high amplitude (>60dB) AE signals acquired after the load drop were selected and analyzed through the weighted FFT algorithm. In fact, signals acquired after the load drop corresponded to much higher frequencies with the peak frequency at 534kHz (Figure 88).

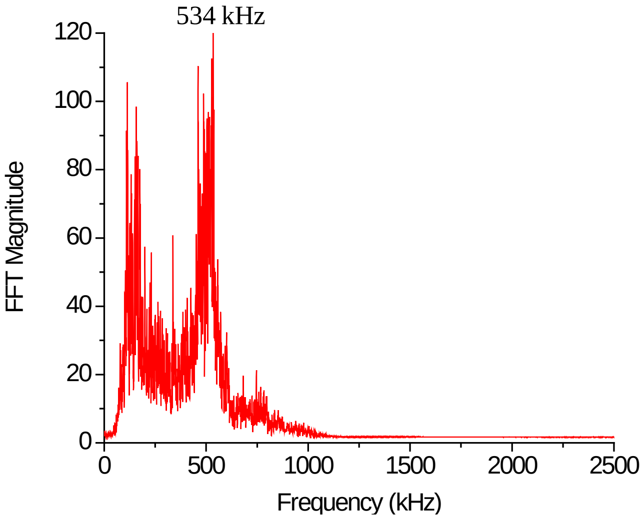

Figure 88: Weighted frequency analysis after load drop

The weighted FFT analysis indeed reveals a shift in the peak frequency after the load drop in comparison to prior to load drop. The same partial power analysis was performed on all the waveforms extracted from this test and is shown in Figure 89. It was noted that the AE signals that corresponded to the crack initiation and growth had high frequencies (> 500kHz) which was not present during the loading and during plastic deformation of the specimen. In order to validate this high frequency observation arises from crack initiation and independent of the loading rate, the AE data obtained from sample 4 was also analyzed in terms of their partial power analysis.

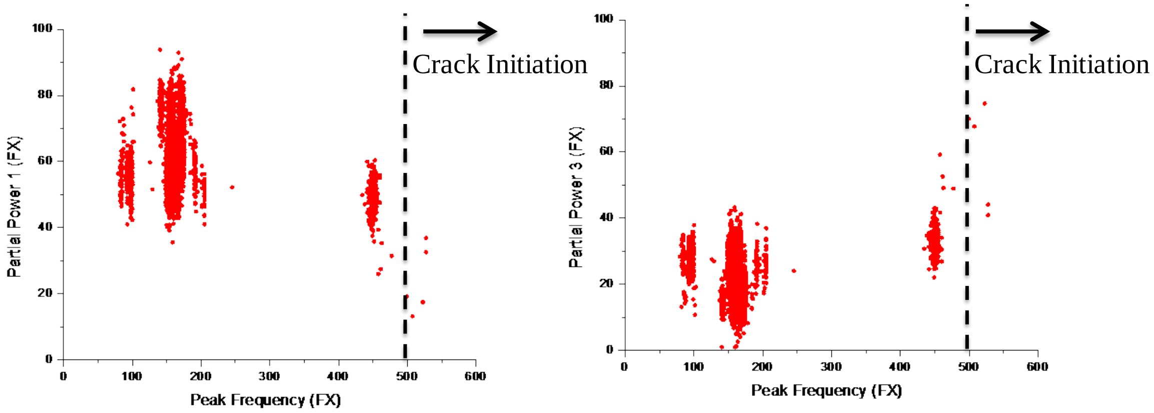

Figure 89: AE Partial power analysis for sample 5

The partial power analysis for the signals acquired from sample 4 is shown in Figure 90. It is evident that the loading rate has an effect on the acquired AE signals. The higher loading rate test (0.5mm/min) was noted to produce more AE data in comparison to the 0.2mm/min test. However, the behavior and the trend of the acquired AE signals were exactly similar. The signals obtained after the drop in the load profile (not shown) for sample 4 also corresponded to high frequency signals (> 500 kHz).

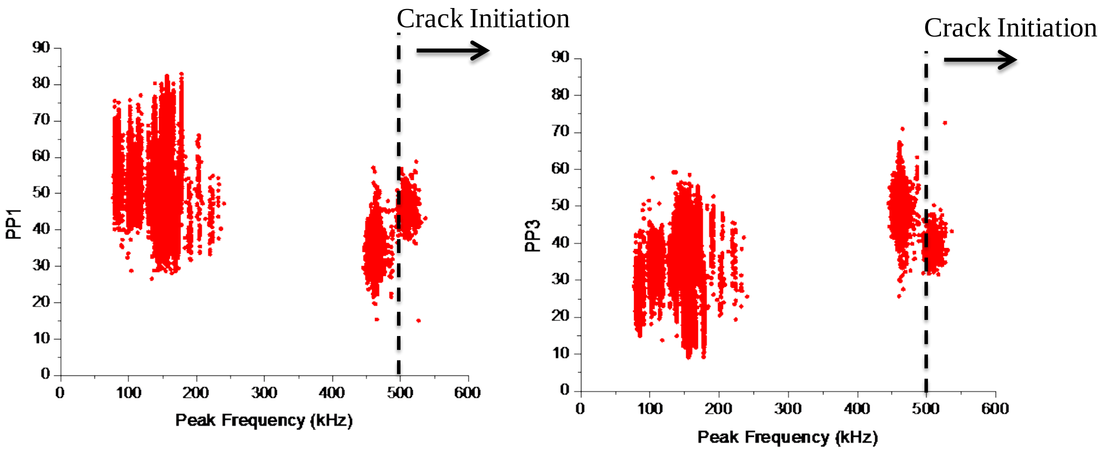

Figure 90: AE Partial power analysis for sample 4

The crack initiation signals and growth in the material across the two loading rates did correspond to the release of high frequency AE signals. Finally, the different features extracted from the DIC and IRT were combined to reliably i) to confirm the crack initiation ii) effectively validate the AE indications observed Figure 91. The average full field strain (ε_x) rate was calculated from the DIC images and the rate of temporal change was calculated from the IRT images and

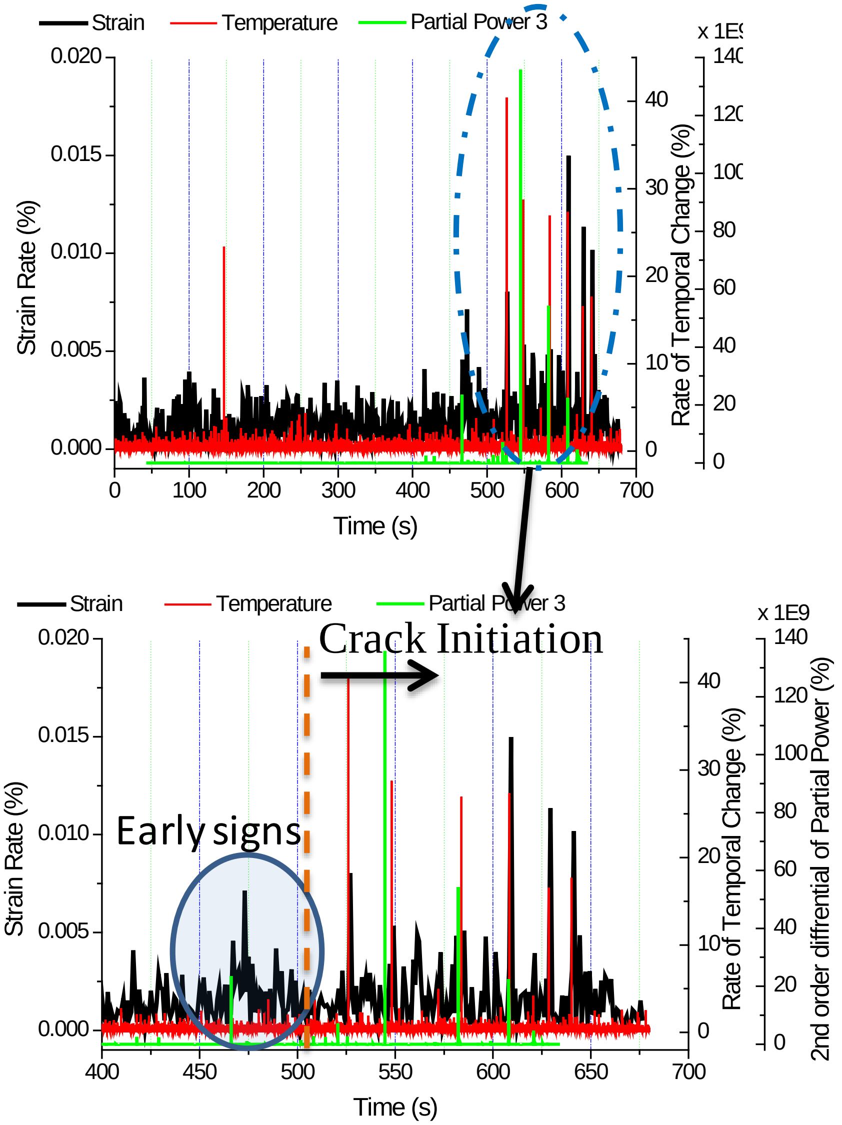

Figure 91: AE Features correlated with DIC and IRT Features

was correlated with the 2^{nd} order rate of the partial power 3. The 2nd order differential of the partial power 3 was calculated using the equation below

$$\ddot{PP}3 = \frac{d^2 PP3}{dt^2} \tag{4}$$

It can be seen that the upon crack initiation, the strain rate, temporal rate and the 2nd order rate of PP3 are seen to have distinct jumps at the same time intervals. Interestingly, there is an increase in the strain rate and PP3 just prior to crack initiation providing early signs of impending damage in the specimen. There is no major increase in the temporal change prior to the crack initiation in the specimen. This could plausibly be attributed to the lack of adequate IR camera resolution. However, upon crack initiation, significant jumps of temperate can be observed. Similarly, the strain and PP3 are noted to increases suddenly at those time intervals.

To identify the AE characteristics of crack initiation reliably and eradicate the effect of geometry on the observed AE phenomenon, the results obtained from the MT specimen were analyzed and compared. Similarly, the DIC and IRT data were also computed to confirm the crack initiation and interpret the AE signals. The full field DIC results and its corresponding strain x visualization at various loading stages is shown in Figure 92. The strain evolution at the crack tip is clearly visualized and significant strain accumulation is noted around the crack tip prior to the crack initiation. The crack initiation was observed just after the load drop similar to the CT specimen. At the time of crack initiation (470s), the load was noted to be 37.5kN. The crack was observed to initiate at the bottom left tip of the initial notch (Figure 92) and subsequently it grew on either side of the notch which resulted in a significant load drop.

The AE results obtained from the quasi-static tension testing of MT specimen is shown in Figure 93. Initially, as the specimen was gripped in the fixture, AE activity was detected which continued

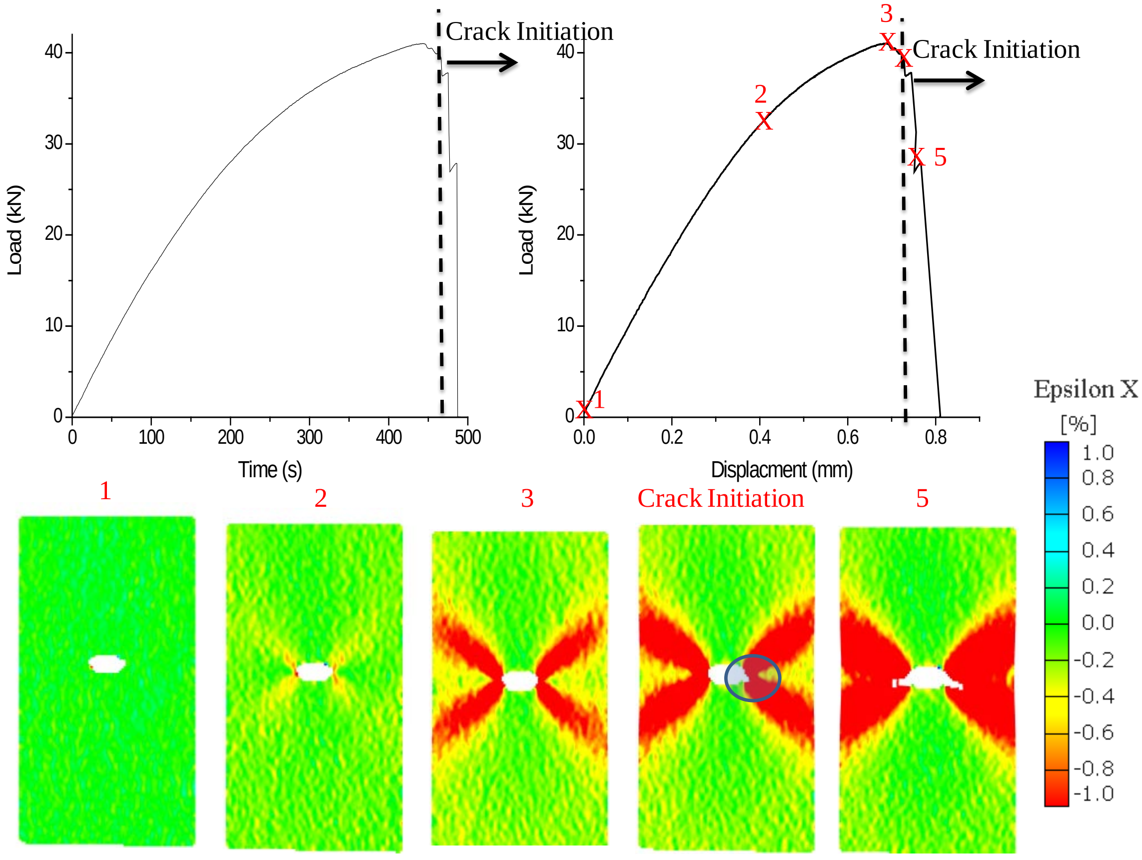

Figure 92: Applied load history and full field dic results

as the load was applied. It should be mentioned that not all the channels detected this AE activity and it was only the channel in the vicinity of the grips that picked up this AE activity. These AE signals were characterized by low amplitude and frequency. This was then eliminated by raising the threshold which resulted in a dormant AE zone until a few seconds before the maximum load was reached. As the applied load approached the maximum load, AE signals were detected and an increasing AE amplitude trend was observed. During this stage, no crack was observed on the specimen. However, just after the load drop, when crack initiation was observed by the DIC, the amplitude reached a maximum level of 100dB and the number of AE signals increased. Interestingly, similar AE frequency signals that was detected precisely at the onset of cracking in the CT specimen was also seen in the MT specimen exactly upon crack initiation. These signals had a peak frequency greater than 500kHz and additionally, the same AE frequency signals that was observed during the gripping and initial load stages were also noted again once the AE signals were seen to pick up.

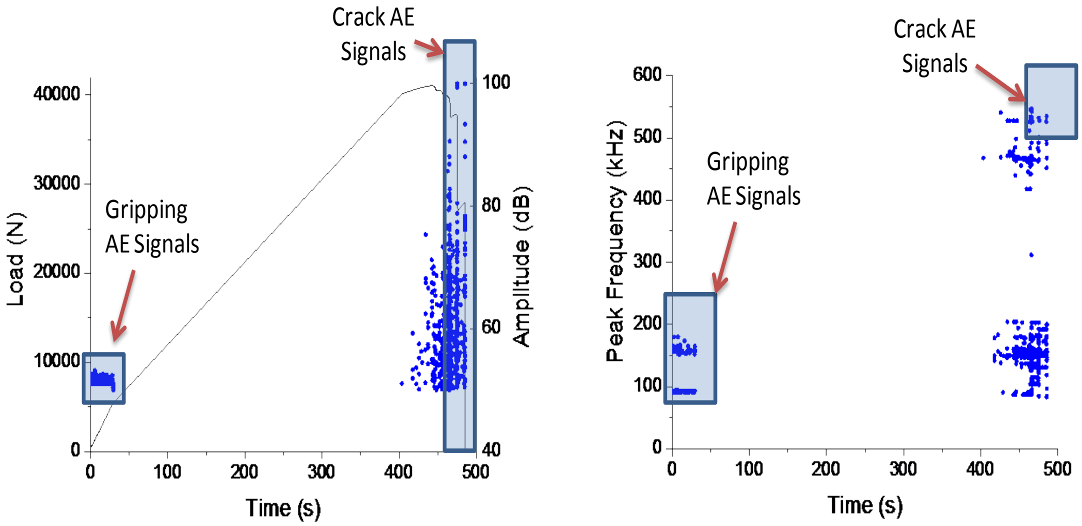

Figure 93: AE results from the MT specimen

The similar data fusion approach was adopted in reliably validating the AE signals due to crack initiation. The AE energy was then correlated with the average full field strain and temporal change along with the applied loading profile as shown in Figure 94. Precisely, as the load began to drop, an increase in the strain and the AE energy was noted. Consequently, as the crack initiated in the specimen, both the AE energy, the strain and the temporal change (which is defined as the difference between the current temperature and the initial temperature) was seen to increase significantly.

It is significant to note that all these heterogeneous features change at the same time instant thereby cross-validating the presence of damage in the specimen and importantly confirming the AE signals due to crack initiation.

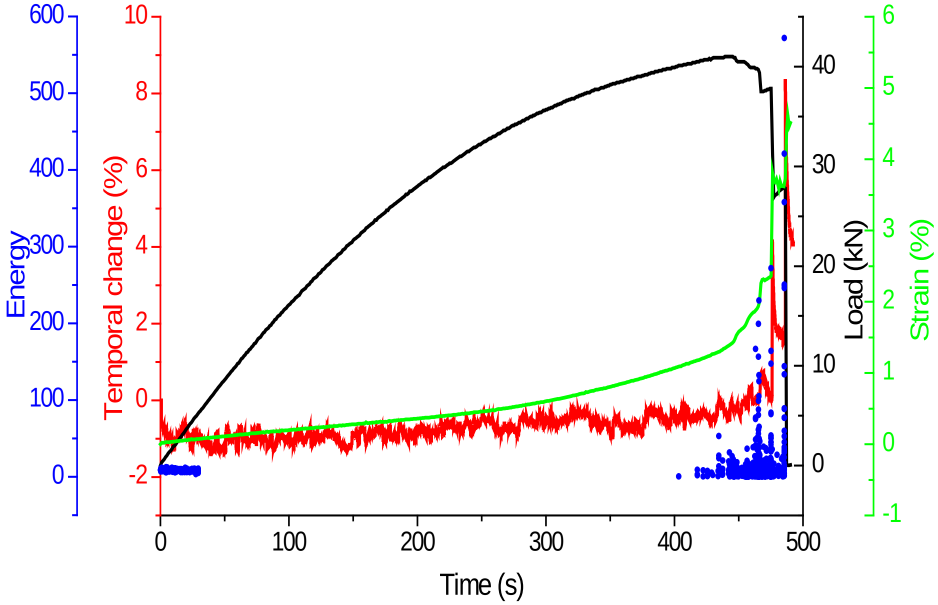

Figure 94: AE results correlated with strain, IRT temporal change and applied load

To characterize the AE signals associated due to crack initiation, the AE waveforms acquired prior to crack initiation and upon crack initiation was extracted and compared. Figure 95 shows the AE signals acquired due to the gripping noted initially in the test and crack initiation. Similar to the AE signature obtained from the CT specimen due to crack initiation, the AE signals obtained from the MT specimen also revealed a burst type AE emission. The AE signals were observed to have a short rise time. However, the crack signals obtained from the gripping was observed to be of continuous type.

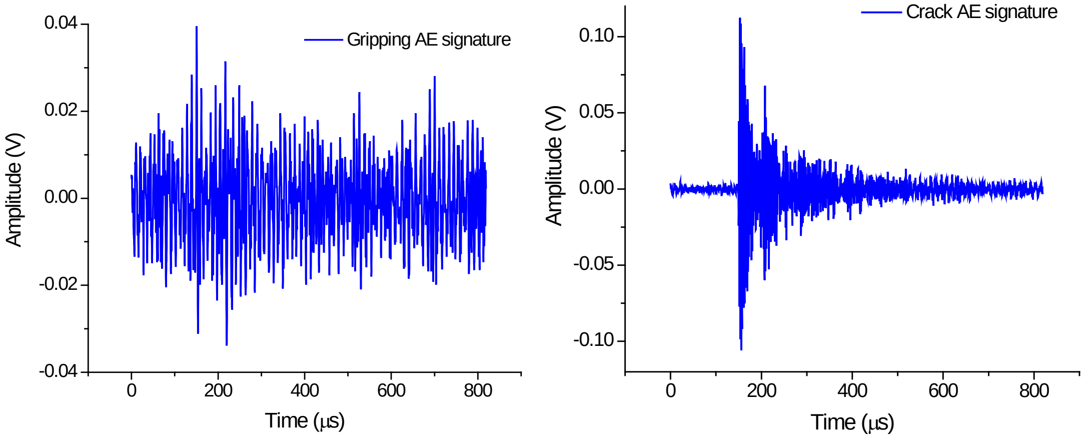

Figure 95: AE Wave signatures obtained from the mT specimen

The AE waveforms were then segmented into the four equally spaced frequency ranges and their partial power behavior was analyzed and compared with the CT analysis to identify similar AE characteristics (Figure 96a). Upon crack initiation, It was observed that the PP3 increased significantly and these signals had a peak frequency of 500kHz while the PP1 decreased significantly. However, prior to the crack initiation, it was noted that the PP1 had a higher percentage of energy than PP3. This behavior was previously noted with the AE signals acquired from the CT specimen (Figure 96b) as well. The signals from the CT specimen upon crack initiation also had a peak frequency of 500kHz and had a higher shift in the PP3.Consequently, it can be stated that the AE characteristics associated with crack initiation for Mode 1 tension testing is of burst type, high frequency (> 500 kHz), higher PP3. However, in order to reliably identify crack initiation and growth irrespective of the loading type, it is important characterize AE signals from other type of loading scenarios as well.

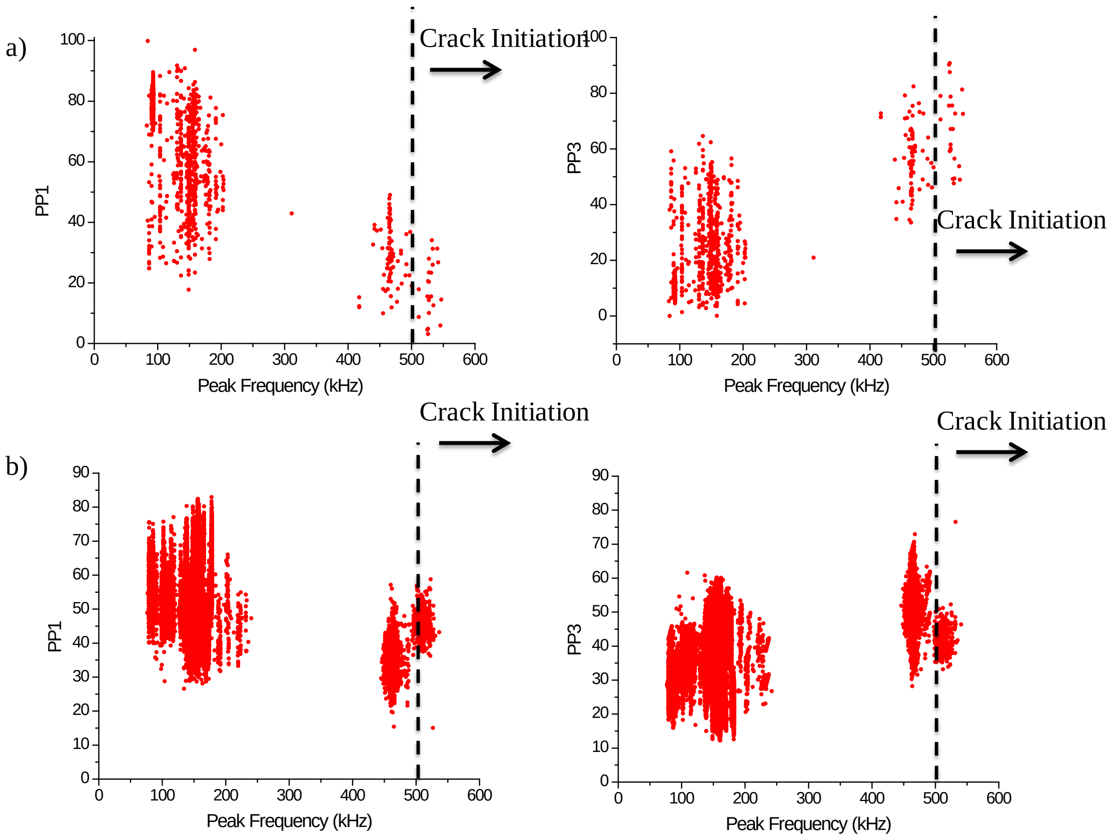

Figure 96: AE partial power analysis (a) MT specimen (b) CT specimen

Consequently, the AE signals arising from the fatigue testing of the CT and MT specimens were analyzed and evaluated. The DIC results were used to identify the onset of cracking in the fatigue testing of the MT specimen. The full field longitudinal strain visualizations corresponding to the various life fraction of the material is shown in Figure 97. The initial increase in the strain is attributed to the loading nature (tensile-tensile fatigue) of the material. During the initial stages of the fatigue life, no major strain accumulation is noted on the specimen However, as the specimen crossed its half life, a slight shift in the strain was noted. Subsequently, upon approaching 0.75 of the life fraction, major strain accumulation was noted at the crack tip. The crack was observed to initiate at 0.88 of the life fraction of the specimen which resulted in the increase of the strain.

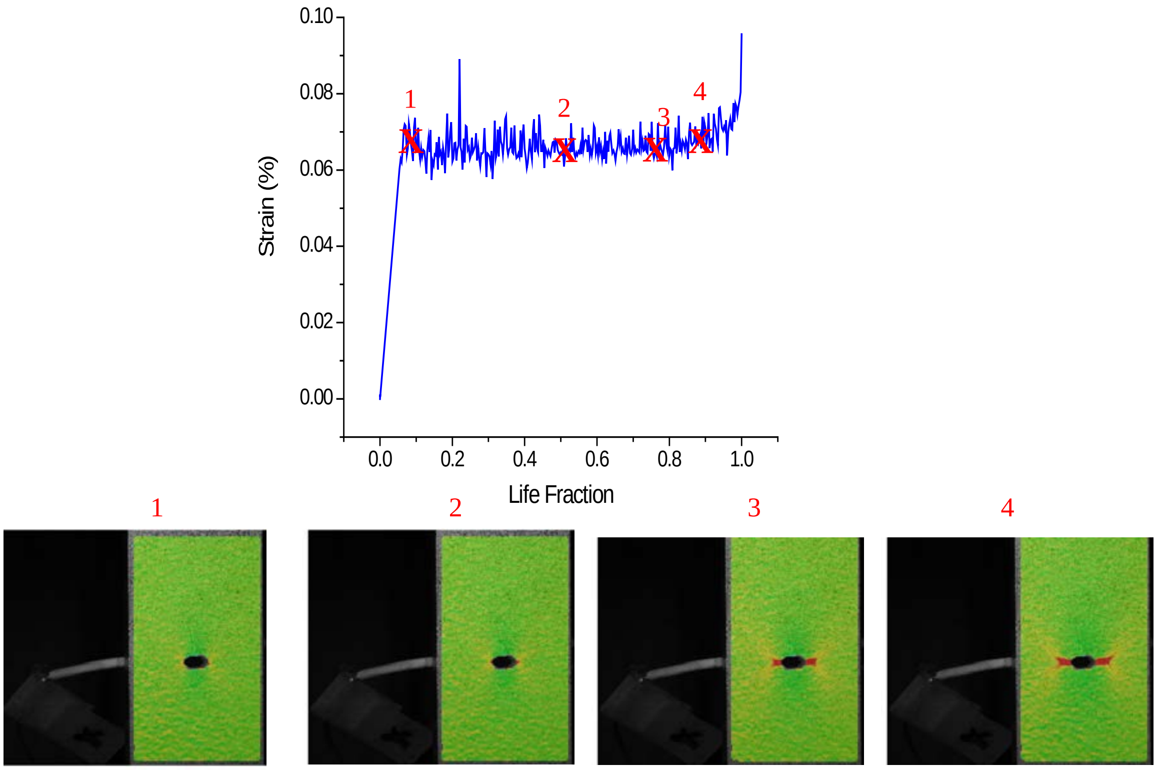

Figure 97: Strain as a function of the Life fraction for the MT specimen

This analysis was used to interpret the unknown AE data collected during the fatigue test and similar analysis that was performed in the tensile specimens were repeated for the fatigue specimens. The amplitude and peak frequency as a function of the life fraction is shown in Figure 98. Although there were minor AE signals detected at the specimen's initial life fraction, the AE amplitude was observed to pick up at the specimen's half life. Furthermore, at 0.88 of the life fraction, the population of the AE signals increased with a shift towards higher amplitude signals. Significantly, as was in the case of the tensile testing of the specimens, upon crack initiation (0.88 of the life fraction), the presence of high frequency (> 500kHz) was detected. This demonstrates the reliability and validity of relying on frequency based AE analysis for failure identification and robust AE monitoring.

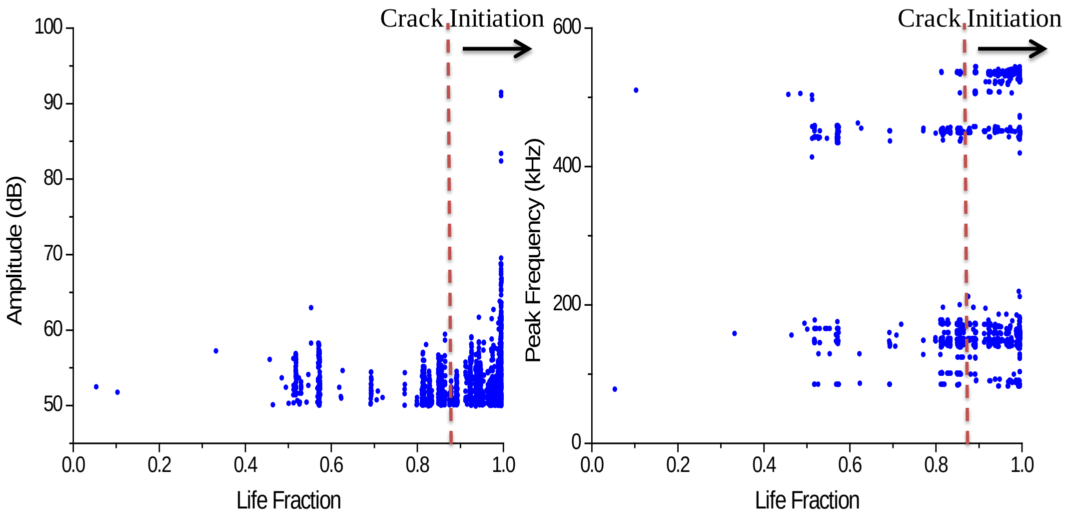

Figure 98: AE features as a function of the Life fraction for the MT specimen

Consequently, the AE signatures at different life fractions were extracted and presented in Figure 99. It is seen that the AE waveforms were of burst type emissions unlike in the tension testing where burst type emissions were noted at the onset of crack initiation. It is noted that waveforms extracted at 50% life fraction is characterized by a short rise time and high amplitude but this amplitude is noted to decrease at 75% life fraction. The amplitude of the waveform was then seen to increase again at crack initiation (88% life fraction) and were noted to have the same wave signature as that obtained during the crack initiation of the tensile specimens. At this stage, it is to be mentioned that micro crack initiation was noted only at the bottom right of the notch tip. Subsequently, at 100% LF, as crack grew on either side of the notch tip, higher amplitude AE waveforms were detected.

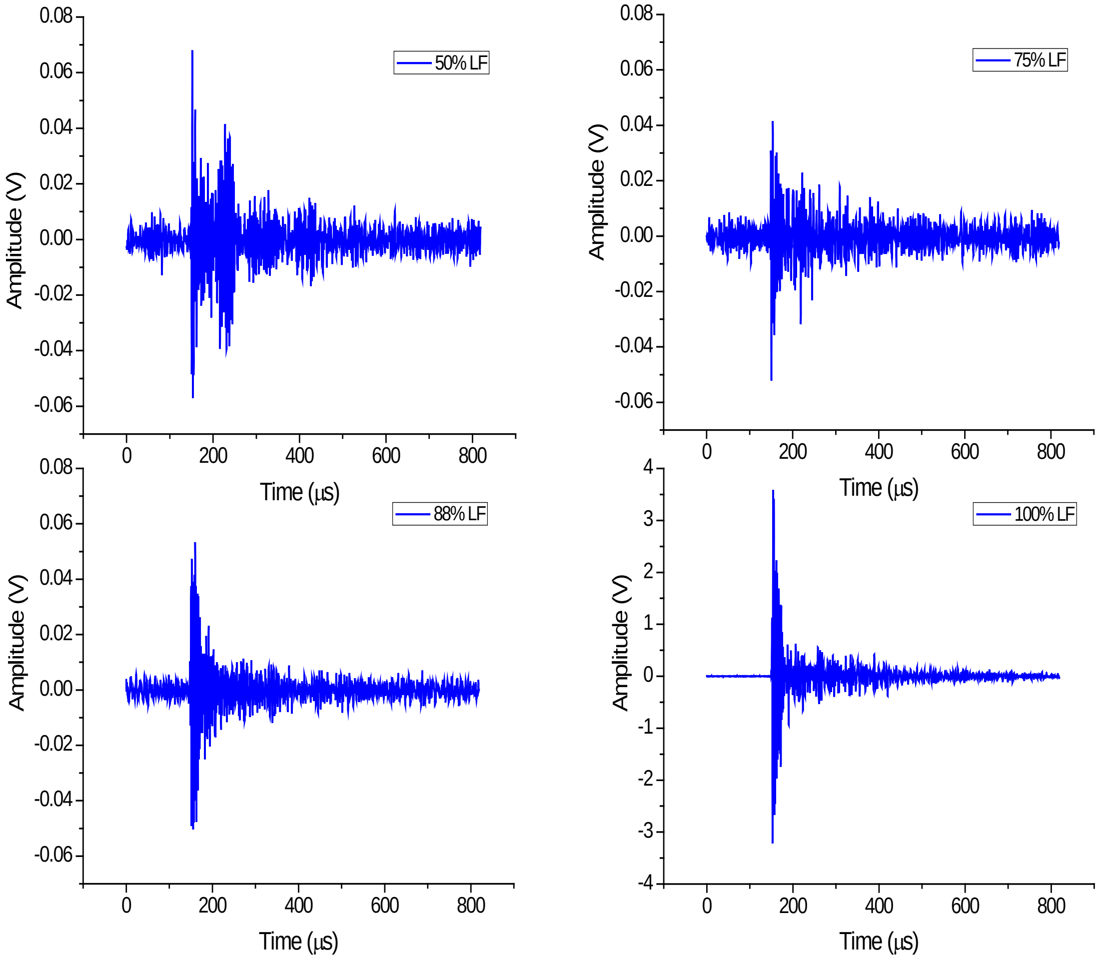

Figure 99: AE waveforms at different life fraction

The partial power analysis of these waveforms were then computed and also compared with the CT fatigue specimens to identify similar characteristics across the fatigue specimens. It can be observed in **Figure 100** that the MT fatigue results show similar behavior to the CT fatigue results (**Figure 101**) in terms of the partial power behavior. The AE signals that corresponded to 0.88 of the life fraction were seen to have high frequency greater than 500kHz and a shift from low PP1 to high PP3 was observed. Similarly the AE signals obtained from the CT fatigue results revealed a similar behavior as well.

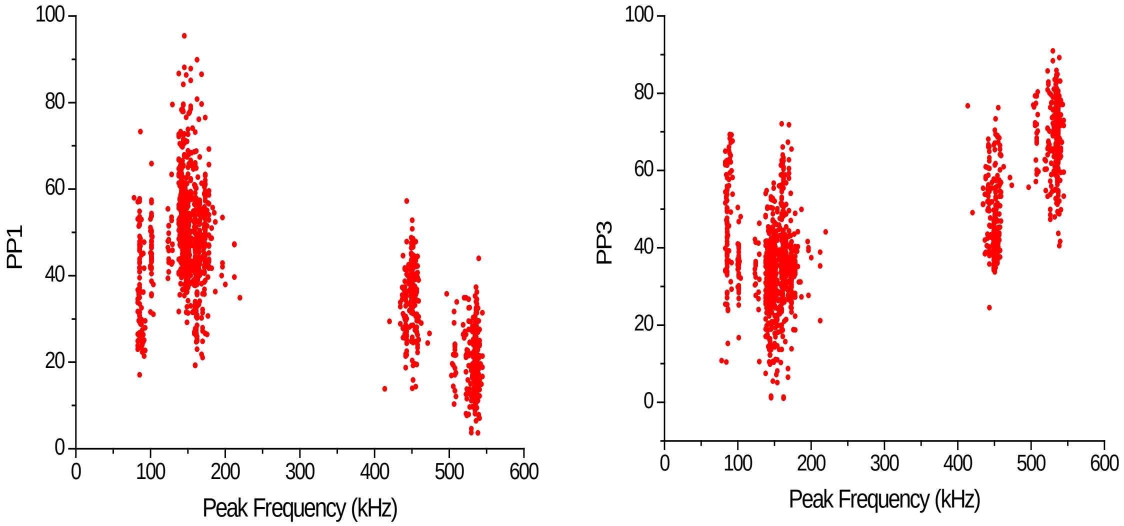

Figure 100: AE partial power analysis for MT fatigue specimen

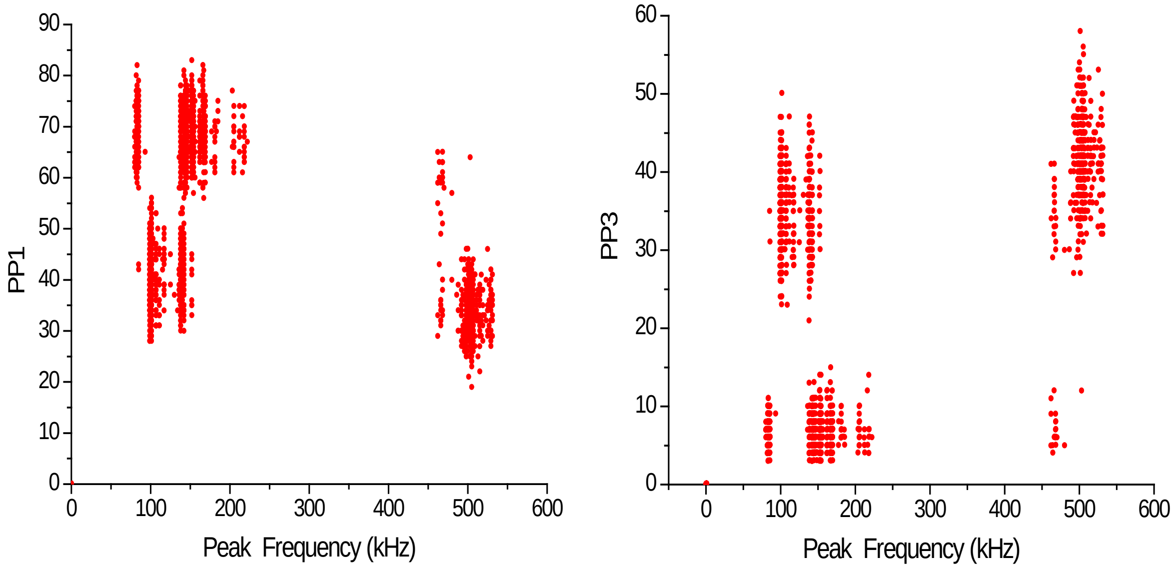

Figure 101: AE partial power analysis for CT fatigue specimen

Thus, the onset of cracking was noted to have similar AE characteristics across the different test specimens and were validated for different type of loading conditions. Thus, the AE characteristics associated with cracking can be reliably identified and utilized for onboard crack monitoring. The final aspect required for onboard cracking monitoring would be i) automated crack detection and ii) novelty damage index that can flag the presence of cracking.

5.3.2.2 PATTERN RECOGNITION USING THE NOVEL FEATURE DESCRIPTORS

For this purpose, pattern recognition algorithms were designed and implemented to separate the AE signals for robust detection. The MT fatigue data was utilized as the input AE data set for this pattern recognition process. K means statistical pattern recognition approach was implemented to identify the natural clusters of the obtained AE data. The objective of this pattern recognition analysis was not to associate every class of signals to a particular AE source but to identify the class associated with cracking. AE features such as average frequency, peak frequency and weighted power was utilized as input AE classifiers. The weighted power (WP) was calculated using the equation

$$WP = \frac{\sum_{1}^{n} PP_i}{PeakPower}; i = 1:4 \tag{5}$$

The input AE features were normalized from 0 to 1 to ensure equal weights for all the features during the clustering process. The features were then used to classify the AE data using the K means clustering algorithm. The K means parameters used in the clustering process are provided in TABLE 10

TABLE 10: K means Parameters

Distance Type	**Euclidean**
Initial Partioning	Time distribution
Initial Clusters	4
Iterations	300

The validity of the classes was evaluated using the R and Tou criteria. The R and Tou critera for the three classes of signals reveals the best combination. The R and Tou values for 3 classes were 0.63 and 2.57 respectively. The clustering analysis for the MT fatigue data set is presented in Figure 102. It is noted that class 0 and class 1 signals are active at the half life of the specimen while the class 2 signals were noted to pick up just after 80% of its life time.

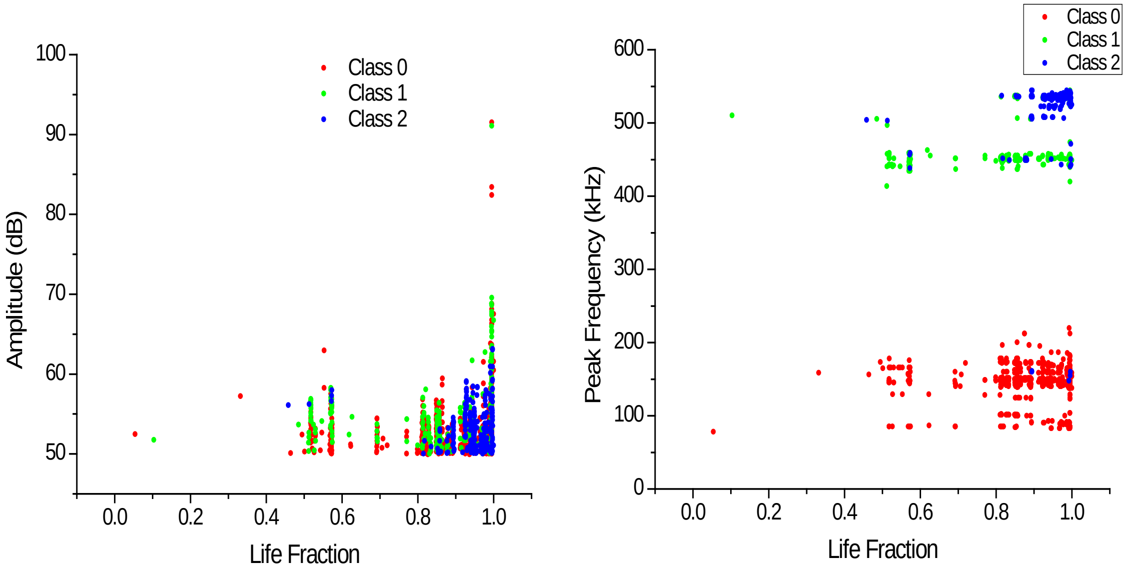

Figure 102: Pattern Recognition analysis for MT fatigue

Furthermore, the class 2 signals were noted to increase at the 0.88 of the life fraction which was precisely the onset of cracking in the specimen. Consequently, the class 2 signals can be associated with the crack mechanism in the MT fatigue specimen. To identify other feature characteristics of this class of signals, the rise time of the different classes was analyzed (Figure 103). Finally, the partial power 3 for the three classes as a function of the peak frequency was evaluated (also shown in Figure 103). It was observed that the class 2 signals were associated with a very short rise time. This was also noted with the burst type emissions were identified during the crack initiation. In comparison, the class 0 signals were noted to have long rise time as the specimen approached its final life time indicating a continuous type emission. These continuous type emissions could potentially be associated with the crack rubbing at the surface after the crack initiation in the material. Expectedly, the cracking signals (class 2) were noted to belong to the high frequency range (> 500kHz) and have a high PP3 upon crack initiation.

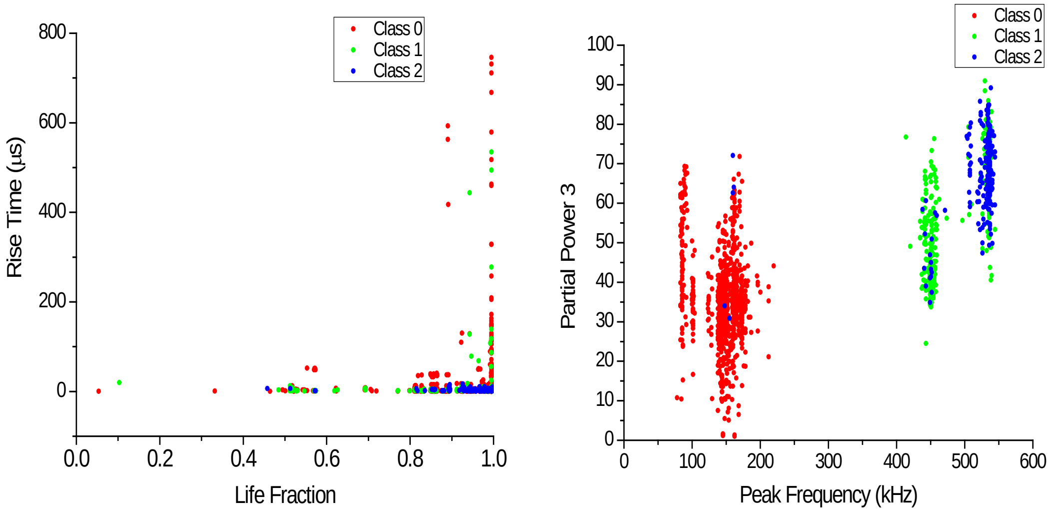

Figure 103: Pattern Recognition analysis for MT fatigue

Based on this pattern recognition analysis, a novel damage parameter based on the AE features were developed for real time and onboard crack detection. This is the first of its kind to identify reliable damage index based on ensemble AE features for cracking identification.

The **novel AE damage parameter** (DP) was developed using the equation below

$$DP = \frac{(PP3 + PP1)/100}{Peakfrequency} \tag{6}$$

The novel AE DP was then computed for all the test specimens (Figure 104 and Figure 105) including tension and fatigue data and a reliable trend was identified across all the specimens.

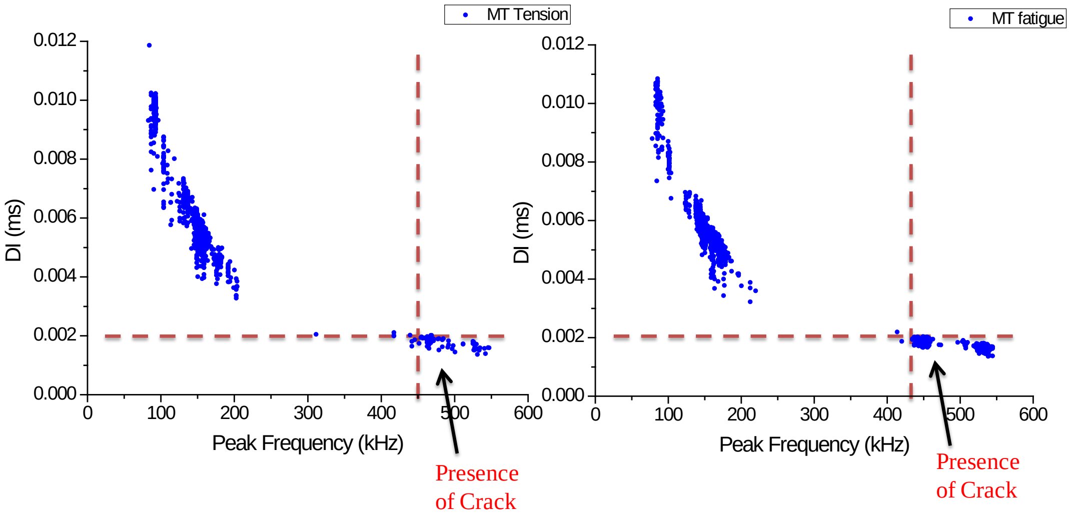

Figure 104: Novel AE Damage index for MT specimens

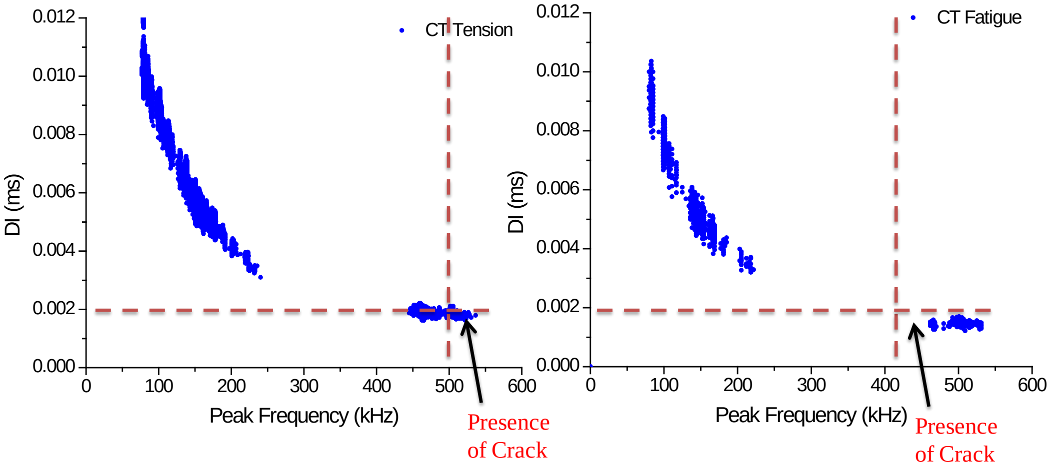

Figure 105: Novel AE Damage index for CT specimens

The damage index showed that the AE crack signals was below 0.002 µs for all the data sets. The crack signals were identified to be above 500kHz and below 0.002µs for both the CT and MT specimen. Consequently, it can be established that the designed novel damage index is robust across the specimen and for the different type of loading and thus can be implemented for robust online cracking monitoring of metallic aerospace materials

5.4 CONCLUSION

The proposed novel data fusion approach was instrumental in reliably identifying the onset of crack across different test specimens. The DIC full field visualization were utilized to effectively interpret the AE signals and identify AE characteristics associated with cracking. The heterogeneous features extracted from the DIC and IRT were combined with AE features to reliably detect the presence of crack initiation. The AE characteristics from two different test specimens, MT and CT were extensively analyzed and novel AE characteristics were identified and validated for the different load conditions. It was identified that the AE characteristics associated with cracking had a burst type emission, short rise time, high PP3 and a peak frequency greater than 500kHz. Finally, statistical pattern recognition algorithms was successfully implemented to separate the AE signals associated with cracking and was then utilized to develop a novel AE damage index for onboard cracking detection. The novel AE damage index revealed that the crack signals had a DI less than 0.002µs for all the test data including tension and fatigue. This damage index was successful in flagging the presence of damage in both the MT and CT test specimens and forms the basis for reliable and robust online cracking monitoring for metallic aerospace applications.

CHAPTER 6: THE IDENTIFICATION OF DEBONDING IN COMPOSITE COMPONENTS

6.1 INTRODUCTION

Over the years, fiber reinforced polymer composites have increasingly been utilized along with aluminum alloys in primary aircraft structures. The application of fiber reinforced polymer composites is justified by their exceptional properties such as superior strength and stiffness to weight ratio, fatigue tolerance and corrosion resistance [158, 159]. This along with the fact that aluminum alloys are susceptible to corrosion and fatigue cracking [160, 161] has justified the increased use of high strength fiber reinforced polymer composites. Consequently, carbon fiber reinforced polymer (CFRP) composites has been utilized to manufacture aircraft fuselage, wing structures, landing gear components and other primary and secondary structures [162-164]. In fact, Boeing 787 and Airbus A350 employ increased percentage of CFRP in its aero structures. Furthermore, fiber reinforced polymer composites exhibit progressive micro failure mechanisms [83, 84] prior to fracture and thus provide early signs of impending failure.

Due to its anisotropic manufacturing process, damage in composite materials is a multi scale process. At the lamina-scale, damage mechanisms such as matrix cracking, fiber breakage and fiber-matrix debonding are the observed damage mechanisms and at the inter laminate scale, delamination is noted to be a dominant damage mechanisms [165]. Often, these damage mechanisms are hidden deep in the material and rarely show any visible damage on the surface. Hence, these damage mechanisms are difficult to detect during normal inspection routines and eventually lead to critical component failure at the structural scale. Hence, it is imperative to study these failure mechanisms at various length scales and implement robust techniques capable of detecting them prior to critical failure. However, the accurate detection of these micro failure mechanisms and its transition to critical damage is still an ongoing area of research and is the prime reason for adopting conservative design approaches for composite materials.

Additionally, with the realization of composite structures, adhesive bonding, and co-curing have become an alternate solution to traditional mechanical fastening techniques [166]. Adhesive bonding is typically used to attach stiffening spars to airfoil skins and ensure that the bond line integrity at the skin-stiffener interface is ensured. Stiffeners are utilized on composite panels to increase the rigidity and provide resistance to buckling. Composite stiffened panels Low velocity impacts are known to cause delamination and debonding in composite structures and are barely visible on the surface [167]. The debonding of skin-stiffener components directly affects the buckling capacity of the structure causing catastrophic failure. Bisagni et al [168] proposed an optimized procedure for the post buckling design of composite stiffened panels. This procedure was based on designing neural network algorithms that evaluated the global structural response extracted from finite element analysis values. Thus, considerable research efforts have been invested in identifying and implementing damage detection strategies both numerically and experimentally to monitor the bond-line integrity of composite aerospace structures.

6.2 EXPERIMENTAL SETUP

6.2.1 COMPONENT PREPARATION

The CFRP skin spar components were composed of a solid carbon fiber composite sheet and a carbon fiber composite I beam bonded together using an aerospace grade epoxy (Hysol EA9394) as shown in Figure 5. The carbon fiber composite sheet and I beam were supplied by a commercial vendor, DragonPlate. Two CFRP components were manufactured in which the first specimen had no initial defect while the second specimen had an initial defect manufactured using a teflon insert.

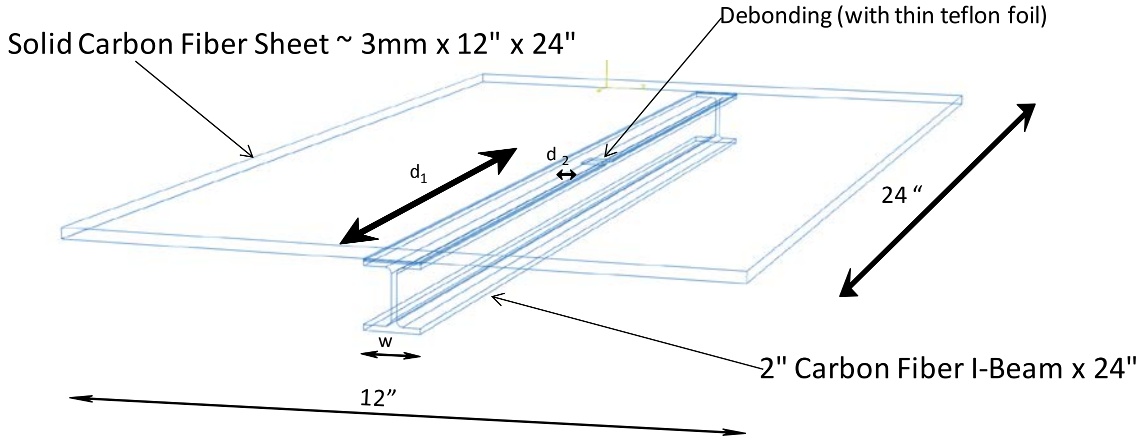

Figure 106: Schematic of CFRP skin spar components

Procedure to fabricate the CFRP skin spar components

- The aerospace grade epoxy was prepared by mixing 100g of Hysol EA9394 Part A and 20g of Hysol EA9394 Part B.
- A thin layer of the epoxy was then applied at center of the carbon fiber composite sheet and I beam surface to ensure maximum bonding at the contact surface between the sheet and the I beam.

- The I beam was then placed on the sheet and dead weights were applied at various positions along the I beam to apply uniform pressure for the bonding process. The component was then allowed to cure in room temperature for 12 hours
- Finally, the component was then post-cured at elevated temperature (95°C) in an autoclave furnace for two hours. The CFRP component fabrication process is shown in Figure 107.


Stiffener location on skin

Application of Epoxy layer

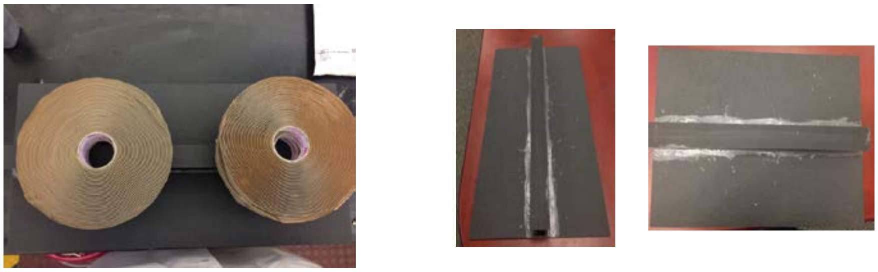
Room Temperature Bonding

Skin Stiffener Configuration

Figure 107: CFRP Fabrication Process

6.2.2 LOADING AND NDT SETUP

The CFRP components were then subjected to three point bending configurations and were tested under quasi-static and fatigue loading conditions while simultaneously recording AE data and GUW after every load cycle as shown in Figure 108. The quasi-static tests were used to identify i) to identify the limits for the fatigue loading conditions and ii) to identify the AE signature associated with the first sign of debonding. Based on the quasi-static results, different fatigue load limits were applied on the composite component while maintaining a constant load ratio of 0.1. The details of the fatigue load parameters are described in Table 11.

The AEwin DiSP system was utilized for these experiments and three Nano-30 AE sensors were placed as shown in Figure 109a. A threshold of 40dB was utilized for both the quasi-static and fatigue load tests and the signals were band pass filtered between 20kHz-2MHz. The use of multiple sensors permitted the implementation of 2D location algorithms. PLB tests were performed to calibrate the sensors and calculate the wave speed in the material. It is challenging to accurately calculate the wave speed in the material due to the anisotropic material properties. Thus, an average wave speed was calculated by performing the PLB tests at various locations and accurately detecting the PLB as shown in Figure 109b. The wave speed that provided reasonable location was determined to be 5800m/sec. A PDT, HDT and HLT of 100µs, 300µs and 600µs were utilized to acquire the AE signals.

Table 11 : Fatigue Load Parameters

Load Range (N)	Number of applied cycles	Loading Rate (mm/min)
100-1000	500	50
120-1200	100	50
150-1500	100	50
200-2000	100	60
250-2500	100	60
270-2700	100	60
350-3500	100	60
420-4200	100	60
450-4500	2000	60
470-4700	500	100
550-5500	500	120
600-6000	100	120

GUW were generated after every applied load cycle using a national instrument PXI (NI-PXIe-1062Q) unit running LabVIEW. GUW were generated and received using similar nano-30 sensors. The nano generator and receiver were separated by a distance of 0.2m. Five cycle tone-bursts with a Hanning window centered in a range of 100kHz-700kHz with a step frequency of 50kHz were generated using a function generator and recorded with a multiple channel scope at a sampling rate of 2MHz. A peak to peak voltage of 20V was used for the generated wave to accommodate the attenuation in the material. The received signals were amplified using an uniform gain of 40dB and were averaged 25 times to minimize the effect of noise on the signals.

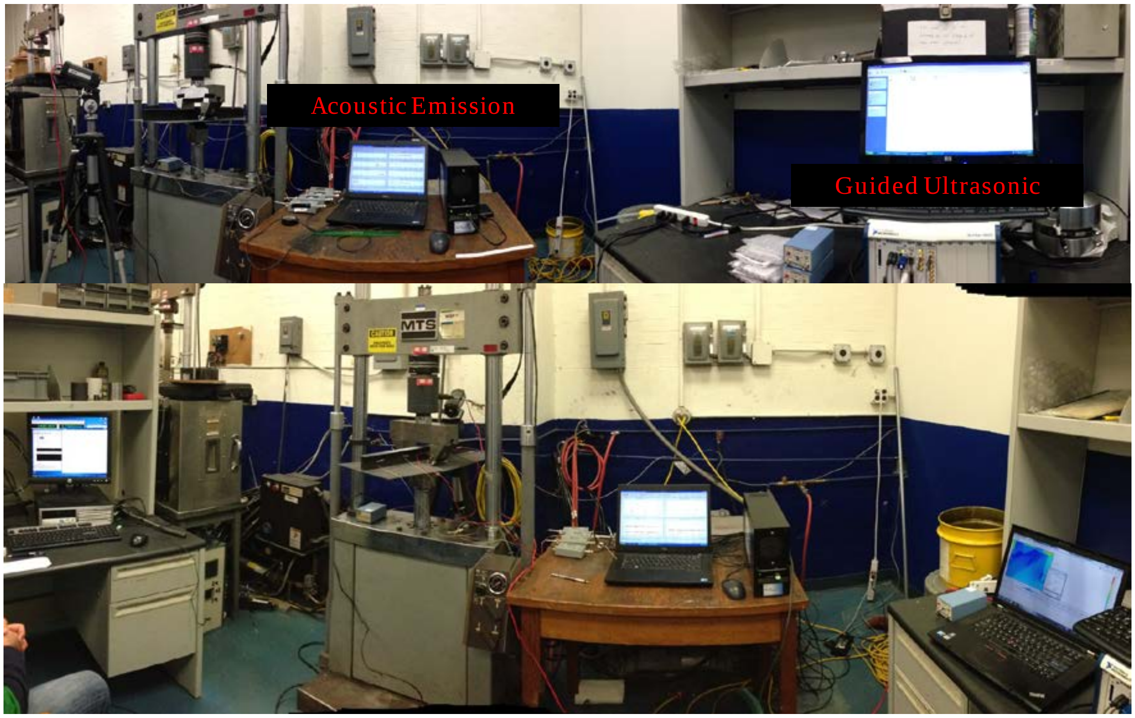

Figure 108: Loading and NDT setup

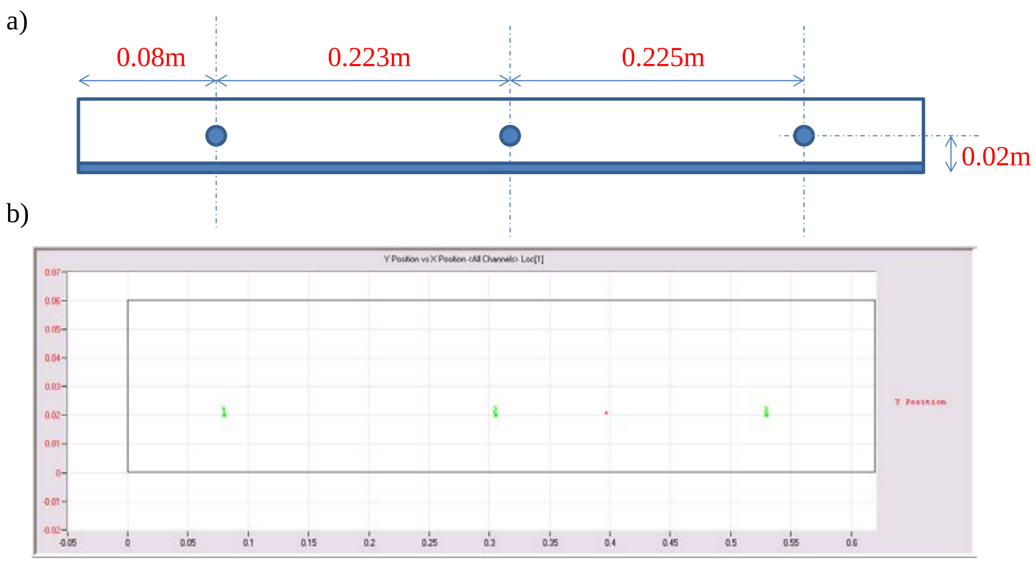

Figure 109: (a) AE sensor locations and (b) PLB location

6.3 RESULTS AND DISCUSSION

6.3.1 NUMERICAL MODELING OF WAVE PROPAGATION IN CFRP COMPONENT

Guided waves in composite materials are very complex due to the nature of multi-layer, anisotropy and viscoelasticity of composites. Understanding the wave propagation is critical for selection and placement of the piezoelectric sensors/transducers, as well as interpretation of detected signals. Consequently, to optimize the damage detection process during experimental observations, a finite element method (FEM) simulation of the wave propagation in the CFRP skin spar component was investigated using the commercially available ABAQUS software. In particular, to evaluate the sensitivity of guided waves to detecting debonded defects and possible sensor locations, four different debonding sizes were simulated with dimensions 5mm x 5mm, 7mm x 7mm, 12mm x 12mm and 24mm x 24mm with the virtual sensors located at 100mm (3.94"), 150mm (5.9"), 200mm (7.87") and 250mm (9.84") from the actuator as shown in Figure 110.

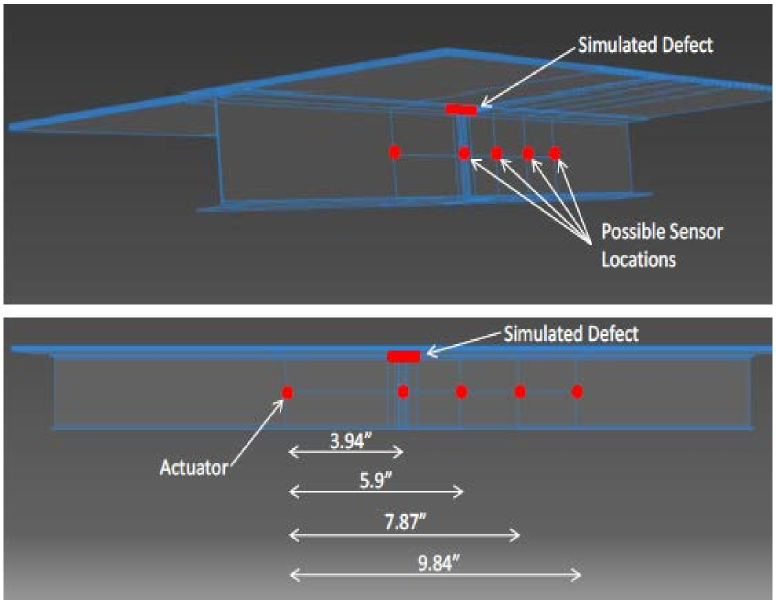

Figure 110: FEM defect simulation and virtual sensor locations in CFRP component

The excitation simulating a PZT transducer was represented by a concentrated force vector. Each force vector has an amplitude that is a function of time. The force time history imposed at the actuator location is a 5 cycle sine tone-burst windowed using a Hanning window and centered at 650 kHz. For each defect simulated a new set of signals were recorded at the four different receiver locations shown in Figure 55. A simulation was also performed for the pristine case where no defect is present in the assemblage. The signal recorded for the undamaged case is named AccNoDefect while the corresponding signals recorded for defects of 0.2”×0.2”, 0.3”×0.3”, 0.5”×0.5” and 1”×1", are named Acc0.2x0.2, Acc0.3x0.3, Acc0.5x0.5, Acc1.0x1.0 respectively. As the signals propagated through the defected region, the variation of the signals were noted to increase. This can be attributed to the fact that with increased defect size, the mismatch in the impedance of the materials restricts the waves to remain in the spar and thus the received amplitude of the wave increases. The variation in the received signals for all the defect sizes at the four different sensor locations are shown in Figure 111, Figure 112 Figure 113 and Figure 114

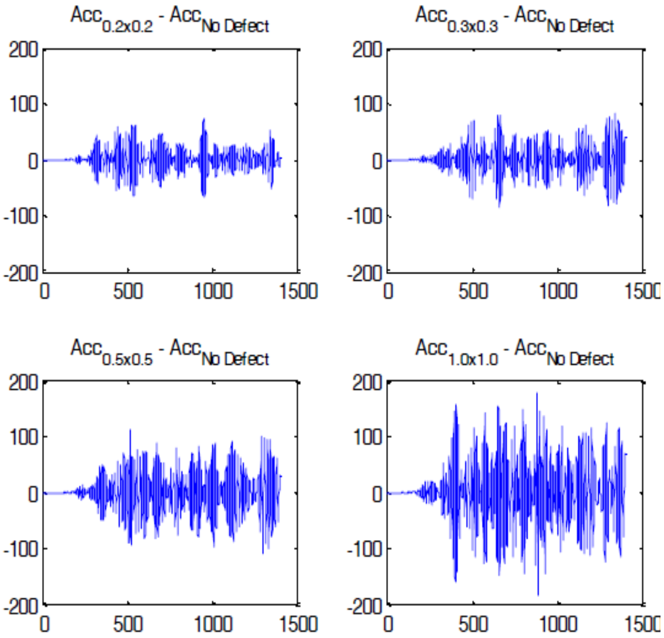

Figure 111: Variation of GUW signals as a function of defect size for the sensor located at 100mm

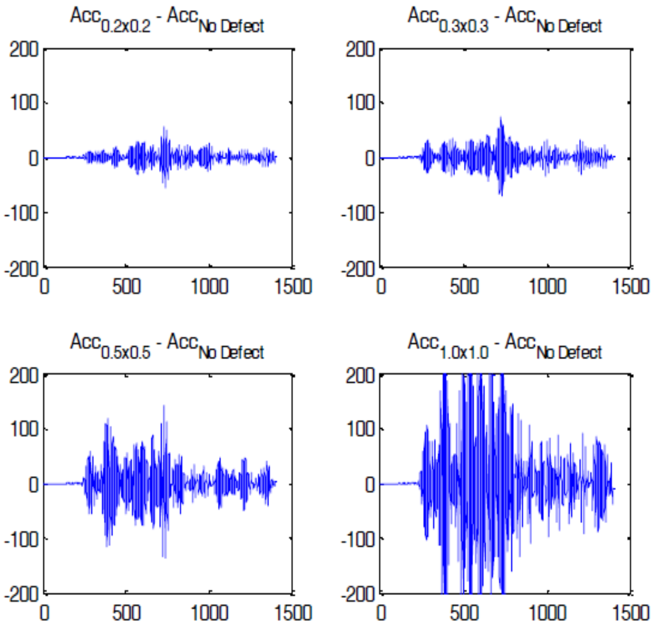

Figure 112: Variation of GUW signals as a function of defect size for the sensor located at 150mm

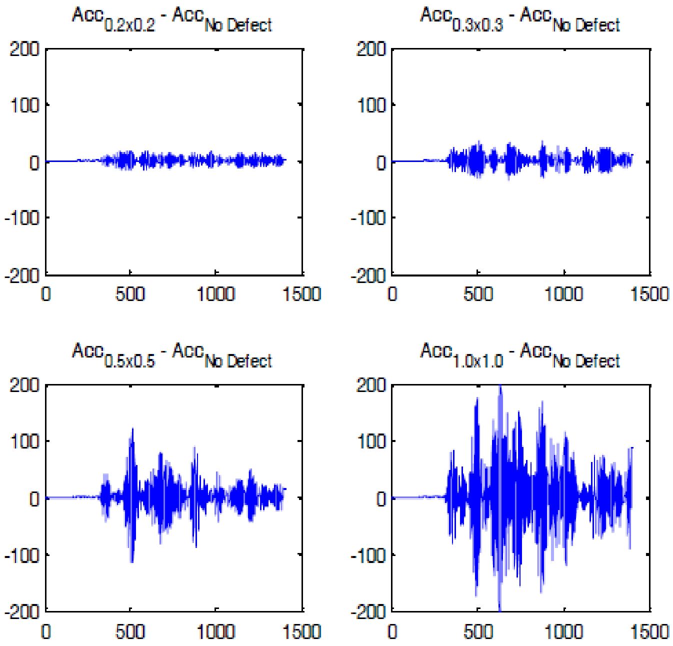

Figure 113: Variation of GUW signals as a function of defect size for the sensor located at 200mm

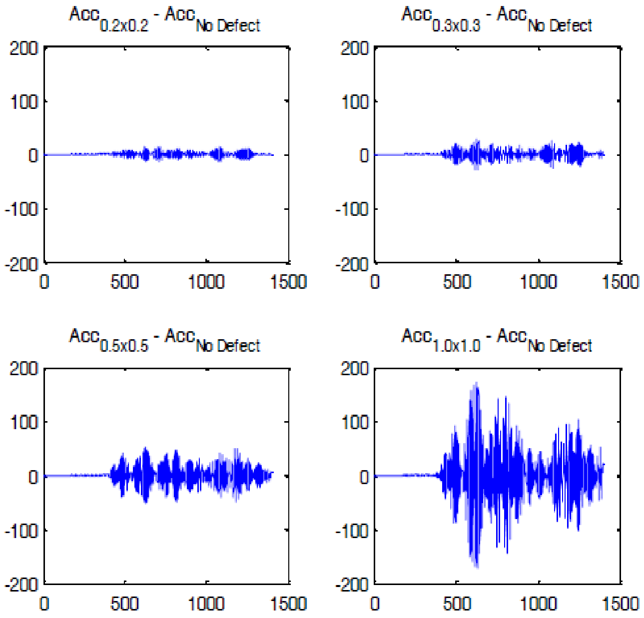

Figure 114: Variation of GUW signals as a function of defect size for the sensor located at 250mm

A trend can be observed that the signal variation increases significantly with the growing debonding sizes. Thus, it shows promising signs that GUW are sensitive to the different debond defects. In addition, it can be noted that this defect size can be detected at all the possible sensor locations. In order to quantify this change in signal variation for the debonding sizes at the various sensor locations, a novel damage index (DI) was developed using the equation below

$$DI=\frac{(Acc-Acc_{nodefect})^{T}.(Acc-Acc_{nodefect})}{(Acc_{nodefect})^{T}.(Acc_{nodefect})} \tag{7}$$

The damage index as a function of the defect size is shown in Figure 115. It can be seen that the minimum detectable defect size using the damage index is 0.3" x 0.3". A significant increase is seen subsequently with the increased defect size and thus this forms the basis to quantify the defect sizes in composite skin spar components using GUW

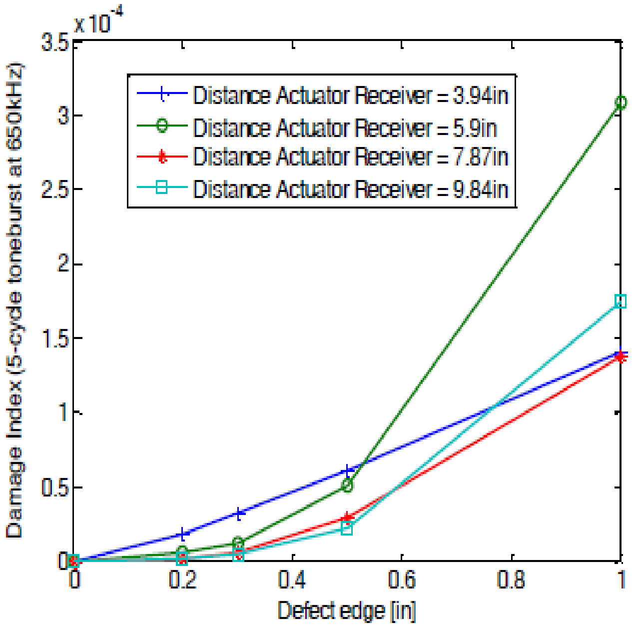

Figure 115: Damage index as a function of the defect size for all sensor locations

6.3.2 AE RESULTS FROM QUASISTATIC TESTING OF THE CFRP COMPONENTS

Component 1 - No initial defect

Similar to the CT and MT specimens, prior to loading the CFRP skin spar component in quasi-static conditions, a preload (~100N) was applied and AE signals were collected. The obtained AE amplitude and peak frequency during the preload is shown in Figure 116. The signals obtained during the preload were noted to be low amplitude and low frequency. The peak frequency of the acquired signals were centered around 100kHz. Further, a representative waveform and its corresponding frequency response acquired during this preload is shown in Figure 117. It is noted that waveform is characterized by low amplitude and duration with a mostly continuous type behavior. A wide spectral behavior is observed characteristic of white noise with a peak frequency at 100kHz.

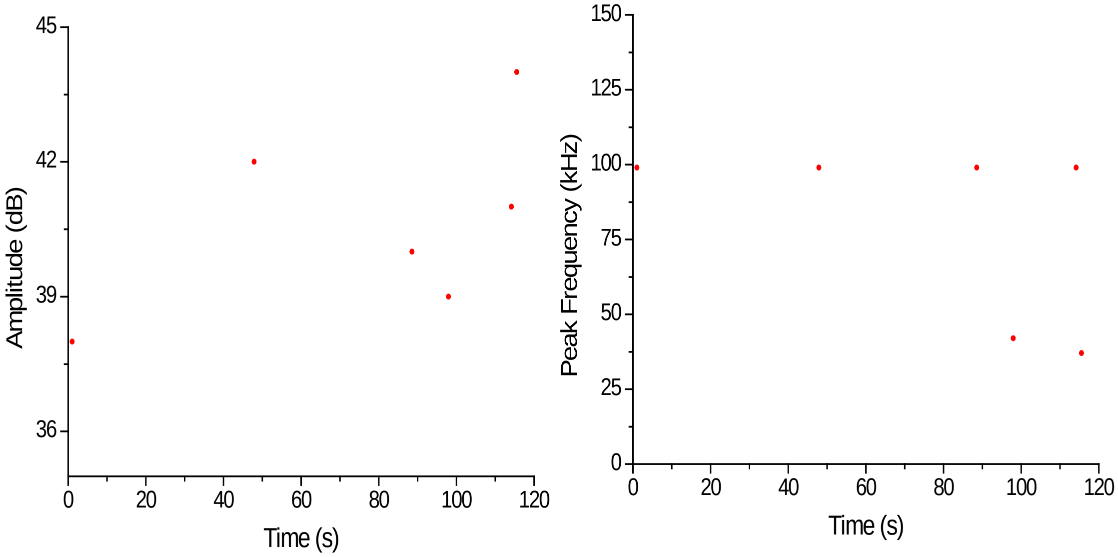

Figure 116: AE analysis during preload of specimen 1

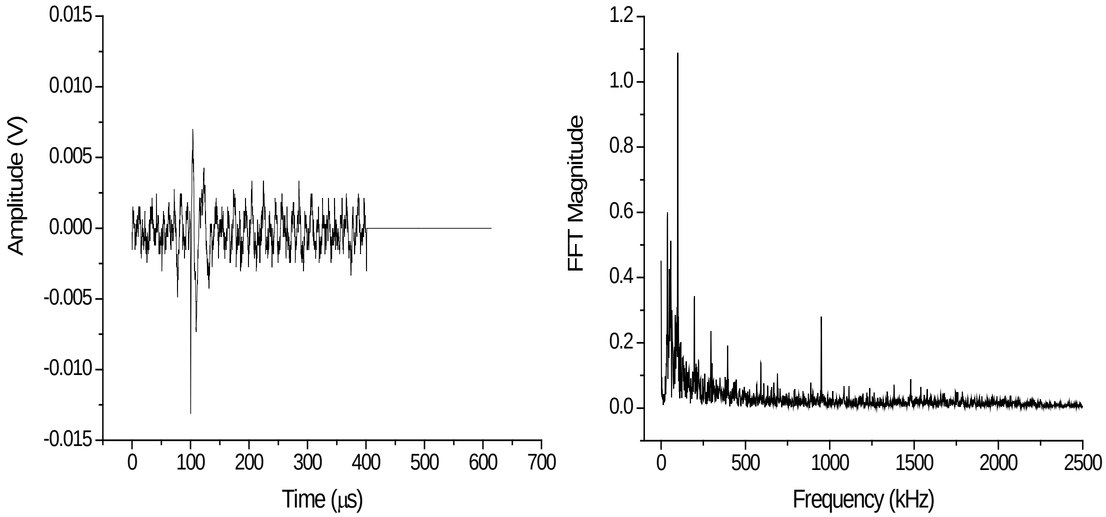

Figure 117: Representative AE waveform and its corresponding frequency spectrum

The AE amplitude correlated with the applied quasi-static load is shown in Figure 118. As the load approached 1200N, high amplitude (90dB) AE signals were recorded which were associated with audible debonding signs although no visual debonding was observed to the naked eye on the skin spar interface. Notably, AE activity is mostly seen only as the load approaches the peak load and thus providing a strong indication about the material deterioration and not secondary or spurious sources. The in-situ recorded peak frequency analysis revealed two distinct frequency spectrums as shown in Figure 118. A cluster of AE signals can be noted above 250kHz and around 100kHz. Additionally, the AE signal acquired at the end of the test (load relaxation) corresponded to a 100kHz signal.

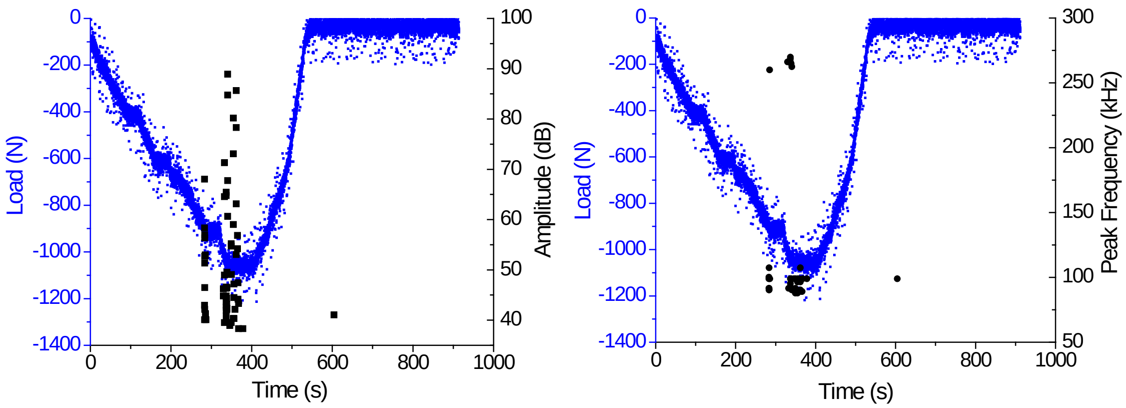

Figure 118: AE analysis from component 1

To gain further insight into the frequency behavior and characterize the wave signatures associated with the AE signals collected during the peak load, all the acquire waveforms were analyzed. The wave signatures corresponding to the high frequency (~220 - 280 kHz) and high amplitude AE hits are shown in Figure 119. It can be directly observed that AE signals consist of rather complex waveforms with a dual frequency behavior and long duration. In this context, previous research has shown that emissions from debonding are a combination of both fiber (high frequency) and matrix cracking (low frequency). Thus, it was beneficial to further analyze the frequency evolution of the waveform using a wavelet analysis. The wavelet analysis performed on the obtained waveform demonstrated that the dominant frequency corresponding to the first arrival was centered around 250kHz, while the later wave packets were associated with low frequency signals of ~100kHz. Hence, the high frequency and amplitude events recorded can be plausibly associated to the debonding process in the specimen. However, while the amplitude provides a good measure of the deterioration in the specimen, it greatly depends on the source-sensor distance. Conversely, the frequency of the signal provides a strong indication of the active damage mechanism in the material and is not directly influenced by the sensor-source location. Hence, it is beneficial to utilize, analyze and identify the signatures associated with debonding based on the frequency characteristics of the obtained waveforms.

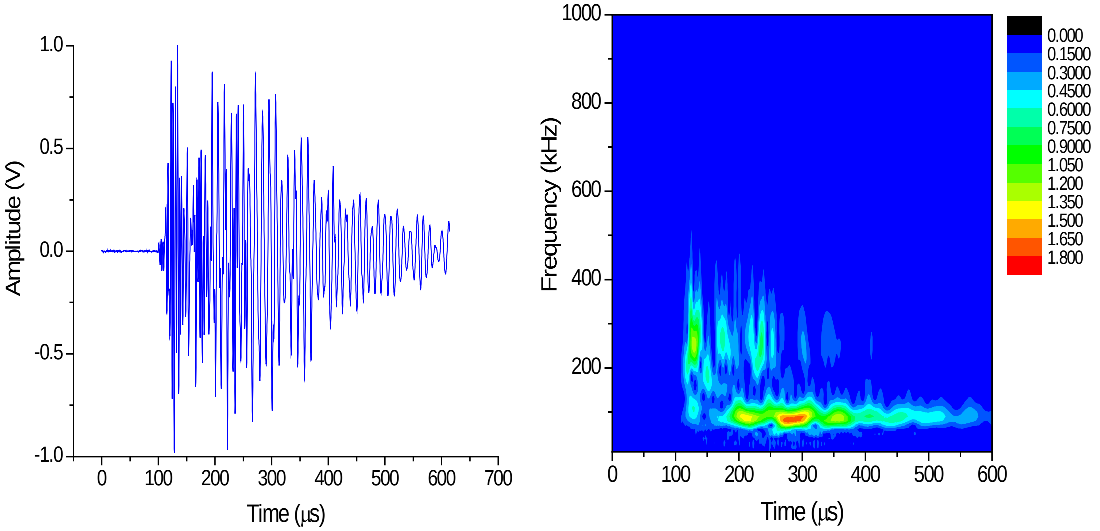

Figure 119: Representative AE waveform during quasi-static testing and its wavelet analysis

Due to this exhibition of dual frequency behavior, their partial powers were analyzed and are plotted in Figure 120. Among the four partial powers, it was observed that PP1 and PP2 were the most dominant throughout the test. Interestingly, the PP1 and PP2 exhibited opposite behavior. The signals that had high PP1 (200-400kHz) value were noted to have low PP2 (0-200kHz) value. This was also noted with the wavelet analysis shown on the acquired signals at the peak load. Since, it was difficult to accurately identify the signals associated with debonding based on peak frequency and partial power analysis, another parameter had to be identified that could be robustly associated with this phenomenon.

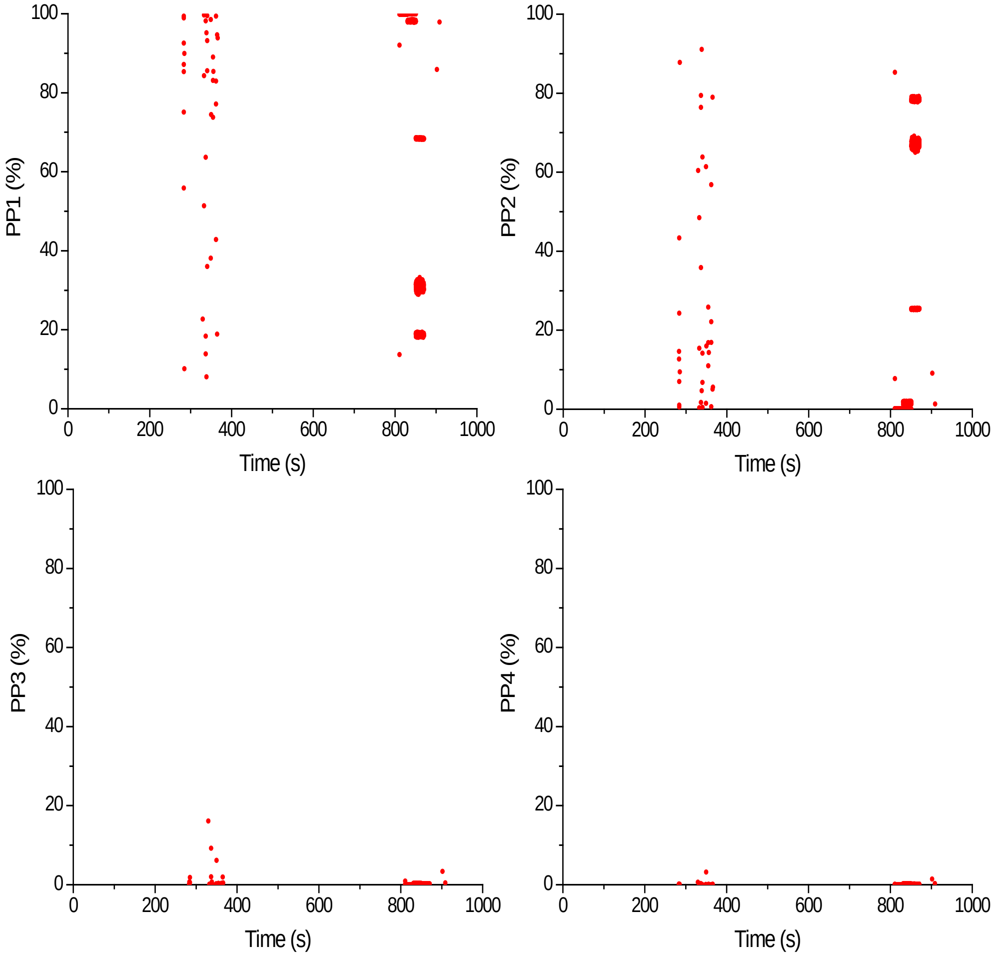

Figure 120: AE Partial Power Analysis

For this purpose, the wave signatures (such as the one shown in Figure 119) were extensively analyzed and it was noted that all their signatures exhibited this initial high frequency content and subsequently low frequency packet. The high frequency content quick attenuates in the anisotropic medium as it propagates. However, since this dual frequency behavior was consistent across all the signals, the frequency centroid of the waveforms were calculated and shown to be reliable in identifying these signatures. As it was noted earlier that the amplitude of these signals were high, the amplitude vs. duration

(Figure 121a) and subsequently the frequency centroid vs. duration (Figure 121b) were plotted.

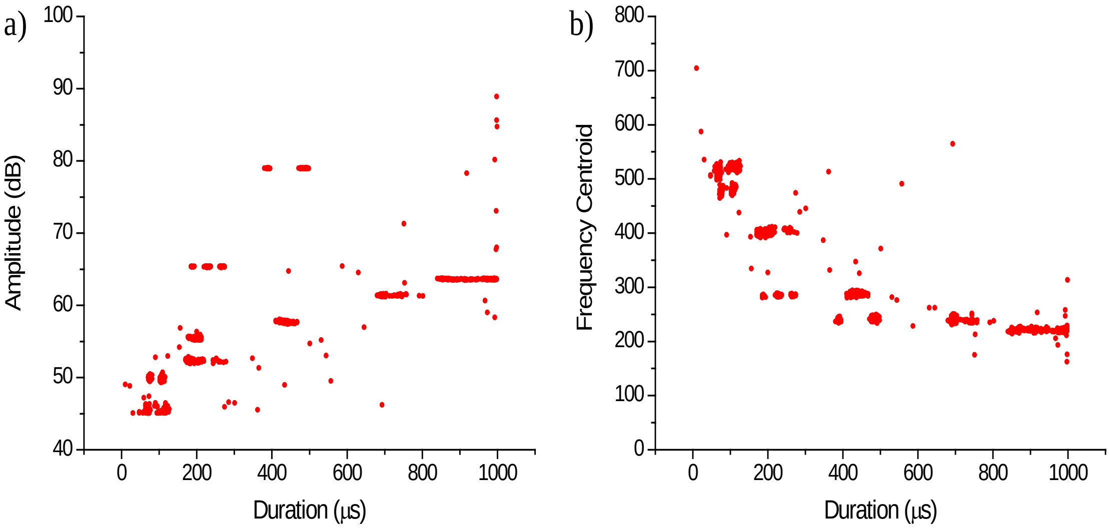

Figure 121: AE features vs. Duration (a) Amplitude (b) Frequency Centroid

Noticeably, a trend was identified with the relationship between the frequency centroid and duration. The signals that corresponded to high amplitude signals were noted to have long duration and low frequency centroid consistently. It be seen that the signals which corresponded to peak load were noted to have low frequency centroid value of 225kHz.. This formed the basis for the analysis of the AE signals acquired during the fatigue testing of these components.

6.3.3 AE RESULTS FROM FATIGUE TESTING OF THE CFRP COMPONENTS

Component 1 - No initial defect

The same CFRP component was then subjected to fatigue load profile with the limits described in Table 11. Although the CFRP component was subjected to several fatigue cycles and load limits, visual debonding was witnessed only upon the load limits of 470-

4700N (Figure 122). Visual debonding was noted at 410s and was associated with a sudden increase in amplitude at the peak load.

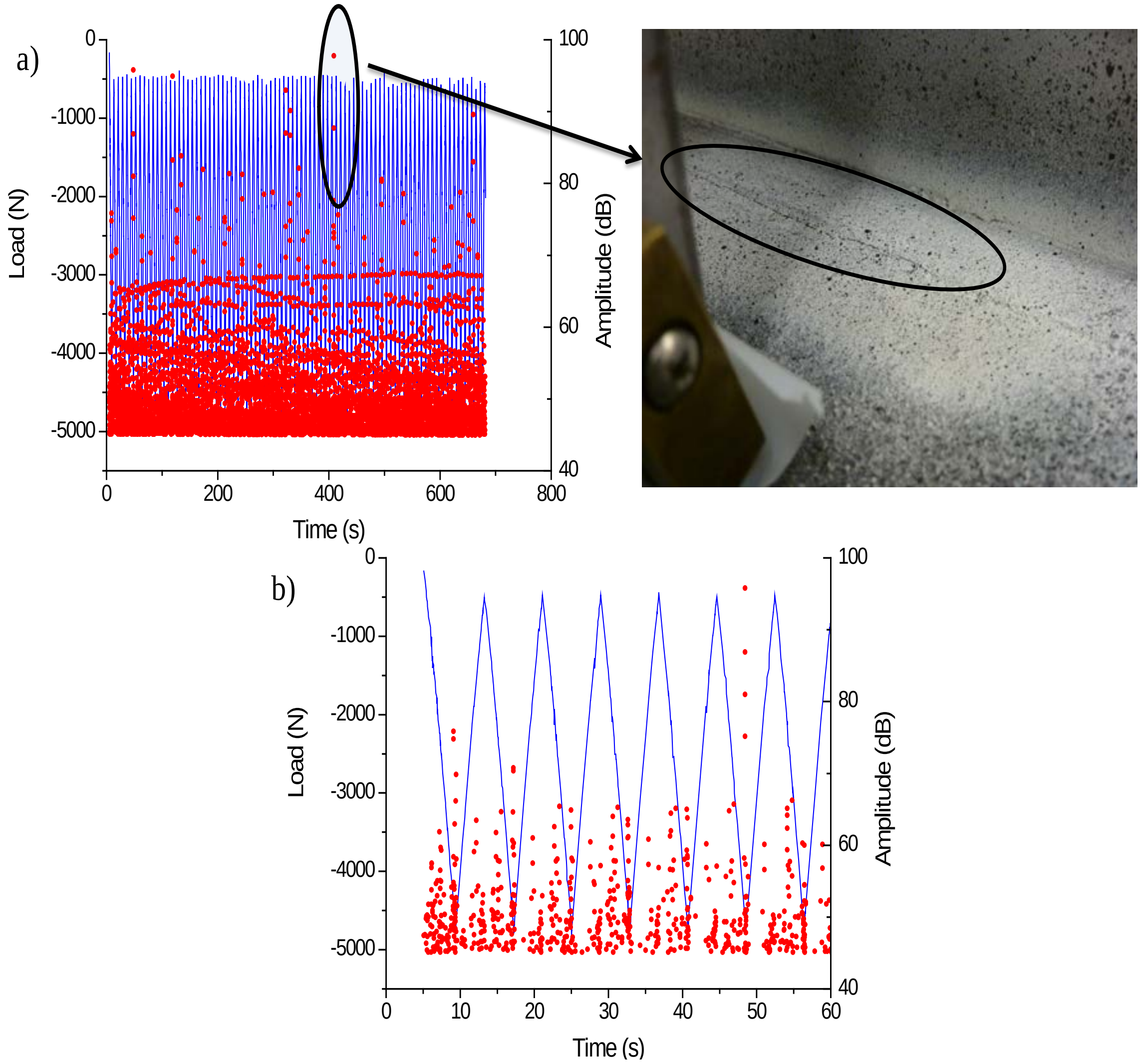

Figure 122: (a) AE Amplitude correlated with the applied fatigue load cycles that resulted in visual debonding (b) initial load cycles

The obtained amplitude during the initial load cycles is shown Figure 122b. Significant AE activity is noted during the early stages of the loading. It must be mentioned that audible debonding was noted during these initial stages and during lower load limits as well but no visual debonding was seen. In addition, during the initial cycles, relatively high amplitude AE signals was observed around the peak loads and more AE activity was observed during the loading portion of the cycle. The 2D location results which identified the region of debonding were further utilized to spatially filter the AE signals associated with debonding and representative AE waveforms obtained from this region are shown in Figure 123.

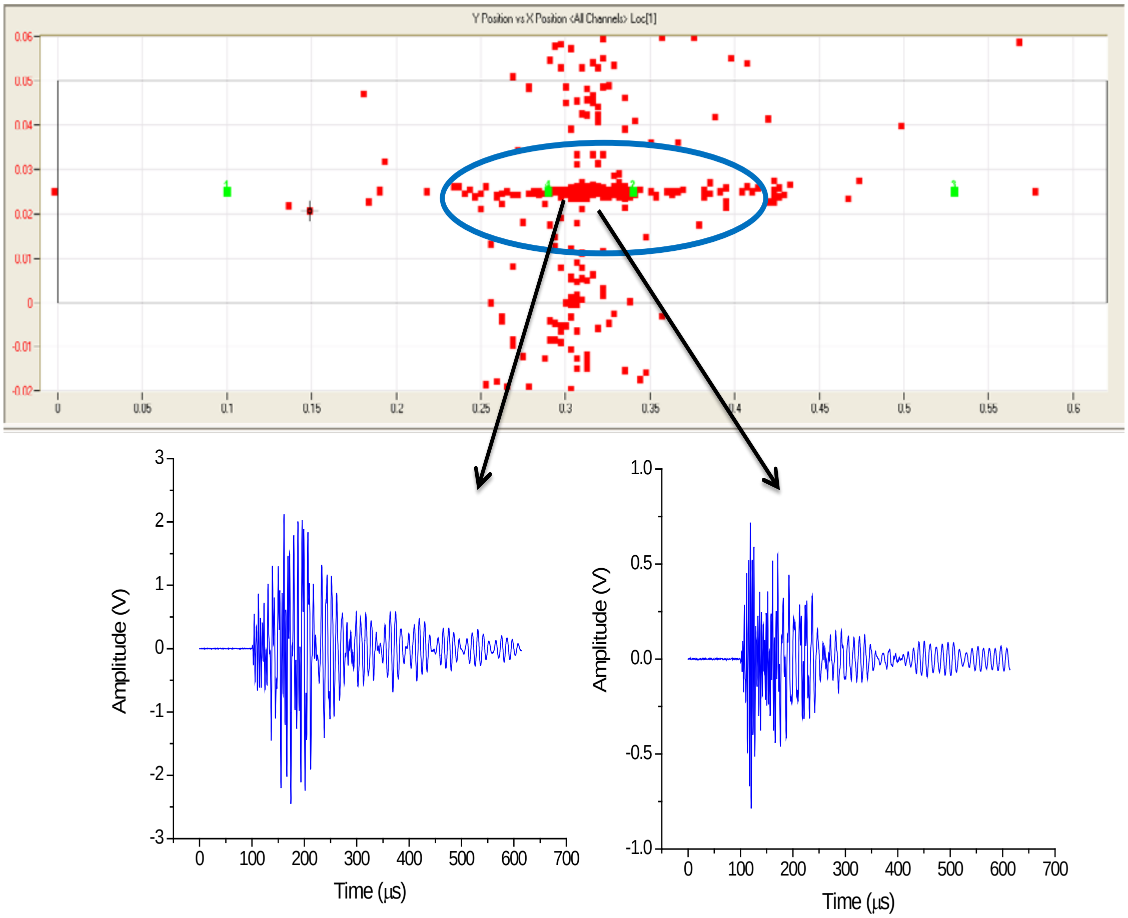

Figure 123: 2D location analysis and representative AE waveform corresponding to the region of debonding

The above waveforms corresponded to different stages in the fatigue cycles The waveform shown in Figure 124a were extracted towards the later fatigue cycles while the waveforms shown in Figure 124b were extracted from the initial fatigue cycles. Although the waveforms had different amplitude, their wave signature were seen to be similar.

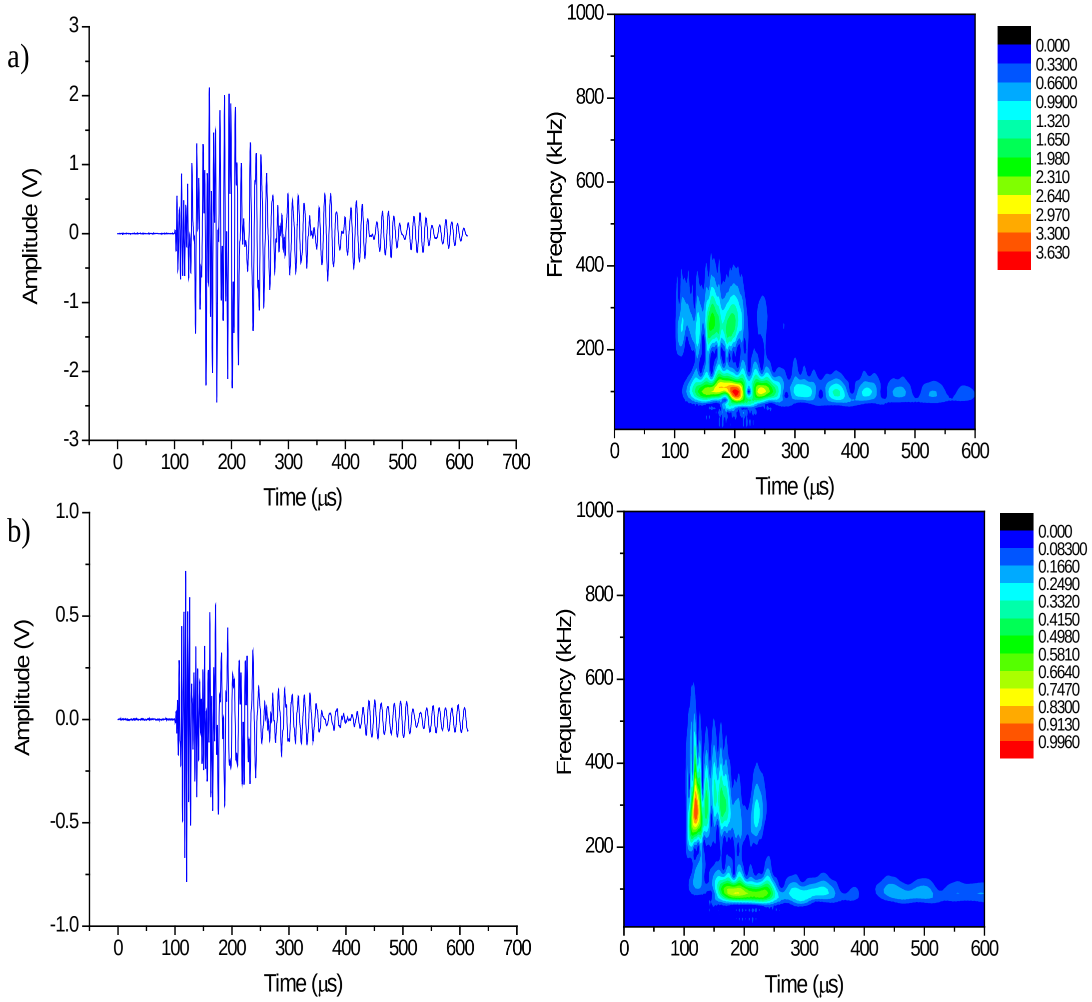

Figure 124: AE waveform and wavelet analysis obtained during (a) later fatigue cycles (b) initial fatigue cycles

Additionally, the obtained wave signature closely resembled the wave signature obtained during the quasi-static loading. The initial high frequency content was followed up with low frequency content as the wave propagated in the medium. Thus, it was clear that wave signatures associated with debonding produced a dual frequency characteristic. Consequently, the frequency centroid of the acquired waveform was calculated and is shown as a function of duration in Figure 125. It was observed that the signals that exhibited the dual frequency behavior and circled in the 2D analysis had long duration and relatively low frequency centroid. This trend was also identified previously with the quasi-static data where the signals that were collected near the peak load were associated with low frequency centroid and long duration. As a result, the frequency centroid were calculated for the lower and higher fatigue limit data , i.e., the frequency centroid was calculated for the fatigue load limit of 100-1000N, 200-2000N, 550-5500N and 600-6000N data sets.

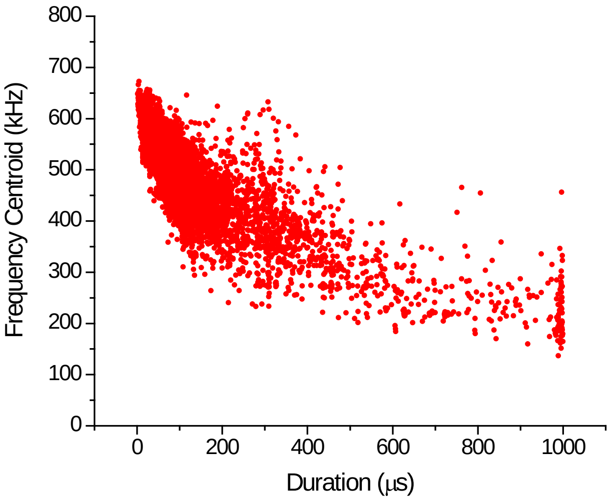

Figure 125: Frequency centroid vs. Duration (470-4700N)

The frequency centroid for the different applied fatigue loads is shown in Figure 126. It is observed that at lower fatigue load cycles, no major AE activity with low frequency centroid and long duration (boxed region) was observed. This is expected as the component was subjected to the max load of 1000N previously during the quasi-static load. Thus, the Kaiser effect postulates that no major AE activity would be detected unless the previous max load is surpassed provided there is no damage. However, as the load is increased (200-2000N), AE signals with long duration and low frequency centroid is seen to pick up. Subsequently, with increased loading, the AE data in the boxed region is seen to significantly increase. These signals were noted to exhibit the dual frequency signature shown previously and also correspond to location where debonding was identified. Thus, the relationship between frequency centroid and duration is noted to be sensitive to the debonding process and provides a qualitative estimate of the severity of debonding in the CFRP component.

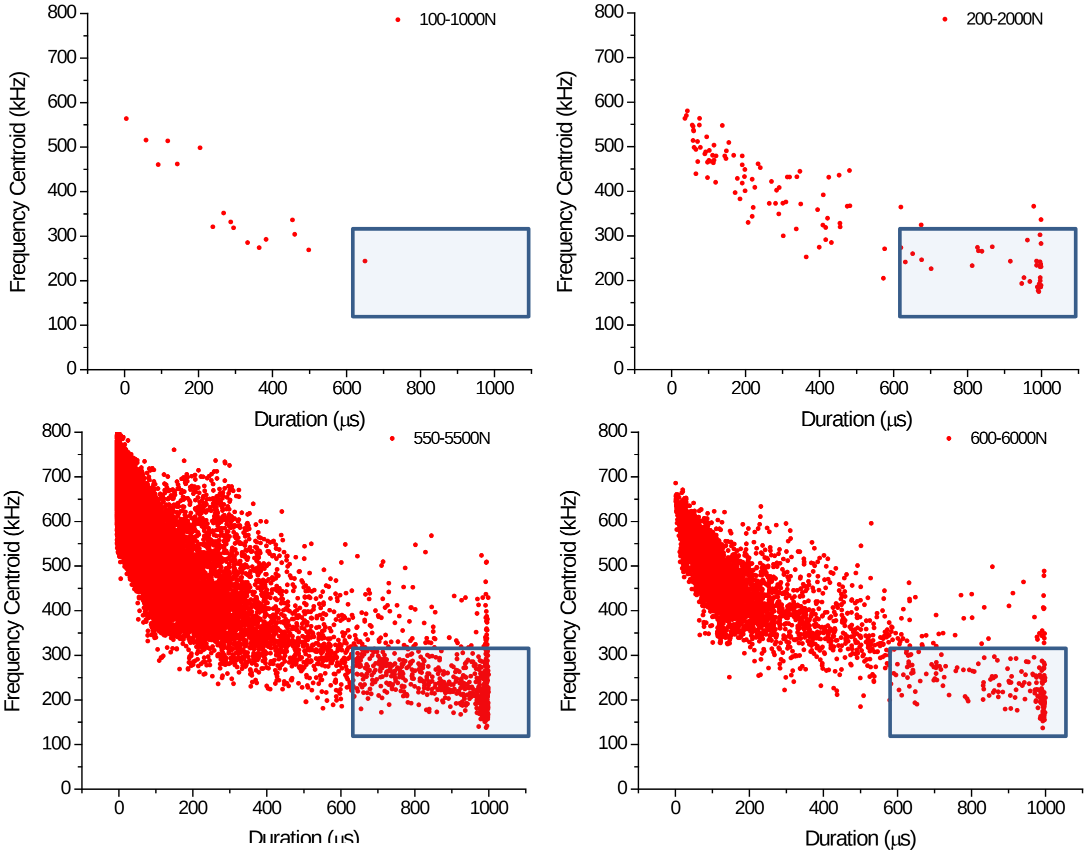

Figure 126: Frequency Centroid vs. Duration for different fatigue load levels

Component 2 - With initial defect

A second CFRP component was also tested that contained an initial defect size of 0.5mm x 0.5mm. This defect was manufactured by bonding a thin teflon strip along the spar as shown in Figure 127. The component was subjected to fatigue load levels as described in Table 12. It should be mentioned that the initial defected component was not subjected to the same number of cycles as the first component. Audible debonding was heard as the specimen was subjected between the loads of 300-3000N but visual debonding signs were seem only during the loads of 500-5000N.

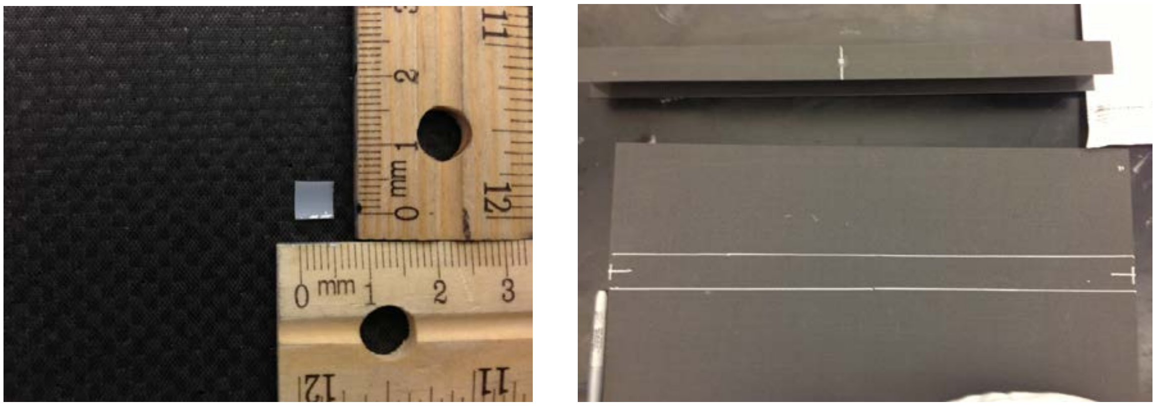

Figure 127: CFRP Component 2 ; Initial defect configuration

Table 12 : Fatigue Load Parameters for component 2

Load Range (N)	Number of applied cycles	Loading Rate (mm/min)
100-1000	50	100
200-2000	50	100
300-3000	50	100
400-4000	50	100
500-5000	100	100
520-5200	100	100
550-5500	100	100
600-6000	100	100
650-6500	100	100

Since the initial debond was created at the center of the skin spar rather than the edges, there could have been significant debonding at the center much earlier than visual debonding was noticed at the edges shown in Figure 128. The frequency centroid was calculated for the different loads and is shown in Figure 129.

Figure 128: CFRP Component 2 ; Visual debonding at 500-5000N

The same trend was observed with the initial defect component with signals associated with debonding exhibiting low frequency centroid and long duration. Thus, a reliable trend was identified across components that picked up signs of debonding at different loads. In fact, these trends demonstrated the capability of identifying signs of debonding before visual debonding was noted on the CFRP components.

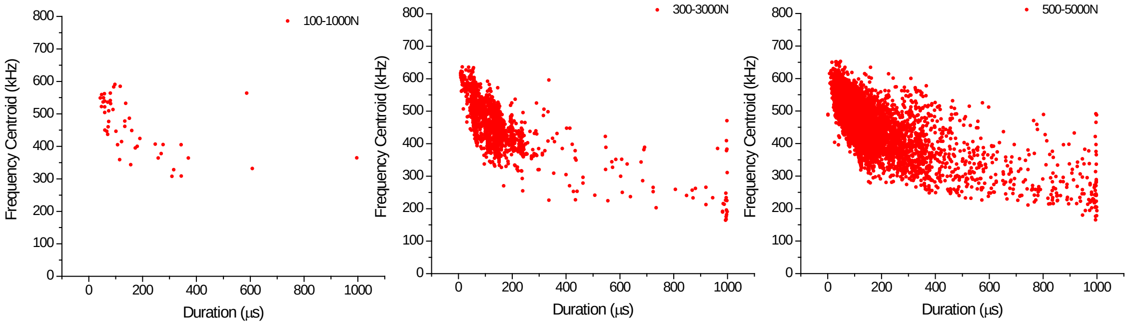

Figure 129: CFRP Component 2; Frequency Centroid vs. Duration for different fatigue load levels

6.3.4 PATTERN RECOGNITION ANALYSIS OF THE AE DATA

Based on these observed feature trends, a pattern recognition (PR) approach was attempted to enhance the robustness of damage detection process. Conventional AE analysis relies on the monitoring of a single or traditional set of features. Although this is sufficient for laboratory monitoring, often this approach has shown less sensitivity to field applications. A number of factors can be attributed to this including environmental variability, extraneous operational noise sources, larger structural dimensions etc. Consequently, it is advantageous to design a PR approach based on ensemble features descriptors to identify other characteristics of the AE signals for enhanced and robust damage detection

For this particular PR analysis, a novel feature descriptor called the Frequency Factor, was designed based on the relationship of the frequency centroid and duration. The frequency factor (FF) was defined using the formula shown below

$$Frequency\ Factor\ (FF) = \mathrm{sqrt}(\frac{\text{Frequency Centroid}}{\text{Duration}*1000}) \tag{8}$$

The frequency factor, PP1, PP3, peak frequency and frequency width 10% were used as input feature vectors for the PR analysis. The data set obtained from component 1 during the 470-4700N was utilized for the clustering data. The feature had a correlation factor less than 0.6 and were normalized in the range of 0-1. K means clustering methodology was utilized to classify the AE signals and the R and tou criteria was used to evaluate the validity of the classification process. The K-means clustering methodology revealed three major classes for the different data sets as shown in Figure 130a. It can be observed all the classes are activated at certain instances of the load. In particular, the class 0 and class 1 signals are noted to be active throughout every stage of loading. These two classes are observed to dominate during both the loading and unloading portion of the cycle. Conversely, the class 2 signals are not seen to be active throughout the loading profile as is observed in Figure 130b. It is noted that the class 2 signals are mostly active close to the peak load and at the minimum load. Unlike the other two classes, Class 2 signals are active during the loading portion of the cycle.

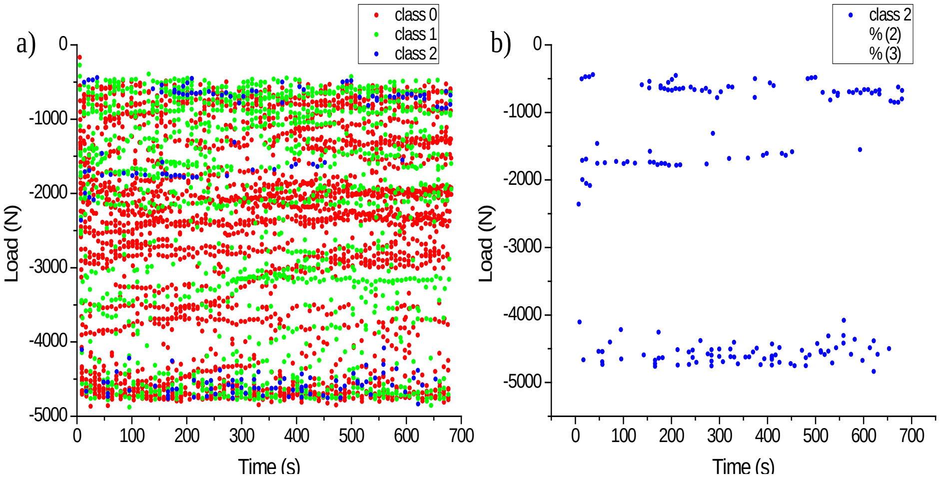

Figure 130: Patter Recognition analysis for CFRP Component 1 (a) Load activation of all classes (b) Load activation of only class 2

Previously, it was observed that debonding signals (identified using the 2D location analysis) were associated with low frequency centroid and long duration. Consequently, the relationship of frequency centroid and duration of the four classes were analyzed and shown in Figure 131a-b.

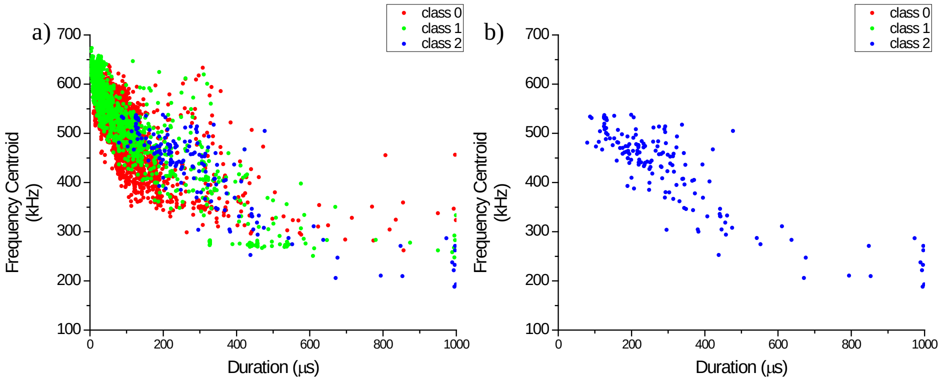

Figure 131: Patter Recognition analysis for CFRP Component 1 (a) frequency centroid vs. duration of all classes (b) frequency centroid vs. duration of only class 2

It was observed that class 0 and 1 signals were noted to have a higher frequency centroid than the class 2 signals. The class 2 signals were observed to have a wide frequency centroid range of 200-550kHz. It was previously mentioned that the debonding signals had a low frequency centroid and based on the 2D location results, it was associated to lie in the range of 200-300kHz. Thus, it was difficult to assess which class was associated with debonding and consequently the waveforms of each class were investigated. The representative waveform from each class is shown in Figure 132a, b and Figure 133 respectively.

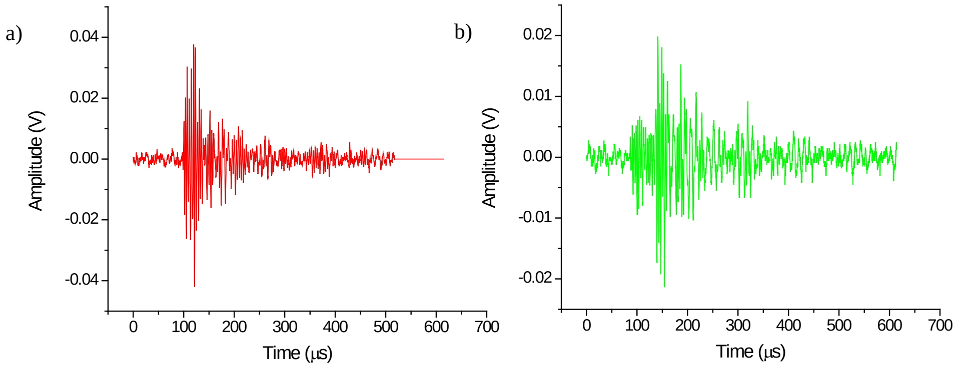

Figure 132: Representative AE waveform for (a) class 0 signals (b) class 1 signals

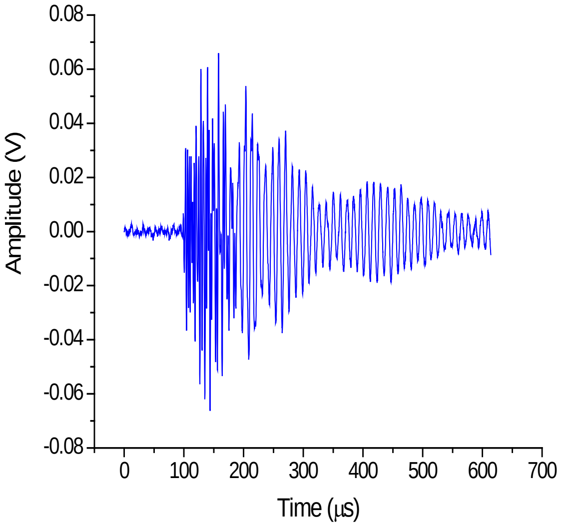

Figure 133: Representative AE waveform for class 2 signals

The class 2 waveforms showed great resemblance to the AE waveform associated with both the quasi-static and waveforms extracted from the region of debonding during the fatigue loading. Consequently, the relatively higher frequency centroid and lower duration of the class 2 signals were noted to be active mostly at the minimum load. Thus, the class 2 signals can be associated with both the debonding and plausibly closing of the bonding process.

6.3.5 EXPERIEMTNAL GUW RESULTS FROM FATIGUE TESTING OF THE CFRP COMPONENTS

The acquired GUW were then utilized to estimated the severity of debonding using the damage index (described in 6.3.1) . The damage index as a function of the applied load cycle for all the generated frequencies is shown in Figure 134 and Figure 135. A significant variation in the DI was observed across the entire spectrum (i.e. for each frequency) towards the end of the test when significant structural damage was finally visible. In particular, the higher frequencies were shown to increase after the 12th load cycle which correlated with visual debonding. Susbequently, it can be noted that the damage index increases with increased loading. This damage index provides the framework to size the debonding in CFRP skin spar components

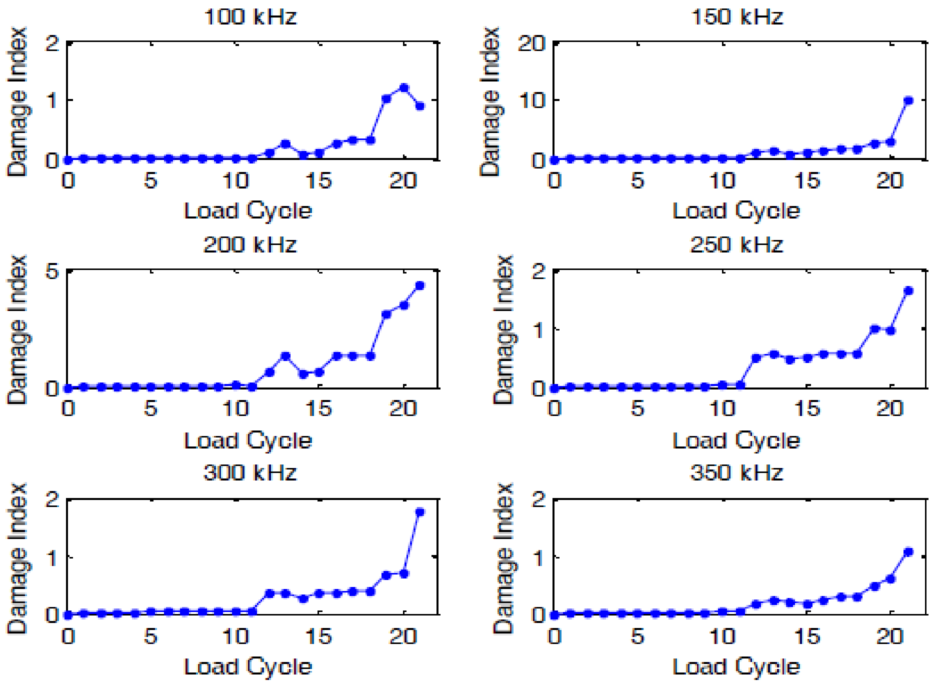

Figure 134: Experimental GUW Damage Index as function of the load cycles for the frequencies generated from 100-350kHz

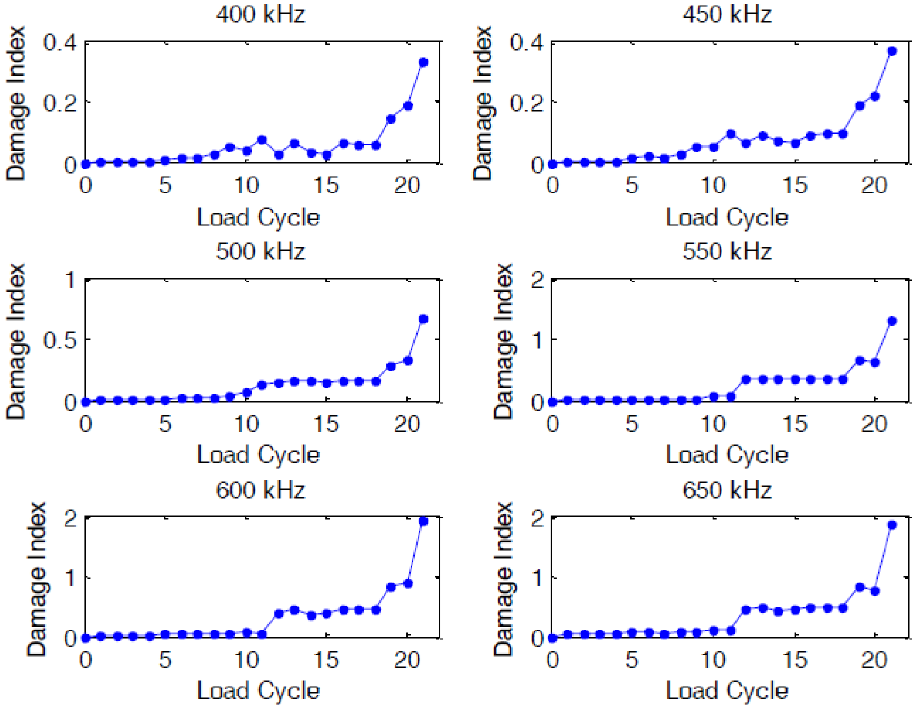

Figure 135: Experimental GUW Damage Index as function of the load cycles for the frequencies generated from 400-650kHz

CHAPTER 7: CIVIL SHM APPLICATIONS

7.1 INTRODUCTION

The potential and advantage of utilizing AE in conjunction with other complementary techniques through the NOAS approach was demonstrated to identify targeted failure mechanisms at the specimen and component level in the previous chapters. To validate its versatility of identifying progressive damage at the structural level for SHM applications, two different structural components were tested i) seven wire steel strands and ii) partially grouted concrete masonry walls (CMW). Seven wire strands in bridge cables and partially grouted concrete masonry wall for building designs constitute a major part of civil infrastructures and are critical to public existence. Thus, it is imperative to identify early signs of failure in these structures long before critical failure to ensure public safety.

The integrity of cables and strands is crucial in bridge systems such as pre-stressed reinforced concrete, post-tensioned and cable-stay bridges. Bridge cables are prone to corrosion, wind effects, hydrogen embrittlement, fatigue loading etc. that severely affect their load carrying capacity. Therefore, monitoring the structural integrity of cables is critical to ensure the overall safety of such bridges. Current periodic investigations, often based on visual inspection, can fail to properly observe cable degradation. For instance, the recent failure of a cable supporting the five years old Martin Olav Sabo pedestrian Bridge in Minneapolis has occurred only few months after a visual inspection had reported no significant signs of cable deterioration [169]. In other cases, visual inspection was capable to observe deterioration, such as severe corrosion of the steel cables. For example, a popular London bridge, the Hammersmith flyover, had been closed and only recently was fully reopened.

Similarly, in the case of partially grouted reinforced CMW that are extensively utilized for building designs in the US, it is essential to evaluate its behavior and characterize its performance under seismic loading conditions. Concrete structures form an integral part of the U.S. civil infrastructure due to their low-cost, ease of construction, versatility, and durability [170]. However, given their relatively high mass and potential lack of ductility, such structures, depending on their specific details, may be quite vulnerable to seismic loads [171]. For example, one particularly economical construction type termed partially-grouted reinforced masonry, is banned in high seismic regions due to concerns over poor performance. To establish the actual seismic vulnerability of this structural system and identify strategies to mitigate any deficiencies, a multi-scale research study was undertaken that includes numerous large-scale wall tests that are planned to culminate with two full-scale dynamic tests of complete building systems. A principal challenge associated with fully understanding the structural behavior lies in capturing the damage progression from its initiation within local regions (which are difficult to identify in an a priori manner) through its progression into a global failure mechanisms that governs its seismic response. Although several research efforts have focused on measuring the strength of concrete masonry walls (CMW) under seismic demands [172-174], limited work has been documented that tracks the propagation of damage and the transition from elastic to plastic behavior at the structural level. The failure mechanisms of reinforced concrete structures under in-plane cyclic loads can be classified into flexural and shear failure. Voon et al [171] studied the behavior of partially and fully grouted concrete masonry under cyclic loading and reported on the effect of shear reinforcement, axial compression load, type of grouting and aspect ratio on the masonry wall shear strength. The study further showed that walls with a small amount of distributed shear reinforcements suffered abrupt strength degradation. CMW that fail primarily in shear reveal rapid strength degradation and exhibit brittle behavior. Conversely, CMW that demonstrate primarily flexural failure exhibit a ductile behavior characterized by the tensile yielding of the vertical reinforcement and/or the compressive crushing of masonry at critical sections [175]. Consequently, identifying the initiation and development of these failure mechanisms and quantifying their effect on the overall structural behavior of the reinforced CMW under simulated seismic loads could i) assist engineering design, ii) optimize building codes in moderate and severe seismic prone regions and iii) assist the development of reliable Structural Health Monitoring (SHM) system capable of monitoring damage as well as predict the remaining capacity of CMW systems. Visual inspection and conventional monitoring techniques such as strain gauges, LVDTs, extensometers etc., can provide only partial insight into failure patterns of heterogeneous concrete structures. Furthermore, the initiation of local deterioration is hard to be tracked by means of point-to-point measurement techniques when the damage location is not known a priori. The uncertainties associated with periodic inspections could be mitigated by switching to condition based inspection. To address several of these challenges, efforts that use advanced non-destructive testing (NDT) techniques to monitor the damage behavior of reinforced CMW have been reported [176]. In particular, AE [177] and DIC [178] have shown tremendous potential in detecting the deterioration in concrete structures.

7.2 EXPERIMENTAL SETUP

7.2.1 IDENTIFICATION OF CABLE BREAKAGE IN SEVEN-WIRE STEEL STRANDS

The seven-wire steel strand had a nominal diameter of 15.24 mm and a gauge length of 1524mm, and it was made of high grade 270 steel with a Young's modulus of 195 GPa. The strand was loaded up to 70% of its nominal ultimate tensile strength (UTS) using a load frame under displacement control, while simultaneously recording AE, GUW and DIC data (Figure 136a). Load-unload cycles were imposed at a rate of 0.02 mm/s; and the load frame was programmed for load holds at specific levels to facilitate the triggering of GUW, as shown in Figure 136b. Pristine and notched specimens (Figure 136c) with depths of 2mm (small notch) and 4.6mm (large notch) respectively were machined in the six peripheral wires to simulate corrosion at the center of the strand. The stress-strain behavior of the pristine strand, where strains were computed by averaging full field DIC strain data was linear in the load range tested, as seen in Figure 136d. The large notch ultimately resulted in complete fracture before reaching the 70% UTS.

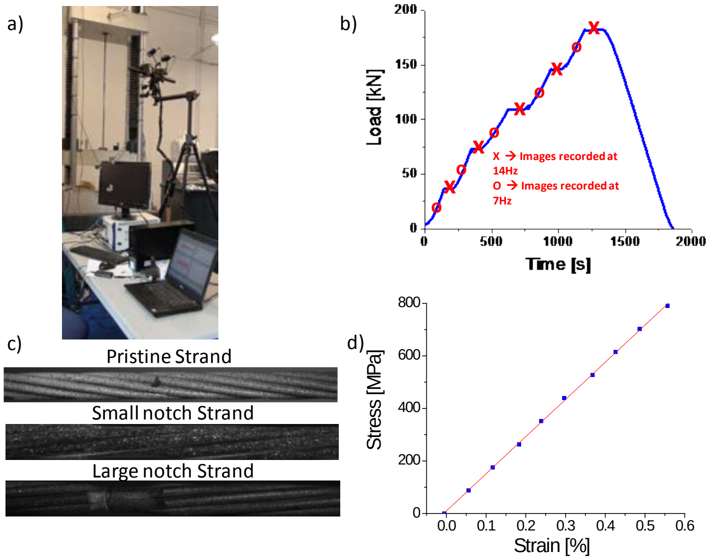

Figure 136: Seven-wire strand (a) Test setup Schematic of CFRP skin spar components

A National Instrument PXI (NI PXIe-1062Q) unit using LabVIEW was employed to trigger and record GUW. Five cycle tone-bursts centered in the range of 300kHz-500kHz with a step frequency of 50kHz were generated using a function generator (Fgen) with a sampling rate of 10MHz. Waves were generated with a Pico transducer bonded on the top of the center core wire and received at the opposite end of the core wire using another Pico transducer. A threshold of 50mV was used and the received signals were pre-amplified with a uniform gain of 40 dB. An input peak to peak voltage of 20V was supplied in to the system and the received signals were averaged 50 times to minimize the effect of noise on the recorded signal. The signal length used was equal to 10,000 points.

Simultaneously, the 4-channel AEWin DiSP system with two piezoelectric transducers (Pico) and preamplifiers with a uniform gain of 40dB was used. The piezoelectric transducers had an operating frequency range of 200-750 kHz with a peak frequency at 500kHz. The received signals were amplified using 2/4/6-AST pre-amplifiers, while a threshold of 50dB was used. This threshold value minimized the recording of unwanted noise, such as mechanical vibrations introduced by the testing machine. The recorded signals were band pass filtered in the frequency range of 100kHz-2MHz and the pick definition time, hit definition time an hit lockout time settings were 300, 600 and 1000 microseconds, respectively. The Pico sensors were placed on the top and bottom of the same peripheral wire to allow linear location during testing. The wave speed in the material was estimated in accordance with ASTM E976 and pencil-lead break tests were carried out to calibrate the system.

The DIC images were captured through the 5M stereo cameras. Tables supplied by the manufacturer and a calibration block was used to sharply focus the 50mm lenses to the FOV, as well as to determine specific testing parameters including: (i) 175x150 mm field of view (FOV), (ii) 1150mm working distance from the sample to the cameras, and (iii) 25 degree camera angle. A random speckle pattern was placed on the surface by the spray paint method and a few pretest images of the sample were taken to determine the system's sensitivity. An exposure time of 44ms was used to maximize the intensity of entering light. For the given test, digital images were captured between and at predetermined load levels (marked in Figure 136b) at sampling rates of 7 (point O) and 14 (point X) frames per second respectively.

7.2.2 IDENTIFICATION OF PROGRESSIVE DAMAGE IN PARTICIALLY GROUTED REINFORCED CONCRETE MASONRY WALLS

A specimen representative of three partially grouted reinforced CMW of 4m x 3.8m x 0.2m in size and composed of concrete units attached together using Portland cement is shown in Figure 137a along with the DIC (Figure 137b) and AE setups (Figure 137c).

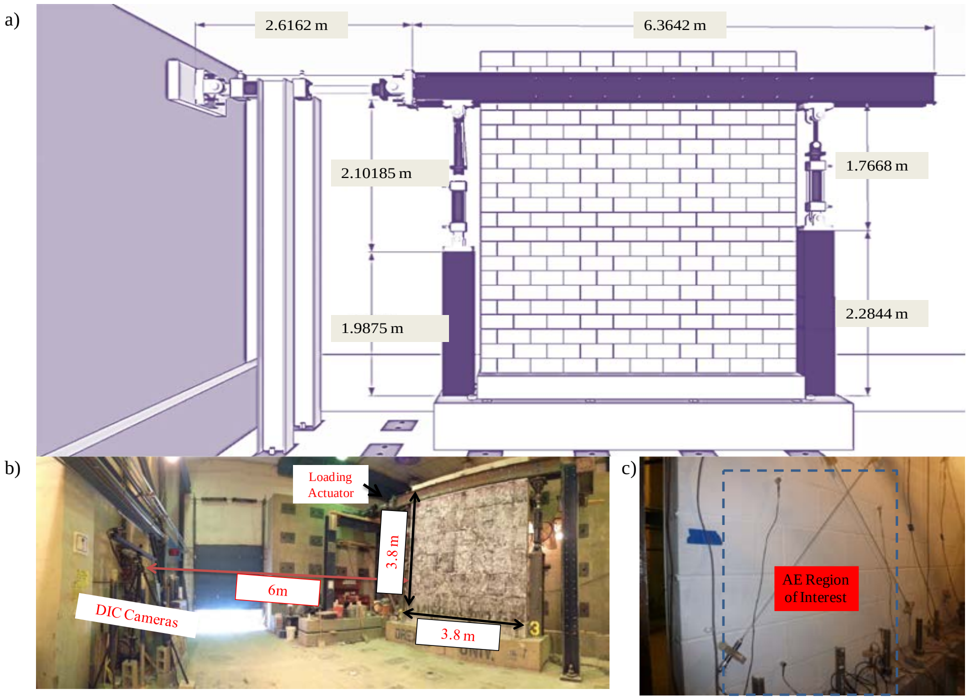

Figure 137. (a) Partially grouted CMW (b) DIC setup at the front surface of the wall (c) Placement of AE sensors at the back of the wall

The DIC cameras were mounted on a custom-made supporting bar and were positioned 6m away from the tested walls. The two camera lenses were separated by a distance of 1.92m. The cameras were calibrated for a field of view (FOV) of 4m x 4m using a dedicated calibration cross. The noise level for strain measurements in this work were consistently estimated to be approximately 100μm/m (με). An exposure of 200ms was utilized according to the available ambient lighting conditions. A random speckle pattern was applied on the front surface of the wall using spray paint and commercially available perforated sheets. For strain measurements a facet size of 35 pixels and step of 17 pixels were used. Throughout the tests, images were recorded with a sampling rate of 1 frame/second. The four channel AEWin DiSP system with four resonant sensors (R-15a) were placed at the bottom right corner on the back surface of the wall (Figure 137c). The four sensors were attached to the wall using hot melt glue and the signals were pre-amplified with a uniform gain of 40dB. Further, the signals were band pass filtered in the frequency range of 20-2000 kHz. The length of the recorded signal was defined to be 6k and a sampling rate of 5 MHz was used. A threshold of 42dB was utilized to eliminate the recording of background and operational noise. Pencil lead break tests were performed to calibrate the sensitivity of the sensors in accordance with ASTM E976. It was noted during the calibration process that the attenuation in the wall changed along different directions of the wall due to its reinforcement and presence of grout. Parametric inputs such as load and displacement were continuously fed in to the AE and correlated with AE features in real time.

The three CMW differed in the quantity and distribution of their horizontal and shear reinforcements (Figure 138). The first wall (hereafter referred to as W1) contained vertical and horizontal steel reinforcements (Figure 138a). The center to center separation of the horizontal and vertical reinforcements was 1.83m. The single type #6 rebar used in W1 was replaced by two type #4 rebars in the second and third walls (hereafter referred to as W2 and W3 respectively). In addition to the reinforcements contained in W2 (Figure 138b), the third wall (Figure 138c) also contained horizontal joint reinforcements (3 mm in diameter) to improve the overall capacity. The specifications of the reinforcements used in the CMW are presented in Table 13. Only the concrete units that contained reinforcements were grouted. The reinforced CMW were fixed at the bottom and tied to the reinforced concrete foundation using tiedowns. Walls 1, 2 and 3 were subjected to cyclic lateral displacements at the top (Figure 138) using a horizontally mounted hydraulic actuator. Each load cycle was repeated once. The wall was bolted to a loading horizontal beam using struts to prevent the out of plane movement during the test and to impose a uniform compressive axial load through two vertical actuators.

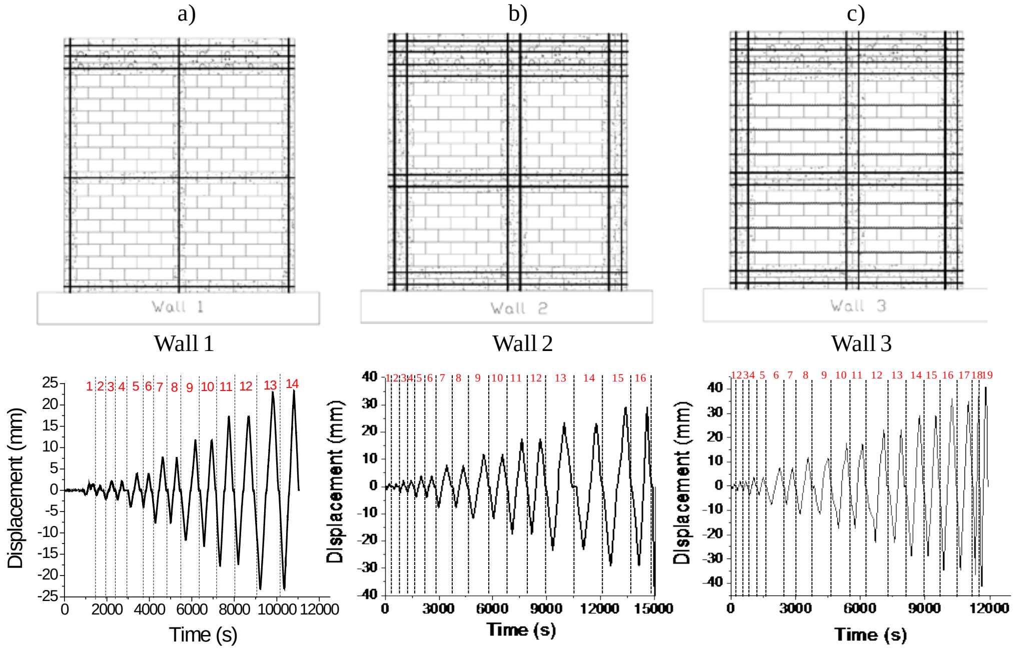

Figure 138. Reinforcement distribution and applied lateral displacement loading time histories for the different CMW

TABLE 13 : *Partially Grouted CMW Specifications*

Number	H_m	L_m	Width	Reinforcement		Reinforcement. spacing mm (in.)	Location of the inflection point	Axial stress MPa (psi)
	mm (in.)	mm (in.)	mm (in.)	Vertical	Horizontal			
1	3,860 (152)	3,860 (152)	200 (8)	No. 6	No. 6	1,829 (72)	Top	0.14 (20)
2 and 3				2 No. 4	2 No. 4			

7.3. RESULTS AND DISCUSSION

7.3.1 IDENTIFICATION OF CABLE BREAKAGE IN SEVEN-WIRE STEEL STRANDS

No wire breakages were observed for the pristine and small notch samples that exhibited linear behavior (Figure 136d). The first wire failure occurred for the strand with a large notch (Figure 139a) at 350 MPa; the load suddenly dropped at that point and then increased again until subsequent wire breakages occurred at load levels lower than 350 MPa, as expected by the occurred reduction in the cross-sectional area after the first wire break. In Figure 139b, the imposed staircase loading pattern is noted as a function of the stages (stages refers to the number of acquired images), while computed full field strain data are shown in Figure 139c. After the first breakage in the large notch sample, the DIC cameras were unable to measure the full field strains as the applied pattern was lost.

The three wire ruptures happened at distinct time instances (*460s*, *975s* and *3165s*) were accompanied by distinct increases in AE amplitude as shown in Figure 140a. The first, second and final breakage also correlated well with sharp increases in the cumulative AE absolute energy plotted in Figure 140b. Interestingly, AE waveforms associated with wire breaks were found to have low peak frequencies in the range of 55-100kHz (circled in Figure 140c) which is in agreement with Casey [179]. Relatively low amplitude AE hits prior to the first breakage, were also recorded, which can be attributed to plastic deformation at the notch also confirmed by the strain accumulation recorded by the DIC system (Figure 139c). Furthermore, Fig. 3d shows that signals with high energy also have relatively smaller number of counts, which agrees with the sudden release of energy associated with wire breaks.

Linear location algorithms were implemented to determine the location of wire breaks along the strand and the results are shown in Figure 141. Such algorithms can be also used to filter out signals originating from other sources including slipping at the grips. In Figure 141, the horizontal axis corresponds to the strand's longitudinal direction; sensor locations are highlighted in green. The majority of wire break events are seen to originate from the center of the strand exactly at the notch location.

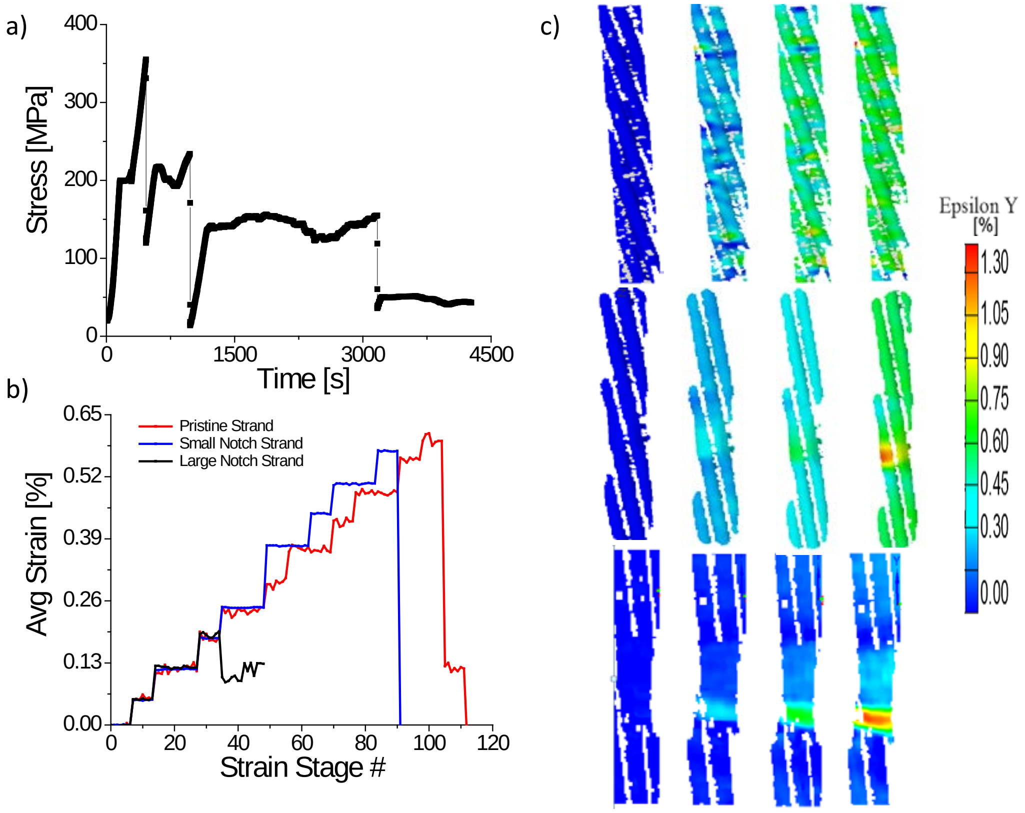

Figure 139 (a) Stress profile for the Large notch strand; (b) associated average strain measured by the DIC; (c) strain visualizations for pristine (top), small notch (center) and large notch strand (bottom)

Additionally, significant AE activity can be seen at the ends of the strand due to slipping that originated at the grips especially after load drops and subsequent reloading. Also, Figure 141 includes as insets typical waveforms of the AE signals and their corresponding frequency content that belong to both wire breaks and slipping. Clearly, wire related events have dominant frequencies less than 100 kHz compared to ~150 kHz for slippage signals. However, AE waveforms from the wire break location seem to have much higher amplitude (>5V) in comparison to the smaller amplitude emissions from signals originating from the grip section. A major challenge associated with conventional AE analyses in SHM applications is their inability to reliably identify features which are sensitive in a robust way to identify the AE sources in the material/structure due to noise, challenging operating conditions, simultaneous failure mechanism activation, etc. These challenges can be mitigated significantly through developed pattern recognition techniques [180-182]

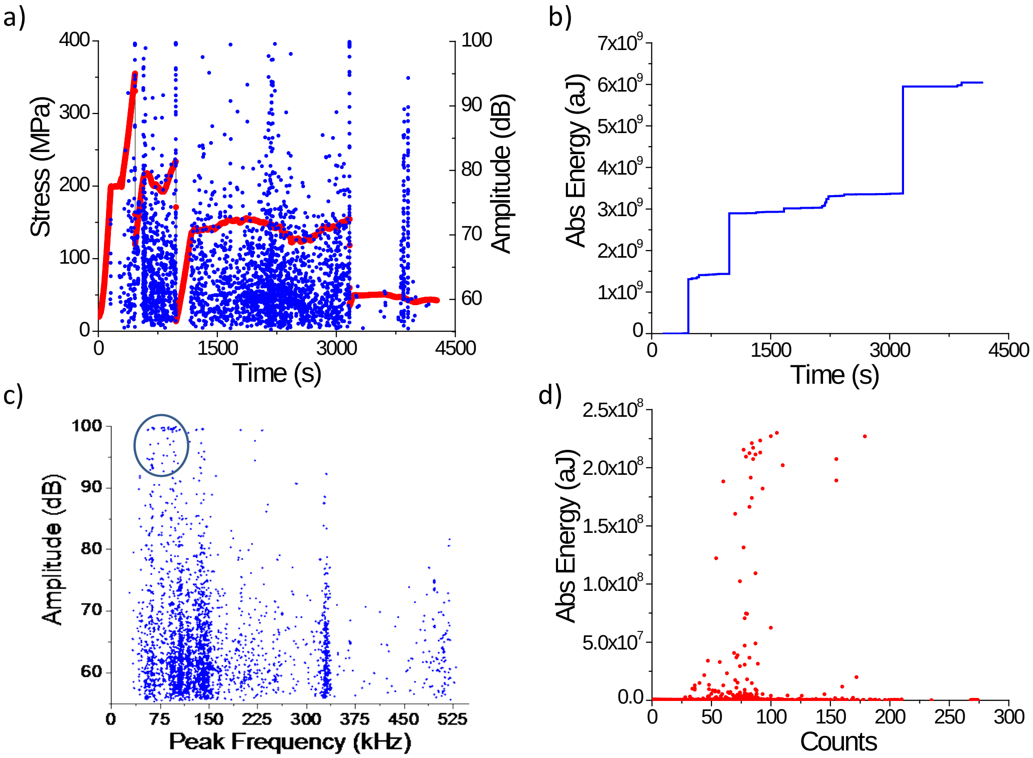

Figure 140 (a) Stress profile correlated with AE amplitude (b) AE Amplitude vs. Peak Frequency Absolute Energy (c) vs. time (d) vs. counts

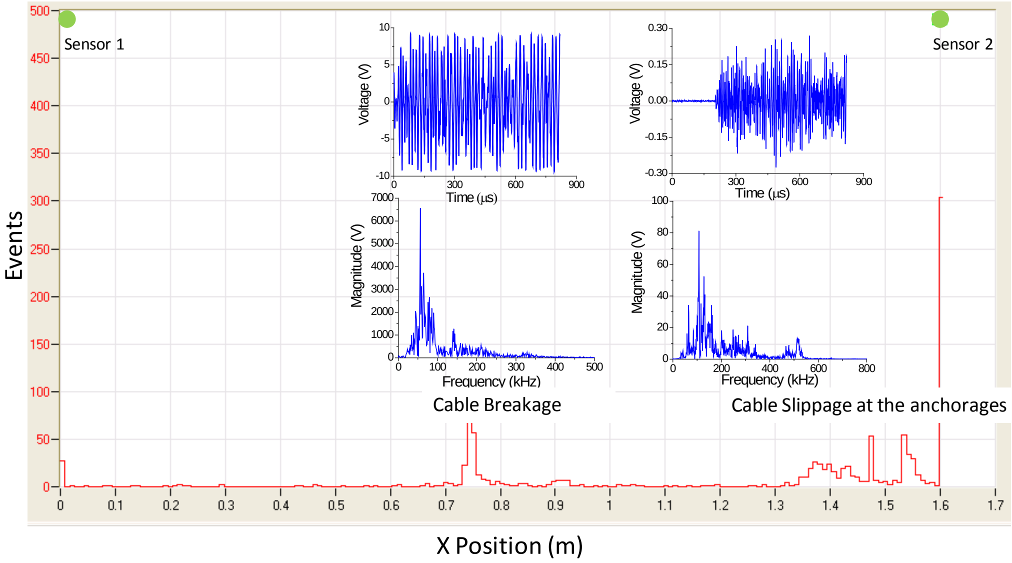

Figure 141: Linear location of AE events. Inset shows typical waveforms for each of the two groups of AE signals and their corresponding frequency content.

The previously mentioned unsupervised SPR algorithms [183] were implemented to further investigate the recorded AE activity and pertinent results are given in Figure 142. Four AE features extracted from the total AE population were used for clustering including peak frequency, absolute energy, amplitude and root mean square (RMS). The correlation index was computed for these features based on the Complete Link Hierarchical Clustering Algorithm based on the maximum distance criterion between two points [184]. The correlation index was kept below 0.5 and the R and τ criteria were used to determine the compactness of the resulting clusters [181]. Several unsupervised SPR algorithms were used to classify and identify the dominant damage mechanisms in the seven-wire strand tests, such as: (1) Max-Min Distance - Cluster Seeking, (2) Max-Min Distance - Forgy, (3) Max-Min Distance - Isodata, (4) K-means (5) Forgy and (6) Max-Min Distance. Two clusters are shown in red and blue in Figure 142; Cluster 2 (blue) is seen throughout the duration of the test, however, Cluster 1 (red) is seen to increase at distinct time intervals that correspond to the earlier reported time instances when wire breaks were recorded. Consequently, Cluster 1 can be associated with great confidence to wire breaks. It is interesting to note that the amplitude and absolute energy associated with Cluster 1 are considerably higher than Cluster 2, which corresponds to the AE events previously attributed to slippage of the strand in the grips section.

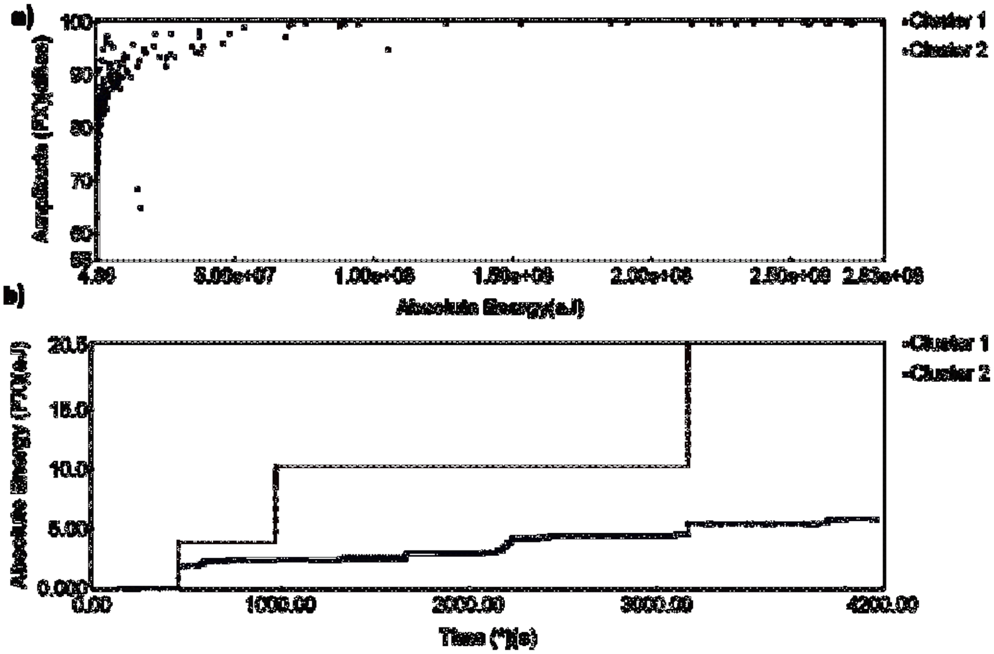

Figure 142: Pattern Recognition Analysis a) Amplitude-Absolute Energy plot b) Energy time activity

7.3.2 CROSS-VALIDATION OF AE INDICATIONS WITH GUW SIGNALS

As noted in this section, the selection of robust ultrasonic features sensitive to both stress level and corrosion/defects in twisted seven wire strands can be extremely challenging. For this and other reasons, the use of GUW can benefit from the complementary use of AE and DIC measurements, as described next. GUW were excited at each load holds. For each step, frequency sweeps were performed generating tone bursts that consisted of 5 cycle sine waves with Hanning window, centered at frequencies between 300 and 500 kHz using a frequency step of 50kHz . Baseline waveforms were initially recorded for the unloaded strands. The first feature considered was the relative change of GUW velocities. Wave speeds in the unloaded strands were used to normalize the wave speeds measured in the progressively loaded strands. The results shown in the following refer to the waveforms centered at 350 kHz. It should be noted that the wave propagation along a loaded strand is affected by the contact/friction between the individual wires causing inter-wire leakage [185] and by the energy leakage at the strand anchorages [37]. Few papers have attempted to rigorously predict wave propagation properties in strands using semi-analytical techniques [186] or the Finite Element Method [38], however the theoretical knowledge of GUW properties in loaded and unloaded strands remains a challenging topic. Many modes are generally present in the waveguide in the frequency range considered (<500kHz) and the narrowband excitation employed can only partially mitigate the complexity of the received waveforms that represent the superposition of several dispersive modes. Wave speed measurements are affected by these complexities and attention must be paid when estimating the GUW velocities. For this analysis, the time of arrival was calculated using the cross correlation technique which computed the delay of the received waveform with respect to the generated waveform. The cross-correlation technique was here applied to the whole received signal. Typical generated and received waveforms are shown in Figure 143. The estimated time of arrival was calculated using the equation shown below in order to calculate the relative change of speed as a function of the stress.

$$\frac{\Delta V}{V_0} = \varepsilon - \frac{l_0}{l_{s0}} \frac{\Delta t}{t_0} \tag{9}$$

where ε is the average strain, l_0 is the initial length, l_{s0} is the initial stressed length, Δt is the time difference between the received signal at stressed and unstressed states and t_o is the time of arrival at the unstressed state. These measurements were repeated for the various strand stress levels obtaining the Acoustoelastic curves [115, 187] shown in Figure 144a. Three curves were obtained for the pristine and the damaged strands with small and large notches. For the pristine strand, the wave speed decreased almost linearly with the stress applied, similarly to what previously shown in [187]. The decreasing trend was also observed for the strand with a small notch. However, the Acoustoelastic curve for the strand with a large notch (which failed at a relatively small load), deviated significantly from the other curves in Figure 144. In fact, the wave velocity in the large notch strand increased after the initial stress was applied.

The second feature extracted from the GUW waveform signals is the root mean square (RMS). It should be noted that while each recorded signal consisted of 10,000 points, only the first arrival (corresponding to the fastest longitudinal guided mode) was considered to calculate the RMS. The selected windows used to isolate the first arrival are shown in Figure 143. The RMS feature was correlated to both stress level and notch size. Figure 144b shows that the RMS has a maximum for the unloaded pristine strand, since in this case the wave generated in the central wire can travel with little or no energy leakage towards the peripheral wires and in the gripped sections [37]. Hence for the unloaded strands small contact stresses are expected between the seven wires, while each one should behave as an independent waveguide [39]. Therefore, dispersion properties such as phase or group velocities versus frequency should be close to those of the isolated central wire that was excited. When the strands are loaded, the contact stresses between the wires increase, "locking" the seven wires together. As a result, the waveguide in this case is a combination of all seven wires. Consequently, a wave generated in the central wire will leak part of its energy in the entire strand. Based on this analysis, the signals recorded in the unloaded strand (Load = 0kN) are substantially different from the signals recorded in loaded strands (Load = 63.6kN, 145.9kN) causing a significant drop of the RMS when the strand is loaded (Figure 144b); subsequently, a progressive load increase corresponds to a monotonic increase of the RMS. In this case, both the pristine and notched strands show similar trends. However, the RMS value for the large notch sample is the smallest due to the large scattering of the wave at the deep defect.

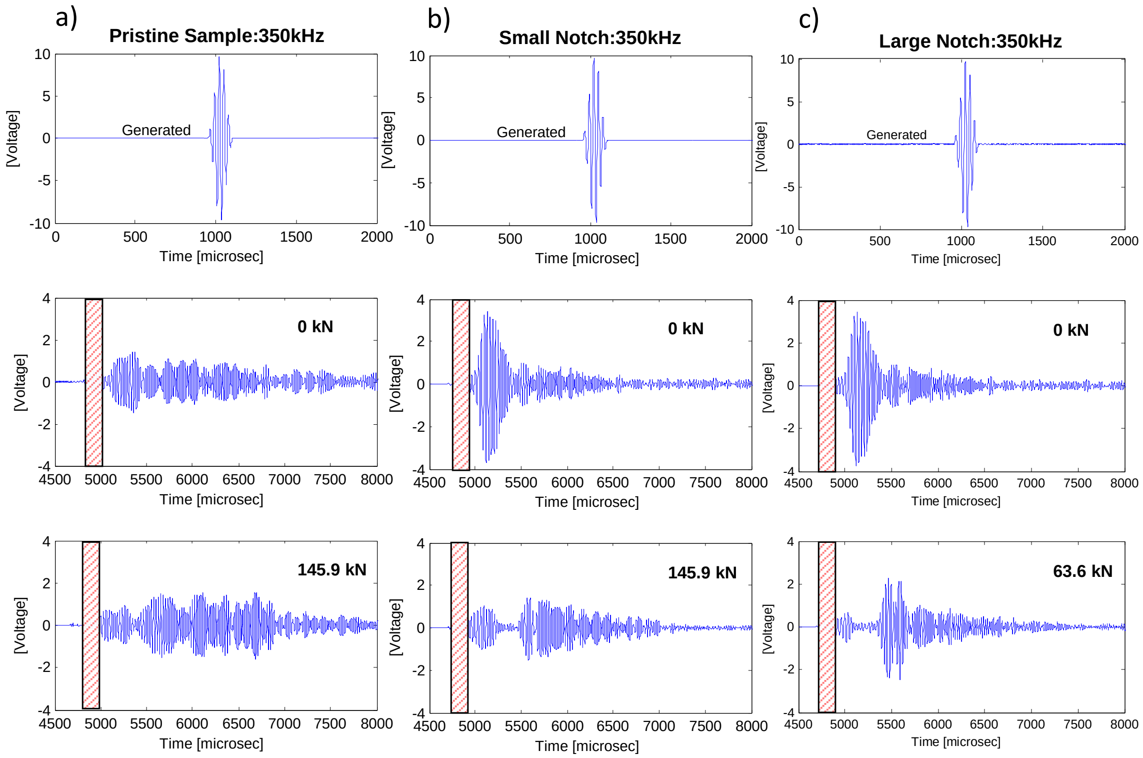

Figure 143: GUW Recorded GUW signals at various load levels a) Pristine sample b) Small notch c) Large notch

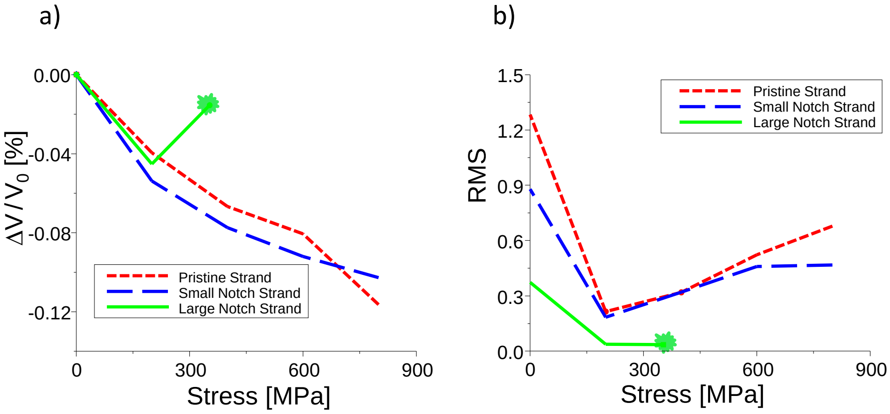

Figure 144: GUW features: a) Acoustoelastic curve and b) RMS vs. applied stress for the pristine and for the notched strands.

7.3.2 IDENTIFICATION OF PROGRESSIVE DAMAGE IN PARTICIALLY GROUTED CONCRETE MASONRY WALLS

7.3.2.1 EXTRACTION OF MECHANICAL DATA

Among the three walls, only testing of W1 resulted in catastrophic failure after the 13th cycle with a significant load drop shown in Figure 145a. The applied cycle number is marked in red. W2 and W3 were subjected to additional displacement cycles (Figure 145c and e) as no catastrophic failure occurred even after the 16th load cycle. The applied load-displacement profiles for all walls are shown in Figure 145b, d and f. The displacement for the load displacement correlation was measured using an LVDT placed on the top section of the wall. It can be noted in Figure 145b that W1 exhibited rapid strength degradation soon after reaching the maximum load which is indicative of shear dominated failure, while W2 and W3 demonstrated gradual strength degradation common in flexural/shear damage behavior. As expected, the improved horizontal joint reinforcements in W3 provided greater energy absorption. Consequently, W2 demonstrated greater shear capacity in comparison to W1 and also the capacity of W3 and W2 were almost the same. In addition, results showed that the joint reinforcement in W3 just makes the hysteresis loops more uniform and has less effect on the shear capacity of wall.

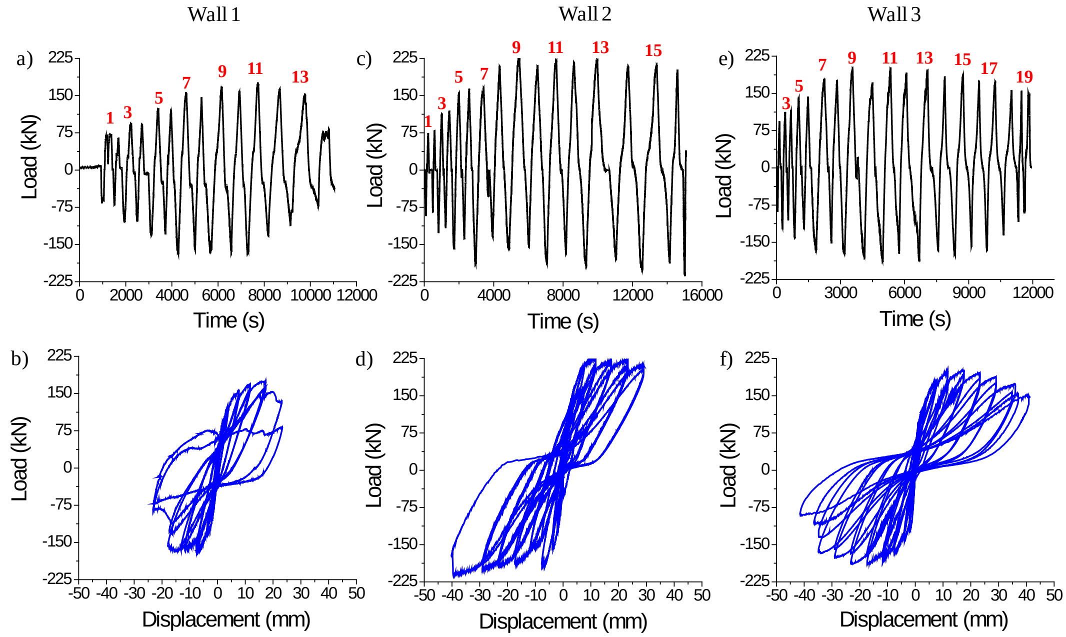

Figure 145. Loading history and loading-lateral displacement profile (a) and (b) W1 (c) and (d) W2 (e) and (f) W3

To gain further insight into the CMW damage behavior, the energy density per loading cycle (area enclosed in the load-displacement curves) was correlated with full field strain maps obtained by DIC, as well as extracted AE features (such as energy and amplitude). The load-displacement behavior for cycle 1, 3 and 5 obtained for W1 is presented in Figure 146a. It should be noted that the odd cycle numbers corresponded to increased load compared to the one applied prior. It can be observed in Figure 146b that the rate of the energy density increases right at the initiation of the 3rd loading cycle remaining constant until the 5th cycle. Thereafter, the rate is seen to further increase at the 9th and

11th loading cycles. Such energy dissipations were correlated with full field principal strain maps obtained from post-processing of DIC data as shown in Figure 146c. The presented strain maps correspond to the maximum measured negative load since strain accumulations were found to be symmetrical, which means that comparable strain accumulations were measured on the left side of the CMW for negative load (pushing) and on the right side for positive load (pulling). These DIC results show that the initial increase of the dissipated energy in the 3rd cycle is coincident with pronounced strain accumulation at the bottom left corner of the wall along the loading direction. Upon the termination of the 4th load cycle, hairline cracks oriented exactly in the direction of the observed strain accumulation in the previous cycle were visually detected. Furthermore, in the 5th loading cycle, strain accumulation was seen to develop diagonally following the staircase pattern of the concrete blocks in addition to the increase of the strain accumulation at the bottom section of the wall. Hence, the computed increase of the energy density in the 5th cycle can be related to the initiation of shear cracks combined to further growth of the previously observed hairline cracks. The subsequent increased loading led to the development of new shear cracks at various locations of the wall as presented later in this section. The rate of formation of these cracks was found to drastically augment after the 9th loading cycle which resulted in the rapid energy dissipation noted earlier in Figure 146b.

7.3.2.2 IDENTIFICATION OF CRACK INITIATION AND PROGRESSIVE GROWTH

The applied load as a function of the DIC image number is shown in Figure 147a. It can be observed in Figure 147b that the longitudinal strain (horizontal strain) is seen to be symmetric with respect to zero during the initial loading cycles. Conversely, upon the initiation of the shear crack in cycle 5, the longitudinal strain increases until failure. The transversal strain (vertical strain) is seen to have a similar trend. However, the increase of the transversal strain is followed by the increase in the longitudinal strain. It is important to note that at the end of the test, the longitudinal strain is higher than the transversal strain. Hence, it can be inferred that strains in the horizontal reinforcements are noted to suffer higher strain than the vertical reinforcements. The full field displacement and strain visualizations in Figure 147c corresponding to the maximum negative load at cycle 7 demonstrate that although the wall undergoes negative displacement, local sections of the CMW exhibit inhomogeneous displacements with these regions revealing positive strain accumulation. This is attributed to the crack formation in these regions that has permanently separated some concrete blocks. In this context it was found that longitudinal strain accumulation is more sensitive to shear crack formations, while transversal strain accumulation is more sensitive to flexural crack formations on the tested walls.

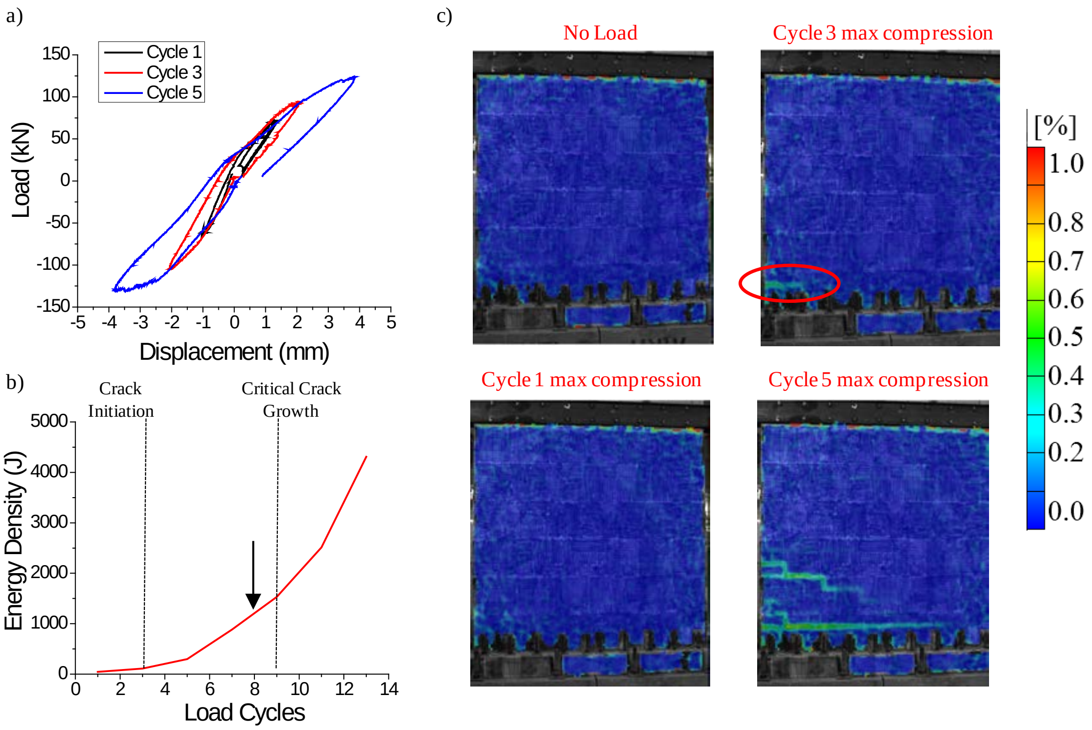

Figure 146. W1: (a) Initial load-displacement behavior; (b) energy dissipation as a function of load cycle; (c) Full field principal strain map

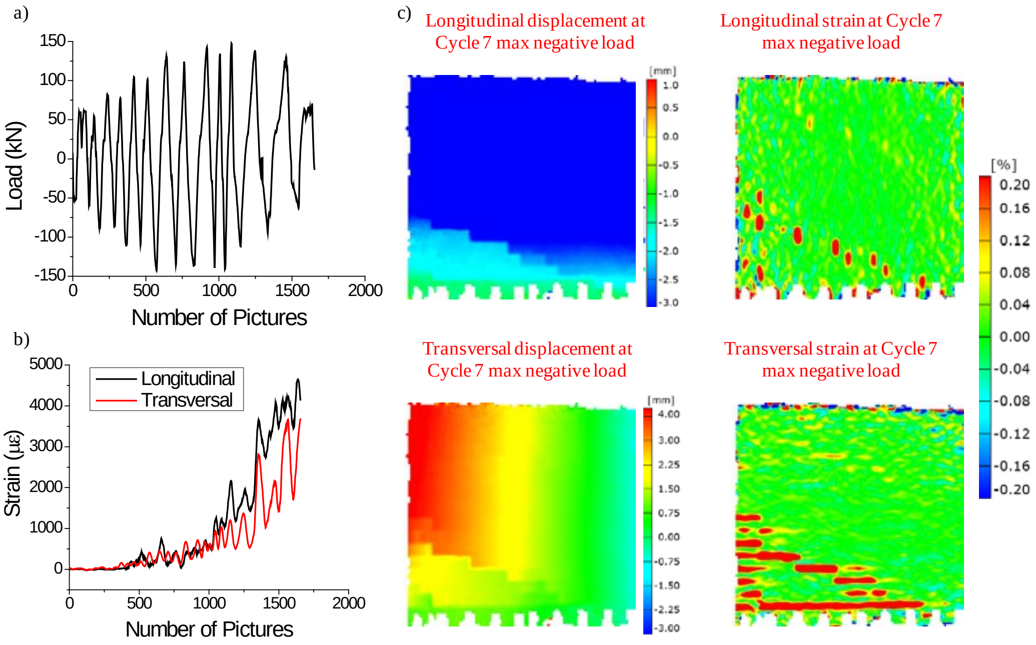

Figure 147. W1: (a) Applied Load vs. acquired images; (b) Average Axial Strain; (c) Full field in plane displacement and strain maps.

To formulate the basis for quantifying the severity of cracking in the tested walls, the maximum principal strain was calculated and results are shown in Figure 148a. Upon the onset of the crack initiation, the principal strain is seen to increase until final failure (when the maximum principal strain reached a value of 13,900με). The corresponding principal strain visualization substantiates this increasing trend as seen in Figure 148b. Furthermore, the AE results obtained for W1 were in good agreement with the DIC results shown in Figure 148c and d. Although AE was recorded during the entire loading history, only the AE features extracted from the increasing (odd number) load cycles are plotted herein. The AE amplitude (Figure 148c) recorded in situ demonstrate the sensitivity of AE to the development of damage. It is observed that the amplitude increases steadily with the applied loading and saturates at 100dB upon the formation of macroscopic crack.

The cumulative AE energy (Figure 148d) shows a similar increasing trend compared with both the calculated dissipation energy and maximum principal strain. The AE energy is seen to increase as shear cracking initiates and increases steadily until load cycle 9, after which the rate increases significantly until final failure. It was noted before that the initial strain accumulations were observed parallel to the loading direction and this fact was used to explain the initiation of hairline cracks. In addition, this procedure can explain the relatively lower amplitude and energy AE signals in the beginning of the loading sequence. The subsequent measured strain accumulations along the diagonals can therefore be directly associated with higher amplitude and energy AE signals, which eventually describe also the formation of macroscopic crack propagation on the wall, as shown in Fig.6b.

Thus, it can be observed that AE signals are sensitive to the integrity of the CMW and the AE signals can be effectively interpreted and cross-validated through the DIC technique. However, importantly, early signs of critical crack growth is noted with the change in the in-situ AE amplitude and energy plots. Thus, this approach forms the basis for real time SHM and intelligently trigger other NDT techniques such as DIC either through the development of smart acoustic alarms (such as the intelligent triggering of DIC using AE described in Chapter 3) or the use of offline inspection techniques precisely where AE signals are located. It should be recalled that the utilized AE sensors monitored only a reduced region of the wall and thus they could not provide comprehensive and overall structural information compared to DIC due to the attenuation in the material. Obviously this could be addressed by placing a larger array of sensors. Nevertheless, AE does provide a volume inspection tool with the potential to track in real time the onset of crack initiation, as indicated in this work by the good correlation between AE features and both mechanical and DIC data. The load-displacement curves of the initial three load cycles for W2 and W3 are shown in Figure 149a and Figure 149b (compare to W1, Figure 146a). In comparison to W2, W3 is seen to dissipate the same amount of energy at relatively lower loads. Energy dissipation for W2 (Figure 149c) appears to increase from the onset of the test although no visual cracks were detected after load cycles 1 and 2. Further, the energy dissipation is seen to increase significantly in the 3rd loading cycle which was coincident with the strain accumulation along the bottom left edge of the wall. Visual inspection after the 4th loading cycle revealed the formation of micro cracks precisely oriented in the direction of the observed strain accumulation.

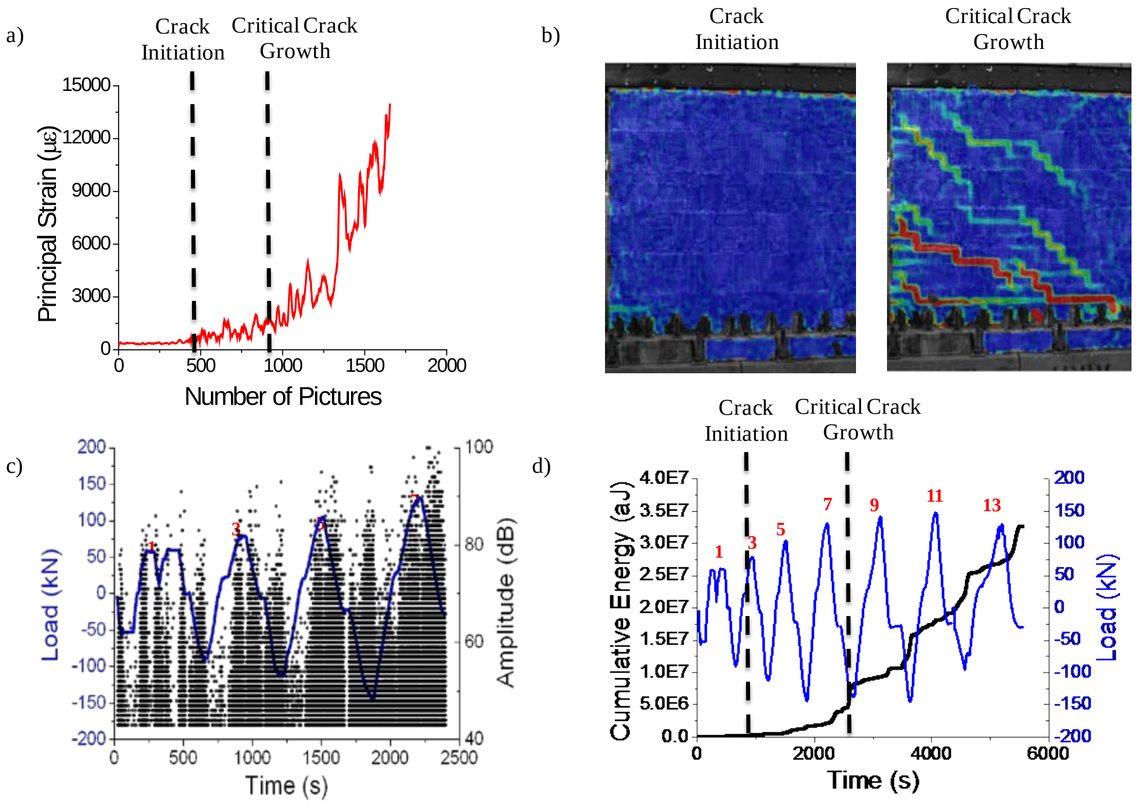

Figure 148. W1: (a) Maximum principal strain correlated with the acquired images (b) Principal strain visualization (c) AE Amplitude (d) AE Energy

Again, similar to W1, W2 exhibited a symmetric strain accumulation under the imposed initial load cycles. It can be further noted that the rate of the energy density increased after the 5th load cycle. This is attributed to the initiation of shear cracks which was coincident with strain accumulation along the diagonals of the wall. Interestingly, the energy dissipated decreases after the 7th load cycle until the 9th load cycle. A possible explanation for this could be the unsymmetrical loading in the 7th load cycle and thus an increase in the area of the load-displacement curve. This asymmetric load behavior was noted in Figure 145c in which the maximum negative load was higher than the maximum positive load. However, the energy density is observed to increase rapidly after the 9th loading cycle due to the crack formation at various locations on the wall. Unlike W1, W2 did not result in catastrophic failure but demonstrated gradual degradation indicative of flexural dominated behavior. Subsequent loading resulted in the increase of the strain accumulation along the same region implying the expansion of the existing cracks.

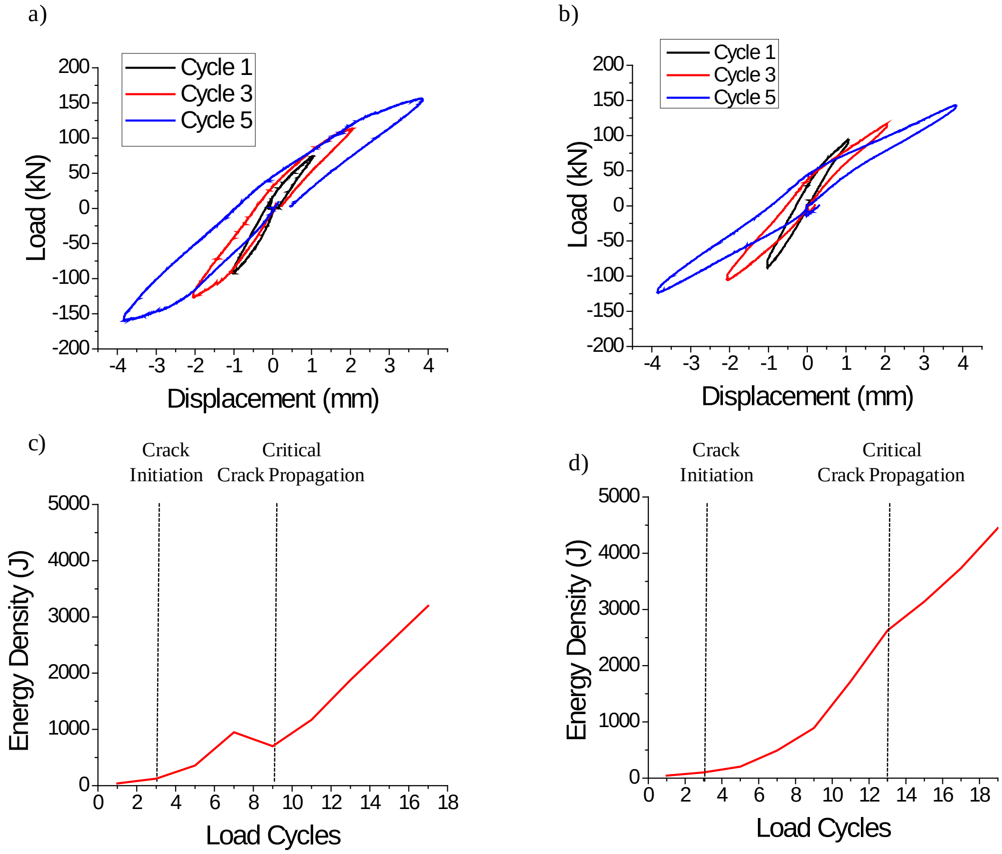

Figure 149. (a) Initial load displacement behavior for W2 (b) Initial load displacement behavior for W3 (c) Energy Density for W2 (d) Energy Density for W3

The energy dissipation profile for W3 is shown in Figure 149d. Similar to W2, the dissipation is seen to increase during the 3rd load cycle and continue to increase with subsequent loading. Furthermore, the rate of energy changed during the 5th load cycle due to the formation of shear cracks in the wall which were coincident with diagonal staircase pattern strain accumulations. A major difference noted between W2 and W3 was the fact that new shear cracks were observed before the expansion of existing shear cracks in W3.

The energy density for W3 is seen to increase considerably only after the 13th load cycle. It is to be noted that the additional reinforcements in W2 and W3 in comparison to W1 had only a minimal effect on crack initiation. However, the increased distribution of reinforcements seemed to arrest the crack formation and thereby delay the unification of individual local cracks. This effect had a direct implication on the overall load bearing capacity of the wall and resulted in a gradual strength degradation.

7.3.2.3 CLASSIFICATION OF CRACK MECHANISMS USING FULL FIELD DATA

The evolution of the crack patterns in W2 and 3 is shown in Figure 150. The severity of the cracks is characterized by the intensity of the strain maps. Figure 150a reveals strain localizations during the maximum negative load in Cycle 3 to Cycle 7 for W2. It can be clearly noted that significant strain is initially seen to develop parallel to the loading direction, which then gradually evolved along the diagonals leading to shear crack formation. This strain accumulation then increased further with subsequent loading, enabling the unification of the cracks along the diagonals to form a percolated network of visible cracks. Conversely, in W3, relatively smaller strain accumulation was noted initially parallel to the loading but quickly evolved along a staircase pattern (Figure 150b). As stated previously, it can be noted that new cracks were formed before the expansion of the previously developed cracks.

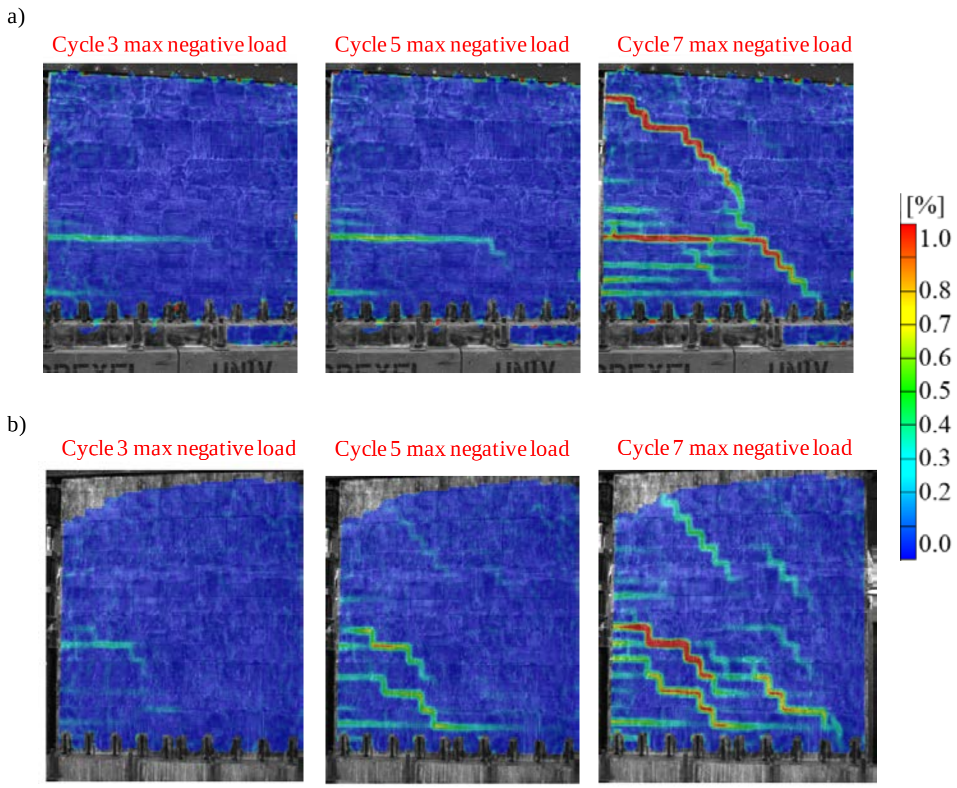

Figure 150. Evolution of crack pattern shown by the principal strain maps: (a) W1; (b) W2.

To understand the in-plane behavior of the reinforced CMW under cyclic loading, the average full-field directional strain were computed. The in-plane strains as the function of the acquired images for W2 are shown in Figure 151a. The vertical strain was found to be symmetrical with respect to zero during the initial load cycles. However, upon the onset of the 3rd loading cycle (image #125), which coincided with the time that cracking was found to initiate in the wall, the transversal strain is seen to increase and continued to increase until the test was terminated. Similarly, the longitudinal strain also follows the transversal strain behavior. It should be noted that similar to W1, the transversal and longitudinal strain in W2 closely follow each other initially but deviate after the 5th load cycle (image # 200). Visual inspection after the 5th loading cycle revealed several cracks parallel to the loading direction as shown earlier in Figure 150a. Conversely, the longitudinal strain is seen to increase later than the transversal strain. It can be further observed from the full field strain visualization, that the cracks initiated parallel to the loading direction and then evolved into the diagonal pattern. Hence, it can be inferred that the transversal strain is sensitive to the flexural crack behavior while the longitudinal strain is sensitive to the shear crack behavior, Consequently, it can be concluded that W2 exhibited predominantly a flexural crack behavior. Figure 151b shows the in-plane behavior of the W3 as a function of the acquired DIC images. As the crack is noted to initiate in the 3rd loading cycle, the transversal strain picks up and continues to increase until the termination of the test. Unlike W2, there is significant delay in the increase of the transversal and longitudinal strains and observed deviation in their behavior. It was pointed out earlier that W3 resulted in the formation of several new cracks rather than the expansion of existing ones and this is reflected in the longitudinal strain behavior.

The full field displacement and strain visualizations provided further insight in to the cause of this deviation. The full field transversal displacement and strain fields for W2 is shown in Figure 151c. It can be observed that although the major part of the wall displaces as a cantilever beam, local regions in the wall are seen to undergo inhomogeneous deformation. This again is attributed to the crack formation in these regions and consequently the wall does not behave as a rigid body. These local regions are further noted to be associated with significant strain accumulations. Similarly, this behavior is noted in W3 as well. However, the major difference is the fact that unlike W2, W3 contains fewer pronounced in homogeneities in both full field displacement and strain maps. This pattern was observed more throughout the wall and therefore it demonstrates the effect of progressive crack formation on the overall structural behavior of the tested CMW.

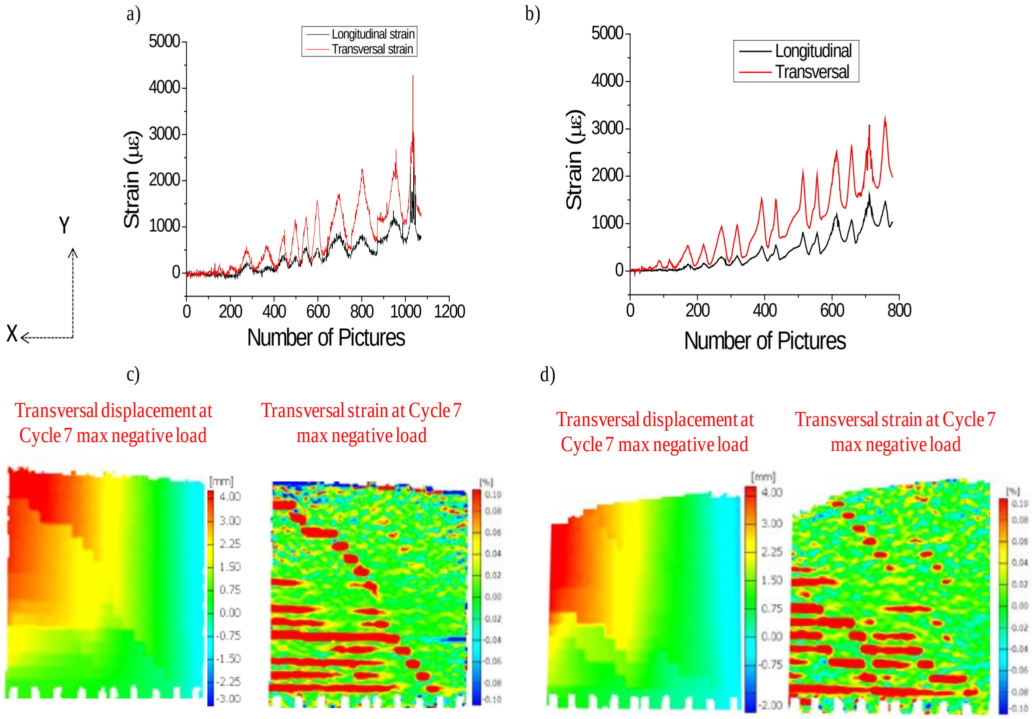

Figure 151. In-plane strain behavior in (a) W2 (b) W3, Full field transversal displacement and strain maps in (c) W2 (d) W3

7.3.2.3 DAMAGE QUANTIFICATION

Furthermore, the maximum principal strain was computed to quantify the severity of damage induced in W2 (Figure 152a). The principal strain is seen to increase at the onset of crack initiation while it continued to steadily increase with subsequent increase of applied loading. The final principal strain in W2 is noticed to be less than in W1. It should be recalled that W1 did result in catastrophic failure while W2 did not. This is also reflective in the maximum principal strain values with W1 resulting in higher strain values. Hence, the additional reinforcements proved to provide greater damage resistance, which enable the wall to sustain higher load levels and therefore prolong its lifetime. In addition, the AE energy shows a good agreement with both measured principal strain and energy density for W2 as noted in Figure 152b.

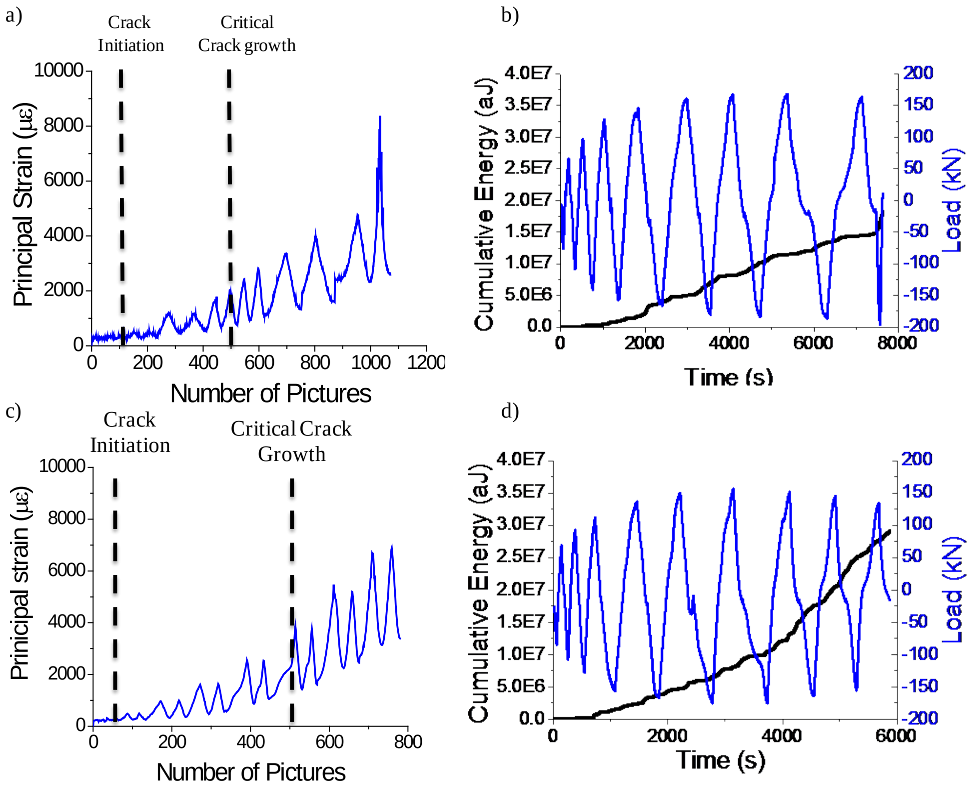

Figure 152. W2 (a) Maximum principal strain (b) AE Energy ; W3 (c) Maximum principal strain (d) AE Energy

Specifically, the AE energy is seen to pick up considerably after the 3rd load cycle due to the crack initiation in the wall. Furthermore, jumps were noted in the AE energy profile indicative of new crack formation with subsequent increased loading cycles. Conversely, the principal strain in W3 is seen to be even lower than in W2 (Figure 152c). Similar to W2, the maximum principal strain is seen to initiate at the onset of crack initiation while it further increased with subsequent load cycles. The principal strain was noted to increase significantly after the 13th load cycle (image # 500) with strain accumulation on several regions of the wall indicating significant crack formations. The increase of principal strain in W3 has good agreement with the AE energy obtained during the test (Figure 152d). Consequently, the maximum principal strain forms the basis to quantify the severity of damage in these concrete structures. Finally, the obtained full field principal strain map at the end of the tests were correlated with the traditional hand sketched crack patterns on the walls as shown in Fig.11. The DIC strain maps are found to reveal strain localizations oriented precisely in the direction of overall crack formation for W1 (Fig.11a), W2 (Fig.11b) and W3 (Fig.11c). These full field maps provide further mechanical information on the severity of cracking as indicated by the darker shades of red. Consequently, the full field strain maps present an accurate method to in situ track progressive crack formation and relate it to the overall structural behavior.

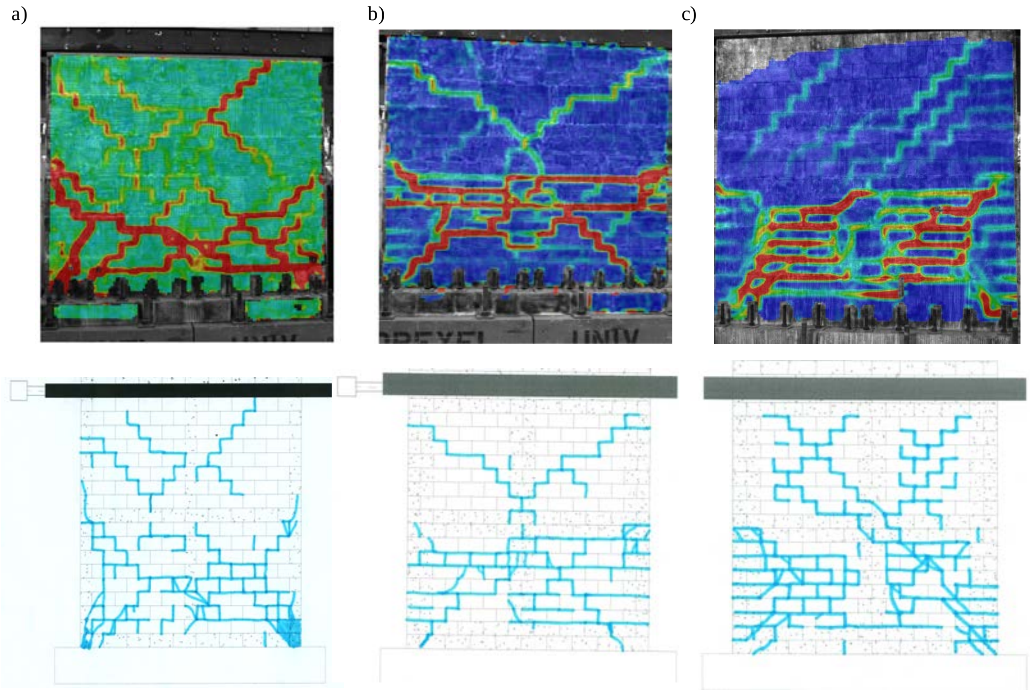

Figure 153. Full field strain maps correlated with conventional crack pattern maps for (a) W1; (b) W2 and (c) W3

CHAPTER 8: SYNERGISTIC CONTRIBUTION AND FUTURE DIRECTION

8.1 SYNERGISTIC CONTRIBUTIONS

The fundamental challenges associated with AE testing is its high sensitivity to noise which can be both secondary sources and unwanted signals and the complexity involved in interpreting the recorded AE signals . These challenges have the potential to mask the true primary sources and raise both false positive signals and false negative signals. In fact, it is this fundamental challenge that has inhibited the extension of AE as a reliable SHM technique for aerospace applications. To address this particular challenges and reliably detect the onset of damage (primary source), this research presented a **novel acoustics-based framework integrating complementary full field NDT techniques** to cross-validate and effectively interpret the unknown and typically large AE data collected. Specifically, the unique concept of developing a smart acoustic alarm system to trigger the DIC camera was developed in this research and has been submitted for patent application [188]. This acoustic alarm system provides the framework for intelligent use of optical techniques in correlation with AE for reliable damage detection and extraction of heterogeneous data. It was noted that synchronous usage of the NDT techniques were beneficial in correlating AE features with mechanical parameters such as energy and strain and shown to be valuable in identifying the reliably the onset of damage.

A major breakthrough of this research was the development of a **novel AE damage parameter** to identify the presence of crack initiation in metallic materials. This novel AE damage parameter was built on the extensive experimental work that was performed for this research and validated for different load profiles and geometries. A major issue with current AE testing is the reliance on threshold dependent features for damage detection. For instance, Aggelis et al [45] demonstrated that the AE duration and rise time are sensitive to crack growth in aluminum alloys. The increase in duration and rise time was attributed to the shift from tensile crack mode to shear crack mode. Consequently, other researches [43, 44] demonstrated the relationship between the rise angle and the average frequency a good feature combination to classify the evolving crack modes. The final fracture was associated with shear crack modes and thus this approach was found to be a good indicator for early detection of crack growth by detecting the tensile crack mode. However, it was further demonstrated that both the rise angle and average frequency (a calculated AE feature) were observed to change as a function of the propagation distance [37] irrespective of the distance. While this is typically not an issue for laboratory testing, it is concluded that the source-sensor distance is critical when evaluating threshold based AE features and could be a source of concern for field application. However, unlike threshold based features, advanced frequency features are not significantly influenced by the propagating distance and provide more robust information about the source mechanism [189]. Thus, this research identified critical frequency based AE features sensitive to damage and consequently developed **novel damage parameter** to in-situ identify the presence of cracks in metallic specimen, particularly aluminum alloys. The novel damage parameter was validated across different geometries and loading conditions and shown to be a robust feature for reliable crack identification. Consequently, this parameter along with other AE feature descriptors were utilized as input features for statistical pattern recognition algorithms and was noted to be promising for online SHM applications.

Another major contribution of this research is the **unique combination of heterogeneous data** through multi-variate data fusion approaches. Specifically, a novelty damage detector using outlier analysis was designed by combining acoustic features such as amplitude, time of arrival and RMS were combined with mechanical features such as strain and shown to be a promising method for both reliable crack detection and quantification with a minimal false positive signals. Additionally, this research also presented a reliable approach for the detection of debonding in fiber reinforced stiffened panels by introducing novel feature descriptors such as frequency factor based on the relationship between the frequency centroid and duration. It was observed that this relationship between frequency centroid and duration was sensitive to the growing debonding in the stiffened panels under fatigue loading. This feature was further used in statistical pattern recognition algorithms and was shown to be instrumental in identifying the debonding between the composite skin and spar across different specimens with and without initial defects. Additionally, it was noted that a novel damage index based on the GUW features was utilized to quantify the debonding damage under fatigue loading conditions.

Finally, the advantage of this unique combination of AE in correlation with full field NDT techniques for SHM applications albeit for civil structures was demonstrated. It was noted that full field DIC images and the corresponding statistics extracted were useful in detecting damage detection and was shown correlate well with change in AE features that were indicative of the different damage modes in the partially grouted reinforced concrete masonry walls. The development of the smart acoustic alarm system would be a potential example of the application of the synergistic use of AE with other full field optical metrological techniques.

8.2 FUTURE WORK

8.2.1 MICROSTRUCTURAL SENSITIVE FATIGUE CRACK IDENTIFICATION

To implement a reliable 'fail safe' approach for aerospace structural applications based on the AE indications, it is essential to **identify damage precursors** to predict the onset of crack initiation. As this research was extensively focused on implementing a robust approach to identify the onset and progression of fatigue crack in aluminum alloys, the future goal of this research would be to identify AE damage precursors in aluminum alloys. In order to achieve this goal, **micro dog-bone aluminum alloy specimens** would be manufactured and loaded in custom designed load stages that will be inserted in a **Scanning Electron Microscope (SEM)** coupled with AE. Specifically, the load stage would be designed to perform complex mechanical testing including fatigue inside the SEM chamber and simultaneously record AE signals in real time.

Such an approach would provide a direct correlation of the micro structural deformation mechanisms to the recorded AE signals. Thus, it would be feasible to determine and reliably characterize the plastic deformation in the material in terms of the AE signals and consequently identify trends leading to crack initiation. Additionally, this would also serve as an efficient filtering tool to clean and interpret the real time recorded AE signals during meso and macro scale mechanical testing.

8.2.2 CRACK PROGNOSIS USING AE DAMAGE PARAMETER

A significant challenge associated with the widespread use of AE for SHM applications is the lack of quantifiable data to estimate the severity of damage. Additionally, a major benefit of the AE technique is its potential to perform damage prognosis, i.e. predict the remaining useful life of the structure. Currently, the major focus on AE testing including this research is driven towards reliably performing damage diagnosis. However, with the development of novel AE damage parameters (as demonstrated in this research), it is possible to quantify the severity of damage and serve the basis for predicting the remaining useful life of the structure.

Based on the developed damage index parameter for crack detection, it is possible to solely isolate the AE signals associated with crack initiation and growth in metallic specimens. A preliminary AE model for crack quantification in aluminum alloys is illustrated in Figure 154. The AE signals corresponding to a DP less than 0.002ms (corresponding to crack as shown in Chapter 5) were selected and their PP1 and PP3 values were combined using a multivariate approach. Specifically, an outlier analysis was designed based on the Mahalanobis equation (Equation 3 in Chapter 5) and is shown to be sensitive to the increasing crack growth in the material.

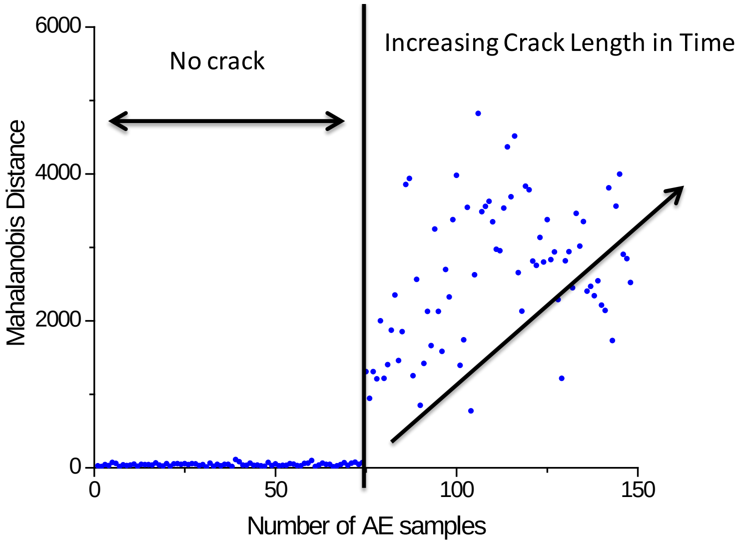

Figure 154: Preliminary AE model for crack quantification

It can be observed that the Mahalanobis distance is significantly low for no crack growth while the distance is noted to increase with increasing crack growth. Thus, this approach based solely on AE features can be utilized to estimate the severity of the crack in real time and predict the remaining useful life of the structure. Additionally, advanced statistical analysis based on machine learning approaches [190, 191] can be developed and implemented to predict the time to critical crack length and accordingly determine appropriate maintenance procedures. In particular, learning algorithms based on regression based approaches or probability density function approaches can be implemented based on the relationship between the damage index parameter and the peak frequency characteristic. Worden et al [191] postulated that machine learning approaches such as support vector machines algorithms can be implemented to perform damage prognosis provided favorable damage diagnosis data is available. This research presented a novel AE paradigm and the use of novelty damage parameter for damage detection at both the specimen and component level. The natural extension of this research framework would be the validation of the novelty damage parameter for large scale structural components and its dependence on environmental factors such as temperature, humidity and other environmental conditions typically encountered during flight conditions. Particularly, the effect of temperature on the variability of the novelty damage parameter needs to be investigated as it has been reported that affects the sensitivity of guided waves [192].

8.2.3WIRELESS AE MONITORING

Another future goal of this research framework would be to implement wireless AE modules for remote sensing applications. Preliminary AE wireless monitoring was performed using a commercially available wireless data acquisition board manufactured by Mistras to monitor the debonding in the CFRP components. This AE board is the smallest, lowest power, full capability AE system ever developed. It is a standalone prognostic system with capability to built in computer, processing and decision making. The board is equipped with ports to input a number of external inputs (for example temperature, pressure, etc) while it can also receive input from a strain gauge. Its total size is 4 x 5.5 inches and its weight is less than 0.5 lbs. It can be powered by 5-18 Volts sources. Its power consumption is relatively very low (<700 mW at peak acquisition rates). It can operate in a temperature range of (-40 to 75 degrees Celcius)

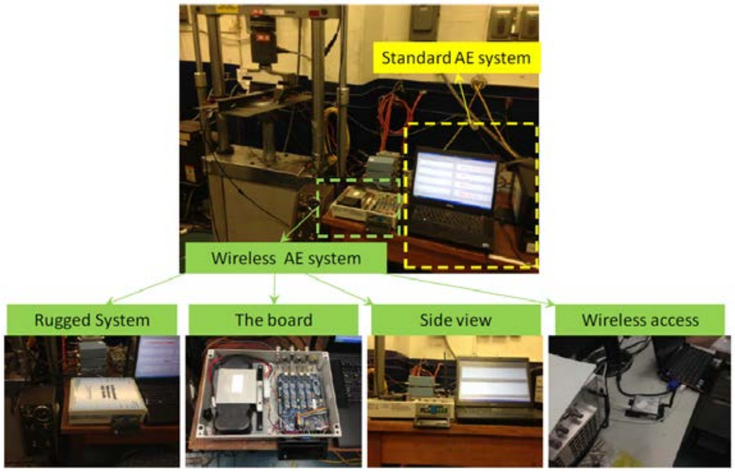

Figure 155: Components of the Wireless AE system

The components of the wireless AE system is depicted in Figure 155. In order to evaluate its capabilities, the AE wireless system was utilized in parallel with the standard AE DiSP system (wired system) to monitor the debonding process. Preliminary analysis of the wireless monitoring capabilities were performed and compared with the standard wired system as shown in Figure 156. First of all, a relatively good agreement can be noticed between the wireless system and the standard wired system. Secondly, it was noticed that the wireless system picked up changes in features that corresponded the debonding in the CFRP component as noticed by the distinct jumps in the energy profile at the same experimental time. Finally, the wireless system also had the capability of recording and saving waveforms for future waveform based analysis and advanced feature extraction as noted in Figure 157.

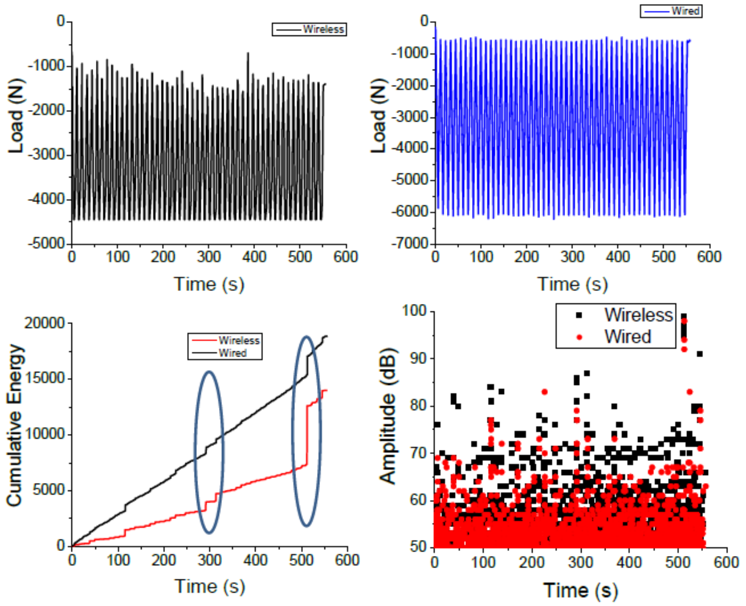

Figure 156: Validation of AE wireless system with the standard AE system

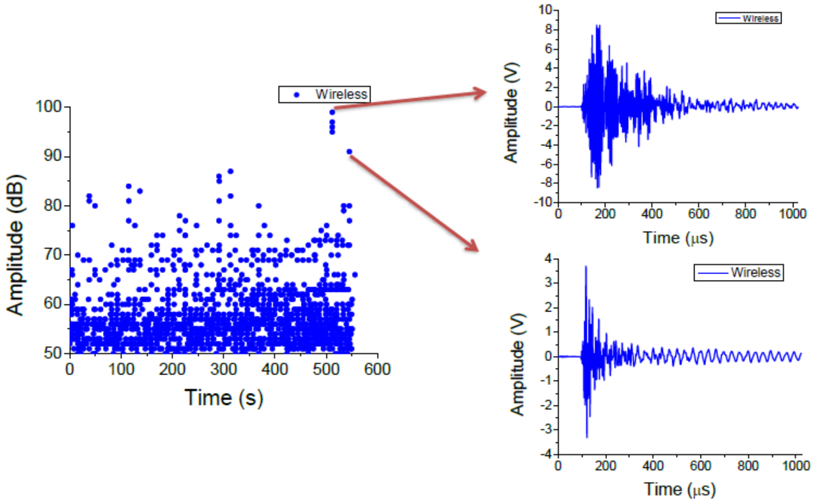

Figure 157: Acquired waveforms by the wireless AE system

This is a major development for the realization of low cost, light weight onboard AE monitoring for SHM applications. This wireless system significantly reduces the additional hardware instrumentation such as preamplifier and the direct connection of the wires between the acquisition software and the hardware setup and more importantly can be utilized for remote health monitoring. This paves the way to developing light weight and embedded sensing technologies for condition based maintenance especially in the aerospace industry where weight and money are a critical issue that prohibits aircrafts from utilizing advanced on-board SHM systems.

Currently, the major drawback of the wireless AE system is related to its lack of computational resources and lack of mass production. Specifically, this particular wireless system is capped to a maximum frequency of 150kHz which makes it difficult to capture high frequency damage mechanisms such as crack, fiber fracture etc. Currently, R-15a sensors are widely utilized as the primary AE sensors for damage detection in field applications. These sensors have a resonant frequency of 150kHz and thus the wireless system is tune to this sensor capability. It is definitely possible to increase the frequency bandwidth of the AE wireless system should the need arise by increasing the power requirements which might translate to increased weight of the system. Additionally, the sampling rate of this system is significantly lesser in comparison with AE PCI-2 system that has the capability of sampling at 40MHz. However, this is not a hard limiting factor of the system and can be improved provided both the power and the onboard storage capacity for the wireless system is increased.

In conclusion, a novel cross-validated NDE framework for damage detection using AE was developed and demonstrated in this research with the ultimate goal for SHM applications. The advantages of utilizing full field optical techniques and other complementary NDT techniques in conjunction with the AE technique is shown to be beneficial in effectively interpreting the AE signatures and identifying the primary AE sources. For instance, DIC adds a new dimension in interpreting AE signals and monitoring damage in CMW by providing visually powerful means to validate progressive failure development. Subsequently, the AE signals were then post processed and novel feature descriptors including damage parameters and novelty damage detectors were designed to reliably flag the presence of damage in critical structural specimen and components.

REFERENCES

1. Li, X., *A brief review: acoustic emission method for tool wear monitoring during turning.* International Journal of Machine Tools and Manufacture, 2002. **42**(2): p. 157-165.
2. Dunegan, H., D. Harris, and C. Tatro, *Fracture analysis by use of acoustic emission.* Engineering Fracture Mechanics, 1968. **1**(1): p. 105-122.
3. Ohtsu, M., *The history and development of acoustic emission in concrete engineering.* Magazine of concrete research, 1996. **48**(177): p. 321-330.
4. Pollock, A., *Acoustic emission-2: acoustic emission amplitudes.* Non-Destructive Testing, 1973. **6**(5): p. 264-269.
5. Anastassopoulos, A. and T. Philippidis, *Clustering methodology for the evaluation of acoustic emission from composites.* Journal of acoustic emission, 1995. **13**(1-2): p. 11-22.
6. Stark, L., M. Hosford, and M.S. James *Southwest Air Emergency: Inspection Program Missed Cracks in Plane*. 2011.
7. International, N.R. *Airbus A380 Superjumbo Airliner*. aerospace-technology.com 2012; Available from: http://www.aerospace-technology.com/projects/a380/.
8. Boeing. *787 Dreamliner* About the 787 Family 2013; Available from: http://www.boeing.com/commercial/787family/background.html.
9. Abrate, S., *Modeling of impacts on composite structures.* Composite Structures, 2001. **51**: p. 129-138.
10. Sundaram, R., G.M. Kamath, and N. Gupta, *Structural Health Monitorin of Composite Structures - Issues and Challenges.* International Journal of Vechicle Structures & Systems, 2012. **4**(3).

11. Burns, S. *Cracks In Airbus A380 Wings Put Pressure On European Aeronautic*. 2012.

12. Bockenheimer, C., H. Speckmann, and S.A.I. Team, *Validation, Verification and Implementation of SHM at Airbus*, in *IWSHM*2013: Stanford, USA.

13. ASTM, *Standard Terminology for Nondestructive Examinations* in *E1316*2004: West Conshohocken, PA.

14. Lemaitre, J. and R. Desmorat, *Engineering Damage Mechanics*. 2005, Netherlands: Springer.

15. Brandon, D. and W.D. Kaplan, *Microstructural Characterization of Materials*. 2008, England: Wiley.

16. Vembar, D., et al. *A Haptic Virtual Borescope for Visual Engine Inspection Training*. in *IEEE Symposium on 3D User Interfaces 2008*. 2008. Nevada, USA.

17. Winter, C., et al., *Automatic Adaptive Enhancement for Images Obtained With Fiberscopic Endoscopes.* Biomedical Engineering, IEEE Transactions on, 2006. **53**(10): p. 2035-2046.

18. Hellier, C., *Handbook of Nondestructive Evaluation*. 1 ed. 2001: McGraw-Hill Professional Publishing.

19. Grédiac, M., *The use of full-field measurement methods in composite material characterization: interest and limitations.* Composites Part A: Applied Science and Manufacturing, 2004. **35**(7–8): p. 751-761.

20. Hanke, R., T. Fuchs, and N. Uhlmann, *X-ray based methods for non-destructive testing and material characterization.* Nuclear Instruments and Methods in

Physics Research Section A: Accelerators, Spectrometers, Detectors and Associated Equipment, 2008. **591**(1): p. 14-18.

21. Krouskop, T., D. Dougherty, and F. Vinson, *A pulsed Doppler ultrasonic system for making noninvasive measurements of the mechanical properties of soft tissue.* J Rehabil Res Dev, 1987. **24**(2): p. 1-8.

22. Rho, J.Y., R.B. Ashman, and C.H. Turner, *Young's modulus of trabecular and cortical bone material: ultrasonic and microtensile measurements.* Journal of biomechanics, 1993. **26**(2): p. 111-119.

23. Langenecker, B., *Effects of ultrasound on deformation characteristics of metals.* Sonics and Ultrasonics, IEEE Transactions on, 1966. **13**(1): p. 1-8.

24. Staszewski, W., C. Boller, and G.R. Tomlinson, *Health monitoring of aerospace structures: smart sensor technologies and signal processing*. 2004: John Wiley & Sons.

25. Ihn, J.-B. and F.-K. Chang, *Pitch-catch active sensing methods in structural health monitoring for aircraft structures.* Structural Health Monitoring, 2008. **7**(1): p. 5-19.

26. Giurgiutiu, V. and C. Rogers. *Electro-mechanical (E/M) impedance method for structural health monitoring and nondestructive evaluation*. in *Proceedings of international workshop on structural health monitoring*. 1997.

27. Giurgiutiu, V., et al. *Active sensors for health monitoring of aging aerospace structures*. in *SPIE's 7th Annual International Symposium on Smart Structures and Materials*. 2000. International Society for Optics and Photonics.

28. Zhao, Z. and A. Haldar, *Bridge fatigue damage evaluation and updating using non-destructive inspections.* Engineering Fracture Mechanics, 1996. **53**(5): p. 775-788.

29. Dinesh Kumar, U., J. Crocker, and J. Knezevic. *Evolutionary maintenance for aircraft engines*. in *Reliability and Maintainability Symposium, 1999. Proceedings. Annual*. 1999.

30. Mandache, C., et al., *Considerations on structural health monitoring reliability*, in *SMART MATERIALS, STRUCTURES & NDT in Aerospace*2011: Montreal, Canada.

31. Farrar, C.R. and K. Worden, *An introduction to structural health monitoring.* Philosophical Transactions of the Royal Society A: Mathematical, Physical and Engineering Sciences, 2007. **365**(1851): p. 303-315.

32. Speckmann, H. and H. Roesner. *Structural health monitoring: a contribution to the intelligent aircraft structure*. in *European Conference on NDT (ECNDT)*. 2006. Berlin.

33. Sohn, H., et al., *A review of structural health monitoring literature: 1996-2001*. 2004: Los Alamos National Laboratory Los Alamos, NM.

34. Farrar, C.R. and K. Worden, *An introduction to structural health monitoring.* Phiosophical transacations of the Royal Society, 2007: p. 303-315.

35. Center, N.R. *Theory-AE Sources*. Available from: http://www.ndt-ed.org/EducationResources/CommunityCollege/Other%20Methods/AE/AE_Theory-Sources.htm.

36. *Acoustic Emission Testing*. Basics for Research-Applications in Civil Engineering, ed. C. Grosse and M. Ohtsu. 2008: Springer Berlin Heidelberg.

37. *Acoustic Emission Testing*. Third ed. Nondestructive Testing Handbook, ed. P. Moore. Vol. 6. 2005.

38. Hellier, C., *Handbook of Nondestructive Evaluation*, 2003, McGraw-Hill.

39. Muránsky, O., et al., *Investigation of deformation twinning in a fine-grained and coarse-grained ZM20 Mg alloy: Combined in situ neutron diffraction and acoustic emission.* Acta Materialia, 2010. **58**(5): p. 1503-1517.

40. Hazeli, K., et al., *In situ identification of twin-related bands near yielding in a magnesium alloy.* Scripta Materialia, 2013. **68**(1): p. 83-86.

41. Roberts, T.M. and M. Talebzadeh, *Acoustic emission monitoring of fatigue crack propagation.* Journal of Constructional Steel Research, 2003. **59**(6): p. 695-712.

42. Scala, C.M. and R.A. Coyle, *Acoustic emission waveform analysis to identify fatigue crack propagation in a mirage aircraft: Journal of Acoustic Emission, Vol. 6, No. 4, pp. 249–256 (Oct.–Dec. 1987).* NDT & E International, 1992. **25**(6): p. 304.

43. Yuyama, S., et al., *Detection and evaluation of failures in high-strength tendon of prestressed concrete bridges by acoustic emission.* Construction and Building Materials, 2007. **21**(3): p. 491-500.

44. Aggelis, D., E. Kordatos, and T. Matikas, *Acoustic emission for fatigue damage characterization in metal plates.* Mechanics Research Communications, 2011. **38**(2): p. 106-110.

45. Jihan, S., A.M. Siddiqui, and M.A.S. Sweet, *Fracture strength of E-glass fibre strands using acoustic emission.* NDT & E International, 1997. **30**(6): p. 383-388.

46. Qi, G., et al., *Discrete wavelet decomposition of acoustic emission signals from carbon-fiber-reinforced composites.* Composites Science and Technology, 1997. **57**(4): p. 389-403.

47. Gutkin, R., et al., *On acoustic emission for failure investigation in CFRP: Pattern recognition and peak frequency analyses.* Mechanical Systems and Signal Processing, 2011. **25**(4): p. 1393-1407.

48. *Theory-AE Sources*. NDT Resource Center, 2014.

49. Drouillard, T.F., *Introduction to Acoustic Emission Testing*. Acoustic Emission Testing. Vol. 6. 2005: ASNT.

50. *Difference between Earthquake Focus and the Epicenter*. 2008.

51. *6.1 magnitude earthquake - Argentina South America + Global Earthquake Swarm*. 2012.

52. Carpenter, S. and F. Higgins, *Sources of acoustic emission generated during the plastic deformation of 7075 aluminum alloy.* Metallurgical Transactions A, 1977. **8**(10): p. 1629-1632.

53. Scruby, C., H. Wadley, and J. Sinclair, *The origin of acoustic emission during deformation of aluminium and an aluminium–magnesium alloy.* Philosophical Magazine A, 1981. **44**(2): p. 249-274.

54. Rouby, D. and P. Fleischmann, *Spectral analysis of acoustic emission from aluminium single crystals undergoing plastic deformation.* physica status solidi (a), 1978. **48**(2): p. 439-445.

55. Wadley, H., C. Scruby, and J. Speake, *Acoustic emission for physical examination of metals.* International Metals Reviews, 1980. **25**(1): p. 41-64.

56. Harris, D. and H. Dunegan, *Continuous monitoring of fatigue-crack growth by acoustic-emission techniques.* Experimental Mechanics, 1974. **14**(2): p. 71-81.

57. Jones, R. and M. Friesel, *Acoustic emission during pitting and transgranular crack initiation in type 304 stainless steel.* Corrosion, 1992. **48**(9): p. 751-758.

58. Gerberich, W. and C. Hartbower, *Some observations on stress wave emission as a measure of crack growth.* International Journal of Fracture Mechanics, 1967. **3**(3): p. 185-192.

59. Ohtsu, M., T. Okamoto, and S. Yuyama, *Moment tensor analysis of acoustic emission for cracking mechanisms in concrete.* ACI Structural Journal, 1998. **95**(2).

60. Roberts, T. and M. Talebzadeh, *Acoustic emission monitoring of fatigue crack propagation.* Journal of Constructional Steel Research, 2003. **59**(6): p. 695-712.

61. Lindley, T., I. Palmer, and C. Richards, *Acoustic emission monitoring of fatigue crack growth.* Materials Science and Engineering, 1978. **32**(1): p. 1-15.

62. Ramadan, S., et al., *Detection of stress corrosion cracking of high-strength steel used in prestressed concrete structures by acoustic emission technique.* Applied surface science, 2008. **254**(8): p. 2255-2261.

63. Fregonese, M., et al., *Initiation and propagation steps in pitting corrosion of austenitic stainless steels: monitoring by acoustic emission.* Corrosion Science, 2001. **43**(4): p. 627-641.

64. Benmedakhene, S., M. Kenane, and M. Benzeggagh, *Initiation and growth of delamination in glass/epoxy composites subjected to static and dynamic loading by acoustic emission monitoring.* Composites science and technology, 1999. **59**(2): p. 201-208.

65. Mal, A.K., F. Shih, and S. Banerjee. *Acoustic emission waveforms in composite laminates under low velocity impact*. in *NDE for Health Monitoring and Diagnostics*. 2003. International Society for Optics and Photonics.

66. Haselbach, W. and B. Lauke, *Acoustic emission of debonding between fibre and matrix to evaluate local adhesion.* Composites science and technology, 2003. **63**(15): p. 2155-2162.

67. Kraus, R., et al., *Investigation of debonding processes in particle-filled polymer materials by acoustic emission: Part I Acoustic emission and debonding stress.* Journal of materials science, 1997. **32**(16): p. 4397-4403.

68. Mathis, K. and F. Chmelik, *Acoustic Emission*, W. Sikorski, Editor 2012, InTech.

69. Kiesewetter, N. and P. Schiller, *The acoustic emission from moving dislocations in aluminium.* Physica status solidi (a), 1976. **38**(2): p. 569-576.

70. Agarwal, A.B., J. Frederick, and D. Felbeck, *Detection of plastic microstrain in aluminum by acoustic emission.* Metallurgical and Materials Transactions B, 1970. **1**(4): p. 1069-1071.

71. Sedgwick, R.T., *Acoustic Emission from Single Crystals of LiF and KCl.* Journal of Applied Physics, 1968. **39**(3): p. 1728-1740.

72. Carpenter, S. and C.-m. Chen, *The acoustic emission generated during the plastic deformation of high purity zinc.* Journal of acoustic emission, 1988. **7**(4): p. 161-166.

73. Bohlen, J., et al., *On the influence of the grain size and solute content on the AE response of magnesium alloys tested in tension and compression.* Materials Science and Engineering: A, 2007. **462**(1–2): p. 302-306.

74. Knezevic, M., et al., *Deformation twinning in AZ31: Influence on strain hardening and texture evolution.* Acta Materialia, 2010. **58**(19): p. 6230-6242.

75. Koike, J., *Enhanced deformation mechanisms by anisotropic plasticity in polycrystalline Mg alloys at room temperature.* Metallurgical and Materials Transactions A, 2005. **36**(7): p. 1689-1696.

76. Talreja, R., *Damage and fatigue in composites – A personal account.* Composites Science and Technology, 2008. **68**(13): p. 2585-2591.

77. Anderson, T.L., *Fracture mechanics: Fundamentals and applications*. Third ed. 2005, Boca Raton, FL: CRC.

78. Ladeveze, P. and E.L. Dantec, *Damage modelling of the elementary ply for laminated composites.* 1992. **43**: p. 257-267.

79. Mehan, R.L. and J.V. Mullin, *Analysis of Composite Failure Mechanisms Using Acoustic Emissions.* Journal of Composite Materials, 1971. **5**(2): p. 266-269.

80. Ramirez-Jimenez, C., et al., *Identification of failure modes in glass/polypropylene composites by means of the primary frequency content of the acoustic emission event.* Composites Science and Technology, 2004. **64**(12): p. 1819-1827.

81. Huguet, S., et al., *Use of acoustic emission to identify damage modes in glass fibre reinforced polyester*. Composites Science and Technology, 2002. **62**(10): p. 1433-1444.

82. Hamstad, M.A., *A review: acoustic emission, a tool for composite-materials studies*. Experimental Mechanics, 1986. **26**(1): p. 7-13.

83. Barré, S. and M.L. Benzeggagh, *On the use of acoustic emission to investigate damage mechanisms in glass-fibre-reinforced polypropylene*. Composites Science and Technology, 1994. **52**(3): p. 369-376.

84. de Groot, P.J., P.A.M. Wijnen, and R.B.F. Janssen, *Real-time frequency determination of acoustic emission for different fracture mechanisms in carbon/epoxy composites*. Composites Science and Technology, 1995. **55**(4): p. 405-412.

85. Godin, N., et al., *Clustering of acoustic emission signals collected during tensile tests on unidirectional glass/polyester composite using supervised and unsupervised classifiers*. NDT & E International, 2004. **37**(4): p. 253-264.

86. Heiple, C. and S. Carpenter, *Acoustic emission produced by deformation of metals and alloys-A review*. Journal of Acoustic Emission, 1987. **6**: p. 177-204.

87. *3.2 Longitudinal and Transverse Waves*. Frazer does Physics, 2011.

88. Moore, P., *Ultrasonic Testing*. Nondestructive Testing Handbook, ed. G.L. Workman and D. Kishoni. Vol. 7. 2007.

89. Lingyu, Y., A.C.L. Cara, and T. Zhenhua, *Study on crack scattering in aluminum plates with Lamb wave frequency–wavenumber analysis*. Smart Materials and Structures, 2013. **22**(6): p. 065019.

90. MISTRAS *Acoustic Emission Sensors*. 2010.

91. Manthei, G. *Characterization of Acoustic Emission Sensors*. EWGAE 2010.

92. *Acoustic Emission Sensors*, V. Systeme, Editor 2012.

93. Kline, R.A., R.E. Green Jr, and C.H. Palmer, *A comparison of optically and piezoelectrically sensed acoustic emission signals.* The Journal of the Acoustical Society of America, 1978. **64**(6): p. 1633-1639.

94. Perez, I.M., H. Cui, and E. Udd. *Acoustic emission detection using fiber Bragg gratings*. in *SPIE's 8th Annual International Symposium on Smart Structures and Materials*. 2001. International Society for Optics and Photonics.

95. Read, I., P. Foote, and S. Murray, *Optical fibre acoustic emission sensor for damage detection in carbon fibre composite structures.* Measurement Science and Technology, 2002. **13**(1): p. N5.

96. Betz, D.C., et al., *Acousto-ultrasonic sensing using fiber Bragg gratings.* Smart Materials and Structures, 2003. **12**(1): p. 122.

97. Tadigadapa, S. and K. Mateti, *Piezoelectric MEMS sensors: state-of-the-art and perspectives.* Measurement Science and technology, 2009. **20**(9): p. 092001.

98. Ozevin, D., et al., *Resonant capacitive MEMS acoustic emission transducers.* Smart materials and structures, 2006. **15**(6): p. 1863.

99. Murayama, R. and K. Ayaka, *Evaluation of fatigue specimens using EMATs for nonlinear ultrasonic wave detection.* Journal of Nondestructive Evaluation, 2007. **26**(2-4): p. 115-122.

100. Murray, P. and R. Dewhurst, *Application of a laser/EMAT system for using shear and LS mode converted waves.* Ultrasonics, 2002. **40**(1): p. 771-776.

101. Lee, J.-R. and H. Tsuda, *A novel fiber Bragg grating acoustic emission sensor head for mechanical tests.* Scripta Materialia, 2005. **53**(10): p. 1181-1186.

102. Wild, G. and S. Hinckley, *Acousto-Ultrasonic Optical Fiber Sensors: Overview and State-of-the-Art.* Sensors Journal, IEEE, 2008. **8**(7): p. 1184-1193.

103. Wild, G. and S. Hinckley. *Fiber Bragg Grating Sensors for Acoustic Emission and Transmission Detection Applied to Robotic NDE in Structural Health Monitoring*. in *Sensors Applications Symposium, 2007. SAS '07. IEEE*. 2007.

104. Tsuda, H., *Ultrasound and damage detection in CFRP using fiber Bragg grating sensors.* Composites Science and Technology, 2006. **66**(5): p. 676-683.

105. Ning, J., et al. *Improving SNR of fiber Bragg grating sensor by digital signal processing* in *SPIE Nanophotonics and Macrophotonics for Space Environments* 2007. SPIE.

106. Welch, P.D., *The use of fast Fourier transform for the estimation of power spectra: a method based on time averaging over short, modified periodograms.* IEEE Transactions on audio and electroacoustics, 1967. **15**(2): p. 70-73.

107. Surgeon, M. and M. Wevers, *Modal analysis of acoustic emission signals from CFRP laminates.* Ndt & e International, 1999. **32**(6): p. 311-322.

108. Bartoli, I., et al., *Modeling guided wave propagation with application to the long-range defect detection in railroad tracks.* NDT & E International, 2005. **38**(5): p. 325-334.

109. Coifman, R.R., Y. Meyer, and V. Wickerhauser. *Wavelet analysis and signal processing*. in *In Wavelets and their Applications*. 1992. Citeseer.

110. Kronland-Martinet, R., J. Morlet, and A. Grossmann, *Analysis of sound patterns through wavelet transforms.* International Journal of Pattern Recognition and Artificial Intelligence, 1987. **1**(02): p. 273-302.

111. Loutas, T., et al., *Damage evolution in center-holed glass/polyester composites under quasi-static loading using time/frequency analysis of acoustic emission monitored waveforms.* Composites science and technology, 2006. **66**(10): p. 1366-1375.

112. Kishimoto, K., et al., *Time frequency analysis of dispersive waves by means of wavelet transform.* Journal of Applied Mechanics, 1995. **62**(4): p. 841-846.

113. Jeong, H. and Y.-S. Jang, *Wavelet analysis of plate wave propagation in composite laminates.* Composite Structures, 2000. **49**(4): p. 443-450.

114. Shen, L. and L. Bai, *A review on Gabor wavelets for face recognition.* Pattern Analysis and Applications, 2006. **9**(2-3): p. 273-292.

115. Marec, A., J.H. Thomas, and R. El Guerjouma, *Damage characterization of polymer-based composite materials: Multivariable analysis and wavelet transform for clustering acoustic emission data.* Mechanical Systems and Signal Processing, 2008. **22**(6): p. 1441-1464.

116. El-Ghamry, M., R. Reuben, and J. Steel, *The development of automated pattern recognition and statistical feature isolation techniques for the diagnosis of reciprocating machinery faults using acoustic emission.* Mechanical Systems and Signal Processing, 2003. **17**(4): p. 805-823.

117. Sause, M., et al., *Pattern recognition approach to identify natural clusters of acoustic emission signals.* Pattern Recognition Letters, 2012. **33**(1): p. 17-23.

118. Kostopoulos, V., et al., *On the identification of the failure mechanisms in oxide/oxide composites using acoustic emission.* NDT & E International, 2003. **36**(8): p. 571-580.

119. Olson, C.F., *Parallel algorithms for hierarchical clustering.* Parallel Computing, 1995. **21**: p. 1313-1325.

120. Likas, A., N. Vlassis, and J. J Verbeek, *The global< i> k</i>-means clustering algorithm.* Pattern recognition, 2003. **36**(2): p. 451-461.

121. Jain, A.K., *Data clustering: 50 years beyond K-means.* Pattern Recognition Letters, 2010. **31**(8): p. 651-666.

122. Johnson, M., *Waveform based clustering and classification of AE transients in composite laminates using principal component analysis.* NDT & E International, 2002. **35**(6): p. 367-376.

123. Oja, E., *Neural networks, principal components, and subspaces.* International journal of neural systems, 1989. **1**(01): p. 61-68.

124. Liu, Q., X. Chen, and N. Gindy, *Fuzzy pattern recognition of AE signals for grinding burn.* International Journal of Machine Tools and Manufacture, 2005. **45**(7): p. 811-818.

125. Omkar, S., et al. *Acoustic emission signal classification using fuzzy C-means clustering*. in *Neural Information Processing, 2002. ICONIP'02. Proceedings of the 9th International Conference on*. 2002. IEEE.

126. Philippidis, T., V. Nikolaidis, and A. Anastassopoulos, *Damage characterization of carbon/carbon laminates using neural network techniques on AE signals.* NDT & E International, 1998. **31**(5): p. 329-340.

127. Emamian, V., M. Kaveh, and A.H. Tewfik. *Robust clustering of acoustic emission signals using the Kohonen network*. in *Acoustics, Speech, and Signal Processing, 2000. ICASSP'00. Proceedings. 2000 IEEE International Conference on*. 2000. IEEE.

128. Marques de Sa, J.P., *Pattern Recognition*. Cocncepts, Methods and Application. 2001: Springer.

129. Farrar, C., R and K. Worden, *An introduction to structural health monitoring.* PHILOSOPHICAL TRANSACTIONS OF THE ROYAL SOCIETY, 2007. **365**: p. 303-315.

130. Rice, J.R., *ELASTIC WAVE EMISSION FROM DAMAGE PROCESSES.* Journal of Nondestructive Evaluation, 1980. **1**(4): p. 215-224.

131. Ohtsu, M. and K. Ono, *A Generalized Theory of Acoustic Emission and Green's Function in a Half Space.* Journal of Acoustic Emission, 1984. **3**: p. 27-40.

132. Andreykiv, O., et al., *Acoustic emission estimation of crack formation in aluminium alloys.* Engineering Fracture Mechanics, 2010. **77**(5): p. 759-767.

133. Khalifa, W.B., et al. *Analytical modelling of acoustic emission from buried or surface-breaking cracks under stress*. in *10th Anglo-French Physical Acoustics Conference, AFPAC 2011, January 19, 2011 - January 21, 2011*. 2012. Villa Clythia, Frejus, France: Institute of Physics Publishing.

134. Green, E.R., *Propagation of impact-induced stress waves in composite plates.* Journal of Nondestructive Evaluation, 1994. **13**(2): p. 45-54.

135. Giordano, M., L. Condelli, and L. Nicolais, *Acoustic emission wave propagation in a viscoelastic plate.* Composites Science and Technology, 1999. **59**: p. 1735-1743.

136. Prosser, W.H., et al., *Finite Element and Plate Theory Modeling of Acoustic Emission Waveforms.* Journal of Nondestructive Evaluation, 1999. **18**(3): p. 83-90.

137. Aberg, M., *Numerical modeling of acoustic emission in laminated tensile test specimens.* International Journal of Solids and Structures, 2001. **38**(36-37): p. 6643-6663.

138. Naber, R.R., H. Bahai, and B.E. Jones, *A reciprocal band-limited Green's function approach for modelling acoustic emission using finite element method.* Journal of Sound and Vibration, 2006. **292**: p. 802-823.

139. Sause, M.G.R., et al., *Pattern recognition approach to identify natural clusters of acoustic emission signals.* Pattern Recognit Lett, 2012. **33**(1): p. 7-7.

140. Sause, M.G.R. and S. Horn, *Simulation of Acoustic Emission in Planar Carbon Fiber Reinforced Plastic Specimens.* Journal of Nondestructive Evaluation, 2010. **29**(2): p. 123-142.

141. Ouyang, C., E. Landis, and S.P. Shah, *Damage Assessment in Concrete Using Quantitative Acoustic Emission.* Journal of Engineering Mechanics, 1991. **117**(11): p. 2681-2698.

142. Derode, A., et al., *How to estimate the Green's function of a heterogenous medium between two passive sensors? Application to acoustic wavesq.* Applied Physics Letter, 2003. **83**(15): p. 3054-3056.

143. Wapenaar, K., J. Fokkema, and R. Snieder, *Retrieving the Green's function in an open system by cross correlation: A comparison of approaches (L).* Journal of Acoustic Society of America, 2005. **118**(5): p. 2783-2786.

144. Minozzi, M., et al., *Dynamic fracture model for acoustic emission.* The European Physical Journal B, 2003. **36**: p. 203-207.

145. Sause, M.G.R. and S. Horn, *Simulation of Lamb Wave Excitation For Different Elastic Properties and Acoustic Emission Source Geomtries.* Journal of Acoustic Emission, 2010. **28**: p. 142-154.

146. Landa, M., et al., *Acoustic Emission Sources By Atomistic Simulations.* Journal of Acoustic Emission, 2002. **20**: p. 25-38.

147. (ATTAR), A.T.T.a.R. *Pressure Vessels. Inspection by monitoring Acoustic Emission*. TECHINFO, 2011.

148. Sause, M., *Identification of Failure Mechanisms in Hybrid Materials Utilizing Pattern Recognition Techniques Applied to Acoustic Emission Signals*, in *Department of Physics*2010, University of Augsburg: Germany.

149. Testing, A.S.o.N., *Acoustic Emission Testing*, in *Nondestructive Testing Handbook*, P.O. Moore, Editor 2005.

150. Berkovits, A. and D. Fang, *Study of fatigue crack characteristics by acoustic emission.* Engineering Fracture Mechanics, 1995. **51**(3): p. 401-416.

151. Meriaux, J., et al., *Identification of fretting fatigue crack propagation mechanisms using acoustic emission.* Tribology International, 2010. **43**(11): p. 2166-2174.

152. Chang, H., et al., *Acoustic emission study of fatigue crack closure of physical short and long cracks for aluminum alloy LY12CZ.* International journal of fatigue, 2009. **31**(3): p. 403-407.

153. Worden, K., G. Manson, and N.R.J. Fieller, *Damage detection using outlier analysis.* Journal of Sound and Vibration, 2000. **229**(Compendex): p. 647-667.

154. Rizzo, P., et al., *Wavelet-based outlier analysis for guided wave structural monitoring: Application to multi-wire strands.* Journal of Sound and Vibration, 2007. **307**: p. 52-68.

155. Sohn, H., et al., *Structural Health Monitoring using statistical pattern recognition techniques.* Jounnal of Dynamic Systems, Measurement and Control, 2001. **123**: p. 706-711.

156. Liang, W. and T.H.T. Chan, *Review of Vibration-Based Damage Detection and Condition Assessment of Bridge Structures using Structural Health Monitoring*, in *The Second Infrastructure Theme Postgraduate Conference: Rethinking Sustainable Development:Planning, Engineering, Design and Managing Urban Infrastructure*2009, QUT Queensland University.

157. Baxter, M.G., et al., *Delta T source location for acoustic emission.* Mechanical Systems and Signal Processing, 2007. **21**: p. 1512-1520.

158. Callus, P.J., et al., *Tensile properties and failure mechanisms of 3D woven GRP composites.* composites Part A: applied science and manufacturing, 1999. **30**: p. 1277-1287.

159. Bakis, C.E., et al., *Fiber-Reinforced Polymer Composites for Construction - Starte of the Art Review*. JOURNAL OF COMPOSITES FOR CONSTRUCTION, 2002. **6**: p. 73-87.

160. Van der Walde, K., et al., *Multiple fatigue crack growth in pre-corroded 2024-T3 aluminum.* International Journal of Fatigue, 2005. **27**(10–12): p. 1509-1518.

161. Chen, G.S., et al., *Transition from pitting to fatigue crack growth—modeling of corrosion fatigue crack nucleation in a 2024-T3 aluminum alloy.* Materials Science and Engineering: A, 1996. **219**(1–2): p. 126-132.

162. Diamanti, K. and C. Soutis, *Structural health monitoring techniques for aircraft composite structures.* Progress in Aerospace Sciences, 2010. **46**(8): p. 342-352.

163. Soutis, C., *Carbon fiber reinforced plastics in aircraft construction.* Materials Science and Engineering: A, 2005. **412**(1–2): p. 171-176.

164. Ye, L., et al., *Functionalized composite structures for new generation airframes: a review.* Composites Science and Technology, 2005. **65**(9): p. 1436-1446.

165. Katnam, K.B., L.F.M. Da Silva, and T.M. Young, *Bonded repair of composite aircraft structures: A review of scientific challenges and opportunities.* Progress in Aerospace Sciences, 2013. **61**(0): p. 26-42.

166. Krueger, R., et al., *Testing and Analysis of Composite Skin/Stringer Debonding under Multi-Axial Loading.* Journal of Composite Materials, 2000. **34**: p. 1263-1300.

167. Polimeno, U. and M. Meo, *Detecting barely visible impact damage detection on aircraft composite structures.* Composite Structures, 2009. **91**: p. 398-402.

168. Bisagni, C. and L. Lanzi, *Post-buckling optimisation of composite stiffened panels using neural networks.* Composite Structures, 2002. **58**(2): p. 237-247.

169. Anderson, M. *Recent exam failed to detect weak Sabo Bridge Cable*. 2012.

170. Sousa Coutinho, J., *The combined benefits of CPF and RHA in improving the durability of concrete structures.* Cement and Concrete Composites, 2003. **25**(1): p. 51-59.

171. Voon, K. and J. Ingham, *Experimental In-Plane Shear Strength Investigation of Reinforced Concrete Masonry Walls.* Journal of Structural Engineering, 2006. **132**(3): p. 400-408.

172. Guan, H., C. Cooper, and D.-J. Lee, *Ultimate strength analysis of normal and high strength concrete wall panels with varying opening configuratiosn.* Engineering Structures, 2010. **32**: p. 1341-1355.

173. Hidalgo, P.A., R.M. Jordan, and M.P. Martinez, *An analytical model to predict the inelastic seismic behavior of shear-wall, reinforced concrete structures.* Engineering Structures, 2002. **24**(1): p. 85-98.

174. Carrillo, J. and S.M. Alcocer, *Seismic performance of concrete walls for housing subjected to shaking table excitations.* Engineering Structures, 2012. **41**(0): p. 98-107.

175. Shing, P., M. Schuller, and V. Hoskere, *In-Plane Resistance of Reinforced Masonry Shear Walls.* Journal of Structural Engineering, 1990. **116**(3): p. 619-640.

176. McCann, D.M. and M.C. Forde, *Review of NDT methods in the assessment of concrete and masonry structures.* NDT & E International, 2001. **34**(2): p. 71-84.

177. Benavent, A., E. Castro, and A. Gallego, *Evaluation of low-cycle fatigue damage in RC exterior beam-column subassemblages by acoustic emission.* Construction and Building Materials, 2010. **24**(10): p. 1830-1842.

178. Lecompte, D., J. Vantomme, and H. Sol, *Crack Detection in a Concrete Beam using Two Different Camera Techniques.* Structural Health Monitoring, 2006. **5**(1): p. 59-68.

179. Casey, N.F., H. White, and J.L. Taylor, *Frequency analysis of the signals generated by the failure of constituent wires of wire rope.* NDT INTERNATIONAL, 1985. **18**(6): p. 339-344.

180. Pan, B., et al., *Two-dimensional digital image correlation for in-plane displacement and strain measurement: a review.* Measurement Science and Technology, 2009. **20**(6): p. 062001-062001.

181. Pappas, Y.Z., et al., *On the characterization of continuous fibres fracture by quantifying acoustic emission and acousto-ultrasonics waveforms.* NDT&E International, 2004. **37**(5): p. 389-401.

182. Pan, B., *Recent Progress in Digital Image Correlation.* Experimental Mechanics, 2010. **51**(7): p. 1223-1235.

183. Kostopoulos, V., et al., *On the identification of the failure mechanisms in oxide/oxide composites using acoustic emission.* NDT&E International, 2003. **36**(8): p. 571-80.

184. Sutton, M.A., J.J. Orteu, and H.W. Schreier, *Image Correlation for Shape, Motion and Deformation Measurements: Basic Concepts, Theory and Applications*. 2009: Springer.

185. Rizzo, P., *Ultrasonic Wave Propagation in Progessively Loaded Multi-Wire Strands.* Experimental Mechanics, 2006. **46**: p. 297-306.

186. Treyssede, F. and L. Laguerre, *Investigation of elastic modes propagating in multi-wire helical waveguides.* Journal of Sound and Vibration, 2010. **329**(10): p. 1702-1716.

187. Chaki, S. and G. Bourse, *Guided Ultrasonic waves for non-destructive monitoring of the stress levels in prestressed steel strands.* Ultrasonics, 2009. **49**: p. 162-171.

188. Kontsos, A., I. Bartoli, and P.A. Vanniamparambil, *Integration of digital image correlation with acoustic emissions*, in *Under Publication (WO2013158933 A1)* U.S.P. Organization, Editor 2013: USA.

189. Sause, M. and S. Horn, *Simulation of Acoustic Emission in Planar Carbon Fiber Reinforced Plastic Specimens.* Jounal of Nondestructive Evaluation, 2010. **29**: p. 123-142.

190. Ince, N.F., et al., *A machine learning approach for locating acoustic emission.* EURASIP J. Adv. Signal Process, 2010. **2010**: p. 1-14.

191. Worden, K. and G. Manson, *The application of machine learning to structural health monitoring.* Philosophical Transactions of the Royal Society A: Mathematical, Physical and Engineering Sciences, 2007. **365**(1851): p. 515-537.

192. *Temperature effects in ultrasonic Lamb wave structural health monitoring systems.* The Journal of the Acoustical Society of America, 2008. **124**(1): p. 161.

CURRICULUM VITAE

PRASHANTH ABRAHAM

2200 BENJAMIN FRANKLIN PKWY, E1706, PHILADELPHIA, PA-19130
TEL : 267 456 3703, EMAIL : prashanth288@gmail.com
WEB: prashanthabraham.wordpress.com

EDUCATION

- June, 2014**: PhD**, Mechanical Engineering, Drexel University, GPA: 3.82/4.0
  Thesis: *A Novel Cross-Validated approach for damage detection using Acoustic Emission*
- June, 2010 : **B.S./M.S.**, Mechanical Engineering, Drexel University, GPA: 3.4/4.0
  Project : *Mechanical Water Softener using Plasma Discharge*

PROFESSIONAL EXPERIENCE

Theoretical & Applied Mechanics Group (TAMG), Drexel University
Philadelphia, PA

Research Associate **September 2010 to present**

Project 1: Identification of Crack growth in Aluminum Alloys (Sponsored by Office of Naval Research)

- Serving as the lead engineer and developing detailed test plans and data acquisition strategies for optimal damage detection
- Designing novel multi-sensing NDT techniques and implementing data fusion algorithms for material characterization and the identification of crack initiation
- Manufacturing experimental specimens based on ASTM standards to confirm to stringent test protocols
- Performing specimen preparation and investigating the micro-structural deformation effects using scanning electron microscope (SEM) and optical microscopy
- Validating experimental data signals with data driven physics based finite element modeling for reliable source interpretation

Project 2: Bond-Line Monitoring in Carbon Fiber Wing Components (Sponsored by NAVAIR)

- Fabricated composite skin spar components in accordance with aerospace standards to implement an in-situ approach for bond-line evaluation and performed 3 point bending fatigue experiments
- Successfully implemented an in-situ acoustics based approach for the identification of debonding in carbon fiber reinforced polymer composite skin spar components
- Utilized Acoustic Emission testing in conjunction with Guided Ultrasonic testing and Digital Image Correlation techniques for fatigue characterization of composite materials

- Performed finite element simulations to model the ultrasound wave propagation effects in the anisotropic medium and identify critical NDT features related to debonding.
- Investigated the feasibility of implementing wireless health monitoring sensors for onboard aircraft applications.

Project 3: Enhancement of Seismic Performance and Design of Partially-Grouted Reinforced Masonry Buildings (Sponsored by National Science Foundation)

- Performed full field deformation measurements using high speed imaging techniques to identify the critical failure regions in a full scale masonry building in collaboration with University of California, San Diego
- Correlated full field in-plane strain measurements using non contact sensors with traditional strain gages to evaluate the feasibility of developing novel health monitoring techniques for infrastructure monitoring
- Identified damage precursors prior to visual indications of critical damage for optimal structural performance and safety

INTERNSHIPS

Systra Consulting, Inc
Philadelphia, PA

Design Assistant **October, 2007 to March, 2008**

- Performed engineering surveys and field investigations to determine the structural impact on electrical and mechanical equipment for the expansion of Madison Square Garden and Penn Station, NY
- Reviewed quality assurance of mechanical systems to co-ordinate with Architectural and Electrical Department and provided efficient design layouts to implement the new products

SKILLS

- Transferrable Skills: Strategic Planning, Technical Writing, Project Management
- Application Programs: Noesis, AEwin, Origin, ARAMIS, ExaminIR, LabVIEW, Wavegen, Abaqus, Pro/Engineer, SolidWorks, AutoCAD, Microsoft Office Suite
- Programming Languages: MATLAB

SELECTED JOURNAL PUBLICATIONS (DETAILED LIST UPON REQUEST)

- **Vanniamparambil, P.A**., Bolhassani, M., Carmi, R., Khan, F., Bartoli, I., Moon, F., Hamid, A., and Kontsos, A. (2014) " A data fusion approach for progressive damage quantification in reinforced concrete masonry walls." Smart Materials and Structures, 23 (1), 015007
- Cuadra, J., **Vanniamparambil, P.A.,** Hazeli, K., Bartoli, I. and Kontsos, A. (2013) "Damage Quantification in Polymer Composites using a Hybrid NDT Approach." Composites Science & Technology, 83: 11-21
- **Vanniamparambil, P. A.**, Bartoli, I., Hazeli, K., Cuadra, J., Schwartz, E., Saralaya, R., Kontsos, A. (2012). "An integrated structural health monitoring approach for crack growth monitoring." Journal of Intelligent Material Systems and Structures 23(14): 1563-1573

SELECTED CONFERENCE PROCEEDINGS/PRESENTATIONS (DETAILED LIST UPON REQUEST)

- **Vanniamparambil, P.A.,** Carmi, R. Khan, F., Bartoli, I., Kontsos, A., "*Novel Optico-Acoustic Sensing System for Cross-validated Structural Health Monitoring*". 11th International Conference on Structural Safety & Reliability, New York, June 2013
- Bartoli, I., Aktan, E., Kontsos, A., **Vanniamparambil**, **P.A**., Hazeli, K., "*An Integrated Health Monitoring Approach for Damage Quantification in Critical Structural Components*". EACS 5th European Conference on Structural Control, Genoa, Italy, June 2012

ACTIVITIES

Secretary, Graduate Student Association **July, 2013 - July.2014**

- Developing a graduate career development network in collaboration with the Office of Graduate Studies, Steinbright Career Development Center and Drexel Alumni Association
- Organizing student life activities and professional development workshop for the Drexel graduate student community
- Coordinating meetings with various executive and administrative board members on a monthly basis for strategic planning, project implementation, etc